

Charles University in Prague
Faculty of Mathematics and Physics

DOCTORAL THESIS



Milan Berta

**Development and applications of
near-field imaging methods in the
terahertz spectral domain**

2010

Advisor: Dr. Filip Kadlec

Department of Dielectrics

Institute of Physics

Academy of Sciences of the Czech Republic

Study programme: F6 – Optics and Quantum Optics

Egy, kettő, három,...

Egy – megérett a meggy.

Kettő – feneketlen teknő.

Három – te vagy az én párom.

Négy – megcsípett a légy.

Öt – érik a tök.

Hat – leszakadt a pad.

Hét – zsemlét süt a pék.

Nyolc – tele a polc.

Kilenc – kis Ferenc.

Tíz – tiszta víz,

Ha nem tiszta, vidd vissza,

A kis cica megissza.

– magyar játékmondóka

Drága Szüleimnek.

Acknowledgements

Any attempt at any level cannot be satisfactorily completed without the support and guidance of learned people. There are various people to whom I wish to express my sincere gratefulness for their help and encouragement while completing the work described in the thesis.

I would like to express my deepest gratitude to my supervisor Dr. Filip Kadlec for his patient guidance, enthusiastic encouragement and useful critiques of this research work and the manuscript.

It is my pleasure to thank Dr. Petr Kužel and Prof. Norbert Klein for their inspiring thoughts and their assistance with the collection of my data in the laboratories of the **terahertz (THz)** group and department IBN-2, Forschungszentrum Jülich (FZJ), Germany, respectively.

It is my pleasure to thank doc. RNDr. Jiří Bok, CSc. (Faculty of Mathematics and Physics of the Charles University) whose lecture provoked me to look at my data from a different point of view and to imagine the $(n + 1)^{\text{th}}$ dimension.

Furthermore, I would like to express my gratitude to Ing. Jiří Hlinka, Ph.D. for his support and tricky questions, to the LAO company for technical support, to Dr. Dagmar Chvostová and Dr. Martin Kittler for measurements on surface profiles of the samples, to Dr. Sergey Leshkov (Institute of Photonics and Electronics of the AS CR) for metallisation of the Teflon probes, and to Petr Ondrejkoč and Fedir Borodavka for Micro-Raman measurements.

Support by the Mechanical and Optical Workshop of the **Institute of Physics of the AS CR, Prague (IoP)**, especially by Antonín Bleha for machining works, by Jiří Fryšťacký for polishing the silicon, the sapphire probes and the samples, by Dr. Jan Fábry for advises on chemical processing and by my closest colleagues and staff of the Department of Dielectrics through listening to and discussing is also very much acknowledged.

I would like to thank the members of the IBN-2 group for their assistance during my stay and work in FZJ, Germany, especially to Dr. Svetlana Vitusevich and to former members Dr. Sergey Danylyuk and Dr. Peter Lahl. Measurements in the microwave region were conducted in cooperation with Dr. Sergey Danylyuk, Dr. Ulrich Poppe and Prof. Norbert Klein (FZJ, Germany). Technical support by Stefan Kirch from the local IT group is also acknowledged.

I wish to thank my parents for their support and encouragement throughout all my studies, as well as to my closest friends for their constant support and friendship.

Last, but not least, I would like to acknowledge financial support by the Grant Agency of the Charles University (project 105 509), by the Ministry of Education of the Czech Republic (project LC-512) and by the Czech Academy of Sciences (project AVOZ 10100520).

Declaration and confession

I declare that the thesis hereby submitted for the Philosophiae Doctor degree at the Charles University in Prague is my own work and has not been previously submitted by me at another University for any degree. I confess I have written my doctoral thesis on my own, using only quoted sources. I agree with lending of the thesis.

in Prague, on September 10, 2010
Milan Berta

Abstrakt v českém jazyce

Název doktorské práce: Vývoj a využití zobrazovacích metod v blízkém poli v terahertzové spektrální oblasti

Autor: RNDr. Milan Berta

E-mailová adresa autora: milan.bera@gmail.com

Školitel: Dr. Filip Kadlec

E-mailová adresa školitele: kadlec@fzu.cz

Školící pracoviště: Oddělení dielektrik, Fyzikální ústav AV ČR, v. v. i. v Praze, Na Slovance 2, CZ-182 21 Praha 8

Konzultanti: Prof. Norbert Klein a Dr. Petr Kužel

Abstrakt: Předkládáme výsledky studia citlivosti a rozlišení kovově–dielektrických sond určených k zobrazování v blízkém poli. Šíření elektromagnetického pole sondou bylo experimentálně studováno pomocí časově rozlišené terahertzové spektroskopie a numericky modelováno v prostředí CST MicroWave Studio® 2008. V blízkosti koncové plochy sondy bylo nalezeno několik zón citlivých na lokální dielektrické vlastnosti a lokální anizotropii vzorků. Byla provedena měření citlivosti a kontrastu v několika různých uspořádáních sondy a vzorků; výsledky byly potvrzeny numerickými simulacemi. Získaná data byla analyzována metodou singulárního rozkladu, která umožnila rozlišit nezávislé fyzikální jevy v měřených datech a oddělit vnější vlivy od užitečného signálu. Byly odděleny a rozpoznány nezávislé složky odpovídající charakteristickým změnám ve výstupním terahertzovém pulzu, například při změnách vzdálenosti sondy a vzorku, a při zkoumání lokální anisotropie ferroelektrického krystalu titaničitanu bárnatého (BaTiO_3). V zobrazení vzorku ferroelektrického BaTiO_3 byly rozpoznány doménové struktury s charakteristickým rozměrem $5\ \mu\text{m}$, t. j. s rozměrem desetkrát menším než byly charakteristické rozměry výstupní plochy sondy a čtyřicetkrát menším než byla nejkratší vlnová délka použitého záření. V terahertzové spektrální oblasti jsme prozkoumali citlivost sondy na index lomu pomocí několika vzorků s volným povrchem a následně s povrchem přikrytým polyetylenovým filmem. Tenký plastový film zapříčinil snížení citlivosti sondy na index lomu vzorků pod ním, ale přesto umožňoval jejich rozpoznávání. Vynaložili jsme úsilí na zhotovení dvojitě kovově–dielektrické sondy složené ze dvou spojených sond s cílem zvýšit rozlišení zobrazování. Zobrazovací experimenty na vzorku s kontrastem kov–dielektrikum prokázaly funkčnost této dvojsondy.

Klíčová slova: mikroskopie s rozlišením pod difrakčním limitem, zobrazování v blízkém poli, dielektrické vlnovody, terahertzové a mikrovlonné záření

Abstract in English

Title: Development and applications of near-field imaging methods in the terahertz spectral domain

Author: M.Sc. Milan Berta

Author's e-mail address: milan.bertha@gmail.com

Advisor of the doctoral work: Dr. Filip Kadlec

Advisor's e-mail address: kadlec@fzu.cz

Training institute: Department of Dielectrics, Institute of Physics of the AS CR, Na Slovance 2, CZ-182 21 Prague 8

Consultants: Prof. Norbert Klein and Dr. Petr Kužel

Abstract: We are reporting on a study of the near-field sensitivity and resolution of a **metal-dielectric probe (MDP)**. The propagation of the electromagnetic field across the probe was studied experimentally by means of time-domain terahertz spectroscopy and numerically simulated by CST MicroWave Studio® 2008. Several localised areas at the probe end facet were distinguished and showed to be sensitive to the local dielectric properties and local anisotropy of the sample. Contrast and sensitivity measurements were conducted in several configurations of a **MDP**; the results were confirmed by simulations. The acquired data were analysed by using singular value decomposition that enabled separating independent physical phenomena in the measured datasets and filtering external disturbances out of the signal. Independent components corresponding to the changes in the output terahertz pulse upon varying the probe-sample distance and reflecting the local anisotropy in a ferroelectric **barium titanate (BaTiO₃)** crystal were extracted and identified. The domain structure with characteristic dimensions of about 5 µm was resolved during imaging experiments on the ferroelectric **BaTiO₃** sample, i. e. the resolved structures were ten times smaller than the characteristic dimensions of the end facet of the probe and forty times smaller than the shortest wavelength employed. Sensitivity of the **MDP** to refractive index was examined employing samples with bare surfaces and consequently with Mylar-covered surfaces. The thin coverage of Mylar film slightly decreased the sensitivity of the probe to the refractive index of the sample underneath, but it still allowed distinguishing among samples. Effort has been put forth to manufacture a metal-dielectric dual probe consisting of two joined **MDPs** with the aim to enhance the resolution at imaging. Imaging experiments demonstrated the sensitivity of the dual probe on a sample with metal-dielectric contrast.

Keywords: microscopy with subwavelength resolution and near-field imaging, dielectric waveguides, terahertz and microwave radiation

Publications

Some ideas and figures have appeared previously in the following publications:

M. Berta and F. Kadlec. Near-field terahertz imaging of ferroelectric domains in barium titanate. *Phase Transitions*, (in print):1–9, 2010.

M. Berta, P. Kužel, and F. Kadlec. [Study of responsiveness of near-field terahertz imaging probes](#). *Journal of Physics D: Applied Physics*, 42(15):155501(6pp), Aug. 2009. [10.1088/0022-3727/42/15/155501](https://doi.org/10.1088/0022-3727/42/15/155501).

Table of Contents

Titlepage	a
Acknowledgements	ii
Declaration and confession	iii
Abstrakt v českém jazyce	iv
Abstract in English	v
Publications	vi
Table of Contents	vii
List of Figures	xi
List of Tables	xiv
Preface	xv
1 Terahertz radiation, spectroscopy and near-field imaging	1
1.1 Terahertz spectrum and terahertz radiation	1
1.1.1 Fundamental applications	3
1.1.2 Safety issues	4
1.2 Sources	5
1.2.1 Glow lamps	6
1.2.2 Sources based on de-/accelerating charged particles	6
1.2.3 Coherent sources (THz lasers)	7

1.2.4	Sources based on Cherenkov-like phenomena	8
1.2.5	Semiconductor electronics sources	8
1.2.6	Sources employing nonlinear optical properties of crystals	9
1.2.6.1	Photomixers	9
1.2.6.2	Sources based on electro-optical rectification	9
1.2.6.3	Surface emitters	10
1.2.6.4	Sources based on photoconductive switching	10
1.2.6.5	Frequency multipliers	12
1.2.6.6	Sources based on parametric amplification	13
1.3	Detectors	13
1.3.1	Detectors based on thermal effects of the THz radiation	13
1.3.2	Detecting broadband pulses	14
1.3.2.1	Detectors based on electro-optical (Pockels) effect	14
1.3.2.2	Photoconductive detection	15
1.3.3	Other detector types	15
1.4	Time-domain terahertz spectroscopy	15
1.5	Noise and artefacts in the TDS system	17
1.6	Terahertz pulse imaging	19
1.7	The near-field and far-field spatial zones	21
1.7.1	The near-field region	22
1.7.2	The far-field region	23
1.8	Feature resolution in imaging	23
1.8.1	Improving the spatial resolution	24
1.9	Overview of the concepts for near-field imaging techniques	26
1.9.1	Tip-enhanced near-field techniques	26
1.9.2	Imaging techniques involving an optical laser beam	30
1.9.3	Tip-enhanced terahertz apertureless near-field optical microscopy	31
1.9.4	Aperture-based near-field techniques	31
1.9.5	Confinement methods	32
1.10	Waveguides and transmission lines	33
1.11	Properties of some materials in the THz frequency range	36
2	Data acquisition and treatment	39
2.1	Metal-dielectric pyramid-shaped probes	39

2.1.1	Characterisation of the probes	40
2.1.2	Teflon probes	43
2.1.3	Concept of the dual probes	44
2.2	Experimental configuration for the terahertz measurements	46
2.2.1	Mounting of the probes	51
2.2.2	Characterisation of the THz beam	52
2.2.3	Optimisation of the coupling of the radiation	54
2.3	Continuous-wave microwave measurements	55
2.4	Computer simulations	56
2.5	Structure of the data obtained at experiments	61
2.6	Multivariate analysis	62
2.7	Data analysis, data manipulation and data extraction	65
2.7.1	Data pretreatment (prewhitening)	66
2.7.1.1	Justification of the pretreatment	67
2.7.2	Singular value decomposition	68
2.7.2.1	Correlation coefficient between two variables/vectors	72
2.7.3	Software environments employed for analyses	73
2.7.3.1	R Project	73
2.7.3.2	Unscrambler	73
3	Results	74
3.1	Experiments preceding the work in the thesis	74
3.2	Fundamental preliminary experiments	75
3.3	Experimental configurations	79
3.4	Calibration and removing artifacts	81
3.5	Characterisation of the field of the MDP	83
3.5.1	On-axis distribution of the THz field	84
3.5.2	In-plane distribution of the THz field	86
3.6	Broadband measurements without spatial resolution	97
3.7	Broadband measurements with spatial resolution	99
3.7.1	Polarisation and anisotropy sensitivity	99
3.7.2	Imaging of BaTiO ₃ domains – sample	102
3.7.3	Imaging of BaTiO ₃ domains – results and discussion	103
3.7.4	Electromagnetic simulations of the domain-stripes	110

3.8	Resolution and sensitivity specification of the dual probes	111
3.8.1	Preparing and positioning of the MDDP	111
3.8.2	Scans by a dual probe with spatial resolution	114
3.9	Continuous-wave microwave measurements	118
4	Conclusions	120
	Nomenclature	125
	List of Acronyms	127
	Bibliography	130

List of Figures

1.1	Electromagnetic spectrum spanning from low-frequencies to γ -rays	2
1.2	Scheme of a photoconductive switch	11
1.3	Photoconductive current and photoconductive emission	12
1.4	Scheme of electro-optical detection	14
1.5	Schematic drawing of a TDTS setup	16
1.6	Emission of a source with a sub-wavelength surface roughness	21
1.7	Interaction of a plane wave with a sub-wavelength structure	22
1.8	Applying classical resolution criteria to two point objects	25
1.9	Near-field techniques (i–vi)	27
1.9	Near-field techniques (vii–xii)	29
1.10	Basic types of transmission lines	34
1.11	Basic types of waveguides	35
2.1	Schematic picture of a metal-dielectric probe (MDP)	40
2.2	Tapering of the MDPs	41
2.3	The holder for manufacturing Teflon probes	43
2.4	Single- and dual-probe concept	45
2.5	Sensitive areas of a dual probe (simulation model)	47
2.6	Schematic drawing of the THz near-field imaging setup	48
2.7	Path of the terahertz beam in the THz setup.	49
2.8	Typical THz waveform reflected from the input facet of the probe	50
2.9	Mounting for probes	51
2.10	Setup for characterising the THz beam waist	52
2.11	Spatio-frequency pattern of the THz beam waist	53
2.12	Metallic horn launcher (photo and simulations)	56

2.13	Guiding of the radiation in the CW-MW and the TD-THz setups	57
2.14	Standing wave in the resonator of MDP (simulations)	57
2.15	CW-MW setup (I): the stepped frequency generator and the positioning stage.	58
2.16	CW-MW setup (II): the holders of samples and MDPs.	58
2.17	Model of a MDP: a capacitor and a transmission line	59
2.18	Silicon probe polished and metallised in a scattering-electron microscope.	59
2.19	Representation of the measurement dataset in a 3D plot and a matrix	62
2.20	Graphical depiction of the SVD and its products	70
3.1	Characterising the THz spectrum by reflection on an aluminium mirror	75
3.2	Input- and end-facet reflections in a sapphire and in a silicon probe	76
3.3	Preliminary measurements on sensitivity of the MDP	77
3.4	Response of a probe touching a wet tissue	78
3.5	Approximation of the transient pulse by two scaled input pulses	78
3.6	Experimental configurations for studying the characteristics of a probe and a sample	80
3.7	Influence of the air-flow and temperature instability onto the signal	82
3.8	Series of simulations with a varying tip-sample distance (decomposition)	85
3.9	Series of simulations with a varying tip-sample distance (summation of components)	87
3.10	Series of simulations with a varying tip-sample distance (spatio-temporal layers (SMs))	88
3.11	Contributions to the radiation field (experiments).	89
3.12	Experimental and simulated datasets in a frequency independent scale	90
3.13	Tip in a coordinate system (model)	91
3.14	Projections of the field components at the tip (simulations)	92
3.15	Metal-dielectric sample used for contrast measurements	94
3.16	Scans of a sample with a metal-dielectric contrast by a Teflon and by a sapphire probe	94
3.17	Scanning of a metal-dielectric boundary	95
3.18	Interaction areas at the end facet of a MDP	96
3.19	Scanning of a metal-dielectric sample with a titled Teflon probe	96
3.20	Sensitivity of the probe to different materials	97
3.21	Components of the sensitivity measurements	98

3.22	Analyses of a rotation dependent measurements on a BaTiO ₃ sample (decomposition)	100
3.23	Analyses of a rotation dependent measurements on a BaTiO ₃ sample (naked eye observation)	101
3.24	Scanning the spontaneous polarisation in BaTiO ₃ domains (photo)	102
3.25	Spontaneous polarisation in BaTiO ₃ domains (model)	103
3.26	Scanned area D (brief comparison)	104
3.27	Scanned area A (overview of main results)	106
3.28	Scanned area B (overview of main results)	107
3.29	Scanned area C (overview of main results)	108
3.30	Scanned area D (overview of main results)	109
3.31	Overview of the results of a simulation on a domain stripe	110
3.32	Dual-probe under a microscope	112
3.33	Scheme of the sequential alignment of the dual probe	113
3.34	Linear scans over a metal-dielectric sample by a MDDP (I): time profiles of the SVD products	115
3.34	Linear scans over a metal-dielectric sample by a MDDP (II): spatial profiles of the SVD products	116
3.35	Spatial profiles of the scans <i>E</i> and <i>F</i> (detailed comparison)	117
3.36	Height measurements in the CW-MW setup	118

List of Tables

1.1	Maxwell's Equations in their classical continuous differential and integral forms.	3
1.2	Material parameters of the samples under investigation	37
2.1	Workflow for data processing	69

Preface

In 2004 preliminary experiments were made in the laboratory of the **terahertz (THz)** group of the **Institute of Physics of the AS CR, Prague (IoP)** to show the possibility of near-field THz measurements with a new method based on radiation waveguiding and focusing [Klein et al., 2005]. The concept consists in concentrating a significant part of a single pulse into an area much smaller than the wavelength used, very close to the sample surface. The idea came from cooperation between Priv. Doz. Norbert Klein (then head of the **microwave (MW)** research group Forschungszentrum Jülich, Germany), and Dr. Filip Kadlec and Dr. Petr Kužel (head of the local **THz** research group), and it became the base of a patent application later. The results of these experiments have shown the potential of the method and the worth of focusing on improving the resolution and sensitivity of the near-field probe in this concept. In that year the **THz** group had also obtained a new room, and shortly, work had been started on building a new **THz** (pulsed) near-field setup from scratch to continue and develop the technique there.

The aim of the present work is to investigate a specific near-field imaging technique suitable for the **THz** and **MW** frequency regions, both experimentally and theoretically. We describe the principles of the experiment and compare it with the state-of-art techniques. We present the experimental setup, the improvements made during the work and the obtained results.

The thesis is divided into four chapters, as follows:

- ◇ Chapter 1 gives an introduction to the subject of the **THz** radiation as well as to imaging, spatial resolution and concepts of near-field imaging. We compare our method to the alternative ones within their principal and also technical differences.
- ◇ In chapter 2 we describe the tools used for obtaining all the data to be evaluated: the probes, the experimental setup in **MW** and **THz** frequency domains, the simulation tool, the structure of our datasets and the application of the method of singular value decomposition, which helped us with data-mining.
- ◇ In chapter 3, we present the original experimental results and compare them to results from simulations, part of which was published earlier [Berta and Kadlec, 2010; Berta

[et al., 2009](#)]. We present results of the preliminary experiments, of the distribution and characteristics of the electromagnetic field at the end of our probe, of the broadband measurements with and without spatial resolution, of the MW measurements and results of the sensitivity of a dual probe.

◇ Chapter 4 summarises and draws conclusions on the presented work.

The electronic version of this document in a PDF format is available upon request at milan.bera@gmail.com for personal needs only. It contains coloured hyperlinks to cross-references and to citations and is identical with the printed publication regarding the content and the format.

Chapter 1

Terahertz radiation, spectroscopy and near-field imaging

In this chapter, we introduce the reader to properties of the **terahertz (THz)** radiation (section 1.1), to techniques for generating and detecting it (sections 1.2 and 1.3), to THz spectroscopy and imaging (sections 1.4 and 1.6), as well as to requirements for imaging with subwavelength resolution (sections 1.7 and 1.8). We explain the concepts behind various techniques used for near-field imaging in the THz frequency range in the past and in the present (section 1.9). Further, a theoretical description is given on waveguides and transmission lines (section 1.10), and at the end, we summarise the properties of the materials that were under study in our experiments (section 1.11).

1.1 Terahertz spectrum and terahertz radiation

Until the early 1980s the electromagnetic spectrum (see fig. 1.1) was loosely divided into two broad areas. The frequencies belonging to the radio and **microwave (MW)** regions ($\lesssim 100$ GHz) were accessed directly with *electronics*, while the frequencies of **infrared (IR)** radiation and above ($\gtrsim 2$ THz) were handled by *photonics*, by the production of photons through quantum transitions [Hwang and Lin, 2007]. The frequency range between the MW and IR hardly accessible, because the electron mobility, crucial for MW techniques, is rapidly decreasing towards higher frequencies, and because of the lack of semiconductor materials with a wide-enough band-gap. This electromagnetic-frequency range between MW and IR waves which

spans over frequencies from 0.1 to 10 THz (according to a commonly accepted definition) is named the the THz gap, THz radiation, THz waves, terawaves, submillimetre radiation, millimetre band, millimetre wave (sometimes abbreviated MMW or mmW), THz light, T-rays, T-light, T-lux, or simply THz. The term T-rays was originally coined by Bell Labs in the mid-1990s, and it gained the most popularity in commerce, but the scientific community still did not fully agree on the best choice of the name of the frequency-domain (FD) [Abbott and Zhang, 2007].

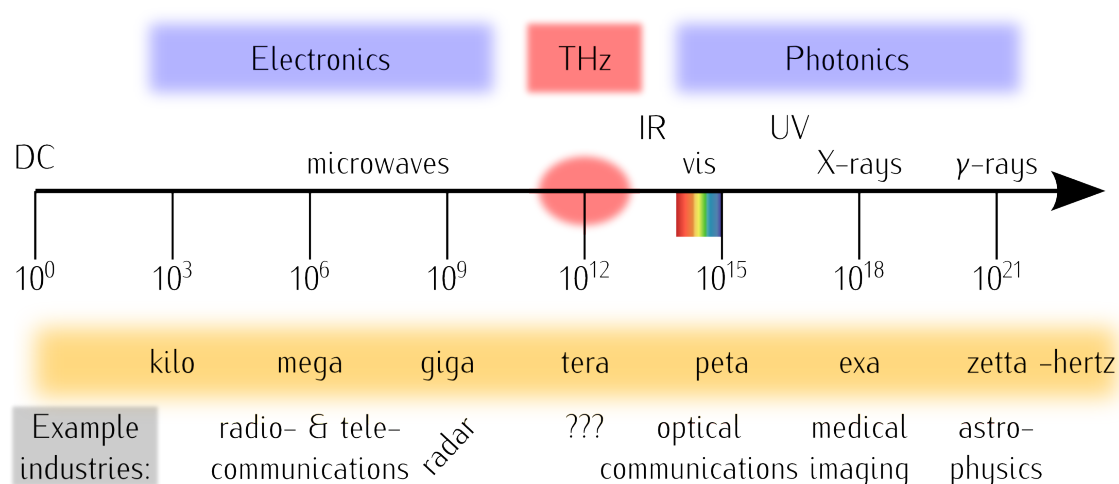


Figure 1.1: Each decade of the electromagnetic spectrum spanning from low-frequencies to γ -rays has its own merits. Examples of industries are displayed below a specific spectral domain. Industries are typical for the domains or are using the domains preferentially. One of the least explored frequency domain is the THz, and it conceals potentiality for many industries.

In recent years there have been many publications released presenting an overview of the current knowledge about T-rays and their use to the wide scientific community, e. g. [Dexheimer, 2007; Lee, 2008; Mittleman, 2004; Sakai, 2005; Tonouchi, 2007].

The value of frequency ν of 1 THz can be expressed by various units as follows:

$$1 \text{ THz} \sim 1 \text{ ps} \sim 300 \mu\text{m} \sim 33 \text{ cm}^{-1} \sim 4.14 \text{ meV} \sim 48 \text{ K}. \quad (1.1)$$

and they are in order of enlistment as follows: frequency, period, wavelength, wavenumber, energy and Boltzmann equivalent temperature. As a part of the electromagnetic (EM) radiation, that of THz also fulfils the Maxwell equations. Their integral and differential forms are displayed in table 1.1.

Name of the law	Differential form	Integral form
Gauss's law	$\nabla \cdot \mathbf{E} = \frac{\rho}{\epsilon_0}$	$\oiint_{\partial V} \mathbf{E} \cdot d\mathbf{A} = \frac{Q(V)}{\epsilon_0}$
Gauss's law for magnetism	$\nabla \cdot \mathbf{B} = 0$	$\oiint_{\partial V} \mathbf{B} \cdot d\mathbf{A} = 0$
Maxwell–Faraday equation (Faraday's law of induction)	$\nabla \times \mathbf{E} = -\frac{\partial \mathbf{B}}{\partial t}$	$\oint_{\partial S} \mathbf{E} \cdot d\mathbf{l} = -\frac{\partial \Phi_{B,S}}{\partial t}$
Ampère's circuital law (with Maxwell's correction)	$\nabla \times \mathbf{B} = \mu_0 \mathbf{J} + \mu_0 \epsilon_0 \frac{\partial \mathbf{E}}{\partial t}$	$\oint_{\partial S} \mathbf{B} \cdot d\mathbf{l} = \mu_0 I_S + \mu_0 \epsilon_0 \frac{\partial \Phi_{E,S}}{\partial t}$

Table 1.1: Maxwell's Equations in their classical continuous differential and integral forms.

Although the first record of observation of the THz radiation is dated late 1800s [Rubens and Snow, 1893] according to some reports [Kimmitt, 2003], this range has stayed outside the main interest of researchers for a long time. While both parts of the spectrum below and above 1 THz have had a long history of research and development, leading to commercially available sources, detectors, meters and many various devices, the THz range is still in its childhood, representing the last unexplored part of the electromagnetic spectrum. This delayed development was mainly caused by difficulties in producing reliable and practical THz-wave sources, as well as by the complexity and low sensitivity of sensors that could detect this unusual radiation.

1.1.1 Fundamental applications

The relation (1.1) suggests an idea of cases in which the observation with THz radiation can be meaningful [Grischkowsky et al., 1990; Miles et al., 2007], e. g. studying:

- ◇ free carriers or charge transport in semiconductors, plasma, liquids, etc.;
- ◇ low-frequency phenomena such as rotations of molecules in gases;
- ◇ lattice vibrations in solids and libration of complex molecules;
- ◇ relaxation of solutions (solvation dynamics) and relaxation of charges.

In diverse basic-research areas, the time-domain terahertz spectroscopy (TDTS), including various ultrafast pump-probe experiments (see section 1.4), are employed as the most versatile techniques for studying the above mentioned phenomena in material research [Schuttenmaer, 2002] and spectroscopy. Other studies employ high frequency-resolution spectroscopy (see sections 1.2.2 and 1.2.6.1), far-field imaging (see section 1.6) or near-field techniques (see section 1.9).

1.1.2 Safety issues

All the IEEE RF [IEEE International Committee on Electromagnetic Safety and Institute of Electrical and Electronics Engineers and IEEE-SA Standards Board and IEEE Xplore (Online service), 2006], ICNIRP [International Commission on Non-Ionising Radiation Protection (ICNIRP), 1998, 2009] and the ANSI Laser safety standards [American National Standards Institute and Laser Institute of America, 2007], have safety limits into the terahertz region, but those are based on extrapolation [Berry, 2003]. (An abstract of the documents above and a statement is available via the National Reference Laboratory of the Czech Republic in Czech language [Jelínek and Pekárek, 2009].) In the first approximation, it is expected that effects of this non-ionising radiation on tissues are only thermal in nature and, therefore, predictable by conventional thermal models [Nussbaum, 1982; Oleson, 1984]. Considering the fact that the outer biological tissues contain ca. 70% water [Johnsen et al., 2009; Warner et al., 1988], dielectric models of water [Kristensen et al., 2010] can be used for modelling the damage of THz radiation on human skin. Successfully, dielectric models (in terms of multiple Cole-Cole dispersion) were applied for modelling biological tissues at frequencies from couple of Hz to tens of gigahertz (GHz), too [Gabriel et al., 1996a,b,c]. The authors also released an interactive database for calculating various dielectric properties for different types of human tissues at frequencies 10 to 100×10^9 Hz [Andreuccetti, 2007].

But, in spite of the non-ionising nature of the THz radiation, there are some concerns regarding its genotoxicity. This is due to proven change in cellular membrane permeability [Siegel and Píkov, 2010] and a theoretical study of Alexandrov et al. that proposed a model describing spontaneous opening of a chain of deoxyribonucleic acid (DNA) [Alexandrov et al., 2010]. However, the predicted peculiar DNA unzipping has not been verified experimentally yet. Also under some specific conditions, epigenetic effects and genotoxicity were shown on dividing lymphocytes [Korenstein-Ilan et al., 2008].

The investigations of biological effects of THz radiation are still at the beginning, as evidenced by absence of safety standards and quantification of maximum harmless power, i. e. the maximum permissible exposure, of THz sources for single-pulse and continuous-wave exposure [Berry, 2003; Berry et al., 2003; Walker et al., 2002]. But, research is underway to collect data to populate the background of experience in this spectral region and validate safety limits [International Advisory Committee, 2006; THz-BRIDGE and Gallerano, 2004].

1.2 Sources

Many of the techniques described further, in section 1.9, make use of a dipole or of its behaviour. A dipole here means an elementary doublet of a small length of conductor $d < \lambda$ carrying an alternating current:

$$I = I_0 e^{-i\omega t}, \quad (1.2)$$

where $\omega = 2\pi\nu$ is the angular frequency, and I is a phasor.

The emission of the dipole is described in [Born and Wolf, 1999], points out the dependence of the field emitted by the dipole vs. the distance r from its centre as varying in inverse power of r , r^2 , r^3 . It is easy to show the the term r^{-1} is associated with a propagating field obeying the energy conservation law. Most of the emitting sources, described in the following, make use of this radiating term. The other two terms cannot be explained simply: they carry no energy and therefore do not propagate. They are often called non-radiating terms. However, they cannot be neglected in near-field optics for they are one of the bases of a sub-wavelength resolution as described in section 1.7 (adapted from [Courjon, 2003]).

On both sides of the spectrum, there have been sources which could reach out more or less into the *terahertz gap*, but most of them have their own limitations of usage.

Sources can be distinguished based on their technical specifications by:

- ◇ frequency range and frequency bandwidth: monochromatic (narrowband and with a single-frequency emission, continuous wave) and broadband, i. e. pulsed radiation;
- ◇ tunability: none, discrete or continuous;
- ◇ power of the emission: ranges from the weakest source of black body background around 300 K to GW-peak-energy radiation from *free-electron lasers (FELs)* [Williams, 2004]; and
- ◇ operability: turn-key systems [Coherent Inc., 2007; TeraView Ltd., 2010], table-top, extras (a need of cryogenic cooling) and large facilities (running under international cooperation).

The list of available sources and detectors written below is derived from [Bogue, 2009; Carlstrom and Zmuidzinas, 1996; Hindle et al., 2009; Lee, 2008; Mukherjee and Gupta, 2008; Sizov, 2009; Ward et al., 2008], and it includes some recent experimental results [Johnston, 2006], too.

1.2.1 Glow lamps

A straightforward way of generating THz radiation is to use glowing objects where the black-body radiation of a heated object, e. g. a Mercury glow lamp emits also at THz wavelengths. The accuracy of the measurement recedes toward lower frequencies due to the rapid decrease of the brightness of the radiation source in relation with Planck's law [Planck, 1901]. Such incoherent sources are used mostly in Fourier-transform infrared (FTIR) spectroscopy, their frequency resolution is usually high (a few GHz) and frequencies down to 0.5 THz can be reliably measured this way [Han et al., 2001; Pashkin, 2004].

1.2.2 Sources based on de-/accelerating charged particles

The THz radiation can be also generated by decelerating or accelerating electrons or other charged particles. Gyrotrons, synchrotrons, FELs and backward-wave oscillators (BWOs) belong here. The gyrotrons, synchrotrons and FELs are massive installations based on a similar concept—utilising charged particles in motion, and they are often results of international collaboration.

- ◇ A gyrotron is a high powered vacuum tube which emits monochromatic THz beams in pulsed or continuous regime by bunching non-relativistic electrons with cyclotron motion in a strong magnetic field [Flyagin et al., 1982, 1983]. Its frequency output is about 0.02 to 1 THz and the typical power is 1 to 1000 kW [Yan et al., 2009]. On the other hand, synchrotrons [Abo-Bakr et al., 2003; Carr et al., 2003] and FELs [Carr et al., 2002] make use of relativistic electrons, thus, they emit higher frequencies up to 3 THz [Williams, 2004].
- ◇ In BWOs (or carcinotrons) [Kantorowicz and Palluel, 1979; Kozlov and Volkov, 1998], belonging to the travelling-wave tube family, the THz radiation is a result of the interaction between an electron beam and a slow-wave structure. Severe conditions are required to operate a BWO such as high temperatures $T \approx 1200$ °C, high precision of 10 μ m in manufacturing the slow-wave structure, high voltage $U \approx 6$ kV, a medium vacuum $p \sim 10$ to 100 mtorr and a highly-homogeneous magnetic field $M \approx 10$ kG = 1 T. Due to the good quality wavefront they emit, prompt tunability induced by $\nu \propto U^{1/2}$ up to 1.5 THz, their high power of 100 mW and monochromaticity $\Delta\nu \approx 10^{-5}\nu$, they find use as illuminators in terahertz imaging [Gompf et al., 2006], see section 1.6. Higher power of 2 MW is available for shorter time of few tens of μ s only [Ginzburg et al., 2002].

- ◇ By combining the concepts of gyrotron and that of **BWO**, a so-called gyro-**BWO** apparatus can be constructed able to emit powerful and broadband 100 MHz-wide pulses [Rozenal et al., 2005].

1.2.3 Coherent sources (THz lasers)

In general, a laser is an example of an extremely coherent source of radiation. To operate a laser on a certain frequency, this frequency has to be present in the band-gap transition in a form of energy-level change. Towards 1 THz, there is only a couple systems capable of lasing.

- ◇ Among **far-infrared (FIR)** lasers, the gaseous (molecular) types [Large and Hill, 1965] are the most effective in their operation. Such a **FIR** laser consist of a resonator (1 to 3 m long) filled with gaseous organic molecules that are pumped optically or using high voltage. The (tunable) narrow-band frequency range of these table-top instruments falls into 0.3 to 10 THz.
- ◇ In case of solid-state lasers, p-doped Germanium is used as a lasing medium [Komiya and Kuroda, 1986], and they are called *p-Ge lasers* or hot-hole lasers [Kinsler and Wenckebach, 2001]. Its emission lines spans over several invcm [Lewis et al., 1992]. The lasing occurs between the energy level of light holes and the energy level of heavy holes and it ranges from 1 to 4 THz, depending on the applied magnetic field B .
- ◇ Compared to all the available **THz** sources, a relatively recent achievement is a **quantum cascade laser (QCL)** [Faist et al., 1994] and it has a potential to become a reliable miniature source of a coherent **THz** radiation . A **QCL** is a quantum heterostructure, in which a stairway of subbands allows a single electron to cascade down generating multiple photons. The **QCLs** produce coherent narrowband emission, the frequency of which is given by the design of the heterostructure (that is, they are not tunable), and their power can reach several mW. The operating temperature of **QCLs** is limited on principle and it is related to the energy of the emitted photon

$$E(T) = k_B T = h\nu, \quad (1.3)$$

where k_B is the Boltzmann constant, and h is the Planck constant. The frequency range of 0.3 to 3 THz corresponds to the temperature range of 15 to 150 K. That means, in the case of **THz QCLs**, cryogenic cooling is needed for their operation [Borak, 2005].

1.2.4 Sources based on Cherenkov-like phenomena

The Soviet physicist [Askar'yan](#) predicted [[Askar'yan, 1962a,b, 1990](#)] and later [Auston](#) from the U. S. A. generated THz waves in a form of a Cherenkov radiation [[Auston, 1983](#); [Auston et al., 1984b](#)]. [Auston](#) excited a LiTaO₃ crystal by subpicosecond laser pulses. The Cherenkov effect is a result of a charged-particle travel, most commonly an electron, through a dielectric (electrically polarisable) medium with a speed greater than that at which light would otherwise propagate in the same medium [[Cerenkov, 1934](#)].

Making use of the Cherenkov-like effect, unusual sources of THz radiation can be set up:

- ◇ Generating the Cherenkov radiation by intense laser pulses in centrosymmetric media such as gases is possible [[Cook and Hochstrasser, 2000](#)]. A fundamental and second-order harmonic-wave mixing is present at the photoionisation of air; in that case the phenomenon can be also described as a third-order nonlinear four-wave mixing process.
- ◇ Instead of an arduous adjustment of the second-order harmonic wave in the above experimental setup, the gas under bias can be photoexcited by an intense single pulse with a similar effect [[Löffler et al., 2000](#)].
- ◇ The Cherenkov-like phenomenon gives rise to a radial broadband radiation in a frequency range of 0.2 to 2.5 THz and this radiation is emitted in the shape of a cone symmetrical around the laser-radiation axis. Studies have shown that radiation can be also emitted in forward direction in preference in so-called transition-Cherenkov process instead of emitting radially [[Amico et al., 2008](#)].

1.2.5 Semiconductor electronics sources

A Gunn diode (also a transferred-electron device) is a diode with a region of negative differential resistance in its I - U curve—that is, an increase in the current entering a port results in a decreased voltage across the same port. Gunn diodes made of gallium nitride (GaN) are able to emit frequencies up to 3 THz with a power of 1 W [[Barry et al., 2010](#); [Gribnikov et al., 2001](#)].

A Schottky diode (also a hot-carrier diode) is a semiconductor diode with a low forward-voltage drop and it is able to emit thermionic radiation [[Ward et al., 2008](#); [Wu, 2008](#)]. It is also used as a THz detector, see section 1.3.3.

1.2.6 Sources employing nonlinear optical properties of crystals

Sources that make use of nonlinear optical properties of crystals such as second- and higher-order susceptibility, $\chi^{(2)}$, or χ_{ijk} , are photomixers, **electro-optical rectification (EOR)**, surface emitters, photoconductive switches and frequency multipliers [Sakai, 2005; Wang, 2005].

1.2.6.1 Photomixers

Photomixing (difference frequency generation, or down-conversion) is a process of emission of tunable monochromatic and coherent radiation based on nonlinear frequency mixing of dual-wavelength laser beam [Sakai, 2005, Chap. 6]. Two continuous-wave lasers with identical polarisation are required, the lasers lasing at frequencies ω_1 and $\omega_2 = \omega_1 + \Delta\omega = \omega_1 + \omega_{\text{THz}}$ are spatially overlapped. The co-linear lasers then illuminate a biased ultra-fast semiconductor material such as low-temperature-grown **Gallium Arsenid (GaAs)**. The photonic absorption and the short charge-carrier lifetime results in the modulation of the conductivity at the desired THz frequency, $\omega_{\text{THz}} = \omega_1 - \omega_2$ [Chusseau, 2007; McIntosh et al., 1995].

1.2.6.2 Sources based on electro-optical rectification

EOR (also optical rectification, or inverse Franz-Keldysh effect) is a nonlinear second-order optical process of generating a DC polarisation in a nonlinear medium at the passage of an intense optical beam [Bass et al., 1962; Yang et al., 1971]. When a nonlinear medium is irradiated by such a continuous wave at a frequency ω , polarisation is induced in the crystal at the difference frequency (static polarisation) and the sum of the individual frequencies (2ω) [Chuang et al., 1992]:

$$P(2\omega) = \chi(2\omega; +\omega, +\omega)E(\omega)E(\omega) \quad (1.4)$$

$$P(0) = \chi(0; +\omega, -\omega)E(\omega)E(\omega) \quad (1.5)$$

For ultrashort laser pulses (usually generated by **Ti:sapphire** lasers) have large bandwidth ($\omega - \Delta\omega, \omega + \Delta\omega$), the static polarisation is replaced by the pulse envelope, and the various frequency components are differenced with each other to produce a bandwidth from 0 THz to several THz ($0, 2\Delta\omega$) [Lee et al., 2003]. Various media are suitable for **EOR** [Bignell and Lewis, 2008], such as bulk semiconductors [Auston and Nuss, 1988; Dakovski et al., 2005], inorganic crystals **LiTaO₃** and **LiNbO₃** [Winnewisser et al., 1997; Wu and Zhang, 1995], **GaP** [Wu and

Zhang, 1997a], GaSe [Liu et al., 2004] and ZnTe [Han and Zhang, 1998; Wu and Zhang, 1997b], metal surfaces [Kadlec et al., 2004, 2005], electro-optical polymers [Nahata et al., 1995, 1996a; Sinyukov and Hayden, 2002] organic crystals (or a highly birefringent organic salt DAST) [Han et al., 2000; Schneider et al., 2003, 2006; Zhang et al., 1992]—used for emission as well as for detection.

EOR can be also employed in a near-field technique called *THz imaging by a local source*, see section 1.9.2, where the THz radiation is locally emitted.

1.2.6.3 Surface emitters

When a bulk semiconductor is illuminated by an ultrashort (100 fs or shorter) optical pulse with its wavelength (energy) above the energy band gap of the material, mobile carriers are photogenerated in the vicinity of the surface (within ca. 1 μm). The surface here plays two main roles: causes band bending and breaks the symmetry.

- ◇ The surface generates a band bending which has the effect of accelerating and separating carriers of opposite charges in opposite directions (normal to the surface) creating a dipole. This effect is known as surface field emission or a photo-Dember effect (see citation within [Johnston et al., 2002]).

The concept of surface field emission is employed in so-called nanoklystrons where the large collective surface of carbon nanotubes is illuminated [Manohara, 2004; Manohara et al., 2001].

- ◇ The surface also causes a break of symmetry and that results in photo-generation of charge carriers being able to move (in average) only into the bulk of the semiconductor. In consequence of the difference of mobilities (or diffusion constants) for holes and electrons, a charge dipole in the vicinity of a semiconductor surface is formed (see citations within [Johnston et al., 2002]). The phenomena is particularly strong in high-mobility semiconductors such as InAs.

1.2.6.4 Sources based on photoconductive switching

The first THz emission by a photoconductive (Auston) switch was based on the idea of Hertz original experiment [Hertz, 1893] and was realised by irradiating a biased semiconductor (aluminium-oxide) plate with high-energy argon ions [Auston et al., 1984a; Smith et al., 1988]. In a photoconductive switch an undoped semiconductor material placed under bias is illuminated

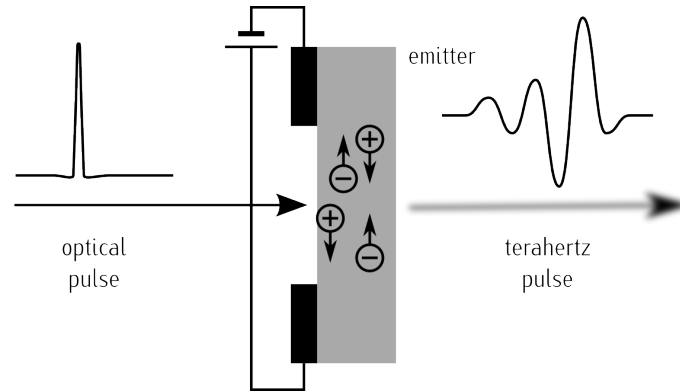


Figure 1.2: The scheme of a photoconductive switch in which the ultrashort laser pulse excite charges in a biased semiconductor and those, accelerated by the bias, emit radiation perpendicular to their travel.

by ultrashort laser pulses ($\lesssim 100$ fs), see fig. 1.2. Necessarily, the photon energy has to exceed the band-gap energy of the illuminated material. A pair of free carriers (an electron-hole pair) created in this process can be well approximated by an elementary Hertzian dipole p [Auston et al., 1984a]. The dipoles are accelerated by the applied voltage and the dipole in motion forms a current $I = \partial p(t)/\partial t$. Finally, the carriers are rapidly trapped or they recombine and the current density returns to its steady-state value. The rapid variation of the current density gives rise to a pulse of a radiation emitted perpendicularly to the biased field:

$$E(t) = -\frac{e\mu_0}{4\pi r} \frac{\partial I(t)}{\partial t} \quad (1.6)$$

at the distance r from the source, where e is the elementary charge and μ_0 is the permeability of the vacuum.

In fig. 1.3 a typical example is this process is shown: the radiated field deduced from eq. (1.6), the current waveform (fig. 1.3a) is depicted in fig. 1.3b and appropriate spectra of both are drawn in fig. 1.3c and (d) respectively.

area photoconductive switches are manufactured, that are in fact, numerous very thin photoconductive switches placed next to each other to form an interdigitated structure [Dreyhaupt et al., 2005, 2006]. Large-aperture antennas have substantial influence on the temporal pulse profile in both the near field and the far field, and usually they result in better forward directivity and homogeneity of the radiation [Gürtler et al., 2000]. Such a switch, able to generate broadband pulses within $\nu \approx 0.1$ to 4 THz, is used in our experiment, see section 1.4 [Dreyhaupt et al.,

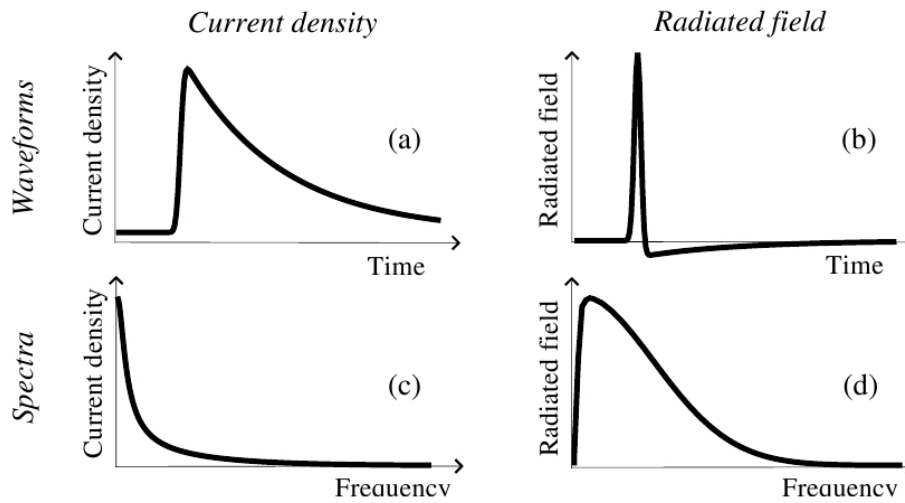


Figure 1.3: (a) The evolution of the current flowing through the emitter. (b) The shape of the electric transient far from the emitter. (c) The spectrum of the current and (d) spectrum of the radiated field. (Picture kindly granted by H. Němec.)

2005; Gigaoptics GmbH, 2009].

For detecting an extremely broad frequency band spanning over 60 THz at room temperatures, a low-temperature-grown GaAs can be used as a substrate [Kono et al., 2002].

THz ellipsometry is possible using multi-contacts photoconductive antenna [Tani et al., 2006] emitting circularly-modulated THz waves.

The photoconductive (see section 1.2.6.4), surface field and photo-Dember (see section 1.2.6.3), and EOR (see section 1.2.6.2) emitters are indirect single-cycle-emission sources, conveniently used mostly in TDS for their broadband characteristics [Sakai, 2005, Chap. 2]. In the case of the EOR source and the photoconductive switch, the emitted THz pulses are (very approximately) the envelopes of the input laser pulses.

1.2.6.5 Frequency multipliers

A frequency multiplier is an electronic circuit that produces an output frequency that is an integral multiple $N \cdot \omega$ of an input angular frequency ω . By frequency multiplication of two coherent MW sources, one can obtain ultra-narrow-linewidth continuous-wave THz sources [Maestrini et al., 2008]. All of the newly created frequencies (and mentioned coherent sources, see sections 1.2.2 and 1.2.3) can be further frequency multiplied to achieve other discrete frequencies.

1.2.6.6 Sources based on parametric amplification

In some cases tunable THz-wave sources with high temporal and spatial coherence are needed. For this option, tunable THz-wave parametric amplification using the resonant frequency of ferroelectric crystal lattices is an optimal solution [Kawase et al., 2002]. In that, a grating coupler fabricated on the surface of an lithium niobate (LiNbO_3) crystal is pumped by a Q-switched Nd:YAG laser, and the idler (Stokes) and the signal (anti-Stokes, THz) waves are generated from the pump (near-infrared (NIR)) wave in the direction consistent with the noncollinear phase-matching condition inside the LiNbO_3 crystal—the group velocity is equal to speed of light in the material, $n_g = n_{\text{THz}}$. The grating ensures a better out-coupling of the THz wave into the free space.

1.3 Detectors

In the next section, we describe the principles and operation of the detectors used for THz frequencies, e. g. those based on thermal effects, see section 1.3.1, those based on electro-optical effect, see section 1.3.2.1 and photoconductive sensors, see section 1.3.2.2.

1.3.1 Detectors based on thermal effects of the THz radiation

When a thermally stabilised THz absorbing material in contact with a thermometer (usually at room temperature, but not rarely cooled at liquid-nitrogen or liquid-helium temperatures) is irradiated, various thermal effects can occur. The thermal energy absorbed by irradiation can cause

- a change of the material resistance** (in a bolometer);
- a rise of an electric potential**, i. e. a thermoelectric effect (in a thermopile detector);
- a variation of the spontaneous polarisation** (in a pyroelectric detector);
- a dilatation of a gas** (in a Golay cell).

The noise-equivalent power (NEP) of these devices is usually 10^{-6} to 10^{-10} W Hz^{-1/2} and the response time is in ms, which is sufficiently good for a passive charge-coupled device (CCD)-type imaging, but limits their usage for terahertz-pulse imaging (TPI) and spectroscopy.

1.3.2 Detecting broadband pulses

Detectors can be also based on the *reverse* phenomena employed at the emission of the THz radiation itself. In most cases, that makes great sense (the response times of the emission and detection and the frequency bands are equivalent), and the experimental setup is more compact. That is ideal for TDTS using a photoconductive switch (section 1.3.2.1) or a nonlinear opto-electric crystal (section 1.3.2.2) allowing for ultrafast and phase-sensitive detection. The response times of a room-temperature photoconductive switch and also of an electro-optical crystal can be as short as a fraction of a ps [Winnerl et al., 2008].

1.3.2.1 Detectors based on electro-optical (Pockels) effect

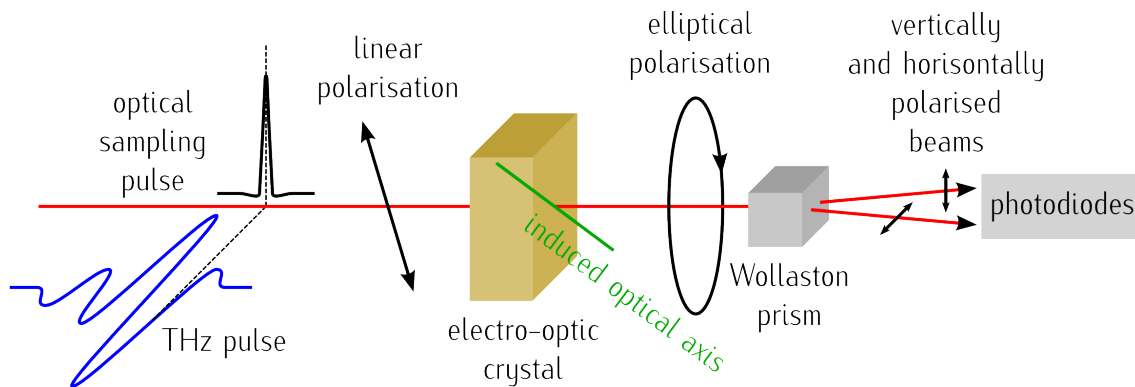


Figure 1.4: Scheme of electro-optical sampling: The polarisation of the optical pulse is modified due to birefringence induced in the electro-optical crystal in the presence of the electric (THz) field intensity E , proportionally to its value. Mapping the resulting intensity difference (representing the ellipticity) by a pair of balanced photodiodes with respect to the relative delay time gives a signal that is proportional to the THz field.

Electric-field induced birefringence in a $\langle 110 \rangle$ oriented zinc telluride (ZnTe) crystal is widely used as a room-temperature THz-pulse detector [Auston and Nuss, 1988; Jepsen et al., 1996b; Nahata et al., 1996a; Wu and Zhang, 1995]. The E of the THz pulse induces a birefringence in the ZnTe crystal which is read out by a linearly polarized visible pulse [Planken et al., 2001; van der Valk et al., 2004], see fig. 1.4. When both, the collinear visible pulse and the THz pulse are present in the crystal at the same time, the polarisation of the visible light will be rotated owing to the induced birefringence. Using a $\lambda/4$ waveplate and a beamsplitting polariser (or a Wollaston prism) together with a set of balanced photodiodes, the relative THz-pulse amplitude

is recorded by monitoring the visible-pulse polarisation rotation behind the ZnTe crystal as a function of delay time with respect to the THz pulse.

A variation of the electro-optic sensing is the magneto-optical sensing employing the Faraday-rotation effect induced by transient magnetic THz field. Instead of an electro-optical crystal, a crystal sensitive to a magnetic field (with high magneto-optical susceptibility) is used and the magnetic component of the THz pulse is mapped. Sensors made of Bi-substituted yttrium-iron-garnet film and SF-59 amorphous glasses were constructed [Elezzabi and Freeman, 1996; Riordan et al., 1997].

1.3.2.2 Photoconductive detection

In section 1.2.6.4 the photoconductive switch is described which is used for generating THz radiation by ultrashort optical pulses. Instead of the bias constant in time, the varying electric field of the THz pulse can be used to accelerate the charges generated by the ultrashort optical pulse. The accelerated charges create a potential difference on the opposite sides of the photoconductive sample and the integrated current in various relative optical-to-THz pulse time delay is recorded—in that the shape of the THz pulse is projected [Nahata et al., 1996b].

1.3.3 Other detector types

In Schottky diodes the THz electric field generates a charge on a metal-semiconductor junction (a Schottky barrier). A typical low-barrier Schottky diode has $NEP = 10^{-10} \text{ WHz}^{-1/2}$ near 1 THz. Also, a setup for detecting THz pulses due to electric-field-induced optical second-harmonic emission in a centrosymmetric media (e. g. silicon) has been demonstrated [Nahata and Heinz, 1998].

1.4 Time-domain terahertz spectroscopy

With the introduction of ultrafast emission and detection systems [Jepsen et al., 1996a; Leitstorfer et al., 1999], see sections 1.2.6 and 1.3.2, in 1980s already mentioned before, TDTS was developed and had been pursued in a couple of laboratories (the pioneer groups were that of Auston and Nuss [Auston and Nuss, 1988; Auston et al., 1984b] and that of Fattinger and Grischkowsky [Fattinger and Grischkowsky, 1988]).

The technique of **TDS** is phase-sensitive [Dragoman and Dragoman, 2004]. This is an important advantage over the **FTIR** spectroscopy where the information about the phase change is lacking, and the technique is much faster for broadband detection than a narrowband system with a tunable **THz** source or with a Mach-Zehnder interferometer. **TDS** uses single-cycle pulses of broadband **THz** radiation generated using ultrashort laser pulses, which have become commercially available. Similarly, ultrashort laser pulses from the same sources are used for detection of the **THz** pulses, see fig. 1.5.

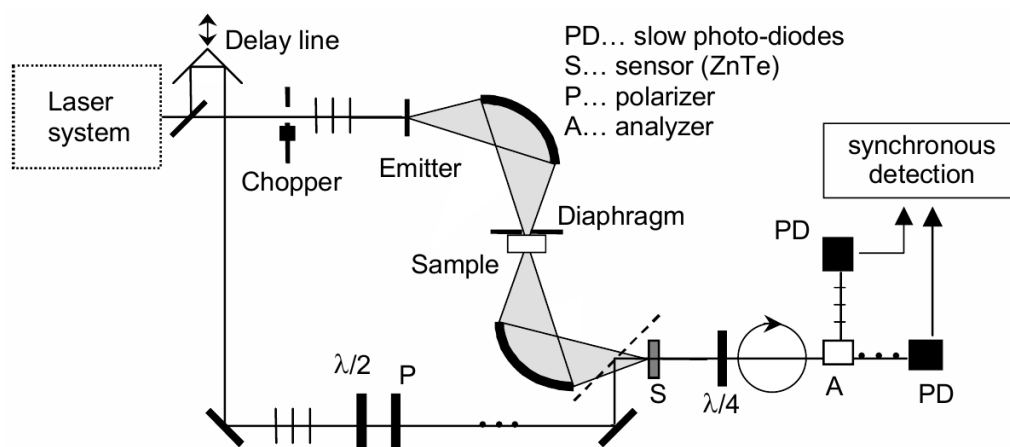


Figure 1.5: Our near-field setup evolved from a standard **TDS** setup of which a schematic drawing is shown above. Optical pulses (solid lines, —) are converted to **THz** pulses (grey beam, ■) at the emitter. A small fraction of these optical pulses deflected by a beam-splitter and delayed by a delay-line is used for electro-optical detection. The generated **THz** radiation is shaped by parabolic mirrors (or by plastic lenses) to create a homogeneous and uniform beam waist where a sample is placed, [Dexheimer, 2007; Nuss and Orenstein, 1998] and [Sakai, 2005, Chap. 7]. (Picture kindly granted by H. Němec.)

Because of the ability to read out the dependence on time of the full electric field, i. e. both amplitude and phase change; a table-top **TDS** is the most useful and versatile for comprehensive material research, and it eliminates many disadvantages of narrow-band, tunable-only and large facilities. This versatility and efficiency of **TDS** caused a boom in exploration of the *vanishing* **THz** gap. **TDS** is currently used in diverse basic-research areas [Hoffmann, 2006; Němec, 2006; Schuttenmaer, 2002; Walther, 2003], e. g. contact-free measurement of complex dielectric response [Kužel and Petzelt, 2000; Micken et al., 2004; Schuttenmaer, 2004], free-carriers transport and concentration of carriers in semiconductors [George et al., 2008], plasma-charge transport in liquids [Kaatze, 1997; Mics et al., 2005], investigation of transient **FIR** dynamics

in condensed-matter research [Němec et al., 2005a,b], biology and medicine [Siegel, 2004; THz-BRIDGE and Gallerano, 2004; Woodward, 2004] and modifications of it for imaging in medicine [Kadlec et al., 2008; Löffler et al., 2002] and security, see section 1.6.

The spectral resolution $\Delta\nu$ of the TDTS is limited by the duration of the optical sampling pulse, sensor time response and also by a long-enough time frame (a temporal scan length) τ available for data acquisition and consequently for fast Fourier transform (FFT) (see [Kammler, 2007; Kauppinen and Partanen, 2001] for more on FFT).

$$\Delta\nu_i = \frac{1}{\tau_i}, \quad \Delta\nu = \sum_i \frac{1}{\tau_i}. \quad (1.7)$$

But ν -resolution better than 1 GHz is rare, i. e. that would involve a ca. 15 cm-long moving delay line and perfectly collimated optics. With substituting the classical moving corner-mirror delay line with a rotary optical delay line [Jin et al., 2008; Kim et al., 2007; Klatt et al., 2009], even spectroscopy of gases with their narrow vibration lines is possible this way [Harmon and Cheville, 2004].

A special class of studies are measurements of dynamical states in the matter by pump-probe experiments. In those measurements, the material is excited by a pump in the ultra-violet (UV), optical, or IR frequency range and it is consequently probed by a THz pulse with a variable time delay. The pump-probe experiments requires strong pump pulse, therefore THz pump/THz probe setup is rare, but feasible [Hoffmann et al., 2009a,b].

1.5 Noise and artefacts in the TDTS system

Noise is a random (correlated or diffuse) process characterized by stochastic properties such as its variance, distribution and spectral density. The spectral distribution of noise can vary with frequency, and its power density is measured in WHz^{-1} . Noise levels are usually viewed in opposition to signal levels and they are often seen as part of a signal-to-noise ratio (SNR).

$$\text{SNR} = \frac{P_{\text{signal}}}{P_{\text{noise}}} = \left(\frac{A_{\text{signal}}}{A_{\text{noise}}} \right)^2; \quad \text{SNR}_{\text{dB}} = 10 \log_{10} \left(\frac{P_{\text{signal}}}{P_{\text{noise}}} \right) = 20 \log_{10} \left(\frac{A_{\text{signal}}}{A_{\text{noise}}} \right) \quad (1.8)$$

In the TDTS system described in section 1.4, there are several possible sources of noise and disturbances influencing the acquired data.

Air impurities and air flow, scattering on dust

First of all, in measurements under ordinary atmospheric conditions, where no vacuum or dry-nitrogen atmosphere is provided, the THz radiation passes the humid air which leaves its own significant pattern in the waveforms and the spectra [van Exter et al., 1989]. Additionally, there is no easy way to regulate and define the air humidity in an open space, which would enable to *remove* it after the measurement [Wang et al., 2009b; Withayachumnankul et al., 2008], unless a sophisticated closed air-circuit is defined and built with defined inputs and outputs, but this is close to a temperature-regulated clean-room facility. The air humidity and circulation affected by an air conditioning system leaves tracks in the measurement (see later section 3.4).

Strong air flow or noise can also affect a pellicle beamsplitter that aligns the optical beam into the THz beam. A pellicle beamsplitter is fabricated by stretching a thin membrane over a metal frame and has many advantages over the conventional glass beamsplitter. Chromatic and spherical aberration in converging beams is negligible and ghost images are virtually eliminated due to the thin nature of the membrane. The pellicle beamsplitter is like a drum and thus is sensitive to acoustical disturbances. Thus it needs to be isolated from this type of environment. The pellicle membrane is usually coated with a metallic coating to produce the desired beamsplitter, thus absorption is present.

Dust are solid impurities in the air and their presence and scattering on them is causing temporal changes in beam intensity.

Beam vibrations

Further, the optical beam generated by a laser is not stable in space. Vibrations in the laser-beam-spot position on the photoconductive switch can cause the THz beams vary in intensity (flicker) due to a changing number of illuminated gaps on the switch participating on the emission. But, within certain limits, the emission of THz pulse by a photoconductive switch does not depend on the angle of incidence of the laser beam, therefore no angle changes of the THz beam are present.

The beam vibrations can cause, on the other hand, change in position of the diodes, the last components in the optical path. The solution for this is to make the focus spot on the detection diode as small as possible

The detection crystal—replicas in the waveform

The electro-optical detection using ZnTe or GaAs crystal (section 1.3.2.1), requires a crystal with a certain optimal thickness and that is about 1 mm for ZnTe and 0.1 for GaAs [Planken et al., 2001; Zhao et al., 2002]. This is due to the not-perfect phase-matching condition in relation with dispersion [Turchinovich and Dijkhuis, 2007] and the necessity to enhance the sensitivity with growing interaction path. The thickness of the crystal conditions the time delay between the replicas of the pulse ≈ 20 ps arising due to inner reflections introduced within the crystal. The problem can be solved by introducing a non-electro-optical medium with a same refractive index just behind the ZnTe crystal which delays the reflection at the sensor–air interface and that the optical and the terahertz pulse are travelling further without an interaction. A platelet made of sapphire (α -Al₂O₃) is very suitable for this case: $n_{\text{ZnTe}}/n_{\text{sapphire}} \approx 2.8/3.0$ [Parshin, 1994; Wang et al., 2007]. Simply, cutting the waveform before the first replica is sufficient, but this method decrease the frequency resolution to ca. 50 GHz. Or one can subtract the replicas assuming there is a certain reproducibility, convolution and shifting of the original pulse [Dorney et al., 2001; Hirsch et al., 2008].

1.6 Terahertz pulse imaging

Imaging with FIR/THz radiation was already performed in 1975, by Barker, Hodges, and Hartwick employing a continuous-wave FIR waveguide laser [Barker et al., 1975; Hartwick et al., 1976]; there a contrast of a hidden metal object (key) was revealed behind an obstacle (a paper box). But, only the invention of a photoconductive switch used for generating a single-cycle broadband THz pulse in the early 1980s by of Auston et al., see section 1.2.6.4, was the marking event of the history of widespread exploitation of THz radiation, when the THz gap interconnecting the MW and IR frequency ranges was *bridged*. Shortly after, the same group introduced ultrafast generation and detection of these pulses. The use of the pulsed THz radiation soon expanded into another dimension—towards pulse imaging.

Once important system issues have been resolved and signal processing optimised for TDTS, TPI came to the scene using THz pulses to image objects in the focal plane. The technique has attracted considerable attention since its first demonstration [Hu and Nuss, 1995] and has gained importance as a promising tool for various basic-research and industrial applications [Abbott and Zhang, 2007; Bogue, 2009; Chan et al., 2007; Fitzgerald et al., 2002; Mittleman, 2004;

Woolard et al., 2005] and [Sakai, 2005, Chap. 9]. It has been increasingly used in diverse areas such as

- ◇ non-invasive packaging inspection (in contrast with X-ray imaging); used for scanning mails [Kawase et al., 2005], e. g. for narcotics, to detect hidden explosives and weaponry in luggage and personal belongings at airports [Leahy-Hoppa et al., 2007; on Assessment of Security Technologies for Transportation and Council, 2007; Woolard, 2007; Yinon, 2007] as they are a common threat [Thiesan et al., 2004];
- ◇ quality control of plastic parts and material inspection [Dean et al., 2008; Duling and Zimdars, 2009; Zhang, 2004] in industrial production;
- ◇ biomedical diagnostics and epidermal tissue imaging [Nakajima et al., 2007; Schade et al., 2005] and
- ◇ imaging in pathology diagnosis [Nakajima et al., 2007; Pickwell and Wallace, 2006; Woodward et al., 2002], e. g. for skin cancer [Wallace et al., 2004] and tumour detection [Gompf et al., 2006], especially, the basal cell carcinoma [Pickwell et al., 2004].
- ◇ dentistry [Crawley et al., 2003],
- ◇ 3D-computed tomography [Ferguson et al., 2002; Withayachumnankul et al., 2007] and even broadband 3D imaging using a reconstruction algorithm based on time reversal [Buma and Norris, 2004].

The primary interest in application is linked to the transparency of commonly used materials [Piesiewicz et al., 2007], e. g. clothes [Bjarnason et al., 2004], plastics [Halpern et al., 1986], wood and paper [Koch et al., 1998], normal glass, soil [Bosq et al., 2005, 2008; Dodson et al., 2005] and non-metallic construction materials.

On the contrary, water [Venables and Schmuttenmaer, 2000] and most metals (for thickness above 30 nm [Walther et al., 2007]) are opaque to T-rays.

When using TPI in the most common uniaxial geometry, an exact 3D-image reconstruction or depth profiling is possible only by knowing the refractive indices of the material in the inner structure [Mittleman et al., 1997]. But, the variety of projections and useful information that is possible to obtain by TPI and consequent artificial feature definition, visualisation and classification techniques [Chamberlain et al., 2002; Löffler et al., 2002] and [Sakai, 2005, pp. 339–341] is surprisingly broad and literally *colourful*, and potentially it represents a powerful basis for tissue or material classification, mainly for biomedical applications.

Many of the imaging tasks above can be accomplished using conventional focal-plane imaging, also called far-field imaging. The interest in high spatial-resolution THz imaging grew

much just after resolving major technical issues of TPI using TDS setups in the mid-1990s [Hu and Nuss, 1995]. Nonetheless, in conventional focal-plane imaging, the spatial resolution is limited by the wavelength used or by the size of an aperture, whereby the intensity of the change in radiation significantly decreases [Zhang, 2002]. Since then many more or less successful approaches were invented and applied to increase the spatial resolution in the THz FD. Most of the ideas were borrowed or inherited from other scientific fields where they were implemented earlier. Some were applied in the THz frequency range due to the electromagnetic scaling law. The section 1.8.1 is dedicated to possible improvements and near-field techniques.

1.7 The near-field and far-field spatial zones

In general, the space between the emitter and detector can be divided into two areas: far-field and near-field region.

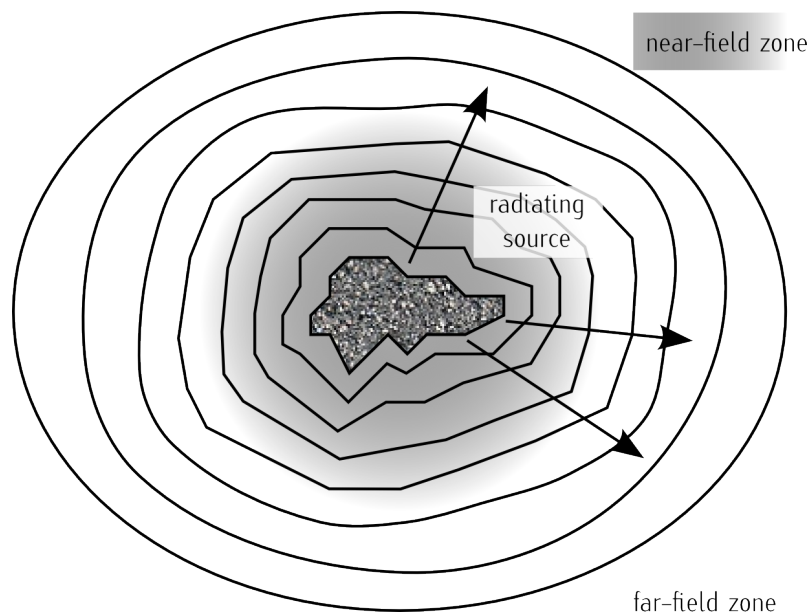


Figure 1.6: The emission of a source with a sub-wavelength surface structure. The field reproduces the shape of the surface in the near zone and reconstruct in a perfect smooth envelope in the far zone. (Adapted from [Courjon, 2003].)

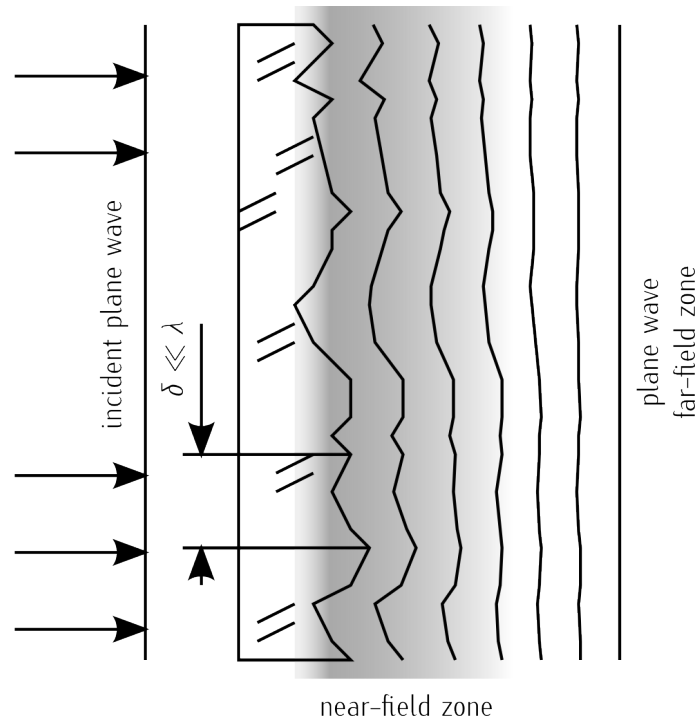


Figure 1.7: The interaction of a plane wave with a sub-wavelength structure. The structure of the field potential depends strongly on the surface shape close to the surface, where the near field is present. Due to constructive interference, the incident wave is reproduced faithfully in the far zone, where no dependence on the surface perturbations is present. (Adapted from [Courjon, 2003].)

1.7.1 The near-field region

The near-field region is also known as *near field*, *near zone* or Fresnel diffraction region, and it is the close-in region of an antenna where the angular field distribution is strongly dependent upon the distance from the antenna [Bass et al., 1994; Born and Wolf, 1999; Saleh and Teich, 2007], see fig. 1.6.

In the study of diffraction and antenna design, the near field is that part of the radiated field of the source or the antenna, which is at distances shorter than the Fresnel parameter $S \lesssim 1$:

$$S = D^2/4\lambda, \quad (1.9)$$

where D is the size or the diameter of the source.

The diffraction pattern in the near field typically differs significantly from that observed at

infinity and varies with distance from the source, see fig. 1.7. Also, in the near-field region a non-propagative, so-called evanescent field is present.

The *Newton's two-prism experiment* on light coupling over the non-zero distance between two perfectly flat and optically clear surfaces was, probably, the 1st reported manifestation of the existence of the evanescent light wave and also probably the 1st non-classical behaviour of a physical phenomenon observed in a lab room, [Courjon, 2003, p. 9], [Newton, 1704, pp. 81–82].

1.7.2 The far-field region

The far-field region is also known as *far field*, *far zone*, radiation field, or Fraunhofer diffraction region—in infinity, and it is the region outside the near-field region, where the angular field distribution is essentially independent of the distance from the source, see fig. 1.6.

In the far field, the shape of the antenna pattern is independent of distance. If the source or the aperture has an overall dimension D that is large compared to the wavelength λ , the far-field region is commonly assumed to exist at distances from the source greater than the Fresnel parameter ($S \gg 1$, see eq. (1.9)). The propagation of the THz radiation in the far-field region can be described sufficiently well by a Gaussian beam, e. g. [Saleh and Teich, 2007].

1.8 Feature resolution in imaging

The question of resolution or minimum resolvable distance is one of the key points when talking about imaging and microscopy, and the angular resolution or the spatial resolution describe the resolving power of any image-forming device. There is a fundamental limit to the resolution of any optical system or any pattern which is due to aberration or diffraction. Several empirical criteria exist which have been extensively used to resolve features in images, e. g. criterion by Sparrow and by Rayleigh. [den Dekker and van den Bos, 1997; Ramsay et al., 1941].

For their use of simplicity and educational reasons we mention the definitions of the classical resolution limits [Bass et al., 1994; Born and Wolf, 1999; Saleh and Teich, 2007]:

The Rayleigh resolution limit uses the model situation of two point-like objects of equal brightness and defines their mutual resolution as the distance, where the maximum in the image of each of these objects occurs at the position where the image of the other object has its 1st intensity minimum.

The spatial resolution for far-field imaging given by the Rayleigh criterion is

$$\sin \theta = 1.220 \lambda/D, \quad (1.10)$$

where θ is the spatial (or angular) resolution, λ is the wavelength used and D is the distance of the two points. Having the function $\sin \theta$ restricted in its natural limits $\langle 0, 1 \rangle$, one is able to find the smallest distance D that can be resolved by a certain wavelength λ . The relation slightly differs for a lens system (such as a microscope) by a factor of the numerical aperture of the system. Nevertheless, it is a fundamental spatial-resolution limit for TPI—a resolution of ca. 0.3 mm at a frequency of $\nu = 1$ THz ($\lambda = c_0 \nu$, where c_0 is the speed of light in a vacuum).

The Sparrow resolution limit defines the resolution as the distance between two point objects at which a dip half-way between these two points ceases to (or starts to) be visible in the superposition of their images; i. e. the 1st two derivatives of the intensity curve along the connecting line become zero. The intensities of the two point-like objects do not have to be equal, in contrast to the Rayleigh criterion, eq. (1.10). In other words, the limit (minimum) distance, at which two point sources can be considered resolved, occurs when the 2nd derivative of the resultant distribution of irradiance in the diffraction image of these two points vanishes on-axis.

Due to independence of the source intensity, the Sparrow criterion is more flexible than the Rayleigh, and it can also be shown that the Sparrow criterion gives higher resolution compared to Rayleigh's. The resolution criteria of Sparrow and Rayleigh are sketched in fig. 1.8 when applied for two sources of equal intensity represented by Airy functions and separated by a distance d .

1.8.1 Improving the spatial resolution

The apodisation technique was the first to *break* the barriers in far-field imaging. It was based on the theoretical scheme of [di Francia](#), it was realised by [Hegedus and Sarafis](#) [[Hegedus and Sarafis, 1986](#)] and later by [Leiserson et al.](#) [[Leiserson et al., 2000](#); [Leiserson et al., 2002](#)]. It is a spatial filtering of the pupil, in which a pinhole aperture allows only the central lobe of the Airy profile to pass and cuts the diffraction pattern (such modification usually introduces higher side-lobes or other distortion).

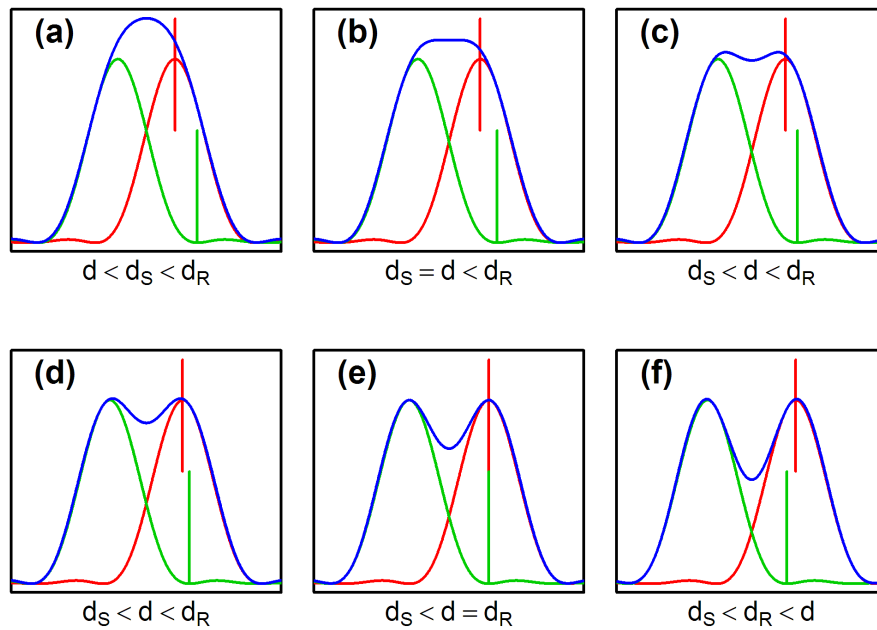


Figure 1.8: The sum of intensity (in blue, —) represented by two Airy functions (green, —, and red, —) of two apertures at various distances. There is no classical resolution criteria resolving two different sources or points for situations (a) and (b), unless more information is known about the sources such as their Point Spread Function. The Sparrow criterion is able to resolve two point for situations (c) and (d) (there is a minimum present between two maxima). While the Rayleigh criterion works only for situations when the distance is larger than the distance of the maximum and the 1st minimum of the Airy function, situations (e) and (f). The vertical lines mark the maxima and the minima of one of Airy functions in respective colours.

The spatial resolution can be improved in other ways, too, such as focusing the THz beam [Löffler et al., 2005], beamspeckle imaging (for bright objects), a conventional lens microscope (improves the resolution by a factor of its numerical aperture), interferometric microscopy (for flat objects under coherent illumination; using the partial images from a holographic recording of the distribution of the complex optical field, where the large aperture image can be reconstructed numerically [Kuznetsova et al., 2007; Schwarz et al., 2003]) or use of superlenses (made of metamaterials) [Pendry, 2000]. Complex-amplitude filters in confocal (non-scanning) imaging [Leizerson et al., 2002] or resolving features first in Fourier space prior to its normal space (Optical Transfer Function method) [Courjon, 1995; Greffet and Carminati, 1997] are also used.

By applying calculation algorithms (computer post-processing) on measured data, it is possible to increase the spatial resolution, too. This can be achieved, e. g. by applying Richardson–Lucy algorithm [Li et al., 2008] or by expectation–maximisation (maximum–likelihood) algorithm [Luo and Fan, 2007; qing Wang and guo Li, 2008].

All these approaches improve the spatial resolution to some extent, but the highest spatial resolution can be attained by applying a near-field based approach in order to overcome the wavelength limitation.

1.9 Overview of the concepts for near-field imaging techniques

The first documented near-field effect at THz frequencies was shown by Budiarto et al. on a diffraction behind an aperture [Budiarto et al., 1998] and the first near-field imaging was shown by Hunsche et al. using tip-enhanced near-field technique [Hunsche et al., 1997, 1998]. Several other methods were developed during the following decade, mainly by migrating near-field methods used in neighbouring frequency regions, either in optics (an overview of optics methods is in [Courjon, 2003; Courjon and Bainier, 1994]) or in MW [Decreton and Gardiol, 1974]. In general, these techniques make use of a sub-wavelength structure (physical or virtual) which disturbs the electromagnetic field or changes its spatial distribution in the vicinity of the sample. The scattered radiation is detected and, as a result, a sensitivity to local sample properties is achieved. Currently, various near-field techniques and approaches are applied successfully, the majority of these are described below.

1.9.1 Tip-enhanced near-field techniques

Tip-enhanced (or scattering-type) near-field technique is currently the easiest method used to achieve sub-wavelength resolution in any frequency range available. A sharp metallic tip is placed close to the sample surface into the place irradiated by radiation, see fig. 1.9i. During the propagation of the pulse a near field is created at the end of the probe. It is affected by the sample characteristics and is again coupled into the far-field radiation—this way the reflected radiation embraces a small changed portion of the field from the very vicinity of the metal tip. Consequently, due to the dimension of the disturbance, only a small part of the incident radiation can be used to retrieve the near-field information. The probe-sample

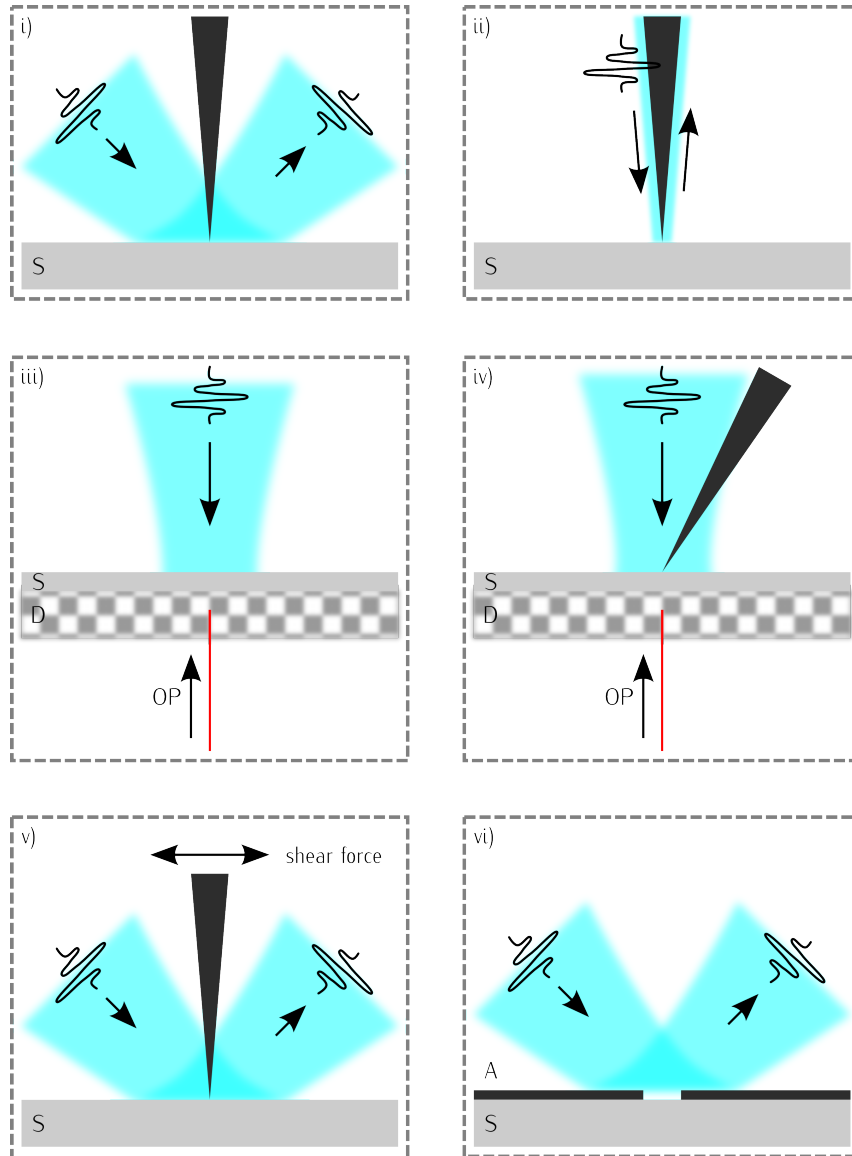


Figure 1.9: Near-field techniques (i–vi): A—aperture, D—THz sensor (opto-electric detector), S—observed sample. (i) tip-enhanced technique—a metallic (or AFM) tip is irradiated by a THz radiation, (ii) Sommerfeld-wire technique—the THz radiation is coupled to the metallic-tip surface, (iii) spot-sized detection technique—the detection area is given by the laser-spot size, (iv) THz-ANSOM technique—tip-enhanced technique is combined with laser spot-sized detection, (v) shear-force technique—contrast is enhanced by a vibrating tip, (vi) aperture-based technique—the useful information is collected from the aperture area. Continued at fig. 1.9

interaction may be non-trivial in the **time-domain (TD)** regime and was recently the subject of other studies [Thoma and Dekorsy, 2008].

This apertureless approach was previously used in the optical frequency region [Betzig and Trautman, 1992; Dürig et al., 1986]), also in the **MW** [Matarrese and Evenson, 1970], and it was first investigated experimentally in the **THz** region in 1998 [Hunsche et al., 1998]. A general, frequency-independent near-field tip-enhanced approach was described by Zuev and Frantnesson [Zuev and Frantnesson, 1998]. Several modification of the concept exist:

- ◇ The group of Kersting and Chen have prepared a near-field probe made of tungsten [Chen et al., 2003], and they were able to detect metal-dielectric [Cho et al., 2005] and doped-dielectric contrast [Buersgens et al., 2006]. Using an idea originating from Chen, Kersting, and Cho, later a shear force technique was employed to enhance the spatial resolution and image contrast [Buersgens et al., 2007], see fig. 1.9v.
- ◇ Call to mind that the resolution of the image is limited by the smallest inhomogeneity of the sensing apparatus, see section 1.8, one is forced to use imaging tips as small as possible. So, **AFM** tips have been irradiated by **THz** radiation and spatial resolution down to tens of nm (equal to the dimension of the **AFM** tip) was demonstrated [Garcia-Etxarri et al., 2009; Hillenbrand, 2007a,b; Huber et al., 2008]. This idea was proposed by Knoll and Keilmann in **mid-infrared (MIR)** spectral range [Keilmann and Hillenbrand, 2004; Knoll and Keilmann, 1999], and later it was combined with tapping mode of the **AFM** tips [Schnell et al., 2009; von Ribbeck et al., 2008].
- ◇ The concept of *Sommerfeld-wire waveguide method* [Awad et al., 2009] can be transformed into the tip-enhanced type. Here, the **THz** radiation is first coupled to a Sommerfeld wave moving along the free-standing wire surface [Sommerfeld, 1899a,b; Wächter et al., 2005], and then it travels along the surface of the metallic tip back-and-forth with a reflection on the sample surface at the end of the probe where near-field phenomena appear, see fig. 1.9ii. A combined method that couples the **THz** wave to the vibrating probe [Wang et al., 2004], see fig. 1.9ii and (v), has the potentiality for pulsed **THz** sensing and diagnostic systems with unreported resolution [Wang and Mittleman, 2007].
- ◇ A free-standing metal wire can be used only for collecting the field at the imaging plane and the longitudinal electric field (polarized along the wire antenna) can be collected with subwavelength resolution [Adam et al., 2009].

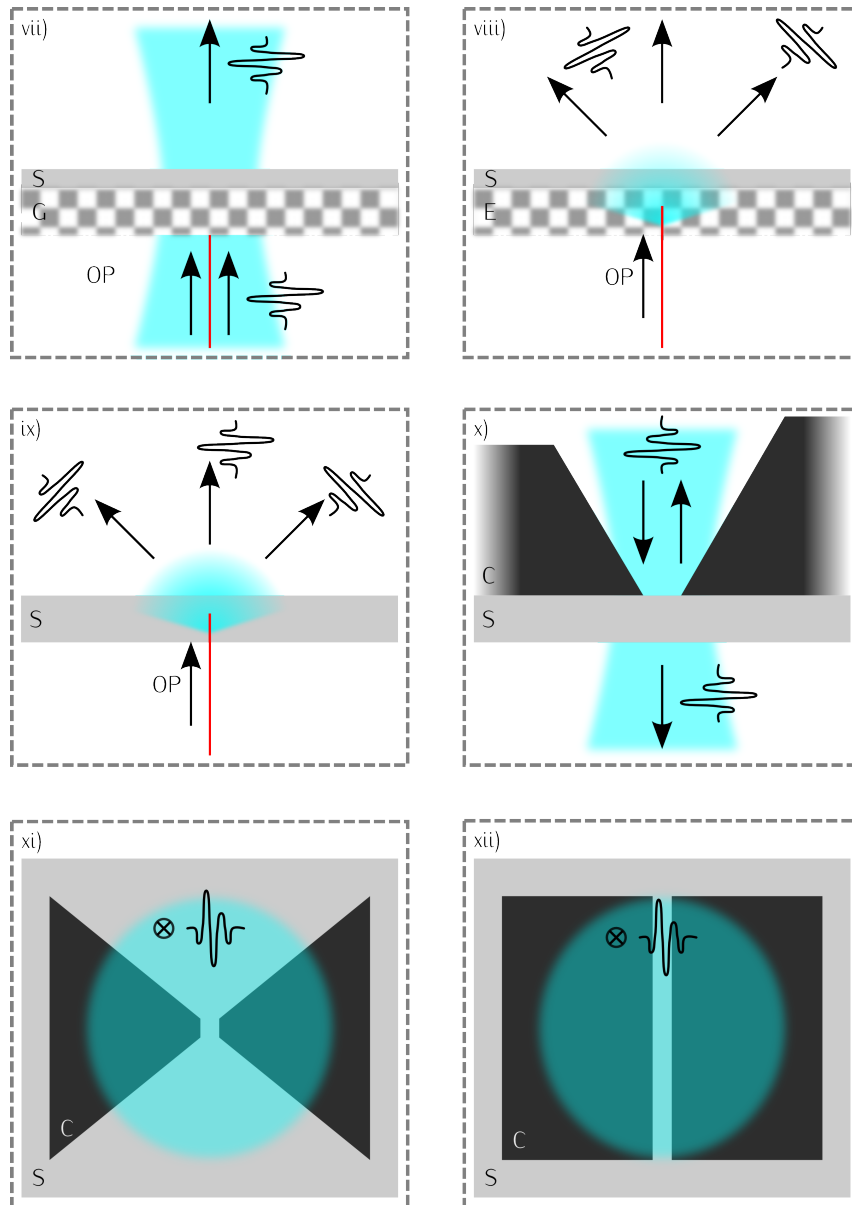


Figure 1.9: Near-field techniques (vii–xii, continuing fig. 1.9): C—confinement structure (usually bulk), D—THz sensor (opto-electric detector), E—THz emitter, G—gating material, S—observed sample. (vii) dynamic aperture technique—the perturbation area enhancing the near field is created by a laser spot, (viii) local-source detection—local source of THz radiation is created close to a thin sample, (ix) LTEM—a local source of THz radiation is created directly in the sample, (x) spatial confinement technique—a pyramid or cone structure is used to constrain the THz radiation, (xi) bow-tie antenna—the structure enhances the THz field between the apices, (xii) nano slit—a nanogap is used as an aperture.

1.9.2 Imaging techniques involving an optical laser beam

Bearing in mind that the spatial resolution is dependent on the smallest characteristic distance of the experimental setup, reducing a certain parameter at the right place might possibly lead to better results. In the following we focus on techniques in which manipulates the laser-beam spot in sensing or creating the near field. In those technique, reducing the shape and choosing the right placement of the laser-beam spot is playing the biggest role.

- ◇ The *dynamic aperture technique* uses a laser beam to create a gating to a part of the incident THz pulse in front of the sample, see fig. 1.9vii. The size of the gating, and thus the spatial resolution, is limited by the size of the laser spot and can be down to $\lambda/20$ [Chen et al., 2000]. A similar concept was earlier developed for MIR [Palanker et al., 1998a,b].
- ◇ Placing the detection area in immediate distance to the (THz-pulse—sample) interaction area, the presence of the near-field created by the sample structure is crucial. By limiting the sampling area of the laser beam on the detector crystal, information from this *spot-sized detection area* is collected only [Wynne and Jaroszynski, 1999], see fig. 1.9iii. Recent results using this concept have been published by Adam et al. [Adam et al., 2008a]. By this approach, field diffraction from subwavelength structures as well as coupling to the surface are possible to follow directly [Jiang et al., 2000; Seo et al., 2007; van der Valk and Planken, 2002]. Near-field images of the spectral amplitude and phase of the electric field are possible to reconstruct, to show the formation, propagation and attenuation of surface waves, and to allow distinguishing between propagating and stationary modes [Bitzer and Walther, 2008; Bitzer et al., 2009]. By contrast, *scanning near-field optical microscopy (SNOM)*-based (tip-enhanced and confinement-type) techniques are mainly sensitive to only the longitudinal electric field component and can not directly provide the magnetic information.
- ◇ The technique of *THz imaging by a local source* (also, imaging by a sub-wavelength source) is a method based on the fact that sub-wavelength sources can exist and are capable of emitting far-field radiation [Dakovski et al., 2005], see fig. 1.9viii. The source of the THz radiation is usually a thin electro-optical THz ZnTe emitter. Theoretical estimation of the spatial resolution of $\lambda/300$ proposed by Dakovski et al. is within results of recent measurements provided by Grésillon's group ($\lambda/10$) [Lecaque et al., 2006, 2008] and Zhang's group ($\lambda/100$) [Yuan et al., 2004a,b].

- ◇ The *LTEM* is closely related to the previous method of *imaging by a local source*. But here, the local THz source is created directly in the studied sample, see fig. 1.9ix. The setup uses a femtosecond laser [Rullière, 2003] to excite THz waves in various electronic materials due to ultrafast current modulation [Planken et al., 2005]. The current modulation is realized by the acceleration or deceleration of photo-excited carriers, and thus LTEM visualizes the dynamic photo-response of substances [Kiwa et al., 2003; Murakami and Tonouchi, 2008].

1.9.3 Tip-enhanced terahertz apertureless near-field optical microscopy

THz-ANSOM is a complex result of combining the tip-enhanced method with the laser-beam involved imaging [Planken and van der Valk, 2004; van der Valk and Planken, 2002]. Here, the THz near field in close vicinity of a metallic (or SNOM) tip is detected by the optical sampling beam in a sensor just behind a thin sample, see fig. 1.9iv. Active works are under progress by Adam et al. [Adam et al., 2007; Seo et al., 2007]. Even an all-component (transversal and longitudinal) field measurement of the near field around a metallic disturbance was proposed and assembled [Adam et al., 2008a,b].

1.9.4 Aperture-based near-field techniques

Aperture-based near-field techniques use a small opening (or an aperture, or pinhole) in front of the sample to enhance the spatial resolution, see fig. 1.9vi. On Babinet's principle, the diffraction pattern should be the same from a tip and from a hole of the same diameter size except for the overall forward beam intensity [Balanis, 1996, chap 2]. And, the power of the useful signal is dependent on the size of the opening and is strongly attenuated [Bethe, 1944; Mair et al., 2004; Mitrofanov et al., 2001b]. Nevertheless, successful experiments were provided by Masson et al. [Masson et al., 2006a,b] and Mitrofanov et al. [Mitrofanov et al., 2000, 2001a], [see also Mair et al., 2004].

- ◇ Recently, it has been shown that using a metallic nano slit, in the shape of a thin nano-sized long perforation in the metal layer or film, see fig. 1.9xii, creates a near field sensitive perpendicular to the opening and spatial resolution down to $\lambda/30000$ [Seo et al., 2009].

1.9.5 Confinement methods

Confinement near-field methods are such techniques in which the radiation is constrained into a small volume by a waveguiding structure. Most of the waveguiding structures are of transmission-line or waveguide types, see section 1.10.

Originally developed for IR waveguides [Keilmann, 1995], it was first experimentally demonstrated using a tapered metal tube [Hunsche et al., 1998] similar to one from SNOM. For a cross-section of such a symmetrical structure, see fig. 1.9x. It can be calculated that an all-side confinement structure (a waveguide) shows a strong frequency cut-off behaviour, see section 1.10. The cut-off can be eliminated by the following enhancements:

- ◇ A conical aperture probe placed into a powerful (synchrotron) beam is able to boost the evanescent field behind the cut-off that a $\lambda/40$ -spatial-resolution at 2 cm^{-1} was possible [Schade et al., 2004].
- ◇ To eliminate the low-frequency cut-off of a constraining waveguide (technique of Keilmann), a small wire [Schade et al., 2005] or a logarithmic coupling structure were introduced [Staats et al., 2006]. So, the confinement of the field at the structure opening is enhanced, coupling is more efficient and the structure is supposed to have no frequency cut-off at all. Chusseau was about to apply this idea to a rectangular waveguide opening [Chusseau, 2007].
- ◇ An open-side pyramidal-shaped dielectric probe also eliminates the frequency cut-off of the tapering, and it has been first used in the MW region in continuous regime [Ash and Nicholls, 1972]. A spatial resolution of $\lambda/200$ at 80 GHz was achieved by a metal-dielectric probe (MDP) [Klein et al., 2005]. It is a 3D structure in the shape of a pyramid metallised from two opposite sides and the idea is the basic concept of the MDP we are using for probing the THz waves, see section 2.1. In parallel with the measurements in our laboratory, a similar project, based on Teflon (PTFE) pyramids, has been launched in continuous regime by Chusseau [Adam et al., 2008b].

Using the concept of an open-side pyramid-shaped dielectric probe, supporting experiments on macro-model were conducted in the MW region [Rosner et al., 2002a] to prove and show the potential of a miniaturised lithography-built scanning probe with all-side coating in the MW and the optical frequency region [Rosner et al., 2002b].

- ◇ Awad and Chevillet used a submillimetre waveguide confinement of broadband THz pulses with a cylindrical-lens coupling of Mendis and Grischowsky [Mendis and Grischowsky,

- 2001], and a metal–silicon contrast was demonstrated [Awad and Chevillet, 2005]. The subwavelength resolution was realised by a narrow spacing in a parallel–plate waveguide.
- ◇ Other near–field methods at microwave frequencies rely on tapered metal transmission lines (section 1.10), for which subwavelength resolution can be easily attained, see e. g. [Tselev et al., 2003] and [Steinhauer and Anlage, 2001]. However, metal transmission lines such as coaxial lines or coplanar tips are very lossy and difficult to machine for the frequency range above 50 to 100 GHz.
 - ◇ The group of Wächter et al. has recently patented a freely–positionable photoconductive near–field probe–tip [Wächter et al., 2009] consisting from two tapered electrodes for field–singularity enhanced sensitivity—in fact, it is a confinement structure in plane.
 - ◇ To decrease or even eliminate the diffraction of the incident THz wave Nikoghosyan et al. tried to emit THz radiation directly in the pyramidal structure ended with a sub–wavelength end–facet [Nikoghosyan et al., 2004]. In this case, the tapering structure with no metallisation lead the wave on a long–enough distance, but side–radiance and outreach of the travelling pulse were present.
 - ◇ A *bow–tie antenna design* is a 2D variant of a pyramid–shaped probe, see fig. 1.9xi. Its manufacturing is easier, and it can also efficiently enhance the sensing field at the region between the apices. The idea is currently under improvement by Chusseau, in continuous–wave regime.

There have been efforts to build a near–field CCD camera (detecting large–area laser pulses modified by the opto–electric element and THz–waves interaction [Hattori et al., 2004]) and a sub–wavelength resolution of $\lambda/2$ was demonstrated [Jiang et al., 2000; Wang et al., 2009a; Wu et al., 1996]. But, this approach does not involve any near–field technique and conforms with the far–field image resolution criteria, see section 1.8, unless the scanning is combined with the spot–sized laser detection, see section 1.9.2.

1.10 Waveguides and transmission lines

Waveguides and transmission lines, are structures used to guide electromagnetic waves from point to point. However, the fundamental characteristics of waveguide and transmission–line waves (modes) are quite different. The differences in these modes result from the basic differences in geometry for a transmission line and a waveguide, see e. g. [Tamir, 1979, Chap. 2].

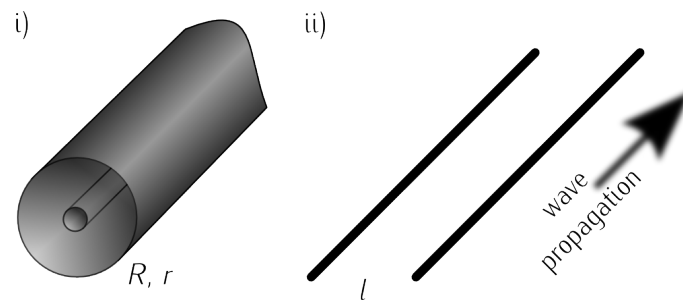


Figure 1.10: The basic types of transmission lines (a coaxial and a wire transmission line) may be characterised by a cross-section and a distance.

Transmission line

- ◇ A transmission line is two or more conductors separated by some insulating medium (two-wire, coaxial, microstrip, etc., waveguides, see fig. 1.10).
- ◇ Its normal operating mode is the **transverse electromagnetic (TEM)** or quasi-TEM mode. It can support **transverse electric (TE)** and **transverse magnetic (TM)** modes, too, but these modes are typically undesirable.
- ◇ There is no cut-off frequency for the **TEM** mode.
- ◇ Significant signal attenuation at high frequencies is due to conductor and dielectric losses.

Waveguide

- ◇ A waveguide is typically one enclosed conductor filled with an insulating medium (with a rectangular, circular, or other shape of its cross-section, see fig. 1.11).
- ◇ Its operating modes are **TE** or **TM** modes (cannot support a **TEM** mode, due to boundary conditions in the Maxwell equations.).
- ◇ A waveguide must be operated at a frequency above the respective **TE** or **TM** mode cut-off frequency for that mode to propagate.
- ◇ There is a lower signal attenuation at high frequencies for waveguides than for transmission lines.

Simple dielectric waveguides (enclosed or not by a conductor) can have a rectangular, a circular or a plate cross-section, and they are characterised by dimensions $a \leq b$, diameter r and plate distance $d \equiv a, b \rightarrow \infty$, see examples in figs. 1.10 and 1.11. The TE_{kl} and TM_{kl}

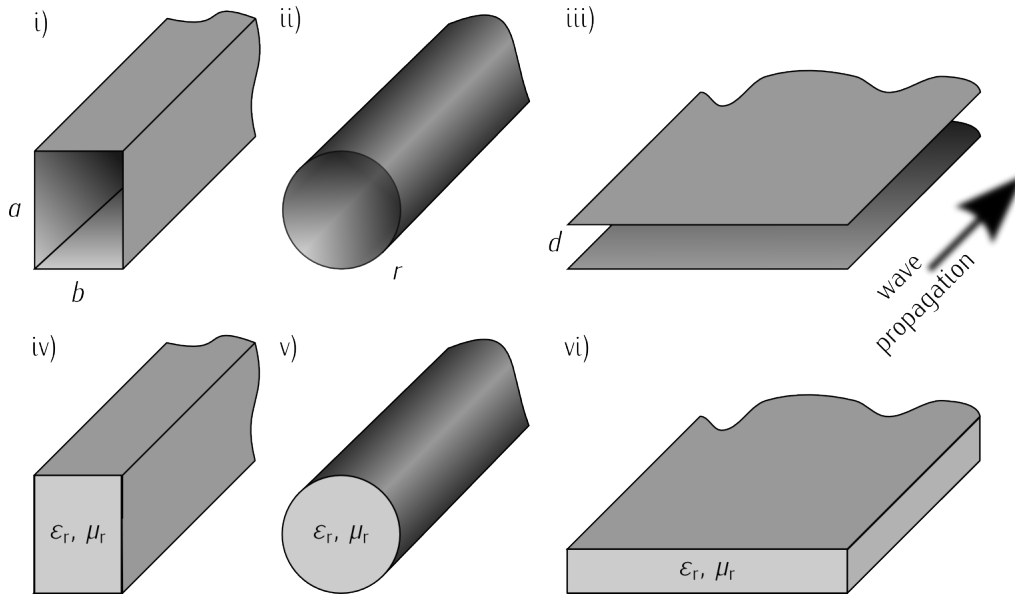


Figure 1.11: The basic types of waveguides (a hollow metallic and a dielectric rectangular, a circular and a plane waveguides) may be characterised by their cross-section and/or filling material properties, ϵ_r and μ_r .

modes for a can be then written as follows:

$$v_{kl} = \frac{c_0}{2\sqrt{\epsilon_r \mu_r}} \sqrt{\left(\frac{k}{a}\right)^2 + \left(\frac{l}{b}\right)^2}, \quad (1.11a)$$

$$v_{kl} = \frac{c_0 \chi_{kl}}{2\pi r \sqrt{\epsilon_r \mu_r}}, \quad (1.11b)$$

$$v_k = \frac{c_0 k}{2d \sqrt{\epsilon_r \mu_r}}, \quad (1.11c)$$

where where k and l are positive numbers, $\sqrt{\epsilon_r \mu_r} = n$ is the refractive index of the insulating medium, χ_{kl} is the k^{th} root of the l^{th} Bessel function $J_l(r)$. For both the TE_{kl} and TM_{kl} modes, one can find that the cut-off frequencies for the fundamental mode ($k = 0, l = 1$) are

$$v_{\min} = \frac{c_0}{2b_{\min} \sqrt{\epsilon_r \mu_r}}, \quad (1.12a)$$

$$= \frac{c_0 \chi_{01}}{2\pi r_{\min} \sqrt{\epsilon_r \mu_r}} = \frac{2.4048 \cdot c_0}{2\pi r_{\min} \sqrt{\epsilon_r \mu_r}}, \quad (1.12b)$$

$$= \frac{c_0}{2d_{\min} \sqrt{\epsilon_r \mu_r}}. \quad (1.12c)$$

and $d_{\min} = b_{\min} = \pi/2.4048 r_{\min}$ are the minimal and critical cut-off dimensions of the critical passageway below which only evanescent wave exists [Saleh and Teich, 2007, Chap. 7]. In other words, frequencies below a frequency $\nu \lesssim \nu_{\min}$ do not propagate further the minimal dimension. Modes higher than fundamental ($(k, l) \neq (0, 1)$) have higher cut-off frequencies.

1.11 Properties of some materials in the THz frequency range

The typical frequency range of the measurement is 0.1 to 1.2 THz ($\lambda \approx 0.25$ to 3 mm) (see fig. 2.8 where a typical waveform of a reflection is depicted with its calculated FFT). This whole frequency range was employed to analyse fingerprints of various samples (section 3.6). In the following, we list characteristics of some selected materials of different types displaying distinct properties within this frequency range. The average material constants within the experimental FD of sensed materials are listed in table 1.2 and they are connected by eqs. (1.13) to (1.15), after [Bass et al., 1994, chap 9.7] and [Wooten, 1972, p. 49].

$$\varepsilon'(\omega) = n(\omega)^2 - \kappa(\omega)^2, \quad \varepsilon''(\omega) = 2n(\omega)\kappa(\omega), \quad (1.13)$$

$$n(\omega) = \sqrt{\frac{\sqrt{\varepsilon'(\omega)^2 + \varepsilon''(\omega)^2} + \varepsilon'}{2}}, \quad \kappa(\omega) = \sqrt{\frac{\sqrt{\varepsilon'(\omega)^2 + \varepsilon''(\omega)^2} - \varepsilon'}{2}}, \quad (1.14)$$

$$n(\omega) = \frac{c_0}{c(\omega)} = \sqrt{\frac{\varepsilon(\omega)\mu(\omega)}{\varepsilon_0\mu_0}} = \sqrt{\varepsilon_r(\omega)\mu_r(\omega)}, \quad (1.15)$$

where $\varepsilon^* = \varepsilon' + i\varepsilon''$ and $\varepsilon' \equiv \varepsilon_r$.

Metal With their highly conducting properties in the THz frequency range, metals act as a shielding for thicknesses above ≈ 30 nm [Walther et al., 2007], and above this thickness, they can be considered as **perfect electric conductors (PECs)**, both for MW and THz radiation, see eq. (2.1). The radiation can be efficiently coupled to a metal surface and guided as has been demonstrated for various near-field-type probes, see section 1.9.1. At normal incidence, their reflectivity is one, $R = 1$. For this reason, metal-dielectric structures with more or less fine patterns are commonly used for testing the resolution limits of imaging experiments (figs. 3.17 and 3.18).

material	ϵ' ($\epsilon_0, \epsilon_{e0}$)	ϵ''	κ	n (n_o, n_{e0})
metal	∞	0	0	∞
BaTiO ₃	56, 2000	–	–	7.5, 45
sapphire	10.5	7	1	3.07, 3.41
high- q Si:B	11.5	1.0 to 0.1	0.02 to 0.16	3.4
mid- q Si:B	11.45	1.0 to 0.1	0.02 to 0.16	3.4
low- q Si:P	–	–	–	–
sample glass	–	–	–	2.08
SiO ₂	2.8	4	1	2.11, 2.15
Mylar	2.8 to 3	0	0	1.67 to 1.78
Teflon	2	0	0	1.433

Table 1.2: Material parameters of samples under investigation with our MDP. Most of the materials are listed in [Halpern et al., 1986]. A range is given when the value varies by more than 5% within 0.1 to 1.0 THz. Only the found and cited values (below) are shown here, the values not found are shown by a missing field (–).

Silicon dioxide (SiO₂) and glass Silica (SiO₂) occurs commonly in nature as sandstone, silica sand or quartzite, and it is one of the most abundant oxide materials in the earth's crust. It can exist in an amorphous form (vitreous silica) or in a variety of crystalline forms, often it will occur as a non-crystalline oxidation product on the surface of silicon or silicon compounds. Its ordinary and extraordinary refractive indices in the THz range are 2.11 and 2.15 [Grischkowsky et al., 1990], respectively. The ordinary axis in our measurement was perpendicular to the sample surface.

A microscopy slide was used as a sample of common glass. Its characteristics may vary from piece to piece, but we considered its refractive index close to that of an amorphous SiO₂, i. e. ≈ 2.1 [Halpern et al., 1986]. The imaginary part usually displays moderate THz losses, in contrast to pure quartz.

Plastics We have used plastics Mylar and Teflon to broaden the family of common material for our measurements.

- ◇ [Krishnamurthy et al., 2001; Loewenstein and Smith, 1971] Mylar is usually used in a form of a thin foil for beam splitting in optics: $n = 1.7(1)$ within 0.1 to 1.5 THz [Krishnamurthy et al., 2001].
- ◇ Teflon $n = 1.43$ @ 0.05 to 1.2 THz [Birch et al., 1981], absorption coefficient is too low to quantify [Halpern et al., 1986] or was found to be below 0.08 cm^{-1} for frequencies

< 0.5 THz [Birch et al., 1981].

High-resistivity and doped silicon The most common metalloid, Silicon (Si) of high bulk resistivity ($\rho \gtrsim 3 \times 10^3$ to $10^4 \Omega \text{ cm}$) is transparent for THz radiation [Grischkowsky et al., 1990], and its transparency slightly decreases for MW frequencies below 100 GHz [Seeger, 1988]. Its refractive index is $n = 3.41$, $\kappa \approx 0$. We investigated three samples of doped silicon differing in bulk resistivity ρ :

- ◇ a high-resistivity sample of boron doped silicon, Si:B, 6 to 12 $\Omega \text{ cm}$,
- ◇ a mid-resistivity sample of boron doped silicon, Si:B, 3 to 6 $\Omega \text{ cm}$,
- ◇ a low-resistivity sample of phosphorus doped silicon, Si:P, 0.09 to 0.1 $\Omega \text{ cm}$.

It was not possible to calculate the dielectric constants for the low-resistivity sample of Si:P due to its low transparency.

Sapphire Sapphire ($\alpha\text{-Al}_2\text{O}_3$) is a material highly transparent at MW frequencies with its absorption coefficient α_{abs} increasing, $\alpha_{\text{abs}} = 4\pi\kappa/\lambda > 2 \text{ cm}^{-1}$ above 1 THz [Grischkowsky et al., 1990]. It is birefringent and its refractive indices are $n_{\text{eo}} = 3.41$ and $n_o = 3.07$ @ 0.1 to 1.5 THz [Grischkowsky et al., 1990].

Silicon and gallium nitrides The nitrides are promising for MW technologies especially for their stable permittivities over a broad frequency range and low tangent of dielectric loss angle, 5.3 to 9.7×10^{-3} Silicon nitride based ceramics (Si_3N_4) have been widely studied because of their potential applications as structural components at room and elevated temperatures [Hampshire, 2007]. Silicon nitride is also a good candidate for high temperature microwave transmission due to the high mechanical strength, good thermal shock resistance, excellent resistance to rain erosion and an acceptable dielectric property [Barta et al., 1985]. For the continuous-wave (CW)-MW measurements, we have disposed of two samples: undoped gallium nitride (Si_3N_4) ($\epsilon_r = 7$) [Kliem and Holten, 1999] and GaN ($\epsilon_r = 9.0$) platelets (section 1.11).

Barium titanate (BaTiO_3 , BT) A flat as-grown barium titanate (BaTiO_3) single-domain crystal platelet was used for domain-imaging and sample-orientation dependent measurement, which exhibits a high anisotropy—its refractive indices are $n_o = 45$, $n_{\text{eo}} = 7.5$ in the THz and MW frequency ranges [Li et al., 1996].

Chapter 2

Data acquisition and treatment

In this chapter, we describe the concept of the **metal-dielectric probe (MDP)**, of the **metal-dielectric dual probe (MDDP)** and the process of their manufacture (section 2.1). The technical implementation of the **terahertz (THz)** and **microwave (MW)** experimental setups (sections 2.2 and 2.3) employed for measurements and the simulation tool CST MicroWave Studio® 2008 employed for numerical simulations (section 2.4) is described further. Further, we give explanation on the structure of our data acquired in experiments and in simulations (section 2.5), and finally, we introduce the reader to multivariate analysis (section 2.6) and to the process of the analysis of our data (section 2.7).

2.1 Metal-dielectric pyramid-shaped probes

Our work concentrates on a broadband measurement method with an asymmetric waveguiding pyramid-shaped probe, which was developed earlier [Klein et al., 2005]. It was developed in order to avoid three limitations of other methods:

1. the problem of low sensitivity introduced by the dimensions of near-field probes—the dimensions of the tips that are necessarily much smaller than the wavelength, see sections 1.9.1 and 1.9.4;
2. to overcome the cut-off problem introduced by the continuous metallisation of the probes' surfaces, see section 1.9.5;
3. and finally, to overcome the problem of losses (introduced by transmission lines) in near-field probes based on a transmission line, see section 1.10.

With this approach ([Klein et al., 2005]), we are able to concentrate THz field without substantial losses into a small volume and provide a near-field interaction.

2.1.1 Characterisation of the probes

The MDP consists of a rectangle-shaped block of a low-loss dielectric material sharpened to a pyramidal tip terminated by a subwavelength-sized plane facet, see figs. 2.1 and 2.18. Suitable materials for MDPs were chosen with respect to transparency and dielectric losses in the MW and THz frequency ranges. Three materials came into question and were studied finally: high-resistivity Si, sapphire ($\alpha\text{-Al}_2\text{O}_3$) and Teflon (PTFE). High-resistivity Si ($\rho \gg 3 \times 10^3$ to $10^4 \Omega \text{ cm}$) is transparent for THz radiation [Grischkowsky et al., 1990], but its transparency decreases for MW frequencies below 100 GHz [Seeger, 1988], see section 1.11. With sapphire, the situation is the opposite: it is highly transparent for MW, but its absorption increases above 1 THz [Grischkowsky et al., 1990], see section 1.11. Furthermore, sapphire is birefringent, so care has to be taken of material orientation at fabrication and polarisation orientation of the input pulse at the experiment. Both Si and sapphire have a very low dispersion in the MW and THz frequency range [Grischkowsky et al., 1990], therefore they are suitable as MW and THz waveguides. Finally, Teflon has very low losses as well as a low refractive index of 1.43 in the THz frequency range, see section 1.11.

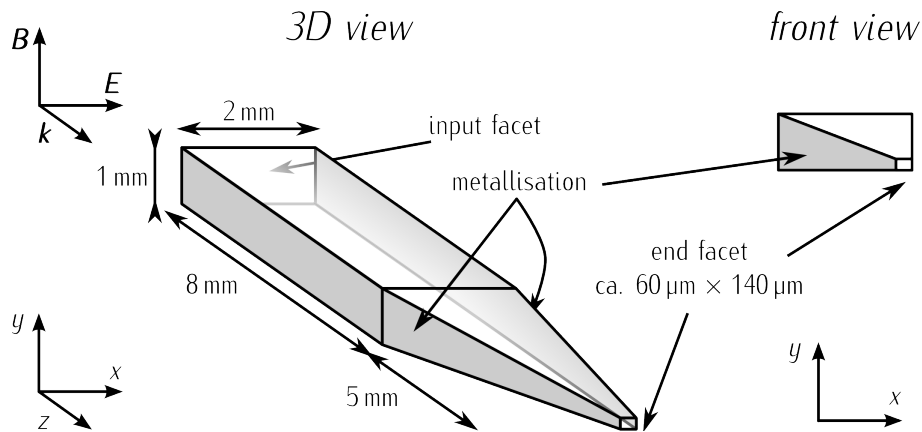


Figure 2.1: The asymmetric MDPs were made of sapphire and Teflon. Two neighbouring sides were tapered and two broader sides metallised usually. (The narrower sides are shown metallised in this schematic drawing.)

The benefit of the relatively *large* wavelength at THz frequencies is that the technical realisation of a focusing near-field probe is easier due to **electromagnetic (EM)** scaling than to build up the same structure for a similar effect at shorter wavelengths. Note that a similar method was applied in the **MW** and optical domain some years ago, where they used etching and electron-beam lithography method for probe manufacturing [Rosner et al., 2002a].

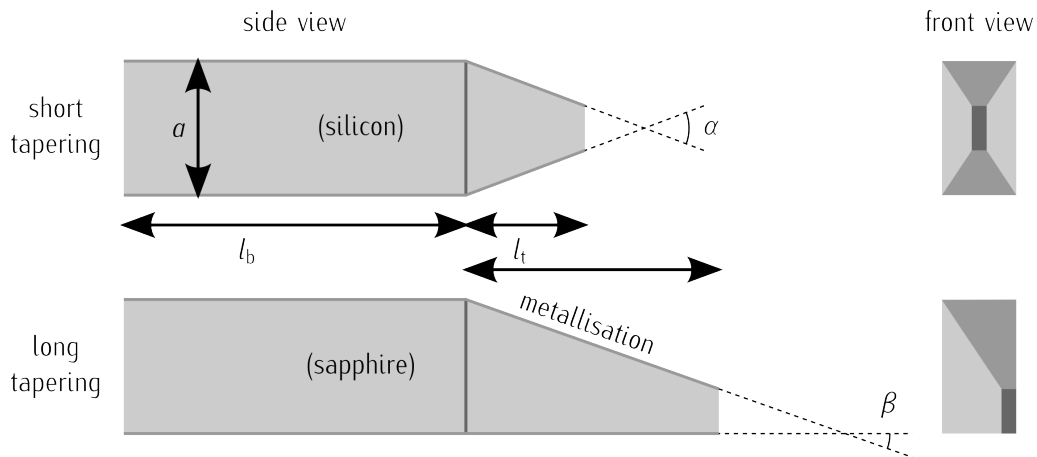


Figure 2.2: Measurements using probes with two different tapering were realised. Probes made of silicon with a cross-section of $1\text{ mm} \times 1\text{ mm}$ or $1\text{ mm} \times 2\text{ mm}$ were tapered on a distance of ca. 2 mm (short symmetric tapering). Probes made of sapphire and Teflon (with a cross-section of $1\text{ mm} \times 2\text{ mm}$ and $2\text{ mm} \times 2\text{ mm}$, respectively) were tapered on a distance of ca. 5 to 6 mm (long tapering), i. e. $\alpha < \beta$. (Here, the dimensions of the probe ends are not to scale for illustration of the tapering and the asymmetry.)

Blocks of dielectrics were prepared with dimensions

- ◇ $1\text{ mm} \times 2\text{ mm} \times 12\text{ mm}$ to 15 mm (silicon probes),
- ◇ $1\text{ mm} \times 2\text{ mm} \times 15\text{ mm}$ (sapphire probes) and
- ◇ $2\text{ mm} \times 2\text{ mm} \times 25\text{ mm}$ (Teflon probes—these could be cut to a shorter length easily).

They were cut and polished into a form of a quadrilateral truncated oblique frustum, i. e. an asymmetric pyramid with a small end facet, see fig. 2.1. The tapering angle of these frusta varied within our set of probes. The pyramidal tips could be symmetric, semi-asymmetric, or fully asymmetric. At first experiments, we disposed of symmetric **MDPs** (made of silicon; the length of the tapering was 1 to $2\times$ longer than the sides of the rectangle in cross-section of the probe). Later we widely employed asymmetric **MDPs** (made of sapphire and Teflon, and of which the length of the tapering was 2 to $6\times$ longer than the sides of the rectangle in cross-section of the probe), see fig. 2.2. Simulations and experiments of Dudorov on waveguide

transitions showed that the longer tapering has less side leakage and less influence on the shape of the transient pulses [Dudorov, 2002].

Two opposite sides of the tapered block were metallised—the coating consisted of a 10 nm titanium as an adhesive layer, 1 μm of silver as a conductive layer and 30 nm of gold as a protective layer. The thickness of the (silver) conductive layer was ca. $4\times$ larger than the skin depth δ_{skin} at the lowest frequencies of our experiments, $\nu_{\text{min}} \approx 76$ GHz (for microwave experiments), i. e. very close to the limit of a **perfect electric conductor (PEC)**:

$$\delta_{\text{skin}} = \sqrt{\frac{2\rho}{2\pi\nu\mu_0\mu_r}} \approx \begin{cases} 0.23 \mu\text{m} & @ 76 \text{ GHz} \\ 80 \text{ nm} & @ 0.6 \text{ THz} \quad (\equiv \nu_{\text{m,THz}}) \end{cases} \quad (2.1)$$

where the bulk resistivity and the relative permeability for silver are $\rho \approx 1.6 \times 10^{-6} \Omega \text{ cm}$ [Lide, 2001, p. 12-43] and $\mu_r \approx 1$ ($\mu_r \equiv 1 + \chi_m$, where the magnetic susceptibility $\chi_m = -2.4 \times 10^{-5}$ [Griffiths and College, 1999, p. 275], derived from [Lide, 2001, p. 4-134]) at 20 °C, respectively. The $\nu_{\text{m,THz}} \approx 0.6$ THz is the mean frequency of the THz range with the typical frequency range sensed 0.1 to 1.2 THz, see fig. 2.8.

The dimensions of the end facets of the tested MDPs spread in the range from $30 \mu\text{m} \times 50 \mu\text{m}$ to $90 \mu\text{m} \times 140 \mu\text{m}$. The metallisation on the two sides prevents a cut-off, which would be, in the case of all-side coating, $\nu_{\text{min}} \approx 1.5$ THz for the extreme end facet of $30 \mu\text{m} \times 50 \mu\text{m}$ of a **sapphire** probe, see eq. (1.12a).

The tapering of a MDP with an angle $\angle \approx 15$ to 30° focuses the incident wave onto the end facet, giving rise to a highly localised EM field. This field is thus sensitive to the permittivity (conductivity) in the close vicinity of the end facet and it is suitable for broadband applications. From simulations, see section 3.7.4, it can be deduced that the near field is split up into multiple lobes and the overall interaction volume of the detected signal is just slightly larger than the area of the end facet. That was also confirmed by experiments by using a sapphire probe (fig. 3.17).

Most of the probes were fabricated in the optical workshop of the **Institute of Physics of the AS CR, Prague (IoP)** (prepared by the former group leader Jiří Fryšťacký); a part of them was prepared by **CrysTec GmbH** company specialized in crystal manufacturing [CrysTec GmbH, 2010]. The optical workshop in Prague was able to process both Si and **sapphire** probes with high quality end facets. The **sapphire** probes polished by **CrysTec GmbH** showed high ratio deformation in the end-facet area—the end facets were elongated, their dimensions varied from

$5\ \mu\text{m} \times 40\ \mu\text{m}$ to $20\ \mu\text{m} \times 150\ \mu\text{m}$ and they were of irregular shape. [CrysTec GmbH](#) reported that they were not able to process Si probes using industrial methods due to the high fragility of the material.

The MDPs were placed into an opto-THz setup that was a modification of a **time-domain terahertz spectroscopy (TDTS)** in reflection geometry (see section 2.2 for a detailed description). The emitting and the detecting part of our experiment were the same in concept as those for a TDTS with a sample in reflection geometry, see section 1.4 and figs. 2.6 and 2.7 for the TDTS setup and for the imaging setup.

The described confinement structure enabled us to concentrate THz pulses into a small (subwavelength) volume at the tip end and near the sample surface. However, the **time-domain (TD)** profile of the output THz pulses is influenced by the inner reflections in the waveguide and by irregularities of the end facet. Also, there is a high impedance mismatch between the MDP end and the adjacent sample medium due to their different ϵ^* . Therefore, a rather small fraction of the output THz pulse is reflected back at the tip-sample interface and only this fraction carries the information about the sample local properties. These features prevented a straightforward evaluation of the raw experimental data; therefore a data-mining technique was used to extract useful information, see section 2.7.

2.1.2 Teflon probes

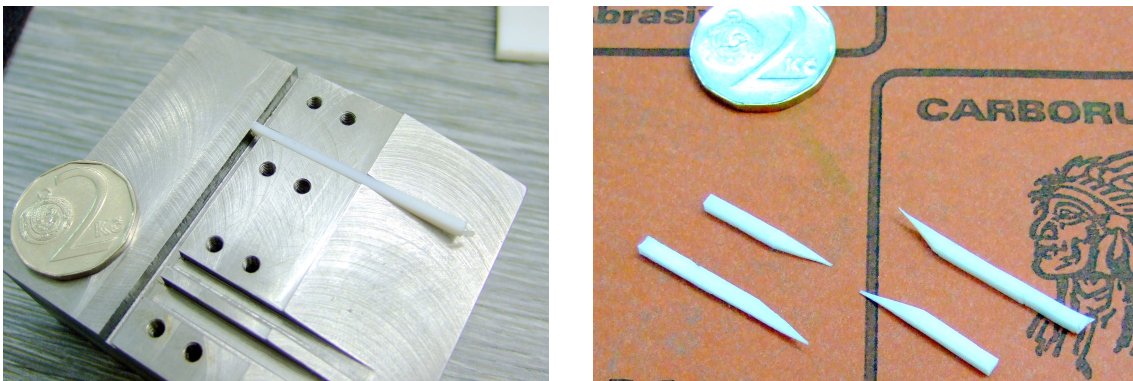


Figure 2.3: The special holder made of a steel block was used for manufacturing the Teflon probes.

The Teflon probes were manufactured by using a holder, specially designed to this purpose. It consisted in a steel block with slots of widths of 2 mm, 3 mm and 4 mm, a tapering under 20°

and fixtures for clamping the Teflon blocks, see fig. 2.3. In order to manufacture a Teflon probe, first, a block of a square cross-section and a 40 mm length was cut from a large plate and the cut sides were polished by emery and sanding papers of different granularity (using granularity gradually from 200 to 2000 and sanding papers used for polishing optically smooth surfaces, too).

Then the block was clamped into a slot and its ending at the tapering was covered by an (ordinary) two-component epoxy resin. The hardened coat of the resin protected the soft Teflon block from fringing and deformation while polishing down to the steel holder. After sanding off the resin and creating a small wedge, the block of the Teflon was turned by 90° in the holder and the process of glueing and polishing was repeated. This way an asymmetric probe (fig. 2.1) was created with no frustum—that protected the yet uncut tip of the probe until it was metallised. By a careful sanding, it was possible to create very smooth surfaces and to polish a Teflon block into a sharp probe with useful dimensions of ca. $100\ \mu\text{m}$ at the end.

The Teflon surfaces to be metallised were modified by ion bombarding by ions of oxygen (O_2^+) at ca. 5×10^{-4} mbar [Lee et al., 2004]. The modified surfaces were covered by a titanium layer of $1000\ \text{\AA}$ by an electron gun ($I_{\text{gun}} = 60\ \text{mA}$, $U_{\text{gun}} = 10.35\ \text{kV}$, vacuum 2 to 3×10^{-7} mbar and decomposition rate of the layer 4.0 to $4.2\ \text{\AA}/\text{s}$) and by a golden layer of $1500\ \text{\AA}$ from a crucible (vacuum of 8 to 9×10^{-8} mbar, grow rate 3.0 to $4.0\ \text{\AA}/\text{s}$). The temperature of the layer close to the samples was $T_{\text{max}} = 29$ to $30\ ^\circ\text{C}$. The metallisation of the MDPs withstand cleaning in a sonicator.

After cutting off the ending as short as possible that was usually distorted by sanding and metallised from all sides, the MDP was ready for measurements. The surface conductivity was checked by measurement of a resistance between two points on each of the sides separately (30 to $60\ \Omega \approx \rho_s$) and between the opposite sides (ca. $0.1\ \text{M}\Omega$). In cases when the probe end was still metallised, a resistance of $30\ \Omega$ was measured. Finally, the probes were used for scanning in a dual probe (section 3.8) or separately with flat or tilted end facet (fig. 3.18).

2.1.3 Concept of the dual probes

In this section, we describe the concept of a MDDP. Experiments employing a MDDP and results of these experiments are described in section 3.8.

The changes of the relatively strong back-reflected pulse reflect the properties of the sample under the probe. To reveal the usually subtle and (at first sight) nonlinear changes in the

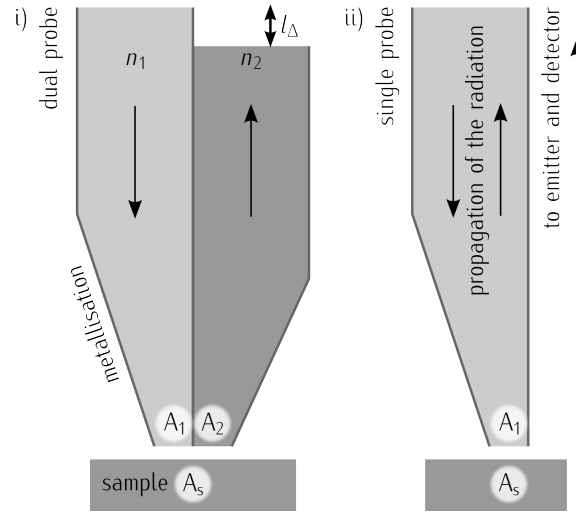


Figure 2.4: (i) The dual-probe concept, where the probe area A_1 emits the radiation and polarises the sample area A_s , which then re-emits the radiation. The interaction area is a weighted intersection of the probing area A_1 , sensing area A_2 and an area on the sample A_w . (ii) At the single probe the sensing area is equivalent to the emitting area, $A_2 \equiv A_1 \equiv A_s$, and the intersection of the probing area A_1 and sample area A_s can be much larger than at the dual probe.

strong background (depicted in fig. 3.3 in section 3.2), a decomposition of the dataset has to be applied, see section 2.7. The useful signal reflecting the sample properties is often 10 to 100 \times lower than the overall signal intensity, see section 3.2. Therefore, it would be more efficient and straightforward to have the background already extracted during the measurement. To achieve that, we proposed a so-called dual-probe structure that consists of two probes made of materials with different refractive indices (*without loss of generality (WLOG)* we establish $n_1 < n_2$) joined together by their metallised sides, see fig. 2.4. The two probes have similar dimensions—especially, their physical lengths are almost equal so that both input facets can be placed at the THz focal plane. A small difference in lengths l_Δ is ensured so that $l_1 \approx l_2 = l_1 - l_\Delta$. This difference $l_\Delta \approx 0.5$ to 1.0 mm between the input facets ensures a time delay of 3 to 6 ps of the input-facet reflections, and it enables a convenient positioning of the dual probe to its proper place, see fig. 3.33. We assume that the sensitive region of a MDP exceeds the borders of the end facet of a probe. This idea was confirmed by results of a simulation and experiment described in section 3.5.2. Therefore, an intersection of two overlapping sensitive regions exists at the junction of the two end facets of a MDDP.

Due to their markedly different refractive indices, the optical lengths of the two probes differ

($l_1 n_1 < l_2 n_2$) and therefore, several distinct pulses can be captured in the waveform, of which three are significant (cf. fig. 2.5):

- ◇ Two pulses each travelling through a different probe—their times of pass are

$$t_1 = 2 \frac{l_1 n_1}{c_0}, \quad (2.2a)$$

$$t_2 = 2 \frac{l_\Delta + l_2 n_2}{c_0} = 2 \frac{l_\Delta + (l_1 - l_\Delta) n_2}{c_0} > t_1; \quad (2.2b)$$

- ◇ Two pulses travelling through one probe and, after interacting with the sample at the overlapping regions, returning through the other probe backwards to the input facet. Both cross-pulses appear at a delay time

$$t_{12} = t_{21} = \frac{l_1 n_1 + l_2 n_2 + l_\Delta}{c_0} = \frac{t_1}{2} + \frac{t_2}{2}, \quad (2.3)$$

- i. e. exactly between the two pulses arriving at times t_1 and at t_2 .

The two cross-pulses interact with the sample surface separately at distinct times and they do not interfere with each other near the surface sample. Instead they meet head-on in the optically denser probe n_2 at a distance $\frac{t_{12} c_0}{2} \stackrel{l_\Delta \ll l_1}{=} l_1 (1 - \frac{n_1 + n_2}{2})$ from the sample surface and no interaction of the two pulses is present due to the weakness of their EM fields. The fact that they do not interact is important for analysing the output signal—the contributions of the separate cross-pulses sum up linearly creating the output signal. At this time-delay (t_{12}) there is also almost no returning (background) signal (fig. 2.5, black line, —), i. e. the ratio of the amplitudes of the signal and the change is highest in the whole collected time domain. Concurrently, the amplitude of the change is comparable at other times (those at t_1 and t_2).

2.2 Experimental configuration for the terahertz measurements

As we have demonstrated in several places in chapter 1, the THz range has become a popular domain in spectroscopy (sections 1.1.1 and 1.4) and imaging (sections 1.6 and 1.9), mostly using single-cycle EM pulses and time-domain spectroscopy (TDS) [Cho, 2009] for their broadband characteristics.

A schematic drawing of our full setup is shown in fig. 2.6 and the THz part of the setup is also shown on photographs in figs. 2.7i and 2.7ii. Free-space propagating THz pulses are generated

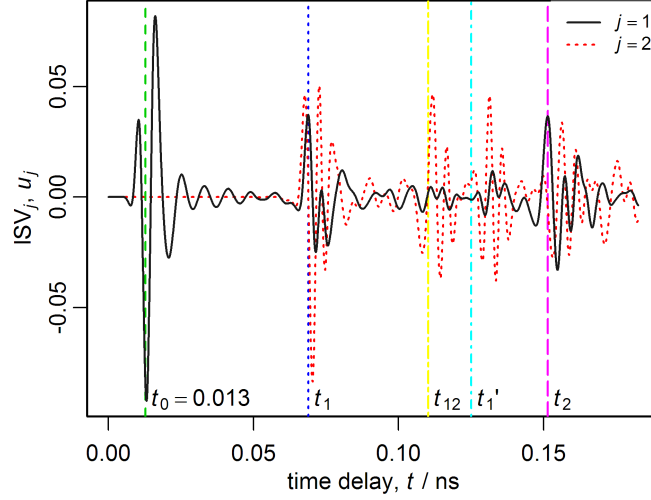


Figure 2.5: The sample-probe distance sensitivity for a dual probe (fig. 2.4) was simulated using CST MWS. A series of simulations (e. g. section 3.5.1) was decomposed using SVD (see later section 2.7). The average of the pulse response over the full simulation time (black full line, —) and the sensitive areas belonging to the near-field component (red dotted line, \dots) are depicted. For sake of simplicity, we assume the lengths of the probes to be equal, $l_1 = l_2 = l$. The input pulse is started to be generated at a time 0 ns, and its maximum appears at a time $t_0 = 0.013$ ns (—). Due to the input facets close to the radiating port, the position of the reflection at the input facets appears almost identical at the creation of the input pulse ($t_\Delta = 4 \times 10^{-4}$ ns). The maximum of the back-reflected input pulse travelling along the optically thinner probe is sensed at a time $t_1 = t_0 + 2n_1l/c_0$ (\dots), and that of the pulse travelling along the optically denser probe, at a time $t_2 = t_0 + 2n_2l/c_0$ (—). Their cross-talk arrives back in between them, at a time $t_{12} = t_0 + (n_1+n_2)l/c_0$ (—). Due to longitudinal/lengthwise inner reflections in the waveguide, the maximum of the 2nd reflection in the thinner probe is visible at $t_1' = t_0 + 4n_1l/c_0$ (—), too. The most sensitive time-delays of the waveform belonging to a reflection are usually located around the maximum of that reflection, e. g. at $t_1 - \Delta$ and $t_1 + \Delta$ for the 1st pulse reflection.

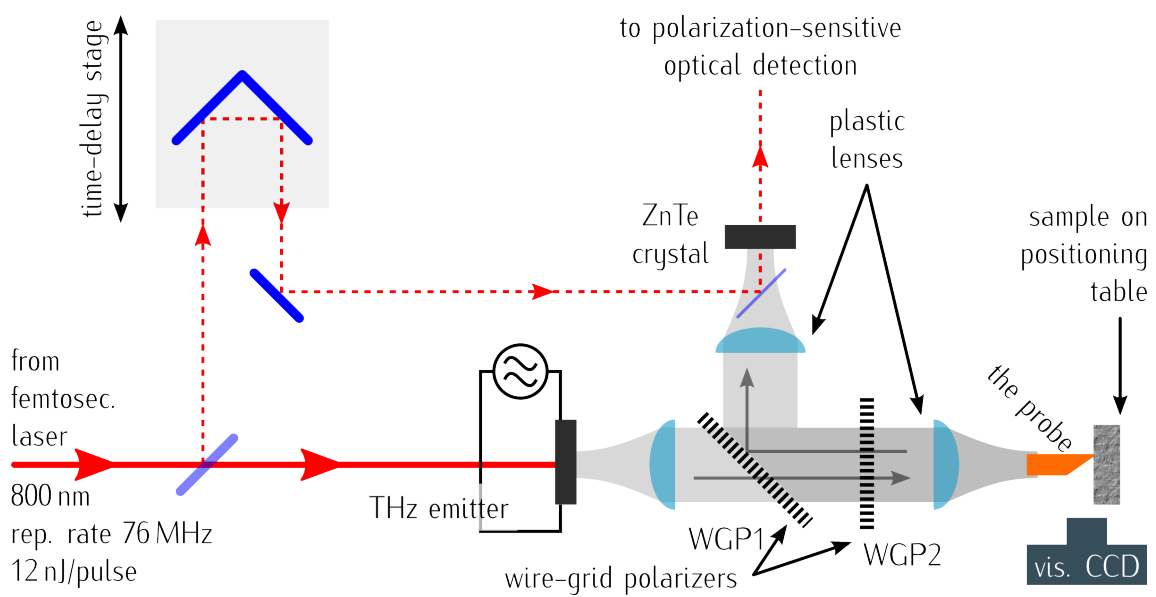
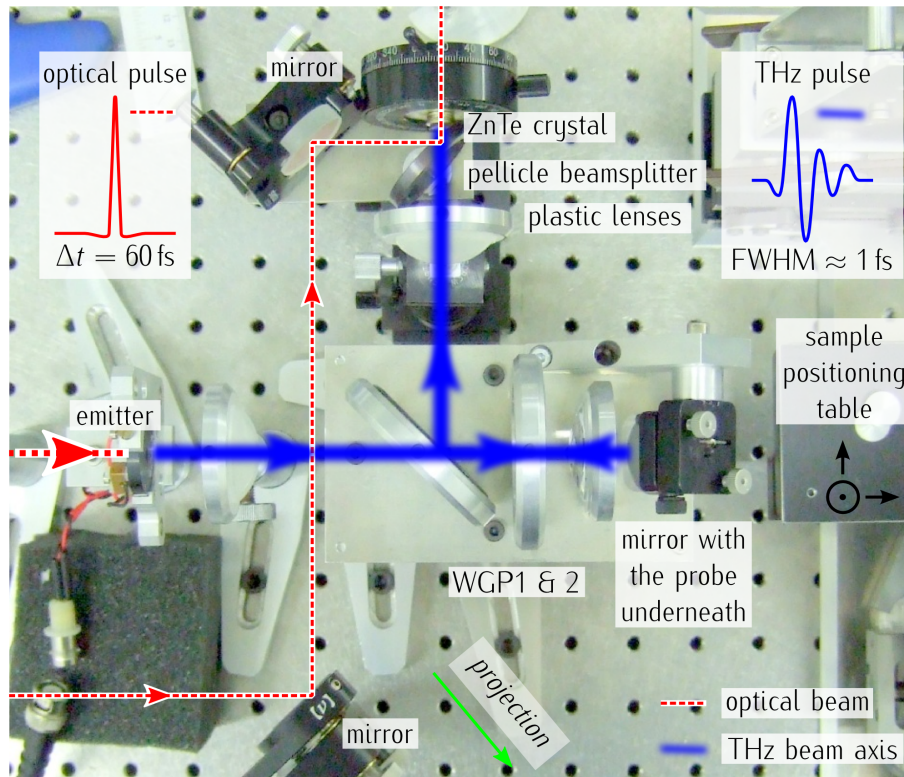
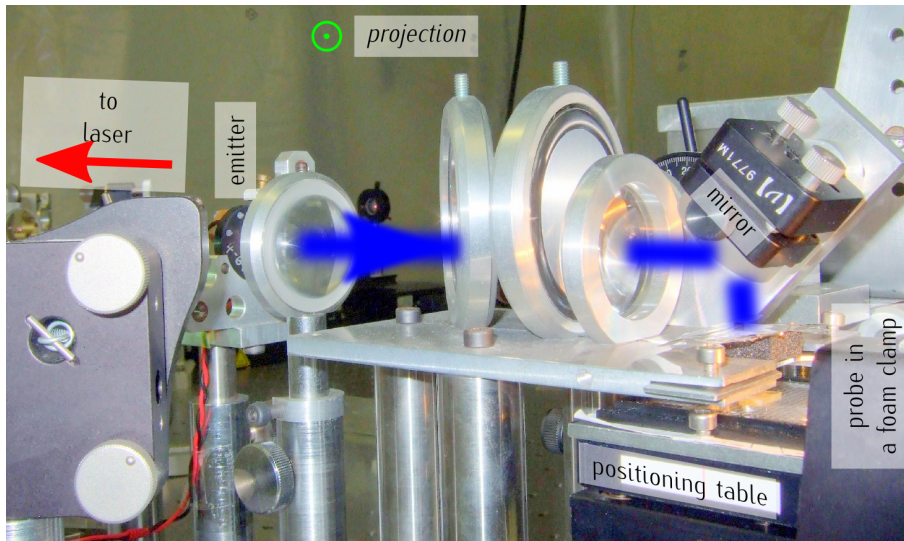


Figure 2.6: A schematic drawing of the THz near-field imaging setup. Optical pulses with an energy of 12 nJ (solid line) are converted to THz pulses (grey area and arrows, ■, →) at the emitter and a small fraction of these optical pulses (dashed line) deflected by a beam-splitter is used for electro-optical detection. The generated THz pulses are directed by plastic lenses and wire-grid polarisers onto the near-field probe.



(i) (top view) There are two polarisers, three Picarin lenses, a pellicle beamsplitter and a mirror in the THz path.



(ii) (oblique side view) The THz beam is directed to the vertically positioned probe by a metallised mirror.

Figure 2.7: Path of the terahertz beam in the THz setup.

using Ti:sapphire 50 fs-long laser pulses and Tera-SED large area biased photoconductive emitter [Dreyhaupt et al., 2005]. The THz pulses are focused by a pair of plastic lenses onto the input facet of the probe, so that the polarisation of the radiation is perpendicular to the metallised surface of the probe. The radiation travels along the probe (see section 2.1) and the focusing in the pyramidal part is enabled by the metallisation on two opposite sides. In this way, the EM field is guided and concentrated around the end facet. The focused field pattern interacts with the close environment of the tip, and a substantial part of the radiation is reflected back. These back-reflected pulses are directed by the wire-grid polarisers and another plastic lens onto the electro-optical sensor—a 1 mm thick zinc telluride (ZnTe) crystal. The orientation of the wire-grid polarisers is such that it is possible to deflect the back-reflected pulses to the detection system: the 1st polariser (WGP1) is oriented along the polarisation of the incident THz radiation, while the 2nd one (WGP2) is turned by $\pi/4$ with respect to the 1st one (see fig. 2.6). The temporal profiles of the electric intensity of the THz pulses $E(t)$, also called waveforms, are detected by electro-optic sampling in the ZnTe crystal, see section 1.3.2.1. Typical examples of an incident THz pulse (input waveform) and of a back-reflected pulse from the tip (output waveform) are shown in fig. 2.8. Different materials placed into the proximity of the tip leave different fingerprints in the shape of the output waveforms (see later fig. 3.2). Our THz measurement setup can be remotely controlled by our internally developed software PKGraph [Kužel, 2010].

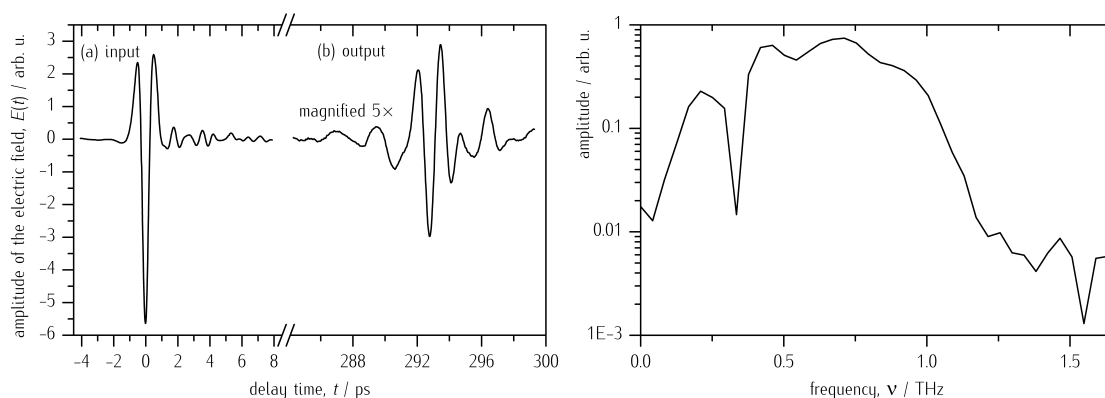
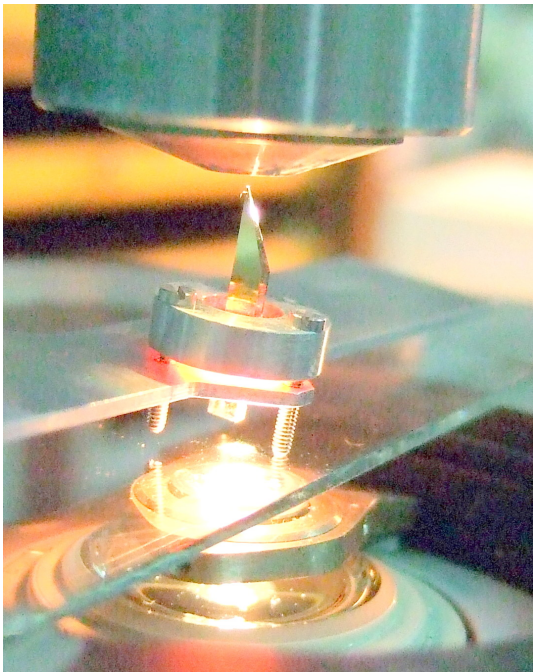
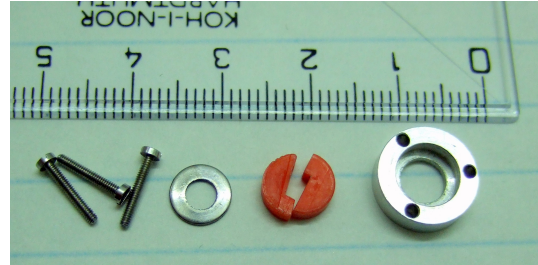


Figure 2.8: The THz waveform reflected from the input facet of the probe (a) and from the end facet (here multiplied by 5) (b) were usually collected (left). The strong after-ringing in the input waveform is due to absorption by water vapour and dispersion of the pulse. The mean frequency of the output pulse frequency range (right) was evaluated to $\nu_{\mu} \approx 0.6$ THz (eq. (3.2)).

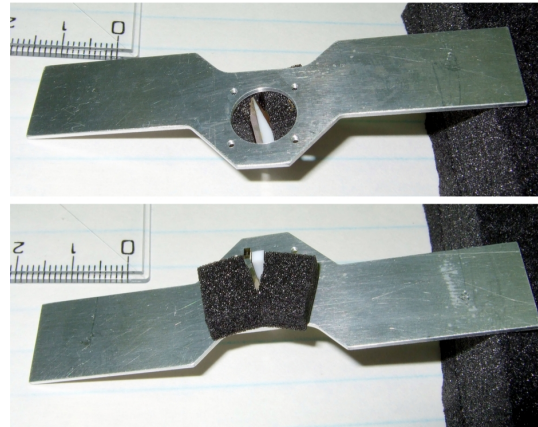
2.2.1 Mounting of the probes



(i) The probes were held in a metal-plastic clamp for a single probe. Here, the clamp with a probe is photographed being above a microscope light and under a microscope ocular. The parts of the clamp are in (ii)



(ii) A metal-plastic clamp for a single probe. The eligibility of such a construction is in repeatability in placement of numerous probes (but those differing in length only, with a specified cross-section).



(iii) The dual probes were fixed by a provisional foam clamp. The eligibility of such a construction is in flexibility to clamp a probe within a range of cross-sections. The repeatability in placement of numerous MDDPs is decreased and additional manual adjusting is needed.

Figure 2.9: Mounting for probes: a clamp for single probe and a foam mounting for a probe with arbitrary shape.

Single MDPs were mounted in a metal-plastic clamp, figs. 2.9i and 2.9ii, which was designed for probes with a specific cross-section, e. g. $1\text{ mm} \times 2\text{ mm}$.

The dual probes introduced a new (larger) cross-section and could even vary in that size; the conventional single probe clamp could not be used anymore. Therefore a simple mounting was used, made of a foamed plastic that was glued to a plate with a hole (the base of the conventional clamp), see fig. 2.9iii. The area around the input facets was shielded by pieces of

an aluminium foil, so that most of the far-field radiation that was not coupled into the probe was screened by this shield. The horizontal positioning of a probe to the optimal place was made by hand while measuring in real-time fast acquisition mode. First, the position of the beam waist was calculated and then the position of the second plastic lens was adjusted to place the waist around the plane of the input facet.

2.2.2 Characterisation of the THz beam

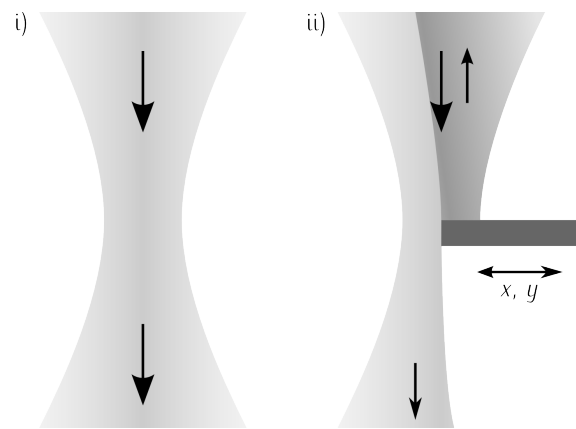


Figure 2.10: The THz beam profile was characterised by using a metallic mirror with a sharp edge shifted across the beam waist. The radiation was partially reflected and the frequency content and intensity content were extracted from the back-reflected waveforms, see fig. 2.11. The influence of the diffraction on the edge was neglected.

As a result of the growing importance of the **TDS** technique, much attention has been paid to characterizing the **THz** beams: divergence, spatial distribution of the frequency modes and polarisation of the radiation. The knowledge of the divergence and focus place of the irradiating beam is important, because a plane wavefront of maximal-illumination density is coupled into the probe ideally, see section 2.1. In optics, one could use visual cameras, but in the **THz frequency-domain (FD)**, we are limited to characterise the radiation by using secondary tools. [Gallot et al.](#) suggested to use two circular apertures (negative and positive) with different radii. Those placed in-axis into the beam would allow for a large beam-waist characterisation. The suggested measurement is technically complex for our purpose due to the in-axis discs alignment and is more suitable for large ratios of the beam waist and beam length [[Gallot et al., 2009](#)].

Therefore, we took advantage of the reflection geometry and we used a sliding edge of a metallic mirror freely positionable in the focal plane by the positioning table, see fig. 2.10.

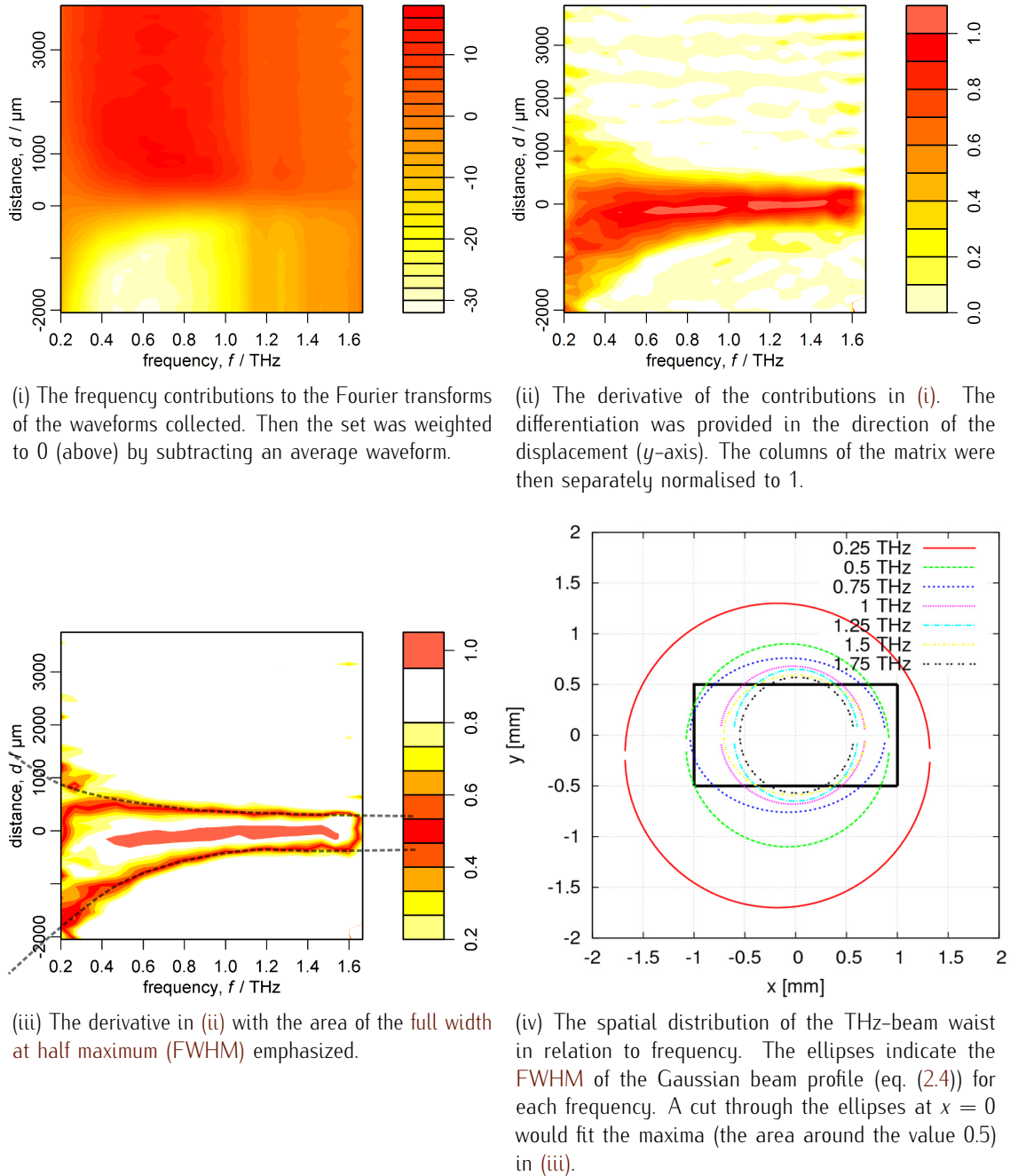


Figure 2.11: In the spatio-frequency pattern of the THz beam waist (at the place of input facets of probes), the FWHMs were calculated for the available frequency range.

The waveforms reflected by the sliding mirror were collected in to a matrix; see fig. 3.1 for an example of such a back-reflected waveform. The dataset were then processed by the the following steps to obtain a visual analysis:

1. The **fast Fourier transform (FFT)** provided an image in the **FD**; that was normalised by subtracting the mean waveform of the dataset, see fig. 2.11i.
2. In the direction of the movement of the mirror, the data-vectors summed up (integrated) the reflected intensity—ideally, into an error function; here, the original Gaussian distribution was obtained by a discrete differentiation (the j^{th} column was subtracted from the $(j + 1)^{\text{th}}$ column, the `diff()` function can be used in MATLAB or in R environments).
3. We normalised the columns so, that the values loosely fit into the range (0, 1) in fig. 2.11ii (all columns were divided by the number equal to the mean value of the first three maxima); then
4. the values around the level 0.5 were enhanced in colour to visualise the **FWHM** fig. 2.11iii.
5. The normalised values were fitted by a Gaussian profile at several frequencies and for both measurement directions (orthogonal to each other). The Gaussian distribution follows the relation

$$f(x) = \frac{1}{\sqrt{2\pi\sigma^2}} e^{-\frac{(x-\mu)^2}{2\sigma^2}}, \quad (2.4)$$

in which parameters μ and σ^2 are the mean and the variance of the distribution. The **FWHMs** $\approx 0.6\sigma$ were extracted from the parameters of the fits and ellipses were constructed using the calculated **FWHMs** as their diameters (fig. 2.11iv).

The profiles for frequencies below 0.3 THz and above 2.0 THz are clearly no more representing a Gaussian distribution; but the **FWHM** for those frequencies can be extrapolated using the frequency range in-between. It can be seen that the **FWHMs** of our beam is strongly dependent of the frequency, especially below 1.0 THz. But it is almost independent on frequency above 1 THz and the intensity of the radiation is also much lower.

2.2.3 Optimisation of the coupling of the radiation

The frequency distribution of the THz-beam profile is depicted in fig. 2.11ii with the approximate intensity distribution and the **FWHM** for some discrete frequencies in fig. 2.11iv. Less than about 50% of the radiation below 0.5 THz is coupled into an aligned 1 mm \times 2 mm input facet

(fig. 2.11iv). We have proposed two improvements to enhance the coupling of these lower frequencies.

We have tried to couple the THz pulses into our waveguide by a horn launcher (based on [Dudorov, 2002]), see fig. 2.12 and by a hemispherical Si lens [Rudd and Mittleman, 2002]. The successful coupling should have had two significant consequences:

- ◇ the coupling would *direct a major part* of the THz radiation available onto the plane of the input facet; and
- ◇ it would *eliminate diffraction* at the edges of the input facet.

Additionally, focusing a Gaussian beam is possible so that one mode is excited in the waveguide [Casperson, 2000; Mendis and Mittleman, 2009]. The coupling of the THz beam into a waveguide and excitation of only one mode (the 1st, fundamental), so-called mode matching, can be realised by a hemispherical lens (personal consultation with Mittleman).

But additional disturbances appeared when introducing a focusing element:

- ◇ The horn launcher introduced internal reflections which distorted the final THz pulse. Unfortunately, this was later shown also by EM simulations.
- ◇ The hemispherical lens curved the radiation so much that internal reflections arose in the probe and the reflection was highly distorted; multiple pulses appeared, and this effect was height independent (within a small range). No useful signal was measured.

Although we had studied both coupling concepts extensively, finally, the best coupling of the THz pulse has been realised by a free-space irradiation of the input facet, at the cost of losing a (big) part of the THz radiation. An obvious solution would be to employ an MDP with a large cross-section ($\gtrsim 4 \text{ mm} \times 4 \text{ mm}$); however, we did not dispose of an appropriate fabrication technology. The holder for manufacturing Teflon MDPs (section 2.1.2) turned out inappropriate for polishing a long tapering.

2.3 Continuous-wave microwave measurements

The CW-MW measurements are same in principal as the TD-THz measurements (fig. 2.13): the radiation is guided to the probe input facet, it interacts with the sample, and it is guided back for detecting the changes. For the MW FD measurements a standard stepped frequency MW generator (fig. 2.15) was used to generate continuous waves in the range 12.5 to 15.0 GHz, a part of the co-called K_u -band. That was amplified and $6\times$ multiplied in an RF multiplier (fig. 2.15) to a range from 75 to 90 GHz, that is a significant part of the co-called M -band.

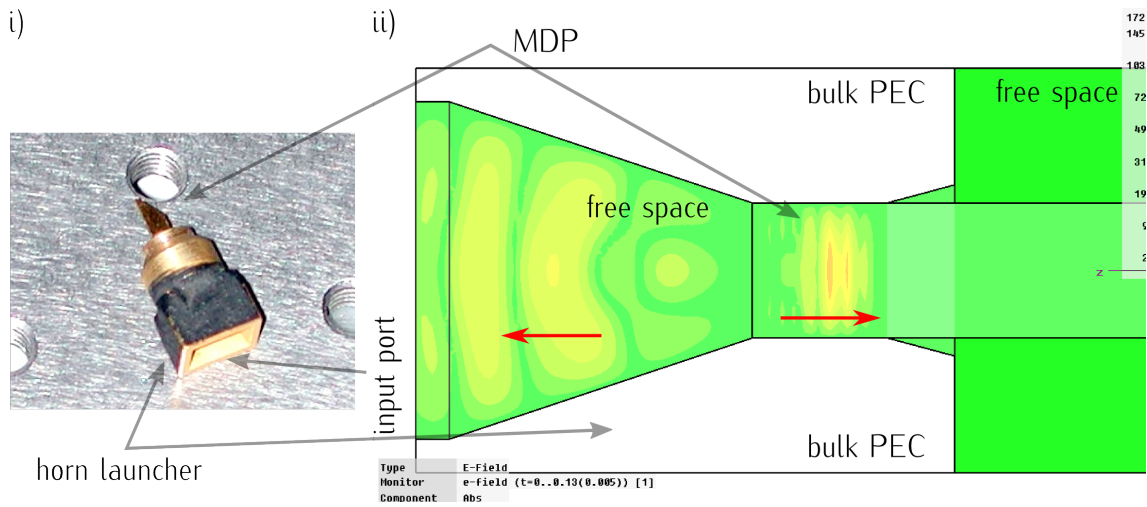


Figure 2.12: The metallic horn launcher (photograph on the left, widely used in MW techniques) tested for focusing the radiation was simulated (the drawing of the field distribution on the right). Two pulses are caught: one reflected from the input facet of the probe and the other propagating in the probe. The red arrows yield the directions of the pulses (\rightarrow). The pulse in the probe has extra power due to the focusing in the horn launcher according to the simulations. But additional after-ringing follows the pulse and it distorts the pulse even more in the experiment (not shown here).

Frequency sweeping and data acquisition were provided via a LabView interface (scripted by S. Danylyuk, Forschungszentrum Jülich, Germany (FZJ)). The probe was clamped in a holder made of Teflon and cameras assisted the positioning process (fig. 2.16).

A different process allows for sensing samples at the vicinity of the tip in the CW-MW experiment than in the TD-THz experiment. The MDP at the end of the standard MW waveguide acts as a part of the whole waveguiding system ended by a semiconductor open end. This system of waveguides has its own resonant frequencies at which standing waves appears in the waveguide, see fig. 2.14. By placing a sample to the vicinity of the tip, the resonant properties of the system are changed and so is changed the resonant frequency fig. 3.36.

2.4 Computer simulations

The probe-sample system can be approximated by a simple model, too, e. g. by a lumped equivalent circuit describing a transmission line [Grant et al., 1989; Krupka, 2006]. The non-collinear metallisation of the probe (fig. 2.17i) can be modelled by a capacitor of which the fringe

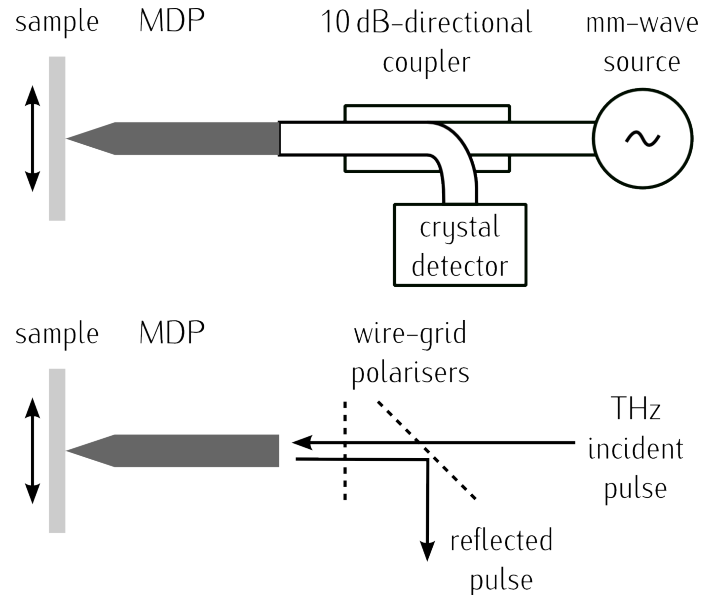


Figure 2.13: Guiding of the **CW-MW** (top) and pulse-**THz** (bottom) radiation in their respective setups. There is no principal difference in sensing using a **MDP** in the two setups other than the guiding mechanism of the two radiations: the **CW-MW** radiation requires shielding while the pulse-**THz** radiation propagates in the free space.

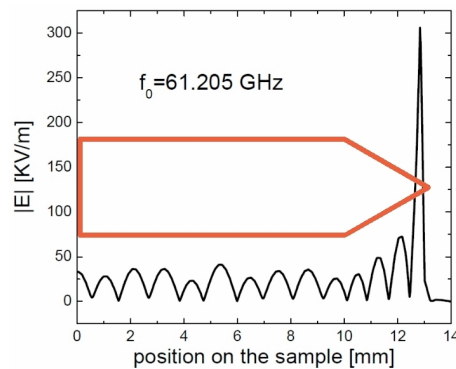


Figure 2.14: Simulated electric-field magnitude as a standing wave at the axis of the **MDP**. The **MDP** acts as an open-ended waveguide, and the resonance frequency is changed by placing a sample in front of the opening (in front of the probe end) (from [Danylyuk et al., 2007b]).

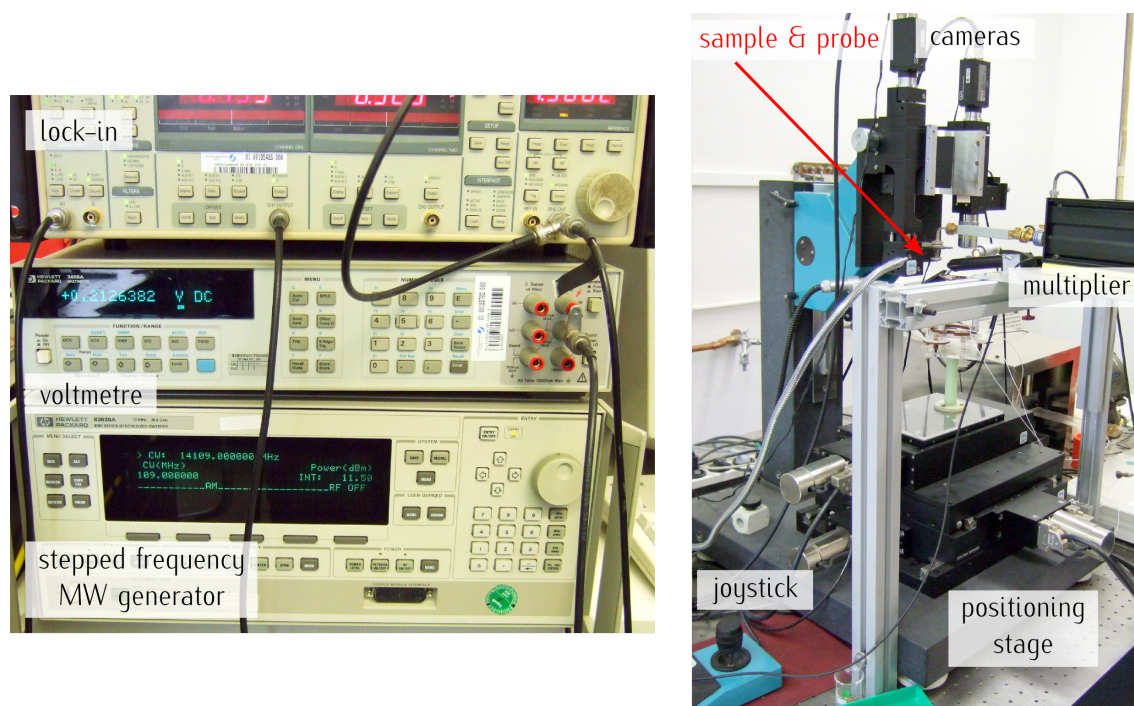


Figure 2.15: CW-MW setup (I): the stepped frequency generator and the positioning stage.

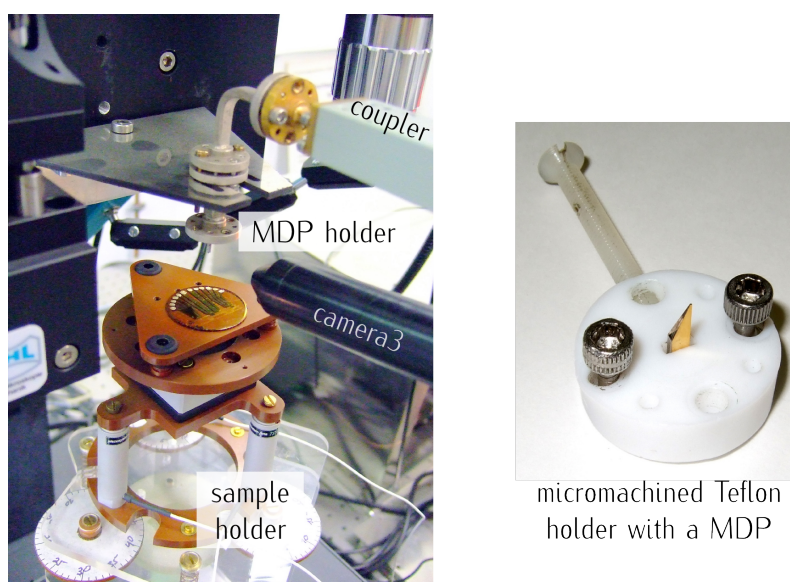


Figure 2.16: CW-MW setup (II): the holders of samples and MDPs.

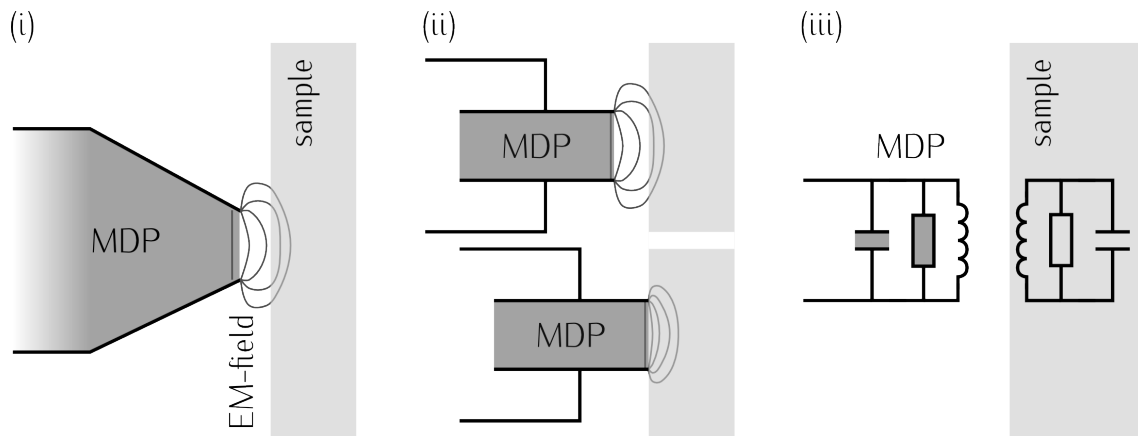


Figure 2.17: The probe can be modelled as a capacitor, in which its sensing ability is related to the change of the capacitance and inductance due to a sample at the opening.

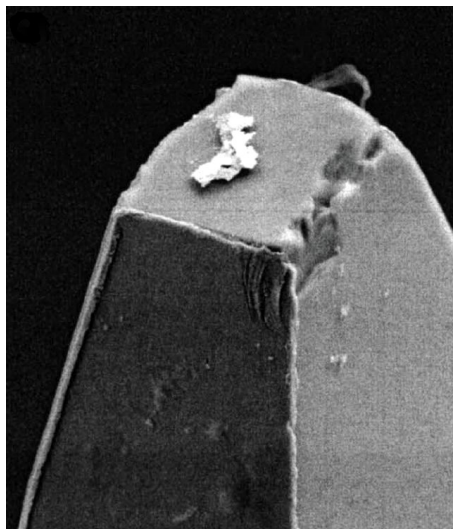


Figure 2.18: Silicon probe polished and metallised in a scattering-electron microscope.

field structure changes due to a presence of a sample (fig. 2.17ii), and the whole system can be modelled using basic passive electrical components: capacitors, resistor and inductor in both the probe and the sample (fig. 2.17iii). But this approximation does not allow for calculation of the field distribution or does not reflect parameters of a real sample; therefore, a more complex tool has to be employed—the EM simulator called CST MWS was used for that purpose.

The CST MWS, a general-purpose EM simulator based on the finite integration technique (FIT), was chosen for the EM simulations. The FIT was first proposed by Weiland [Weiland, 1977]. The FIT is a numerical method providing a special and universal discretisation scheme, applicable to various EM problems, ranging from static-field calculations to high-frequency applications in either the time or frequency domain. Like most numerical methods, FIT also discretises the integral form of Maxwell's equations, rather than discretising their differential forms. Both forms are displayed in table 1.1. In order to solve these equations numerically a finite calculation space is defined, enclosing the considered application problem. This space is split up into several small cuboids, so-called grid cells, by a suitable meshing algorithm. The spatial discretisation of the Maxwell's equations is then performed within this mesh system and so the Maxwell's equations are formulated for each of the cell facets separately [Weiland, 1996].

The calculation is based on the solution of the space-discretised set of Maxwell's Grid Equations (their continuous form is in table 1.1). The electric voltage E and flux Φ are the variables of the calculation. Both unknowns are located alternatively in time, well known as the frog-leap scheme [Noakes and Kozera, 2001]. In a simplified situation that means that the magnetic entities at a time $t = (n + 1)\Delta t$ are computed using the magnetic entities at time $t = n\Delta t$ and the electric entities at a half time step before, i. e. at time $t = (n + 1/2)\Delta t$.

In the frame of this work, the TD solver was mainly used for calculating the transient of a broadband MW pulse (with a frequency from 10 to 300 GHz, or for exceptional cases from 20 to 600 GHz) in the MDP. We focused on the computation of scattering parameters (S -parameters, i. e. a description of the electrical behaviour of linear electrical networks when undergoing various steady state stimuli by electrical signals) and field distributions to check the efficiency of coupling and leakage of the field.

The CST MWS is a general-purpose EM simulator based on the FIT. All our EM simulations were processed using the CST MWS module [CST, 2008] for EM analysis in the high-frequency range. This module is a part of the CST Studio Suite™ (CST SS) [Technology, 2009] software package. The CST SS contains different modules each suitable for a particular application. The models of the structures to be analysed are created within the suite by a powerful computer-aided

design (CAD)-type front-end which allows for full parametrisation of a 3D structure. A mesh grid is created based on the modelled components by an automated meshing procedure, and the simulation engine calculates the required properties of the EM field on this grid.

The CST MWS comprises several solvers applying different approaches to the calculation depending on the desired result. The main solvers are the TD and the FD solver; the simulation results can be visualized with different options and manner in each of these solvers. The TD (transient) solver is used for EM transient problems, mainly high-frequency applications, e. g. connectors, transmission lines, filters and antennas. In this solver an entire broadband frequency behaviour of the model and S -parameters can be calculated. The transient solver becomes less efficient for low frequency problems where the structure is much smaller than the shortest wavelength. On the other hand, the FD solver is used for electrically small structures, or devices with a high quality value (Q -value), in which the direct calculation of the operating modes is easily achieved by a frequency stepping approach.

The CST MWS also features an eigenmode solver, which efficiently calculates a finite number of modes in closed EM devices, e. g. filters and resonators. As a result, CST MWS is capable of both the analysis and design of EM devices in combination with the built-in optimizer and parameter sweep tools.

2.5 Structure of the data obtained at experiments

Although the concept of the MDP is simple, it was experienced that small deviations in the adjustment of the probe with respect to the incident THz beam, irregularities in its geometry caused by fabrication (mainly the shape of the end facet) and also dynamic perturbations (e. g. air density fluctuations in the free-air THz beam path). Changes in the waveforms caused by the dynamic deviations are often comparable in size with the level of the useful signal linked to the sample. It appears therefore difficult to extract the information relevant to the sample properties without applying a calculational post-processing method on the experimental data.

3D-datasets are usually generated during broadband THz imaging experiments using TDTS, when a THz waveform is recorded over a varying discrete measurement parameter or a condition state α . The parameter α is usually a common physical entity, such as temperature, a substance concentration, a distance or a position (of a sample or of delay line), or an angle of rotation, but it can even represent a position of a pixel of a charge-coupled device (CCD) camera [Janesick and Blouke, 1995], or it can be just (macroscopic) time t . For each condition state α , a waveform

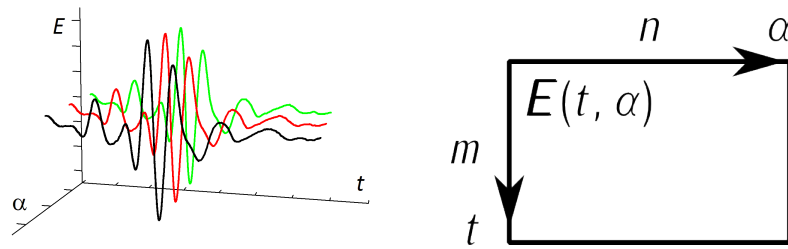


Figure 2.19: Representation of the dataset $E(t, \alpha)$ in a form of a 3D plot and of a matrix E .

is obtained, i. e. a function of the electric field over time, $E(t)$. The set $E(t, \alpha)$ consists of experimentally obtained amplitudes E over a time delay t and parameter α (cf. fig. 2.19). The set can be represented by a matrix $E(t, \alpha)$ with m rows (equal to the number of measurement points on the time-delay axis t) and n columns (equal to the number of measurement states α). The dataset $E(t, \alpha)$ is usually created with a view to resolve the relation between α and t (thus $E(t)$), by using multivariate analysis.

2.6 Multivariate analysis

In the following, we introduce the multivariate statistics, its application and display examples of use. Multivariate statistics is a form of statistics encompassing the simultaneous observation and analysis of more than one statistical variable. The application of multivariate statistics is called **multivariate analysis (MVA)**. The **MVA** in its various forms is used in many fields, such as in consumer and market research (e. g. as a vital part of many rating methods [Liessmann, 2008, pp. 58–61]); quality control (e. g. industries of food and beverages, paints, pharmaceuticals, chemicals, energy, telecommunications); process optimization and process control; face recognition and signal processing [Haykin, 2001], and research and development (e. g. gene expression profile analysis, that is sometimes also referred to as microarray-data analysis [Berrar et al., 2002])

The main reasons of using a **MVA** are:

- ◇ Obtaining a summary or an overview of a dataset. This analysis often requires **principal component analysis (PCA)**, **SVD** or **factor analysis (FA)**, see below. It is possible to identify the dominant patterns in the data, such as groups, outliers and trends.

- ◇ Analysing groups in a dataset, how these groups differ, and to which group individual data rows belong. This type of analysis is called Classification and Discriminant Analysis and belongs to so-called Clustering methods.
- ◇ Finding relationships between columns in datasets, for instance relationships between process-operation conditions and product quality. The objective is to use one set of variables (columns) to predict another, for the purpose of optimization, and to find out which columns are important in the relationship. The corresponding analysis involved can be Multiple Regression Analysis or Partial Least Squares.

The results of *MVA* can be further examined by a low-level data analysis meant for bi- or univariate-data analysis, e. g. Regression analysis and Descriptive statistics.

In the following, we focus on the terminology used in *MVA* and display examples of use of some of the multivariate methods. The family of *MVA* methods (models) that can be applied to a dataset is wide and rich, see [Hair et al., 2009, Chap. 1]. Among them, we focus here on methods for reducing the dimensionality of a given vector set (of a measurement) and extracting significant independent components [Bevington and Robinson, 2003; Rencher, 2002, Chap. 2.6, Chap. 3.5] [Press et al., 2007, Chap. 2.6]. In the following we describe some methods of this family, their main characteristics and fields of usual application.

SVD, PCA and Eigenvalue decomposition: Both the *SVD* and *PCA* are rooted in the concept of eigenvectors and eigenvalues, which are the solutions to the equation:

$$A\mathbf{x} = \lambda\mathbf{x}, \quad (2.5)$$

where $A \in \mathbb{R}^{n \times n}$, $\mathbf{x} \in \mathbb{R}^{n \times 1}$, and $\lambda \in \mathbb{R}$, i. e. in order to compute the eigenvalues, the A must be a square matrix. The *PCA* is computed by determining the eigenvectors and eigenvalues of the covariance matrix [Berrar et al., 2002, p. 93] [Coombe, 2006]. (The covariance of two random variables is their tendency to vary together.) The *SVD* is closely related to *PCA* and to eigenvalue computation, but the *SVD* is less restrictive on dimensions of the matrix A and it can be performed on any $m \times n$ matrix [Bilodeau and Brenner, 1999, Chap. 1]. The singular values of a matrix A solve the equations:

$$A = U\Lambda V^T, \quad (2.6)$$

$$A\mathbf{u} = \lambda\mathbf{v}, \quad A^T\mathbf{v} = \lambda\mathbf{u}. \quad (2.7)$$

And while one can end up with complex eigenvalues and (even worse) complex eigenvectors, the *SVD* always yields real results.

In these methods, the dataset $E(t, \alpha)$ can be regarded as vectors/columns in an N -dimensional space—the matrix \mathbf{A} . By a mathematical procedure, the methods transform a number of possibly correlated variables into a smaller number of uncorrelated variables called *left singular vector (LSV)* and *right singular vector (rSV)* (in case of *SVD*) or *principal components* (in case of *PCA*). The observed variables can be reconstructed as linear combinations of the *singular values (SVs)* (called also *factors*) and singular vectors, plus *error* terms. The information obtained about the interdependencies between observed variables and their weights can be used to reduce the set of variables in a dataset or to reduce the amount of stored data [Henry et al., 1992; Leskovec, 2006; Martens and Næs, 1991; Schmidt et al., 2002]. Examples of use in research:

- ◇ in general: reducing dimensionality and visualising data, e. g. [Pei et al., 2007];
- ◇ in pathology: diagnosis of a cancer tissue (*PCA*) [Nakajima et al., 2007];
- ◇ in signal processing: noise separation and noise analysis [Schmidt et al., 2002];
- ◇ in information technology: clustering a database by user-specific rating [Bell et al., 2007, 2009];
- ◇ in biology: to understand the neural representation of broadband and dynamic sounds in primary auditory cortex the analysis in spectra-temporal space was applied employing *SVD* by Depireux et al. [Depireux et al., 2001];
- ◇ in social sciences: revealing relations or belongings in groups of people, e. g. revealing a relation among representatives in connection with sponsorship and cosponsorship records in form of a political spectrum (a civic project *GovTrack.us* [GovTrack.us and Civic Impulse, LLC., 2010]);
- ◇ in *infrared (IR)* spectroscopy, the widely used 2D-correlation spectroscopy [Noda and Ozaki, 2002, pp. 91–94] [Jung, 2004; Sasic and Ozaki, 2001] is based on *SVD*, too. The difference from *SVD* is that 2D-correlation spectroscopy applies an exponential factor for calculating *SVs* and so minimises the influence of the noise components.

For definition and deeper mathematical insight, see: [Härdle and Simar, 2007, pp. 46–47] [Härdle and Hlávka, 2007, Chap. 8] [Bilodeau and Brenner, 1999; Timm, 2002].

For sake of curiosity, we mention that there is a quicker and more general decomposition than *SVD* with a few restrictions called *generalized low-rank approximations of matrices*

[Ye, 2004] that might be suitable for larger datasets.

For our work, the **SVD** appears as one solution and a fair alternative tool for decreasing the dimensionality of the **TSTS** data and for a simultaneous optimising of their sensitivity with respect to the studied properties.

Factor Analysis: The **FA** is another statistical method used to describe variability among observed variables in terms of a potentially lower number of unobserved variables/factors. But these factors are conceptualised as *real world* entities such as depression, anxiety and disturbed thought and are classified by levels. This is in contrast to **SVD** and **PCA** where the components are geometrical abstractions that may not map easily onto real world phenomena [Hair et al., 2009, Chap. 3]—those methods are sometimes referred to as *abstract FA*. The **FA** originates from psychometrics and is used in behavioural sciences, social sciences, marketing, product management, operations research and other applied sciences that deal with classified data.

Pattern recognition: (as an example of Statistical classification); For this method, an artificial feature of the dataset is predefined, e. g. the time position of the global or local extrema, or their mutual relative time delay and the total area of the waveform. Each measurement is then quantified by this feature and replotted to the α -space. This method is usually applied during tomography or in-plane imaging measurements (section 1.6) to visualise the measurements for naked-eye sample inspection, e. g. [Löffler et al., 2002; Yin et al., 2007].

Analysis of variance (ANOVA) and others: Methods of bivariate statistics, for example ANOVA and correlation, are special cases of multivariate statistics in which two variables are involved.

It is important to note that application of **SVD**, **PCA**, **FA** and others to spectral analysis is relatively recent, and these methods are evolving and consists of iterative applications of interactively performed analysis methods of which each has its *pro et contra* for a task given. The detailed process of any analysis might depend on the specific scientific questions that are being addressed.

2.7 Data analysis, data manipulation and data extraction

We adopted the **SVD** approach to decompose the dataset to elementary components. For the processing of our data, we used a **SVD** (a detailed description of the method is presented in

section 2.7.2) to identify independent processes in the detected waveforms, and also the frequency distribution of these processes, which is a prerequisite for performing near-field imaging with a spectral resolution. The decomposition was aimed to identify the influence of the parameter α on the measurements or, possibly, also to increase the experimental sensitivity with respect to this parameter. By using this simple linear transformation to reduce the dimensionality of the problem, we were able to detect very weak changes in the frequency spectra. This enabled us to evaluate the responsiveness of the MDP method (section 2.1) with respect to the spatial position, permittivity and local anisotropy of a sample.

The R programming environment [R Development Core Team, 2010] for statistical computing was used to decompose the data by using its core `svd()` procedure and to manipulate the results. The overview of the calculational environment is in section 2.7.3.1.

The data processing consisted of several consequent steps:

1. a pretreatment of the raw dataset, at which the dataset was *prewhitened* in order to obtain data less sensitive to numerical errors (section 2.7.1);
2. a decomposition of the dataset to elementary components by using SVD (section 2.7.2);
3. a clustering of the components based on their (non-)specific α -behaviour or a clustering within a correlation matrix; and
4. finally, a separation of the contributions corresponding to evanescent and to radiating fields, contributions due to sample-specific properties and to fluctuations of the laboratory environment.

The steps above and the workflow are described in table 2.1 with links to equations and with examples.

2.7.1 Data pretreatment (prewhitening)

A useful pretreatment strategy before applying a SVD on a raw non-smoothed data, as well as in many numerical calculations related to linear algebra of matrices, is to lower the condition number of the matrix [Golub and van Loan, 1996, pp. 80–81] [Press et al., 2007, p. 113] [Kaw and Kalu, 2008; Trefethen and Bau, 1997]. In general, some kind of pretreatment is requested for most matrix calculations as the very first step. The reason is that in the numerical analysis, the condition number associated with a problem is a measure of that problem's amenability to digital computation, i. e. how the problem is well-conditioned numerically. A problem with a low condition number is said to be well-conditioned, while a problem with a high condition number

is said to be ill-conditioned. Thus, the reason to decrease the condition number of the matrix is to obtain a dataset less sensitive to errors arising from numerical computer calculations.

We chose a very easy and simple step to preprocess our datasets: the subtraction of the arithmetic mean by rows or by columns. This method is sometimes also referred to as *prewhitening* of a matrix. In most of our data samples, this proved to give smoother results compared to a non-pretreated results. In all our data, we calculated the mean waveform, i. e. we calculated the means through rows in consistency with the definition of our datasets in fig. 2.19. The reason for this is that the area integral of the \mathbf{E} of a THz pulse is approximately zero (see eq. (1.6) for \mathbf{E}). That would mean that averaging the columns of the matrix \mathbf{E} would yield a function close to 0 and subtracting that would be useless. Therefore, we chose to average the rows of the matrix $\mathbf{E}(t, \alpha)$, to get an average waveform. The average vector $\overline{\mathbf{E}(t, \alpha)}|_{\alpha}$ was subtracted from the rows of the original dataset, i. e. the data matrix $\mathbf{E}(t, \alpha)$ (or the frequency-dependent data $\mathbf{E}(v, \alpha)$ in which the FFT is calculated for each of the waveforms) is prewhitened by subtracting its row means.

2.7.1.1 Justification of the pretreatment

To prove that the condition number κ was reduced to justify the need of some kind of pretreatment and ensure the adequacy of the results, we calculated that for some measurement data (following [Golub and van Loan, 1996, pp. 80–81]).

Paradoxically, the `svd()` procedure was used as an intermediate step to calculate the inverse matrix \mathbf{E}^{-1} . And it is also known [Press et al., 2007] that in the Euclidean (ℓ_2) space, the condition number is the ratio of the largest and the smallest SV (λ_{\max} and λ_{\min}) of a matrix \mathbf{E} .

$$\kappa(\mathbf{E}) = \frac{\lambda_{\max}(\mathbf{E})}{\lambda_{\min}(\mathbf{E})}, \quad (2.8)$$

So, the factor by which the whitening reduced the condition number is the ratio of the 1st and the 2nd SV in the final dataset: In most of the cases, we have found that the conditioning number was reduced only by a factor of $\approx 10^2$. And the reciprocal of the condition number of the measurement datasets was usually in a range 10^{-3} to 10^{-5} , i. e. several orders above the machine's floating-point precision (10^{-15}) [Press et al., 2007, p. 69], which would be one of possible weak points in data manipulation. Nonetheless, the pretreatment helped us to eliminate some causeless and obscure results, spikes, or reveal weak dependences hidden in an otherwise strong 1st singular matrix (SM). The pretreatment did not influence the results too much when

calculating with large matrices (e. g. scan of an area on a saple surface, section 3.7), but it influence results when working with small matrices (e. g. measuring an permittivity-dependent response of samples, section 3.6).

2.7.2 Singular value decomposition

The **SVD** is a kind of a linear transformation which we applied to analyse the raw experimental data obtained at different experimental configuration and to separate the independent vectors corresponding to experimental parameters and so reduce the dimensionality of the problem. This decomposition was first introduced by [Golub and Reinsch](#) in 1970 [[Golub and Reinsch, 1970](#)], but it reached wide practical use only much later, e. g. [[Wall et al., 2003](#)].

An important feature distinguishing **SVD** (and **PCA**, too) from other analysis methods is the ability to detect weak signals in the data. Even when the structure of the data does not allow separation of data points, causing other clustering algorithms to fail, it may be possible to detect scientifically meaningful patterns [[Wall et al., 2003](#)].

According to a known theorem [[Hogben, 2006](#), Chap. 5] [[Trefethen and Bau, 1997](#), pp. 25–37], it is always possible to decompose a matrix E into $E = U\Lambda V^T$ eq. (2.9), where

- ◇ the matrices U and V and the vector Λ are unique;
- ◇ U , V are column orthonormal, i. e. columns are unit vectors, orthogonal to each other;
- ◇ $U^T U = I$; $V^T V = I$, where I is an identity matrix;
- ◇ Λ is diagonal: $\Lambda = \text{diag}(\lambda_1, \lambda_2, \dots, \lambda_n)$
- ◇ λ_j are **SVs**, that are positive and sorted in decreasing order, see eq. (2.12).

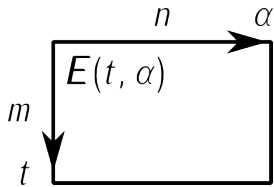
A graphical depiction of the **SVD** and resulting matrices is in fig. 2.20.

Having whitened the raw dataset, the remaining data matrix $E^*(t, \alpha)$ was decomposed to two normalised orthonormal matrices and a multiplication number which can be consequently written as a sum of N **SVs** and **SMs** [[Martens and Næs, 1991](#); [Sharma, 1995](#)]:

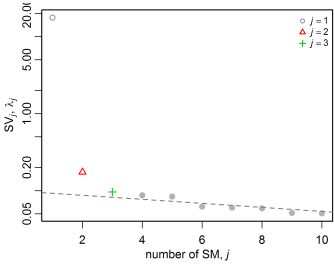
$$E^*(t, \alpha) = U\Lambda V^T = \sum_{j=1}^N \lambda_j \mathbf{u}_j(t) \mathbf{v}_j^T(\alpha) = \sum_{j=1}^N E_j(t, \alpha); \quad (2.9)$$

here in eq. (2.9), only the amplitudes of the spectra $E^*(t)$ are taken into consideration. The j^{th} term is factorised and consists of a product of three terms: a **SV** λ_j (a weight coefficient) and normalised amplitudes $\mathbf{u}_j(t)$ and $\mathbf{v}_j(\alpha)$ (**ISVs** and **rSVs**). A single **SM** that is a layer of the

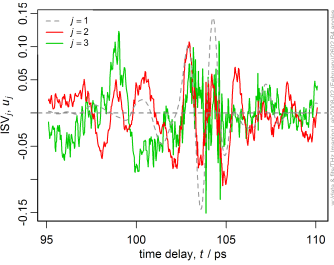
1. Create a dataset $E(t, \alpha)$ in a form of a $m \times n$ matrix:
2. Prewhiten the matrix:
 - ◇ subtract the average vector $\overline{E(t, \alpha)}|_{\alpha}$ from each row of the original dataset $E(t, \alpha)$.
3. Decompose both the average and the subtracted matrices:
 - ◇ apply eq. (2.9) to $E^*(t, \alpha)$ and to $\overline{E(t, \alpha)}|_{\alpha}$;
4. Merge results:
 - ◇ paste the 2 vectors and the multiplying factor from eq. (2.14) as columns and number to the objects U, V and Λ obtained from eq. (2.9). The merging obeys eq. (2.12), but in all our measurements, the multiplying coefficient of the subtracted $\mathbf{u}(t)$ (in eq. (2.14)) was assigned to index 1.
5. Analyse the results:



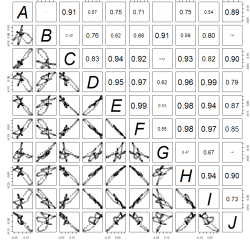
(b) apply the scree test and look for valid SVs,...



(c) ...cluster and identify the processes comparing the ISVs (their distribution over the delay time t) to previous measurements;...



(d) ...or by calculation their correlation matrix



6. Continue with lower level (univariate) analyses.

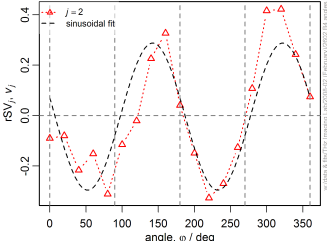


Table 2.1: Workflow for data processing

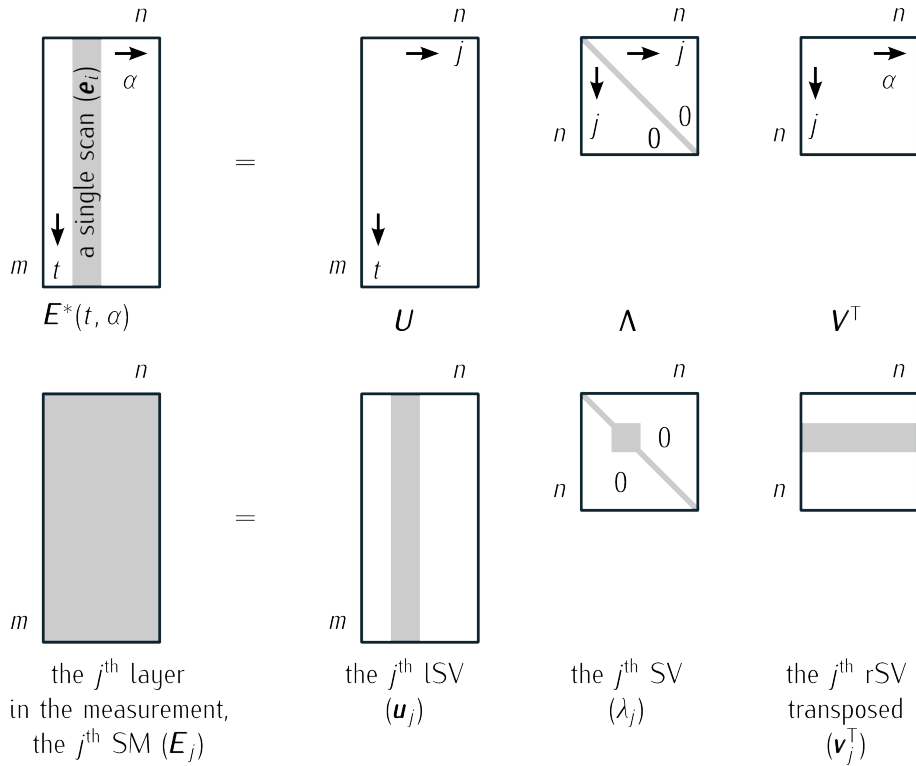


Figure 2.20: (first row) Graphical depiction of the SVD (eq. (2.9)) of the prewhitened matrix $E^*(t, \alpha)$ with notations adopted in this chapter and according to fig. 2.19. The $\min(m, n) \equiv n$ applies in this case, e. g. the number of the steps in α is lower than the number of the data points in measuring the time delay). (second row) Graphical depiction of a calculation of a SM (eq. (2.10)). For more on these and other relations among the components and products, see [Wall et al., 2003].

original dataset can be easily constructed by a matrix multiplication of a LSV and a rSV:

$$E_j(t, \alpha) = \lambda_j \mathbf{u}_j(t) \mathbf{v}_j^T(\alpha). \quad (2.10)$$

Here, the Euclidean (ℓ_2) norm of the singular vectors is equal to unity:

$$\|\mathbf{u}_j\| = \sqrt{\mathbf{u}_j^T \mathbf{u}_j} = 1, \quad \|\mathbf{v}_j\| = \sqrt{\mathbf{v}_j^T \mathbf{v}_j} = 1. \quad (2.11)$$

The total number of the SVs, is equal to $\min(m, n)$, i. e. the minimum of the two dimensions of the matrix $E(t, \alpha)$: the number of the experimental values of the parameter α and the number

of the measurements points of the time delay. The *SVs* are ordered in decreasing order:

$$\lambda_{j+1} \leq \lambda_j, \quad (2.12)$$

but in practice the experimental data exhibits

$$\lambda_{j+1} < \lambda_j. \quad (2.13)$$

Only components up to a certain index j bear a physical meaning. The so-called *scree test* [Cattell, 1966] was used to select the significant components and to reject the so-called noise components—those creating the noise floor. An example of the applied scree test is in fig. 3.11 and the itemized workflow is described in table 2.1.

The average data matrix $\overline{E(t, \alpha)}|_\alpha$ was decomposed by *SVD*, too. But only the 1st component has a meaning when decomposing $\overline{E(t, \alpha)}|_\alpha$ (due to the columns identity). The decomposition follows the relations:

$$\overline{E(t, \alpha)}|_\alpha \stackrel{\text{SVD}}{\equiv} \bar{\lambda}|_\alpha \overline{\mathbf{u}(t)}|_\alpha \overline{\mathbf{v}}|_\alpha. \quad (2.14)$$

and $\overline{\mathbf{v}}|_\alpha \equiv \mathbf{1}$ due to condition of the normalisation. The waveform $\overline{E(t, \alpha)}|_\alpha$ was calculated as a mean, therefore the products of its decomposition ($\bar{\lambda}|_\alpha$, $\overline{\mathbf{u}(t)}|_\alpha$ and $\overline{\mathbf{v}}|_\alpha$, from eq. (2.14)) may act as normalisation values. In order to achieve that, these products have to be extended in dimensions to match the dimensions of the products of eq. (2.9), and they also have to fulfil the condition for normalisation (eq. (2.11)):

$$\overline{\mathbf{u}}|_\alpha \rightarrow \mathbf{u}_{\text{norm}}, \quad (2.15)$$

$$\overline{\mathbf{v}}|_\alpha \equiv \mathbf{1} \rightarrow \mathbf{v}_{\text{norm}} = \left(\frac{1}{\sqrt{\min(m, n)}}, \dots, \frac{1}{\sqrt{\min(m, n)}} \right), \quad (2.16)$$

$$\bar{\lambda}|_\alpha \rightarrow \lambda_{\text{norm}} = \sqrt{\min(m, n)} \bar{\lambda}|_\alpha. \quad (2.17)$$

Because usually, this set has the highest magnitude among all calculated *SVs* λ_j (due to observations only), we hold it to belong to the 1st *SVs* ($j = 1$). As such, the products of eq. (2.14) were placed to the first places into the matrices \mathbf{U} , \mathbf{V} and into the $\mathbf{\Lambda}$ of eq. (2.9). To maintain the correct dimensionality of the matrices, the very last columns and the last *SV* (the components of the smallest contribution to the noise) were dismissed after the merge. Thus, importantly, creating a normalisation factor did not remove any useful information from the

acquired dataset.

With this selective double decomposition, we ensured that the very first and usually strong component is independent of the α parameter and that the other components (due to somehow decreased condition number of the problem) have a more valuable shape. In many cases, we resolved less number of significant SVs or the scree test, that is necessary to resolve significant SVs, became less questionable.

Another view of the meaning of lSV and rSV is offered by Haykin: one can look at them as projection onto the axes of an hyperellipsoid in n -dimensional space [Haykin, 2001, Chap. 11].

2.7.2.1 Correlation coefficient between two variables/vectors

We learned (see later chapter 3) that different experimental features display different patterns (fingerprints) in the TD (due to orthogonality of the SVD solution) image of the measured waveforms. These patterns tend to persist over time, but subtle differences might appear from measurement to measurement. A certain experimental feature can be followed through a bunch of consequent experiments by identifying its correlation with other lSVs extracted from measurements.

The correlation coefficient indicates the degree of linear relationship between two variables, i. e. it gives the value of similarity between two vectors. Through this value the components can be clustered into groups belonging to a shared experimental feature. The correlation coefficient always lies between -1 and $+1$. -1 indicates perfect linear negative relationship between two variables, $+1$ indicates perfect positive linear relationship and 0 indicates lack of any linear relationship. In practice, the value of 0.5 has questionable significance of correlation.

Where needed, the so-called Pearson correlation coefficient r_P was calculated. It is defined for two samples of paired data (x_i, y_i) as follows:

$$r_P = \frac{1}{n-1} \sum_{i=1}^n \left(\frac{x_i - \bar{x}}{\sigma_x} \right) \left(\frac{y_i - \bar{y}}{\sigma_y} \right) \quad (2.18)$$

in which $\frac{x_i - \bar{x}}{\sigma_x}$, \bar{x} and σ_x are the standard score, sample mean and sample standard deviation, respectively. For two lSVs extracted from two consequent measurements, we substitute $(x_i) \equiv \mathbf{u}_{i,\text{meas1}}$ and $(y_i) \equiv \mathbf{y}_{i,\text{meas2}}$.

2.7.3 Software environments employed for analyses

We employed two software environments for the data analysis described above: R and Unscrambler. The description of the environments and our gained experience are presented in the following paragraphs briefly.

2.7.3.1 R Project

We have processed most of our measurements using R [[R Development Core Team, 2010](#)], an open-source and free software environment for statistical computing and graphics. R provides a wide variety of statistical (linear and nonlinear modelling, classical statistical tests, time-series analysis, classification, clustering,...) and graphical techniques, and it is highly extensible. The environment provides useful features, e. g. powerful scripting language that allows for automation and extension and a public help and discussion mailing list that represent a strong knowledge base.

2.7.3.2 Unscrambler

We have processed some measurements using a trial version of the Unscrambler® v9.8 software [[AS CAMO Software, 2008](#)] in order to compare methods and results. The Unscrambler is a commercial software for multivariate-data analysis that is a product of the CAMO company. The **graphical user interface (GUI)** of the program is specialised for the multivariate analyses with various templates and interactive dialogue boxes; however the program lacked automation. Data tables had to be treated individually involving user interaction, and processing all the measurements would be time consuming and cumbersome. Because we obtained very similar results for some typical studied cases both by calculating in R and Unscrambler, we used the software only for a guidance and an assistance in rare cases.

Chapter 3

Results

In this chapter, we show the results of the experiments in probing and scanning samples by several **metal-dielectric probes (MDPs)**. At first we summarise the state-of-art of the project at the start of the doctoral work (section 3.1). Then we show preliminary results displaying the sensitivity of probes and acquired on a newly built **time-domain (TD)-terahertz (THz)** experimental setup (section 3.2), followed by summary of experimental configurations (section 3.3) and processes of calibration (section 3.4) and field characterisation (section 3.5). Results on broadband measurements with and without a spatial resolution follow—we investigated in depth

- ◇ the relative sensitivity of the probe to samples (section 3.6), and also
- ◇ possibilities of imaging on domain structures of a **barium titanate (BaTiO₃)** sample (section 3.7).

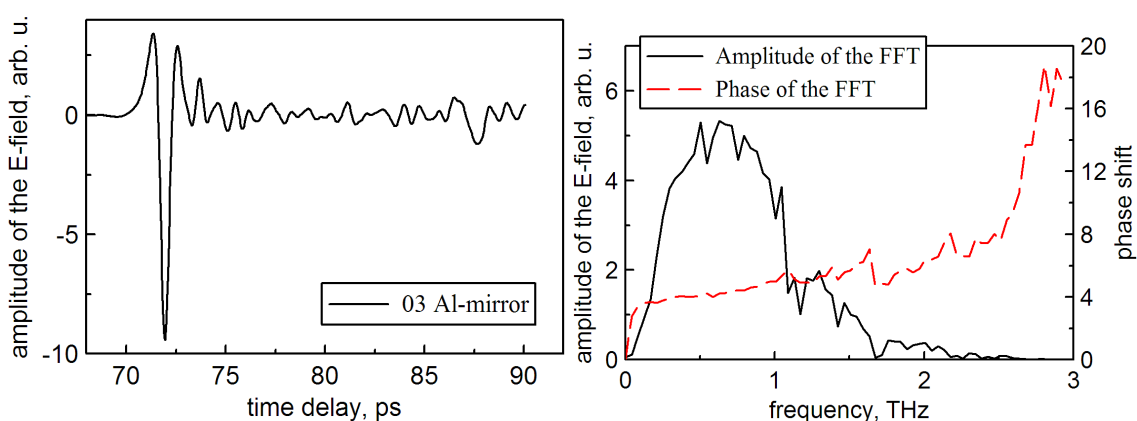
These are followed by results of experiments by using a **metal-dielectric dual probe (MDDP)** (section 3.8). At last we describe some results from **continuous-wave (CW)-microwave (MW)** measurements (section 3.9).

3.1 Experiments preceding the work in the thesis

The development of a promising technique of the near-field **MDP** by P. Kužel, F. Kadlec (assoc. with **Institute of Physics of the AS CR, Prague**) and N. Klein (formerly assoc. with **Forschungszentrum Jülich, Germany (FZJ)**) in 2004 was reported in [Klein et al., 2005]. Contrast of the signal on metallic stripes deposited onto a dielectric substrate was measured both in **CW-MW** and **TD-THz** setups. From these measurement, a resolution of $36\ \mu\text{m}$ ($\lambda/100$ for THz

frequencies) and $17\ \mu\text{m}$ ($\lambda/200$ for MW frequencies) was proven, i. e. much smaller than the wavelength in free space. The method showed a potential for MW and THz near-field imaging and for spectroscopy at THz frequencies with micrometer or submicrometer spatial resolution. Preliminary electromagnetic simulations were made using the CST Studio Suite™ (CST SS) in the MW frequency range and an enhanced electromagnetic (EM) field was shown. It was proposed to make the silicon MDP sharper by ion-beam etching to achieve a higher spatial resolution (below 100 nm) [Danylyuk et al., 2007b], and possibly to employ a higher THz field suitable for ultrafast writing of (sub)micrometer-sized domains in ferroelectric films. Also effort had been put forth in both laboratories in the following years to improve and analyse the MDP method.

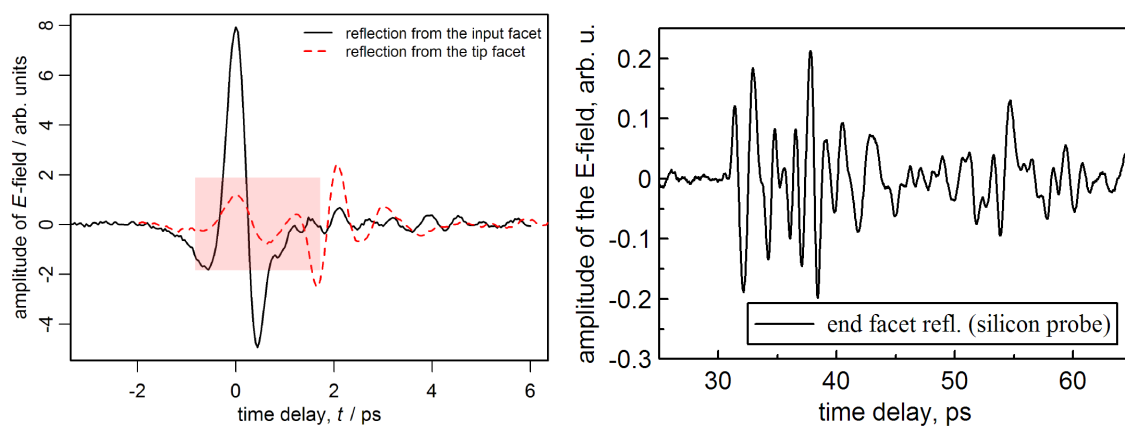
3.2 Fundamental preliminary experiments



(i) The frequency characteristics of the THz beam can be obtained via a reflection from the surface of an Al-mirror placed into the beam waist. (ii) The frequency and phase characteristics of the waveform (left) obtained by using FFT.

Figure 3.1: The THz waveform of a reflection on a mirror at the beam waist (left) and its frequency distribution and phase shift obtained by FFT (right).

One of the primary tasks of the work was building, completing and adjusting the opto-THz setup. During that time we implemented a new laser source and replaced optical components in order to increase the signal-to-noise ratio (SNR). The adjusted opto-THz setup was a time-domain terahertz spectroscopy (TDS) system in reflection geometry (fig. 2.6) providing a broadband THz spectrum, see fig. 3.1. Besides, it was also used for another experiment with



(i) Response of a sapphire ($\alpha\text{-Al}_2\text{O}_3$) probe in comparison with the input-facet reflection. The region in red rectangle (■) was significantly sensitive to a presence of a sample (fig. 3.3).

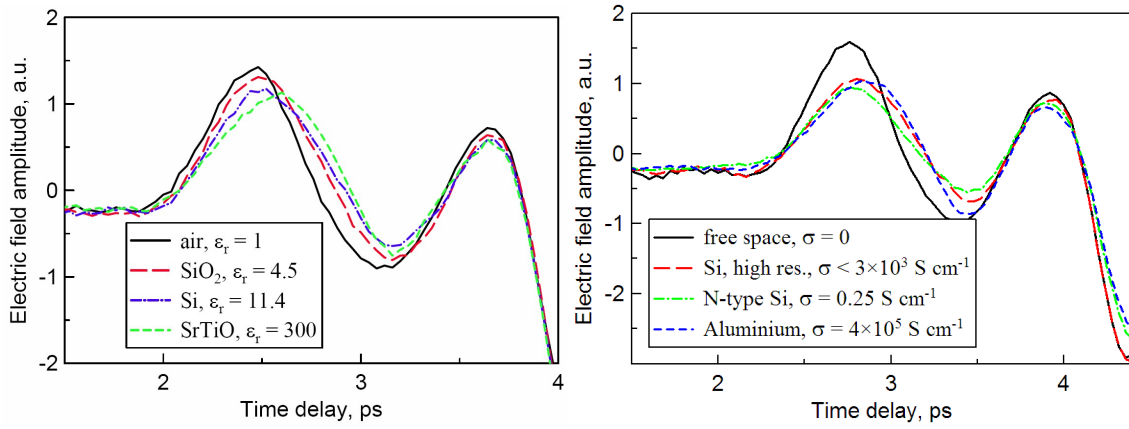
(ii) Response of a silicon probe was usually more complex due to geometry of the probes (e. g. the blunt tapering, see fig. 2.2) and dispersion.

Figure 3.2: Changes in the end facet reflection were significant in the first part of the reflection. Additionally multiple reflections or an after-ringing appeared behind the first reflection.

the aim of monitoring the response of the skin and its hydration in a group of patients under haemodialysis treatment [Kadlec et al., 2008]. The main aim of the construction was to allow placing of a MDP into the THz beam waist, and guiding the THz radiation through the probe into a small volume in the vicinity of the sample.

First, the system without a sample was observed thought installing available silicon (Si) and sapphire probes varying in length, in tapering and in dimensions of the end facets. It was observed that the waveforms back-reflected from the end facet of the MDPs vary their characteristics from probe to probe. The sapphire probes provided waveforms with shorter useful time-delay window than the silicon ones, usually, see examples in fig. 3.2. The response of the silicon probes were more complex due to wider tapering angle, probably. Also the frequency spectra of the waveforms (the FFT of the waveforms) could not be compared to each other and they displayed various anomalies, e. g. dips due to multiple pulses in the waveform (fig. 2.8).

The preliminary measurements were conducted with material samples differing in dielectric constant and conductivity in order to show the near-field sensitivity at the end of the MDP. The samples were placed in contact with the tip and results showed clearly that the response is related to the dielectric and conductivity properties of the sample material (fig. 3.3). Usually, various parts of the back-reflected waveform were affected by the presence of the sample and most notably the first peak displayed a shift in the time delay and change shape. These changes



(i) Response of the pulse to samples with different permittivity.

(ii) Response of the pulse to samples with different conductivity.

Figure 3.3: Samples differing in permittivity and conductivity were placed into the vicinity of the MDP and caused changes in the end-facet reflection.

displayed a monotonic behaviour in relation with the permittivity and the conductivity of the samples, as shown in fig. 3.3. Further, strong and reproducible changes were observed when the tip reached the water surface and for the situation when the tip was emerged into the water slightly deeper, fig. 3.4.

From preliminary experiments, it was concluded that the complex structure of the reflected E -field accounts for

- ◇ non-ideal geometry of the tip,
- ◇ coupling of the pulse into the probe,
- ◇ dispersion of guided modes,
- ◇ waveform changes due the sample presence (could be quite small).

Thus, it is necessary to have the optical setup very stable and to perform additional decomposition of the experimental data. Later, we enclosed the optical table in plastic foil to reduce the temperature changes in the opto-THz part of the setup and to cut down the influence of the air-conditioning, the mixing of air with different humidity, especially in the part of the setup with the THz radiation. Additionally, we have whitened the raw dataset by a suitable data manipulation—singular value decomposition (SVD), that is described in section 2.7.

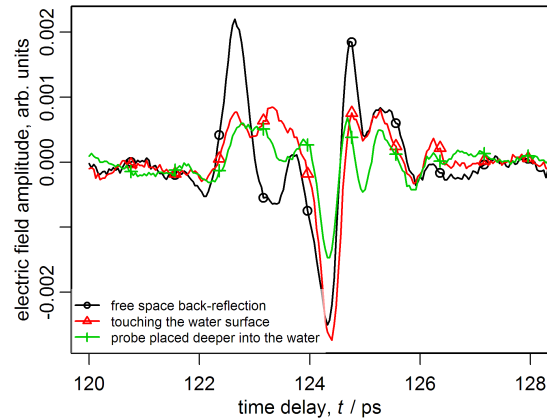


Figure 3.4: Reaching a water surface or a wet tissue with the probe tip significantly changes the response of the probe. This acts as a zero-approximation approach to find a proper sensing place or verifying the delay time for later more precise measurement.

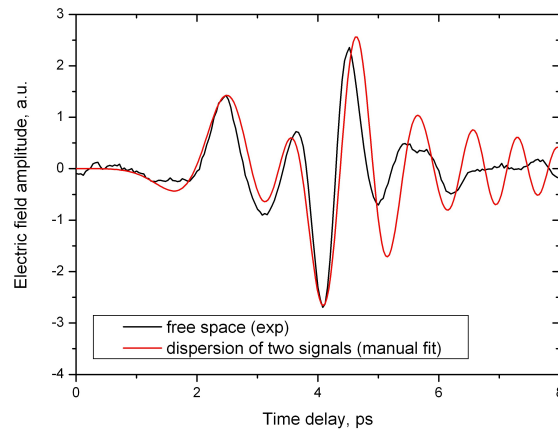


Figure 3.5: The pulse (except the after-ringing) altered by the transition in the **MDP** can be fitted by two scaled input pulses. The method of manual fitting can possibly be enhanced by finding the proper places of the repeating pulses, e. g. by an autocorrelation method.

We even tried to fit the after-ringing by multiple overlaying pulses (fig. 3.5), but this simple approximation could not describe the pulse completely.

$$\text{measured waveform}(t) := f(t) = A_1 F(t) + A_2 F(t + A_3), \quad (3.1)$$

where $f(t)$ is the output obtained by measurement (e. g. see the red dashed line (– –) in fig. 3.2i), $F(t)$ is the input reflection (e. g. see the black line (– –) in fig. 3.2i), and $A_i \in \mathbb{R}$ are variables to fit. The fit by the overlaying pulses did not match perfectly any place of the waveform, especially, the tail of the back-reflected pulse (the after-ringing) had a different shape. Therefore, a different analysis had to be applied to model the waveforms, and the SVD method has shown to be promising (section 2.7).

3.3 Experimental configurations for studying the characteristics of a probe and a sample

The behaviour of the output spectrum was analysed in various configurations (fig. 3.6) in experiments and simulations to provide characteristics of the probes and samples:

- ◇ Usually at first, the performance of an experiment was characterised in a situation when no sample was present in front of the tip and no additional changes during the experiments were made (fig. 3.6i). The measurement provided calibration for further experiments (section 3.4).
- ◇ Waveforms were collected with the probe in various distances from the sample surface. The sample surface was moved (vertically) from a position when it was slightly pushing the probe ($x < 0$ in our plots of v_j) to a distance of a few λ (fig. 3.6ii). With this measurements, the EM-field in the near-field region of the MDP was mostly affected and the results appointed the most sensitive regions in the waveform for that particular probe-sample combination (section 3.5.1). Then the region of the time-delays could be limited to the useful region and measurement time could be saved in later experiments.
- ◇ Besides using a wet tissue (fig. 3.4), the sensitivity of the probe may be also checked by a scan on a sample with a metal-dielectric contrast. The scan was lead perpendicular to the border of the metal deposited on a dielectric substrate (fig. 3.6iii) (see later section 3.5.2).

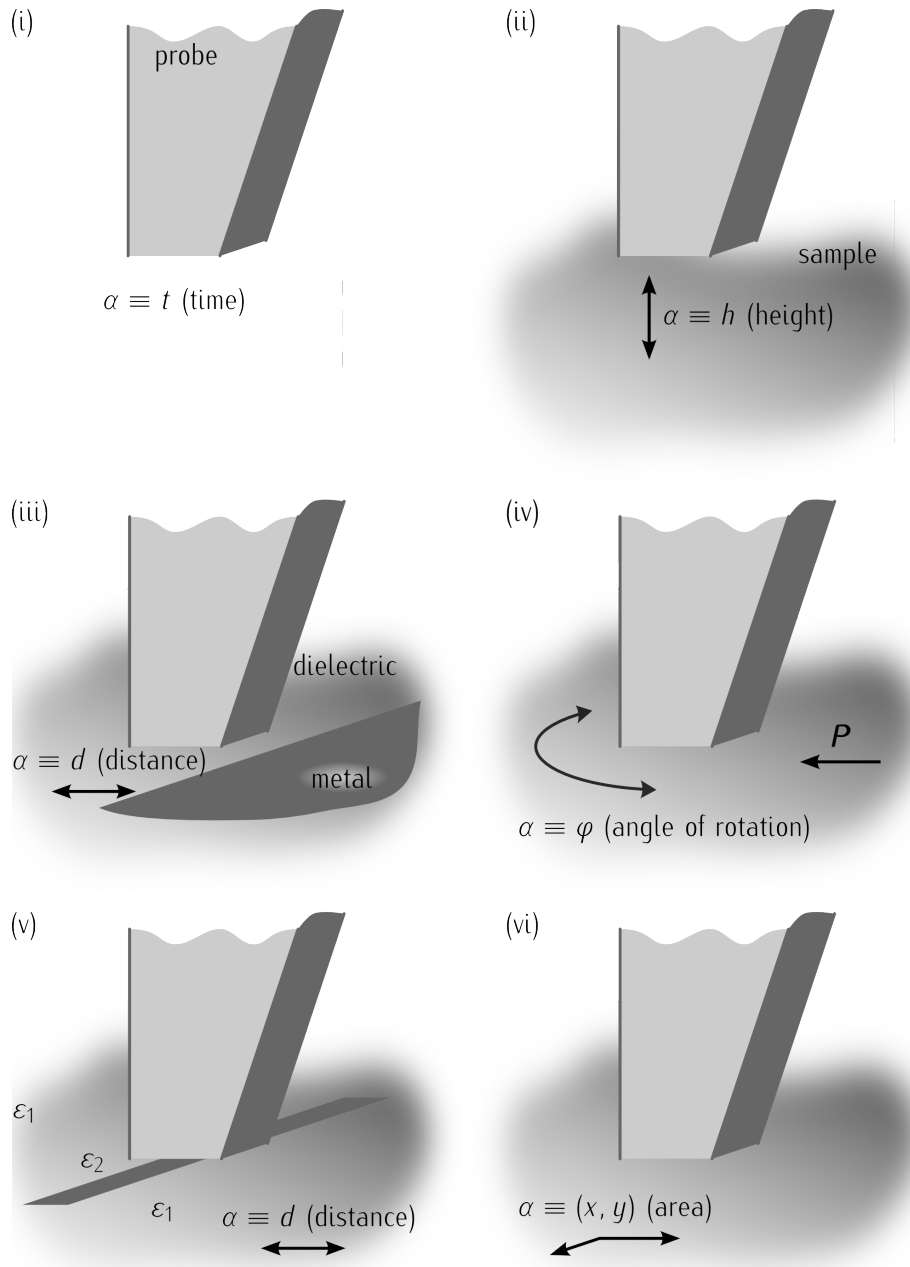


Figure 3.6: Various experimental configurations of a probe and a sample were executed to study the characteristics of both

- ◇ Configurations (iv), (v) and (vi) in fig. 3.6 were a slight variation of the configuration (iii). But instead of crossing a sample with a metal–dielectric contrast, a response to a (ferroelectric) sample turning under a probe was measured (iv) (section 3.7.1), a probe crossing a domain stripe was simulated (v) (section 3.7.4), or a probe scanning a surface of a ferroelectric sample with domains was executed (vi) (section 3.7.3).

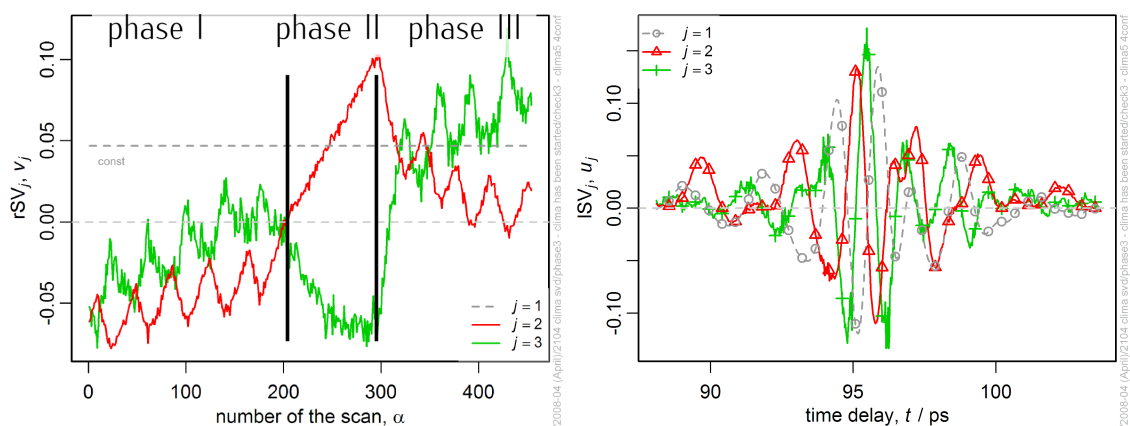
3.4 Calibration and removing artifacts

For sensing and imaging a sample, a specific place in the waveform may be selected (fig. 3.3); provided that the dielectric contrast is strong enough for resolving it in the waveform. It turned out that with a help of a height measurement and the following SVD, that task can be accomplished very easily (see later section 3.5.1). First we tried to find places in the waveform which would be the most sensitive to the presence of a sample in front of the tip and provide measurements in those. Later we have found that there are zones in the waveforms in which extremes of the *left singular vector (LSV)* appear, that LSV representing the near-field exponential component *right singular vector (rSV)* (section 3.5.1). Unfortunately, the extremes for a given probe and certain setup are not stable in time (within the range of minutes to days).

Additionally, the vector decomposition applied to the results of the experiments and simulations allowed us to extract the independent processes contributing to the dataset. These independent processes were represented by singular vectors that were orthonormal to each other (their correlation coefficient were close to experimental zero). But, the decomposition does not provide any information about the nature of the independent processes. To identify the extracted processes, it was necessary to compare them with components extracted and identified previously in earlier experiments. For this, experiments aimed at identification and calibration were executed usually before each experiment.

The behaviour of the output spectrum was analysed in two measurement configurations to provide a calibration or information for further experiments.

1. First, the performance of the experiment was characterised in a situation when no sample was present in front of the tip and no additional changes during the experiments were made (fig. 3.6i). The analysis of this 1st configuration revealed *singular values (SVs)* originating from time-varying disturbances, such as thermal oscillations of the surrounding air (within 1 °C) and air flow irregularities. Thus, it was possible to identify these SV in further experiments and configurations.



(i) Functions of two significant $rSVs$ during an experiment with three phases. The experiment was let to stabilise (phase I lasted for 80 min), then the air conditioning was switched off (phase II lasted for 35 min) when the temperature went under control, and finally, the air conditioning was switched back to its normal function and the setup has been stabilised in temperature within its limits (phase III lasted for 60 min).

(ii) The temporal profiles (ISVs) of the two $rSVs$ belonging to air conditioning (left). These components were confronted with components in later and more complex experiments by visual comparison or by employing a correlation matrix.

Figure 3.7: The influence of the air-flow and temperature instability, especially, that of the air conditioning, is identified by one of the calibration experiments.

2. In some cases, the waveforms were collected with the probe in various distances from the sample surface (fig. 3.6ii). With this measurements, the EM-field in the near-field region of the MDP was mostly affected and the results appointed the most sensitive regions in the waveform for that particular probe-sample combination. Then the region of the time-delays could be limited to the useful region and measurement time could be saved in later experiments.

Noise components with various scales of periodicity can be distinguished in the experiment. Noise with a quick run causes spikes or changes in the signal in periods of seconds or minutes. Noise of such a nature originates usually in temporal changes that can be avoided to some extent:

- ◇ air-conditioning (fig. 3.7);
- ◇ mechanical vibrations (those are causing changes in the position and the amplitude of the THz pulse);
- ◇ vibrations expanding through walls (doors, steps, other machines in neighbouring rooms);

◇ electromagnetic loops in the circuit of the measurement devices.

The influence of the air-conditioning and the temperature changes could be somehow reduced. Covering the optical table with plastic sheet during the measurements reduced their influence by a factor of 3, see section 3.2. There are more complex solutions to this problem, e. g. enclosing the part of the experiment with THz radiation into a box made of Plexiglas (PMMA) and purging that by dry nitrogen gas, but that would require rebuilding the experiment and solve some configuration issues.

Long run noise causes continuous changes in the signal in periods of minutes or hours. Noise of such nature originates usually from long-term changes, such as temperature changes due to opening the doors, stabilising the setup or slow misalignments arising during the daytime (the rising slope of the oscillation in fig. 3.7).

3.5 Characterisation of the field of the MDP

In this section, we elaborate on the spatial distribution of the field at the end of the MDP. Both in experiment and in simulations, two approaches were adopted to get better understanding of the field distribution:

1. a sample was placed to different distances from the tip (ranging from the vicinity of the tip—distance $0\ \mu\text{m}$, to few tens of μm usually) and waveforms were collected for each position (fig. 3.6ii);
2. a discrete longitudinal scan was performed through a border of dielectrics and metal with the metallisation of the MDP parallel or perpendicular to the border (fig. 3.6iii); waveforms were collected during the scan at reasonably small steps being a fraction of the dimensions of the probe end facet (ca. 1 to $15\ \mu\text{m}$);
3. EM pulse was numerically simulated in a model of a MDP to analyse the E -field distribution in the probe.

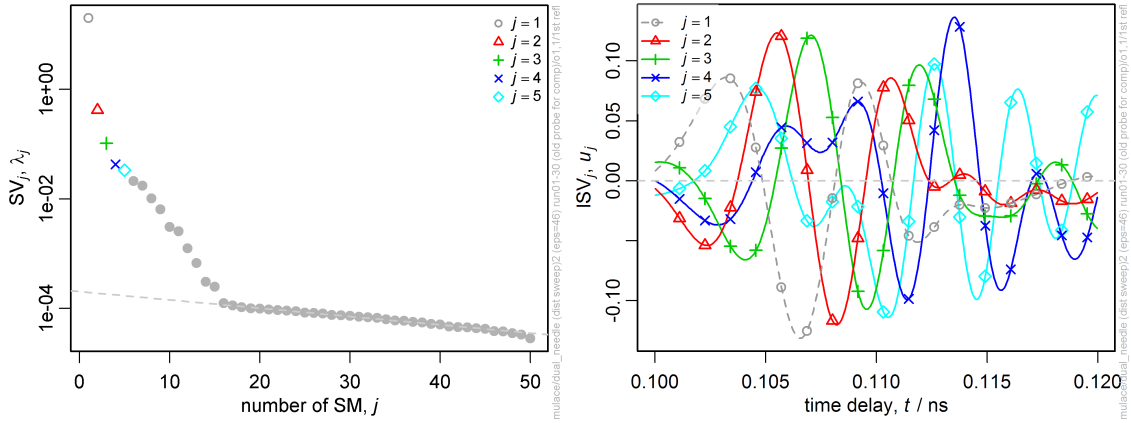
In approaches (1) and (2), sets of waveforms were collected, each waveform being a results of a measurement or a simulation at a given distance d and h . Then, this set was usually analysed by multivariate methods, see section 2.7.

3.5.1 On-axis distribution of the THz field

To provide a clear explanation on the character of the field at the tip, we examined results from a series of EM simulations as well as from experiments. In the simulations, a setup analogous to a calibration within the experiment was simulated: the responses of a probe-sample system were simulated, each with a different tip-sample distance h (fig. 3.6ii). The tip-sample distance was varied within 0 to 3000 μm in 50 discrete points and in view of the frequency range of 10 to 300 GHz, i. e. the change in distance with respect to the employed wavelength was: 0 to 1.5 of λ_μ ($\lambda_\mu = c_0/\nu_\mu$, see eq. (3.2)).

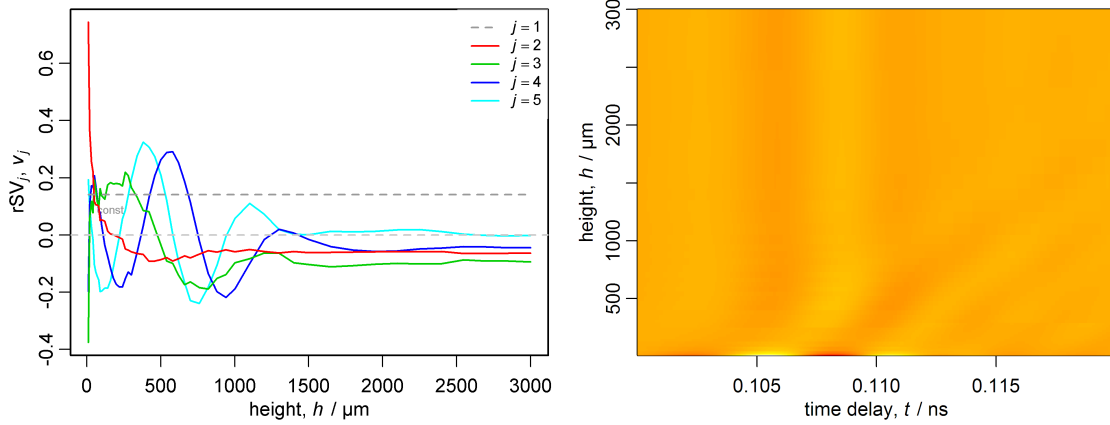
SVD of simulations, which were obtained by using the CST MicroWave Studio® 2008 ver.06 (CST MWS) software tool, also revealed several SVs depending on the tip-sample distance (fig. 3.8). A model was created of a shorter probe with a $50\ \mu\text{m} \times 100\ \mu\text{m}$ end-facet and fed with a Gaussian excitation pulse in the frequency range of 10 to 300 GHz. This lower frequency range was required by the software tool capabilities with respect to model proportions and extended meshing. The permittivity of the sample was chosen to match that of BaTiO₃ (section 1.11)—making it possible to compare the simulation results with the analogous experiments on a BaTiO₃ sample. The output pulses yielded by the simulations were analysed by SVD and five significant SVs were identified. Here we note that in simulations, there was an unstable region occurring when the probe tip was placed within few μm s from the sample surface. Simulations regarding the close vicinity of the EM-field of the tip were not trustful. In the following, we associate (the sums of) the singular matrices (SMs) with the near- and far-field radiation. The $v_1(h)$ represents a mean that may be used as normalisation value for the other rSVs and lSVs. The rSV that represents the near field displays an exponential-like profile (usually for $j = 2$); this component result in a sensitivity on the permittivity of a sample. In the other significant components a rising number of oscillations appears: one oscillation for $v_3(h)$, two for $v_4(h)$ and so on (fig. 3.8iii); the oscillations become denser in h as their order j increases. This tendency was explained by summing up the SMs (fig. 3.10) for various j (a SM_j is a product of the SV_j , lSV_j and rSV_j).

A similar experiment was conducted with a real BaTiO₃ sample under a probe with the dimension of the end facet of $80\ \mu\text{m} \times 140\ \mu\text{m}$. The distance h between the tip and the sample (with a permittivity $\varepsilon = 56$) was then varied across an interval of 100 μm with steps of 4 μm . For a comparison with the amplitudes $u_j(h)$ extracted from the experiment, see fig. 3.12. The abscissas were rescaled to $h\nu_\mu$, where the mean frequency ν_μ takes on the values of 0.155 THz



(i) The 1st 5 SVs with the scree test.

(ii) The 1st 5 LSVs.



(iii) The 1st 5 rSVs displaying rising number of oscillations.

(iv) The prewhitened dataset $E^*(t, h)$, where both the near-field and the far-field radiation are present.

Figure 3.8: The decomposition of the results of a series of simulations a varying tip-sample distance. Clustering of the components to contributions to the near field and to the far field is shown in fig. 3.9.

and 0.60 THz in case of simulations and for the experimental data, respectively.

$$v_\mu = \begin{cases} 0.155 \text{ THz} \equiv 2000 \mu\text{m} & \text{of the frequency range of the simulations,} \\ 0.60 \text{ THz} \equiv 500 \mu\text{m} & \text{of the frequency range of the experiments.} \end{cases} \quad (3.2)$$

The probe is 1 to 30λ long @ 10 to 300 GHz ($\lambda \approx 1$ to 30 mm), while in the experiment it is long 25 to 300λ long @ 0.100 to 1.2 THz ($\lambda \approx 0.25$ to 3 mm). Then, the shape identity after rescaling the distance is a direct consequence of the scalability of Maxwell's equations.

The 1st non-constant rSV $v_2(h)$ appears to have a decaying shape similar to that shown in recent absorption measurements using a microstrip-line near-field THz waveguiding technique [Byrne et al., 2008]. In that work, the evanescent electric field above THz on-chip waveguides was used to measure properties of dielectric samples.

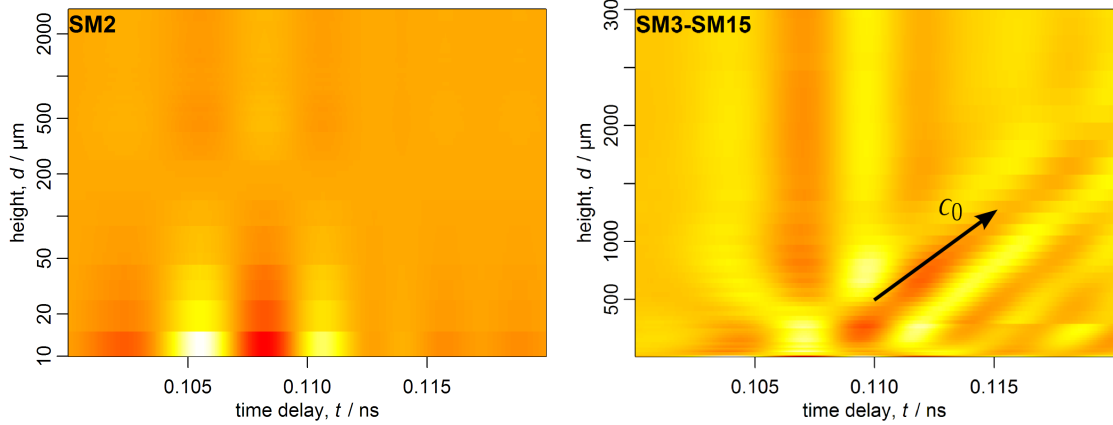
Further, we compare the simulation results (figs. 3.8 and 3.9) to an experimental one (fig. 3.11). In figs. 3.9ii and 3.11iii the direction of the speed of light c_0 is displayed by a vector:

$$v = \frac{2\Delta h}{\Delta t} (\equiv c_0). \quad (3.3)$$

There is an agreement between the speed of light and the velocity of the far-field radiation in the experiments and also in the simulations within the error of ca. $\pm 0.5 \times 10^8 \text{ m s}^{-1} \approx 0.15c_0$.

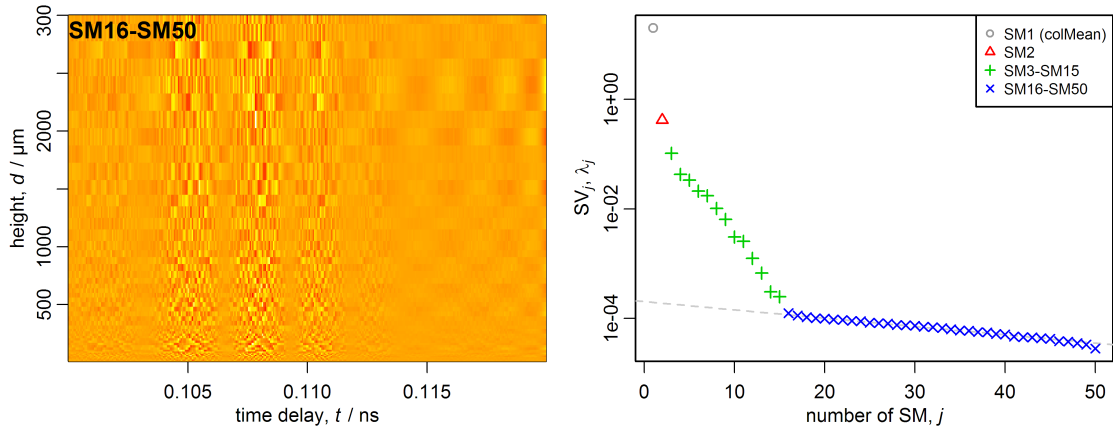
3.5.2 In-plane distribution of the THz field

The in-plane distribution of the field at the end facet of the probe was studied by simulations of the transient EM pulse and by scanning of a sample with a metal-dielectric contrast. The simulations showed that the extrema of the E in the vicinity of the end facet of the probe are located in several lobes (fig. 3.14, see fig. 3.13 for the Cartesian coordinate system in 3D). Additionally, each component of the E displays extrema at different places, thus each component is sensitive to a different projection of the local permittivity. The E_x and E_y are sensitive to the horizontal components of the local permittivity (the 1st and 2nd column in fig. 3.14, respectively). But the E_x displays the broadest lobe of all, and only the E_y determines the resolution at imaging. These four lobes of the E_y determined the resolution and sensitivity at imaging experiments on a ferroelectric sample (section 3.7.2). The extrema of the E_z are located in two



(i) The SM_2 in a logarithmic scale (pertaining to the symbol Δ in (iv)); here, no far-field radiation is present.

(ii) $\sum_{j=3}^{15} SM_j$ (pertaining to the symbols $+$ in (iv)). The break in the data around $300\mu m$ is associated to a step in the meshing within the series of simulations.



(iii) $\sum_{j=16}^{50} SM_j$ displaying the noise in the dataset (pertaining to the symbols \times in (iv)).

(iv) The λ_j values with the scree test clustered to the mean (\circ), near-field (Δ), far-field ($+$) and noise (\times) components.

Figure 3.9: Contributions (i) to the evanescent (near-), (ii) to the radiation (far-) field and (iii) to noise were separated. The components from earlier results fig. 3.8 obtained by SVD were tot up; cf. fig. 3.8iv.

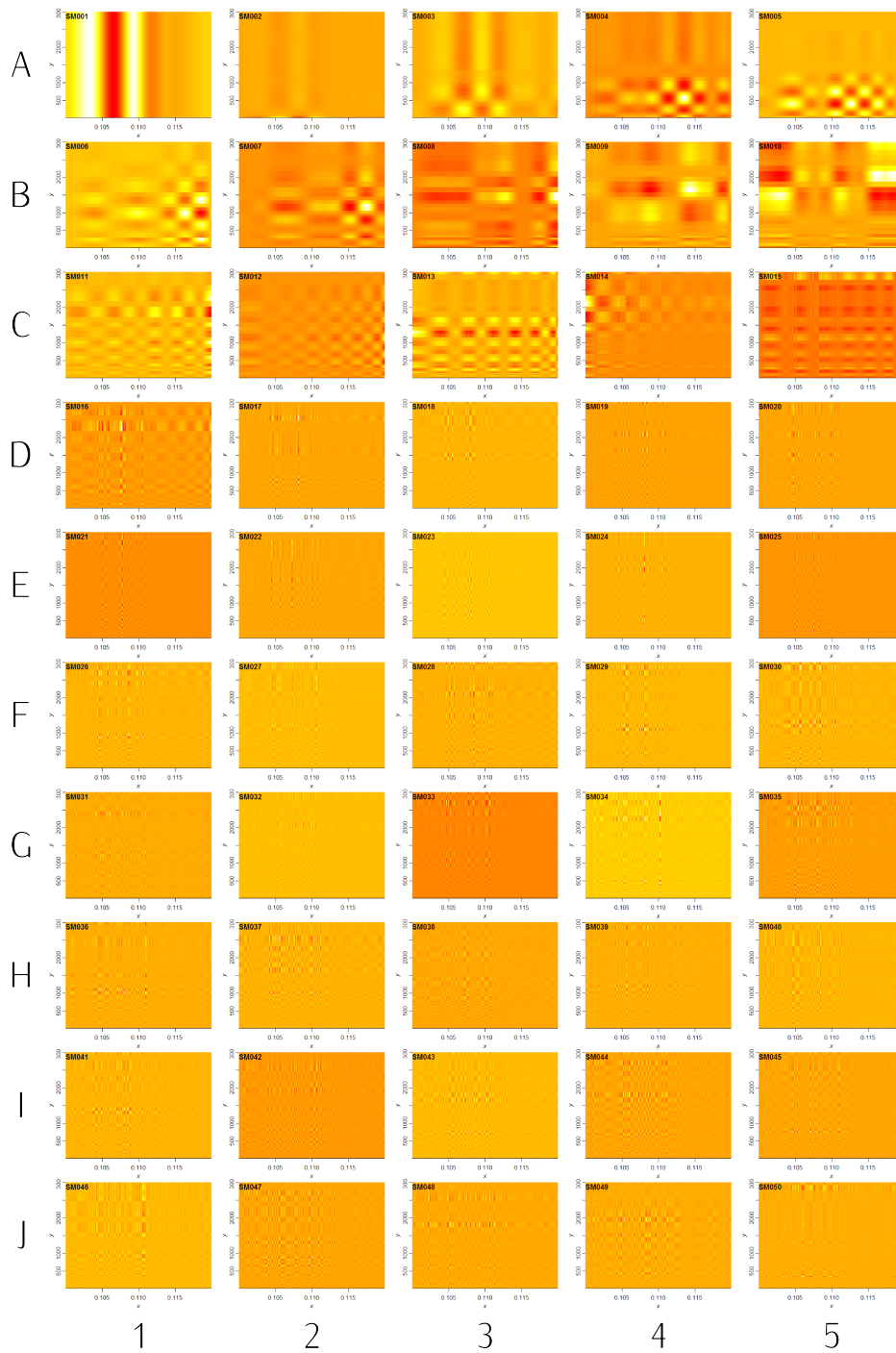
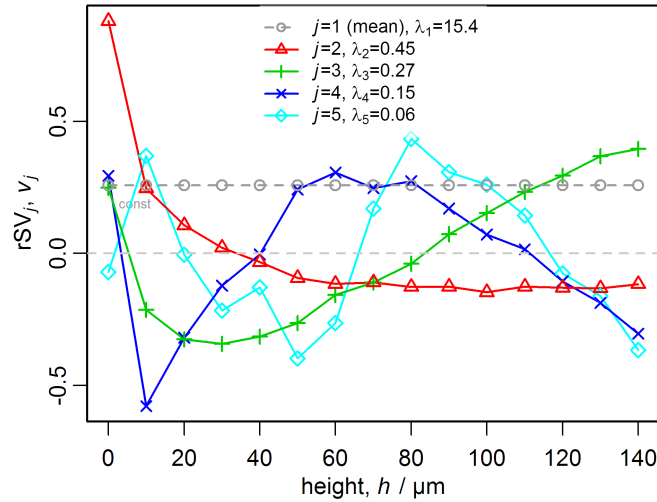
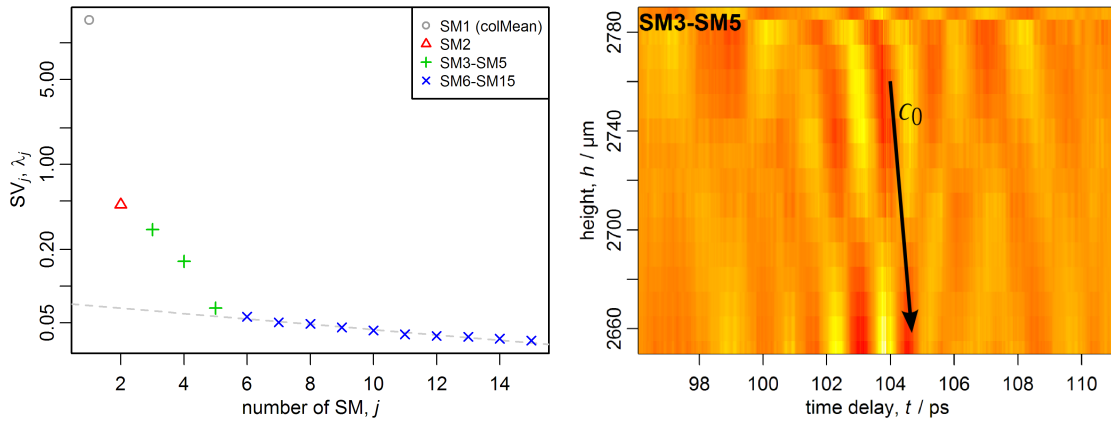


Figure 3.10: Example of the spatio-temporal layers (SMs) that were extracted from the series of simulations with varying sample-tip distance (fig. 3.8). The mean component (SM_1) is placed to indices A1, and the SM components run in left-to-right and top-to-bottom order in the table. The axis and limits of all the layers are identical with those in figs. 3.9ii and 3.9iii.



(i) Characteristic examples of amplitudes $v_j(h)$ (rSVs) of the experimentally obtained output THz pulse depending upon the tip-sample distance h , for $j \leq 5$ (ii) display characteristic oscillations. (The colours and symbols in (i) and (ii) does not correspond)



(ii) The separated components were clustered and the SVs λ_j are shown here belonging to different sums of SMs. The scree test (section 2.7.2) is plotted, too, to demonstrate the noise level.

(iii) $\sum_{j=3}^5 SM_j$, belonging to symbols $+$ in (ii). The sample touches the probe at $y = 2790 \mu\text{m}$, and it is away $140 \mu\text{m}$ at $y = 2650 \mu\text{m}$. The c_0 is displayed by the arrow (eq. (3.3)).

Figure 3.11: Contributions to the radiation field (experiments).

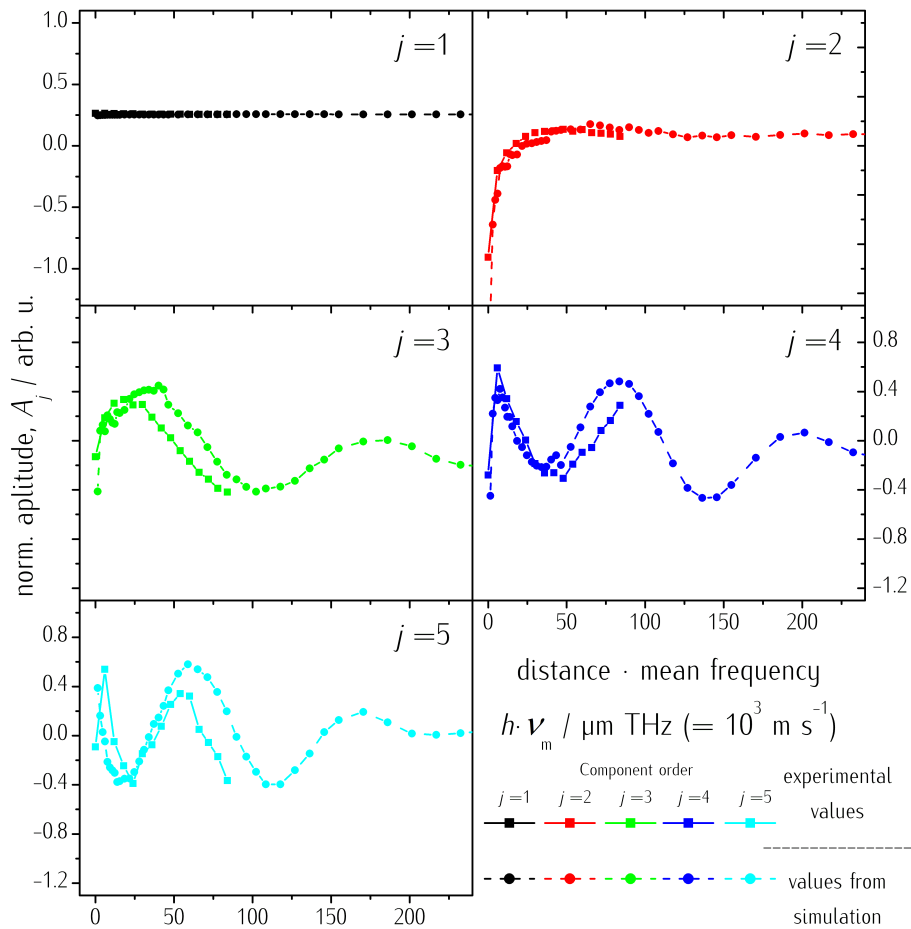


Figure 3.12: Comparison of the amplitudes $u_j(h\nu_\mu)$ extracted from the experimental and simulated datasets. The amplitudes are plotted against the entity $h\nu_m$, where h is the distance between the sample and the end-facet of the probe, and ν_m is the mean frequency of the frequency range of the output pulse.

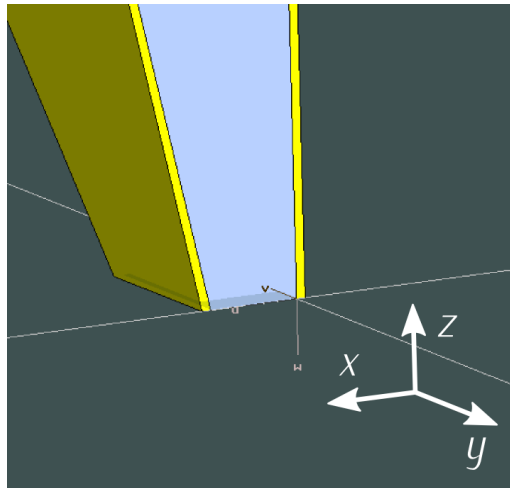


Figure 3.13: The end facet of a simulated MDP at the vicinity in a sample surface (view of a model in 3D). The Cartesian coordinate system matches that in fig. 3.14.

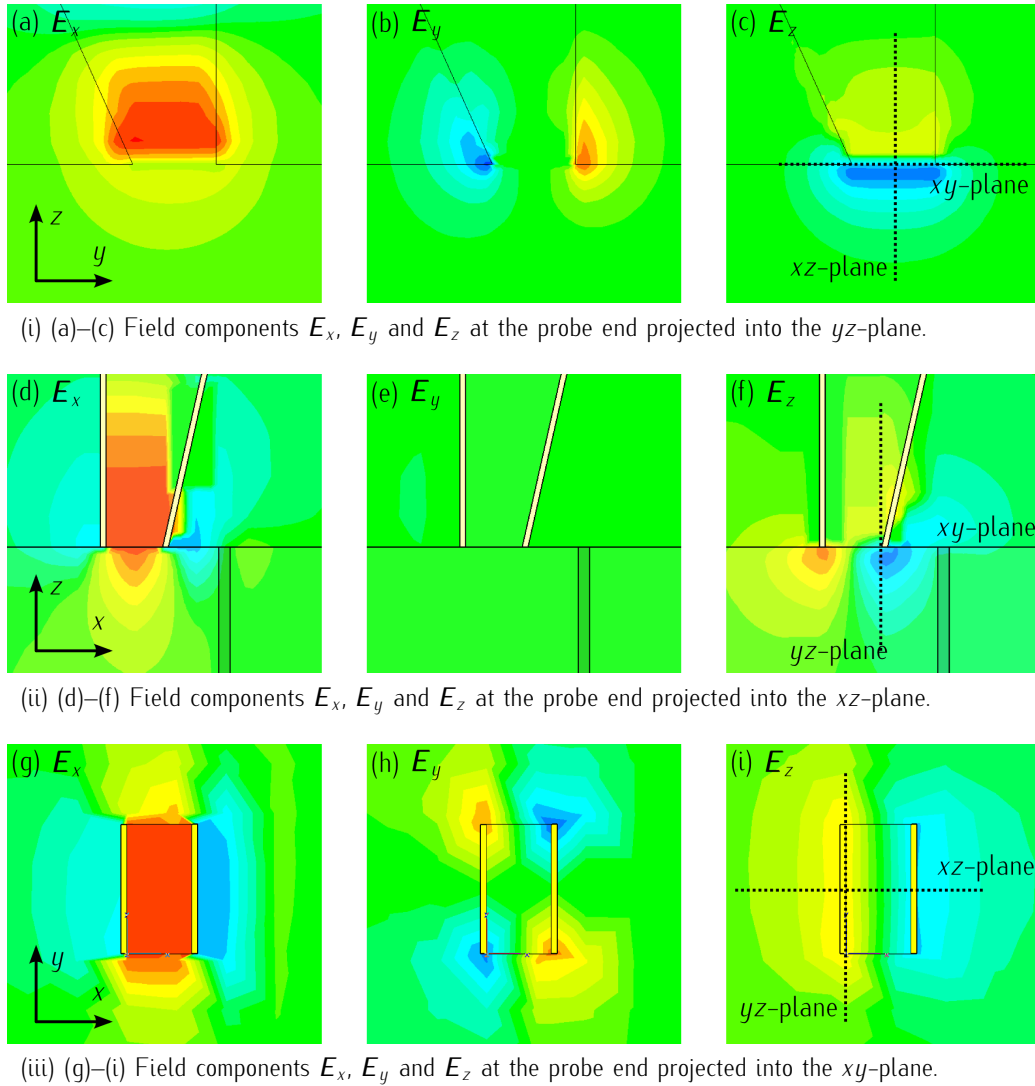


Figure 3.14: Field components at the end of the probe from a simulation with a thin stripe (fig. 3.6v, with complete results in section 3.7.4) were projected onto the three Cartesian planes crossing the probe end facet. The field pattern is displayed for the time when the pulse arrived to the sample and displayed the highest sensitivity (fig. 2.5, at $t_1 + \Delta$). The time equals to the first sensitive time-delay appearing in ISV_2 , that displaying the sensitivity on permittivity of the sample (fig. 3.31). The orientation of the axes and a 3D view of the tip end of the simulated probe are depicted in fig. 3.13 for better illustration. All the projection planes are displayed in the 3rd column by dotted lines ($\cdot\cdot\cdot$). The 3rd column, figs. (c), (f) and (i), shows the E_z component that is sensitive to the domain stripe in the simulations (the domains were isotropic). The distribution of this component matches the response of the probe to the stripe (fig. 3.31). But these components should not be sensitive to the domains in a real $BaTiO_3$ sample—the E_x and E_y components should be sensitive in that case (fig. 3.25).

lobes (the 3rd column in fig. 3.14) around the border of the waveguide and the metallisation, and they are sensitive to the projection of the permittivity to the z -axis.

In the experiment, the sample in fig. 3.15 was scanned by a Teflon (PTFE) and a sapphire MDP, those probes creating a MDDP for later measurements (fig. 3.32), i. e. the sample was scanned by a MDDP within the time-delays corresponding to sensitive time domains of the particular MDP (fig. 2.5). Two selected time cuts of the measurement sets obtained by the two probes are shown in fig. 3.16. Two observations can be made by looking at them:

- ◇ the scan by a Teflon probe displays worse resolution;
- ◇ the scan by a sapphire probe displays ghost images.

The reason for worse resolution of a Teflon probe may be a worse sensitivity to a contrast in refractive index for probes that have a low refractive index of the waveguide. This would be a consequence of the measurements on sensitivity described later in section 3.6. The smaller refractive index of the waveguide means longer wavelength in the probe, and that may cause wider lobes, too (fig. 3.14).

A part of the scan (the area within the four corners in fig. 3.16ii) obtained by the sapphire MDP was analysed for slopes. Two slopes and steps found in the projection onto the y axis (fig. 3.17i) may be a consequence of the localised lobes at the sides of the end facet fig. 3.14. The numerical derivative of a smooth approximation of the step-like function in fig. 3.17i is depicted in fig. 3.17iii. The two maxima with a spacing of ca. 70 μm reflects the characterisation of the sensitive lobes at the end facet of the probe (fig. 3.17ii). End facets of smaller dimensions may have even one the sensitive area (the two lobes on the sides would overlap, see fig. 3.18).

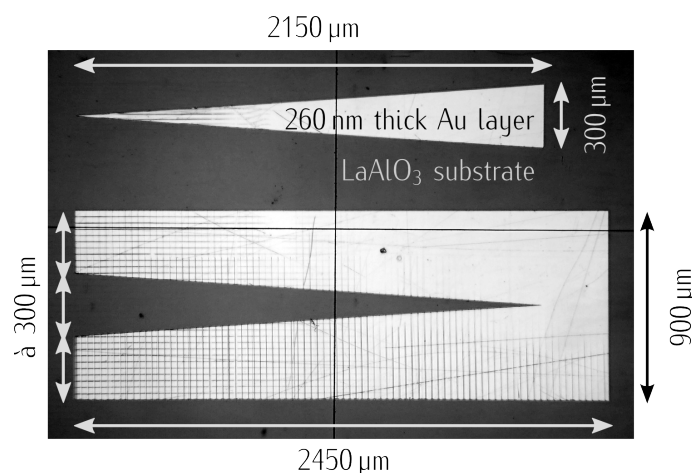
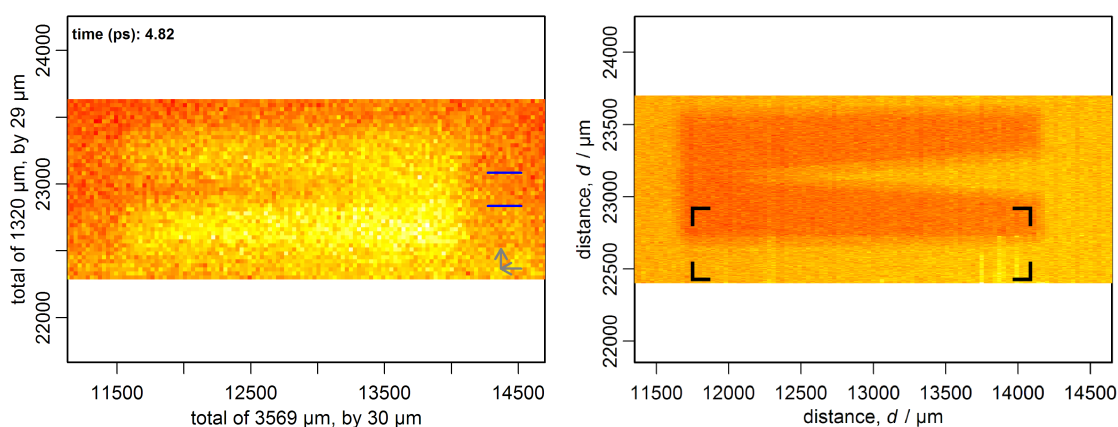


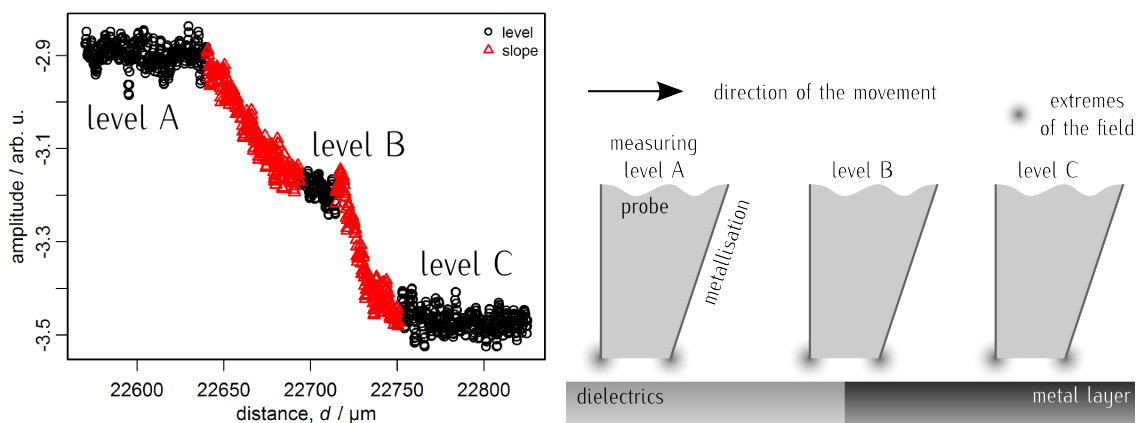
Figure 3.15: Metal–dielectric sample used for contrast measurements. It consists of gold (light regions) deposited on LaAlO_3 substrate (dark region, background); $n = 5.0$ ($\epsilon' = 25$) at 1 THz. The hatched region (mostly visible in the bottom–left corner) are striae made by a sapphire probe—the hard sapphire furrow channels into the soft metallisation. These striae did not affect later measurements.



(i) A metal–dielectric sample was scanned by a Teflon probe (its metallisation and the primary and secondary scanning directions are depicted on the right). The boundaries between the dielectric substrate and the metallic layer are blurred due to a wide end facet of the probe ($300\ \mu\text{m} \times 300\ \mu\text{m}$, see fig. 3.32) and weak response of the signal.

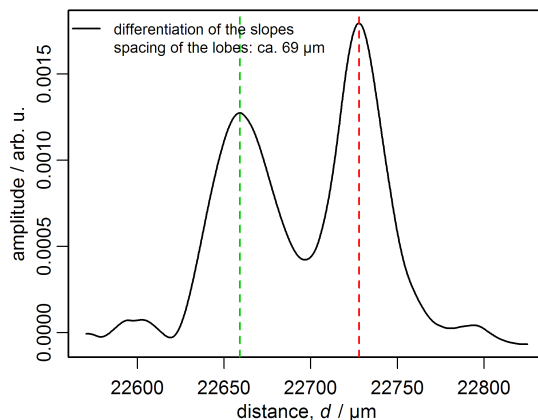
(ii) A metal–dielectric sample was scanned by a sapphire probe. The area within the four black corners were analysed for linearity and slope later fig. 3.17i.

Figure 3.16: Scans of a sample with a metal–dielectric contrast (fig. 3.15) by a Teflon (end facet of $250\ \mu\text{m} \times 250\ \mu\text{m}$) and by a sapphire probe (end facet of $60\ \mu\text{m} \times 140\ \mu\text{m}$) were performed. The measurements were performed by a dual probe (see later section 3.8) and waveforms were collected at two distinct time–delays each specific for one of the probes (fig. 2.5, at $t_1 + \Delta$).



(i) The slope (in symbols \triangle) of a part of the area scan in fig. 3.16ii. The data in the rectangle (fig. 3.16ii) were averaged in the horizontal dimension and plotted here. The 1st slope (from left) is long $53\mu\text{m}$ while the 2nd slope is long $36\mu\text{m}$. The parts of the curve plotted black (in symbols \circ) are considered for horizontal levels.

(ii) Model of a scan through a metal-dielectric boundary with two localised sensing areas. The positions of the probe when the no change was sensed by the sensing areas are marked in the graph on the left correspondingly.



(iii) Numerical derivative of a smooth approximation of the step-like profile in (i) displaying two sensitive areas at the end facet of the probe (ii).

Figure 3.17: Scans of a metal-dielectric boundary (see fig. 3.15 for the sample) revealed that the field at the end of the probe is not isolated at one single area, but that the end facet has actually two localised sensing areas.

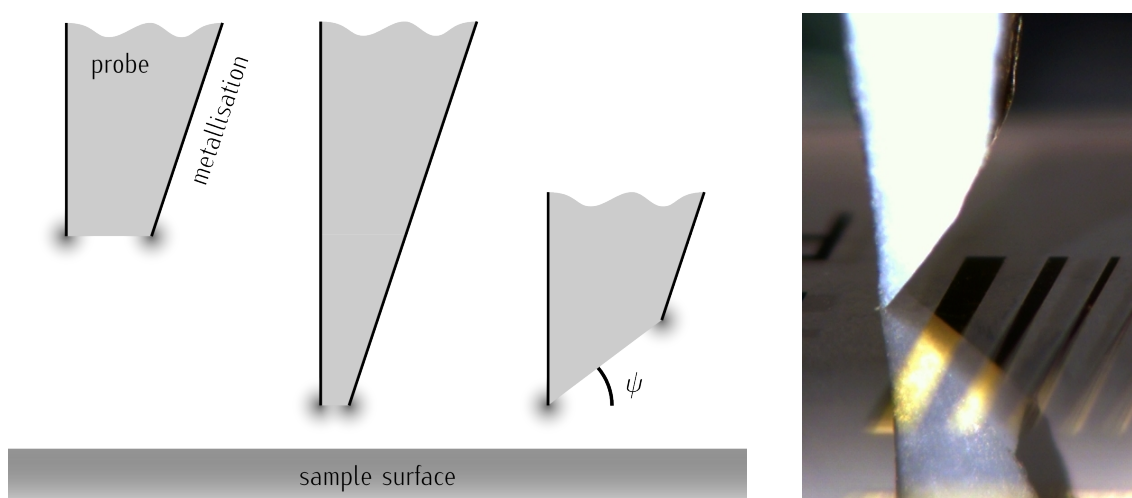


Figure 3.18: It was observed in experiment that a MDP has two main interaction areas, both located around the borders of the metallisation (left). The smaller the facet is, the closer the two interaction areas should be. For a size of the end facet smaller than a given limit, the two interaction areas are undistinguishable from each other (middle)—this resolution limit contribution to the overall resolution limit (section 1.8). To avoid ghost images in the scanning or images that are a convolution of the two sensing areas, tilted end facet can be used for scanning (right, and photo). The end facet can have a tilt of $\psi \approx 10$ to 50° to the sample surface, and the only allowed interaction area is located at the sharper end.

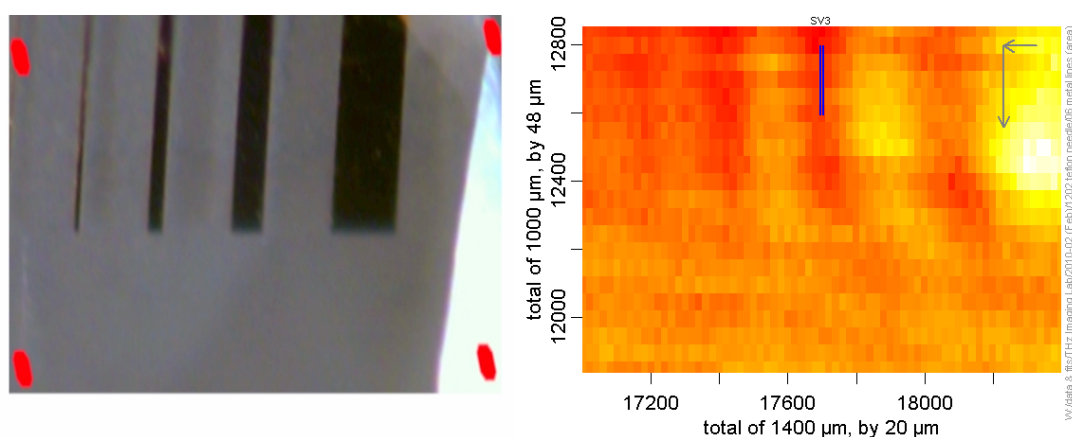


Figure 3.19: The scan (left) of a metal-dielectric sample (right) with a titled Teflon probe provided a much better resolution than with a traditional rectangular flat end facet (cf. fig. 3.16i). Features with dimensions of $25\ \mu\text{m}$, $50\ \mu\text{m}$, $100\ \mu\text{m}$ and $200\ \mu\text{m}$ are displayed (right) and were resolved (left) here.

3.6 Broadband measurements without spatial resolution

In the following experiment, the response of the probe on various samples was analysed in details. The typical investigated frequency range of the measurements was 0.1 to 1.2 THz (see fig. 2.8 where a typical waveform of a reflection is depicted with its calculated FFT). We selected materials of different types displaying distinct properties within this frequency range (section 1.11) to examine them by using the MDP in order to characterise the sensitivity of the probe in contrast with respect to a difference of the refractive indices of samples. The following materials were examined: silica and glass, Mylar and Teflon, doped silicon samples, sapphire, metal and BaTiO₃. The average material constants within the experimental frequency-domain (FD) of sensed materials are listed in table 1.2.

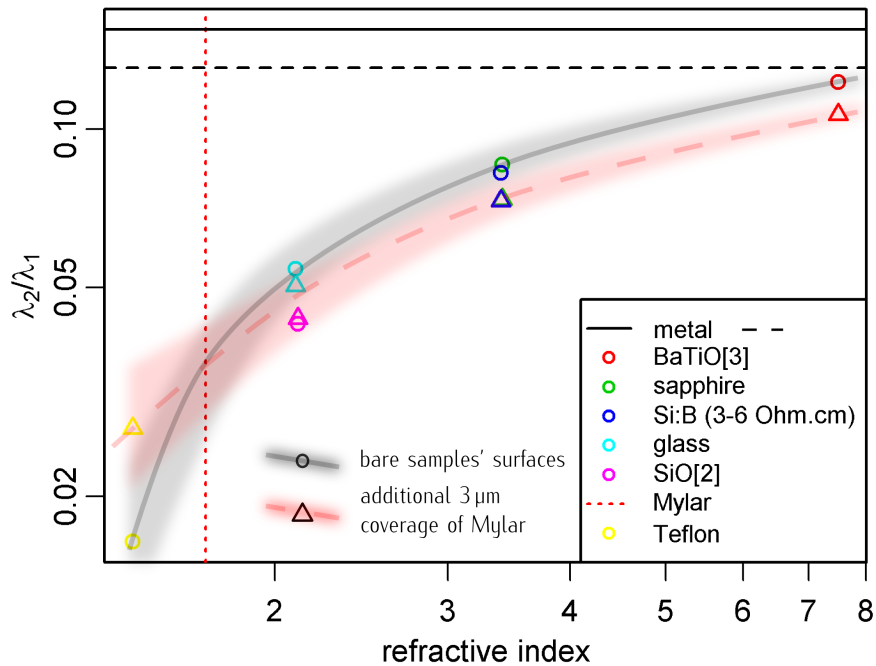
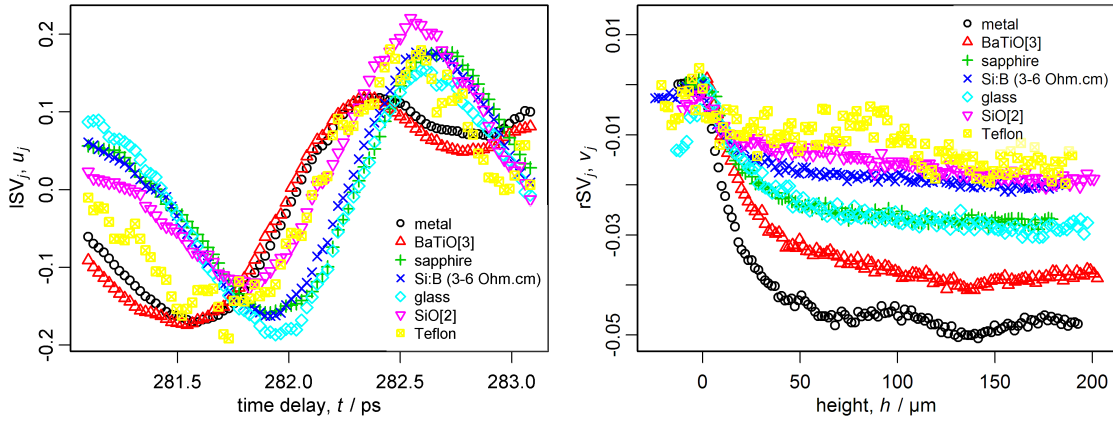


Figure 3.20: The ratio of the 1st two SVs (λ_2/λ_1) represents the reaction of the probe to the material properties (to their refractive indices n). The derivative of the curved lines represent the sensitivity of the probe for a given n . The blurred area represents the values within the calculational error of $\approx 10\%$.

Waveforms were collected for various distances of the sample and the tip (fig. 3.6ii—in principle, the experiments were identical with one of the calibration experiments, see section 3.5.1). The dataset acquired for each sample was analysed by SVD, and from the results, the 2nd rSV



(i) The time profiles u_j of the components being sensitive to material properties ϵ^* . The time profiles for metal (o) and BaTiO₃ (Δ) are flipped around $y = 0$ with regards to their spatial profile (ii).

(ii) In order to allow comparison of the influences of various materials on the near field of the probe, the height profiles v_j multiplied by λ_2/λ_1 and they were offset on the x and y -axis to share the $(x, y) = (0, 0)$ value for the position when the MDP touched the sample.

Figure 3.21: The time and spatial components of the height measurements on material sensing in colours (not symbols) corresponding to data in fig. 3.20.

(the most sensitive to the presence of the samples) displayed the exponential-like behaviour for all measurements (fig. 3.21ii). But, the complementary LSVs may be split into two clusters according to their correlation factors (see fig. 3.21i for u_j):

- ◇ metal and BaTiO₃; and
- ◇ sapphire, Si:B (3 to 6 Ω cm), glass, silica (SiO₂) and Teflon.

The correlation factors among the u_j within these two clusters were ≈ 0.90 to 1.00, but they were ≈ 0.30 to 0.60 between the two clusters. The ratio of the obtained 2nd (near-field) and the 1st (mean) components was calculated for each sample. These values are displayed by circles in fig. 3.20 depending on the refractive index of the samples. A grey line (—) and grey blurred area (■) displays the tendency of the values and their error range ($\approx 10\%$), respectively.

Additionally, the response of the samples was measured when the samples were covered with a 3 μm wide Mylar layer (section 1.11). The same ratios were calculated; these are displayed in fig. 3.20 by triangles. A red line and light-red blurred area display the tendency of the values and their error range ($\approx 10\%$), respectively.

The tendency of the values extracted from measurements with samples under the Mylar layer (red line, —) is very similar in shape to the tendency of the values extracted from

measurement with samples having bare surface (grey line, —). That means that the samples may be distinguishable by the MDP method under a thin film of a transparent material (of Mylar in this case). Covering by a plastic foil might be important for samples that are dangerous or unstable (e. g. chemicals), contains liquids or have a soft surface (e. g. biological samples).

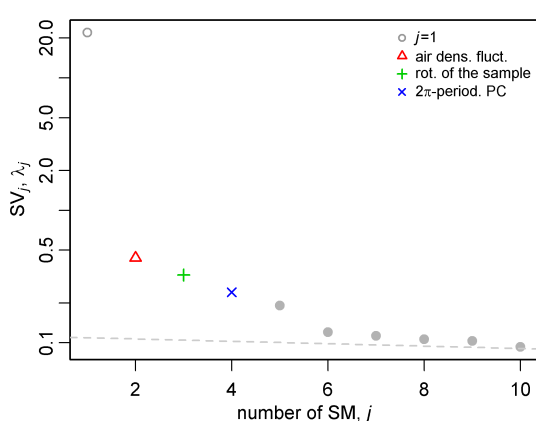
3.7 Broadband measurements with spatial resolution (imaging of BaTiO₃ domains)

The sensitivity of a near-field imaging method is often validated by scanning across a metallic pattern on a non-metallic substrate (dielectric) ensuring a high contrast in the image pattern. However, for potential applications, it is crucial to investigate the imaging capabilities on samples in which contrast in permittivity is lower. With this intention, we demonstrated earlier that our method is able to reveal local anisotropy in ferroelectrics (section 3.7.1) [Berta et al., 2009]. In section 3.7.2, we present results of imaging ferroelectric domains using a sapphire MDP [Berta and Kadlec, 2010].

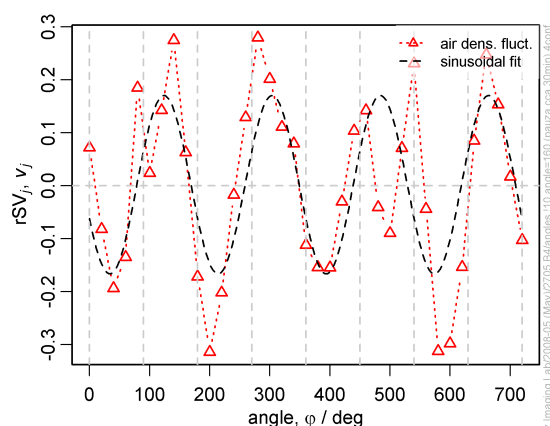
3.7.1 Polarisation and anisotropy sensitivity

To check the sensitivity of the tip to the anisotropy of a sample, sample-orientation dependent measurements were performed. In this configuration, a flat as-grown BaTiO₃ single-domain crystal platelet was used which exhibits a high anisotropy (section 1.11); its refractive indices are $n_o = 45$, $n_{e0} = 7.5$ in the THz and MW frequency ranges [Li et al., 1996]. The sample surface was placed in touch with the probe, perpendicular to its axis and rotated around this axis by an angle φ (fig. 3.6iv). The output waveforms were recorded at each orientation. Analysis of the data revealed a rSV which is orientation dependent. A sinusoidal fit of the amplitude of this SV ($j = 3$) is shown in fig. 3.22iii. The response is π -periodical which means that this component reflects chiefly the sample anisotropy itself and it is not due to other raw measurement errors due to, e. g. tilted sample surface. The rSV for $j = 2$ showed an uncorrelated behaviour and was assigned to air density fluctuations. Finally, rSVs for $j = 4$ and $j = 5$ showed a 2π -periodical behaviour which is probably due to a small misalignment between the normal axis of the sample and the vertical axis of the probe. In this way, it was demonstrated that the output THz pulses are influenced by the anisotropy of the probed samples. We compare

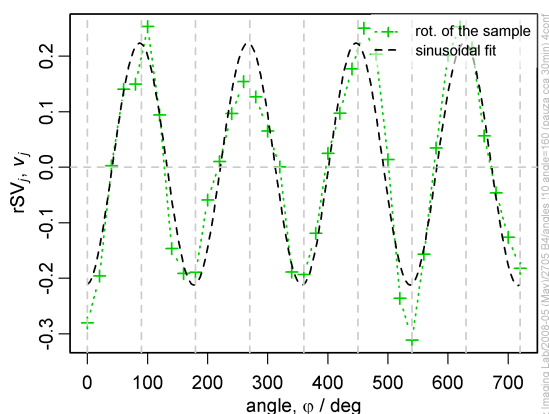
the results of the **SVD** with a manual selection of the significant time cuts, which might be likewise effective in finding significant patterns in the dataset, but otherwise it is time and labour consuming (fig. 3.23).



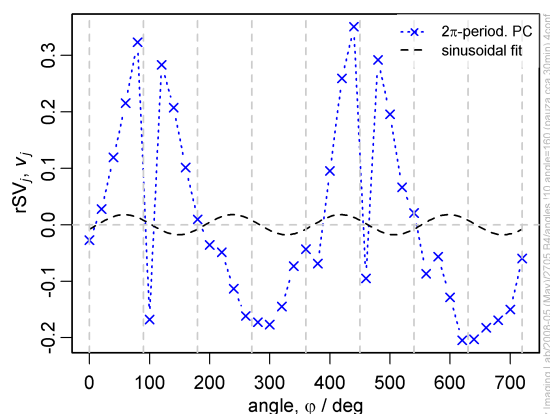
(i) Power λ_i of the contributions.



(ii) Normalised contribution (v_2) of air density fluctuations.

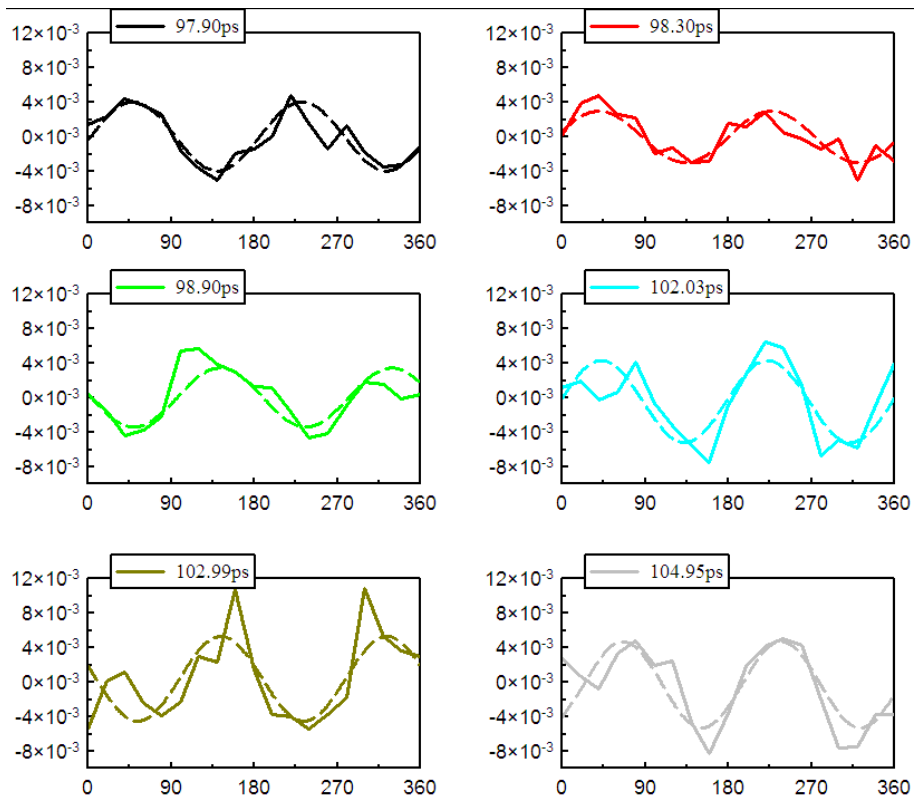


(iii) Normalised contribution (v_3) of the rotation of the domains.

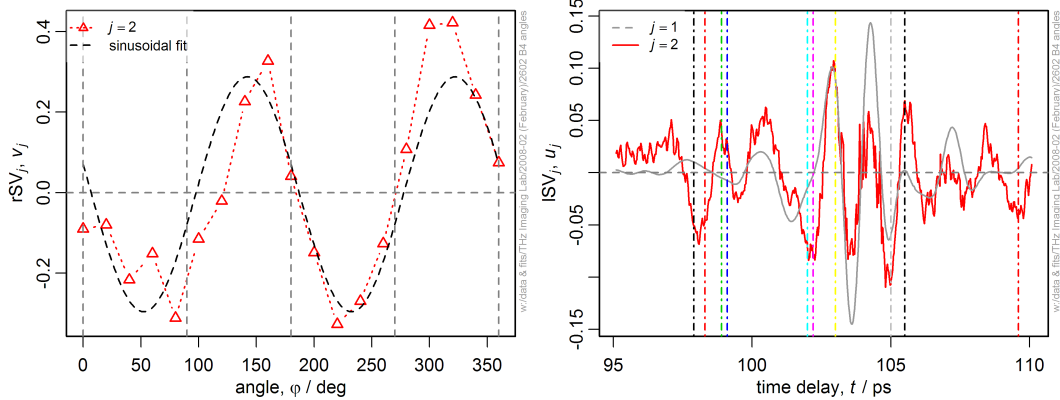


(iv) Normalised contribution (v_4) of rotation of the sample.

Figure 3.22: The response of the probe was analyse at various angles of rotation of an anisotropic sample BaTiO_3 . A π -periodical sinusoidal fit (dashed line, $--$) to the amplitude $v_3(\varphi)$ (in symbols $+$) describes the angular dependence of the output THz pulses when the anisotropic sample was turned by $2 \cdot 360^\circ$ (4π).



(i) Cuts (—) through the dataset extracted at delay-times (iii), at which a sinusoidal behaviour (---) appears; observed by a naked eye.



(ii) The rSV_2 belonging to the sample rotation fitted by a sinusoidal function.

(iii) The time profile ISV_1 (mean, —) and ISV_2 (matching extrema of the rSV_2 , —) with marks of the cuts (i) in corresponding colours.

Figure 3.23: The dataset of waveform gathered at varying angle of the sample was analysed by naked eye, too (i). The match with a sinusoidal fit and with a component of the SVD (ii) is very good for some time-delays, but the results is unpredictable and subjective.

3.7.2 Imaging of BaTiO_3 domains – sample

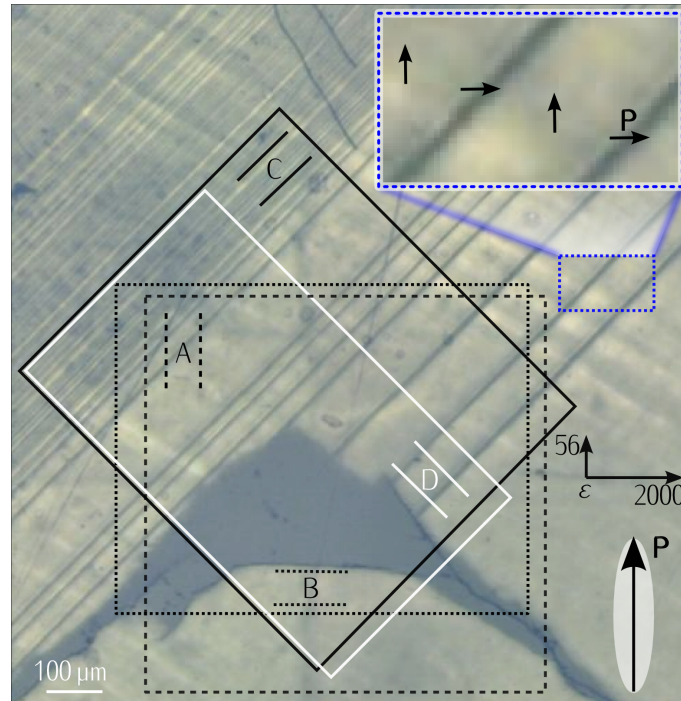


Figure 3.24: Spontaneous polarisation on a BaTiO_3 polished surface with schemes of the scans. Scans were collected from large areas on the BaTiO_3 surface positioned under significant angles (configurations A–D). Areas embraced thick and thin naturally grown domains, a defect and a part of an inclusions.

Imaging scans were performed on a polished surface of a 1 mm thick BaTiO_3 single-crystal platelet. Crystals of this ferroelectrics exhibit a high anisotropy; its refractive indices in the THz frequency range are $n_o \approx 45$, $n_{eo} \approx 7.5$ [Li et al., 1996]. For performing imaging, we chose an area with a characteristic inclusion (defect) and multiple straight domain stripes (fig. 3.24). Micro-Raman measurements showed us the orientation of the optical axes as well as that of the polarisation in and aside the domain stripes (inset of fig. 3.24). The in-plane polarisation clearly alters by 90° . The narrower domain stripes of a width of 5 to 7 μm were separated by a few tens to 100 μm wide monodomain areas. Measurements were performed in four configurations A–D with different orientations of the MDP with respect to the sample features; these configurations are denoted in fig. 3.24 and the configurations A and B are shown schematically in fig. 3.25.

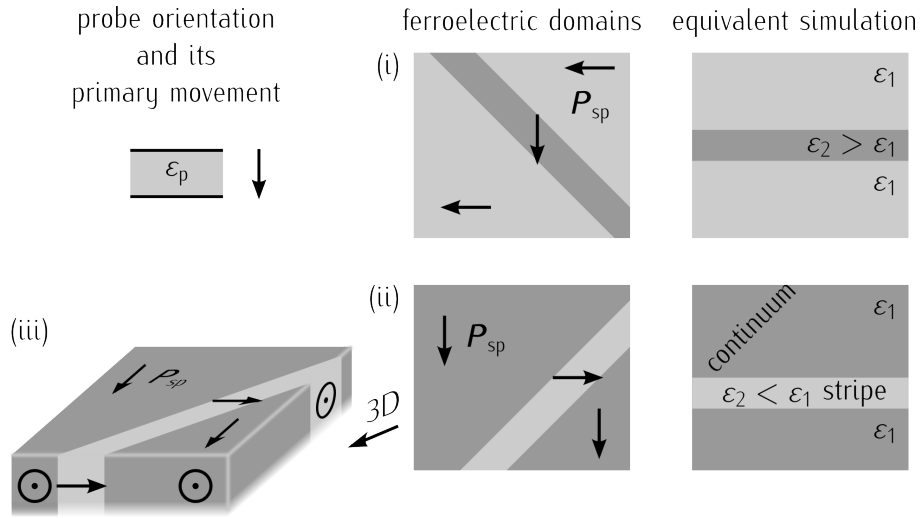
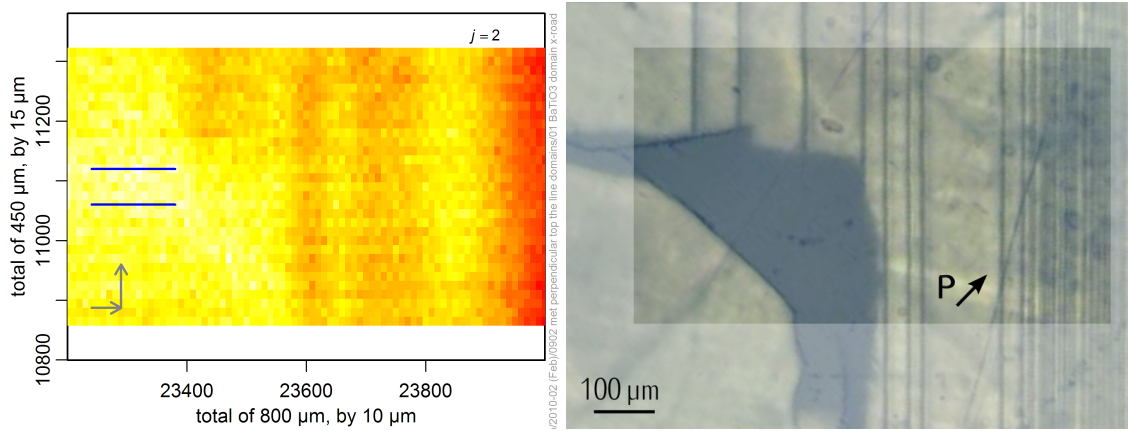


Figure 3.25: Sketch of the domains with relative permittivity dependent on the orientation of the sample under **MDP**. $\epsilon_p = 10.4$, (i) $(\epsilon_1, \epsilon_2) = (200, 60)$, (ii) $(\epsilon_1, \epsilon_2) = (60, 200)$. In the ferroelectric sample the permittivity in z -axis remains constant (iii). See the fig. 3.14i for the field distribution around the tip, especially the (h) and (i) subfigures.

3.7.3 Imaging of BaTiO_3 domains – results and discussion

The detected patterns could be attributed to the sample surface features only in two of the four measurement (sample-probe) configurations.

In the configuration B, we clearly identified components representing the domain structure besides those belonging to experimental artefacts. We could resolve the domains that were 5 to 7 μm wide although the probe had a larger width, 60 μm (fig. 3.28iv, rSV₃). Moreover, it is possible to resolve the domain structure also in a time slice of the prewhitened waveforms, e. g. at $t = 190.97$ ps, see fig. 3.28v. The difference between the rSV₃ component and the time cut at $t = 190.97$ ps is minor, but that is not a rule in other measurements. The reason for this is a strong interaction of the ferroelectric domains with the near-field in this configuration. Therefore, in this case, it would be equally possible to perform such an imaging without the necessity to collect waveforms. Instead, a detection of the THz intensity during the scanning would be done at a fixed delay-time position for which the strongest response was revealed previously, see fig. 3.28ii. The metallisation on the probe was tilted by 45° with respect to the stripe domains and parallel with the polarisation within them (fig. 3.25ii). There was no restriction on the primary movement of the probe, that could have been selected arbitrary, because the influence of the sample would vary with the same *periodicity* in both cases.



(i) The delinearised rSV2 reveals the domain stripes perpendicular to the probe metallisation. The arrows in the corner project the movement of the positioning stage: from left to right and from bottom to top.

(ii) A photograph of the scanned area D. We manipulated fig. 3.24 for better visual comparison with intensity profile (left).

Figure 3.26: A comparison of the photograph of the scanned area D (left) with one of the extracted SVD components (right). The patterns display matching features. Comparison with a selected time-slices is in fig. 3.30.

In the configurations A and C, we were not able to resolve significant features that could be linked to the sample surface structure (figs. 3.27 and 3.29). In the case of the configuration C, the projection of the polarisation \mathbf{P} onto the probe-field axis was the same for both types of domains. Therefore, it is presumable that the electromagnetic field at the probe end did not sense any contrast in this case. Surprisingly, even in such a case, we identified components representing a part of the domain structure in the configuration D (figs. 3.26i and 3.30). This result was observed, although the projection of polarisation in the sample parallel with that of the near-field should be constant through the whole scanning area. The reason for this was possibly an inhomogeneous distribution of \mathbf{E}_x and \mathbf{E}_y (fig. 3.14) near the probe metallisation end caused by a non-perfect focusing in the probe. The metallisation on the probe was perpendicular to the stripe domains, i. e. positioned under 45° to all the polarisations in the surface of the sample. The primary movement was perpendicular, too, to ensure better separability of the SVs sensitive to the sample (to the domains) and those to external influences. Note, that the common area $B \cap D$ covers ca. 60% of the area B and ca. 80% of the area D.

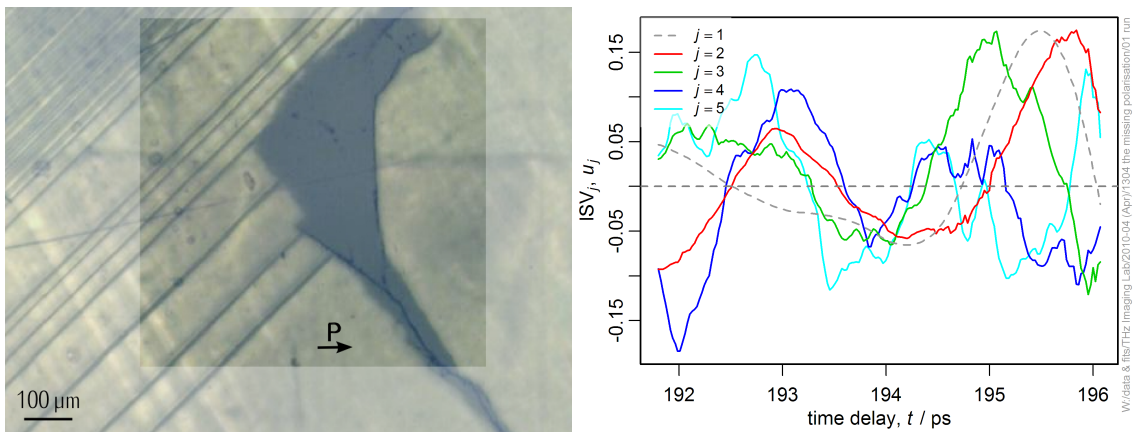
The configuration A was indeed very similar to the configuration B. The projection of the polarisation of the domains into the axis parallel to the metallisation of the probe altered during

the scanning, in both cases. The difference between the configuration B and the configuration A was in altering the optically dense to optically thin domains and their widths. While in the configuration B, the probe field was scanning over slim optically dense stripes ($\varepsilon = 2000$, $d = 7 \mu\text{m}$) in an optically thin continuum ($\varepsilon = 56$, $d > 100 \mu\text{m}$); in the configuration A, the probe field was scanning over slim optically thin stripes ($\varepsilon = 56$, $d = 7 \mu\text{m}$) in an optically dense continuum ($\varepsilon = 2000$, $d > 100 \mu\text{m}$). We performed simulations to get a possible explanation of this observation, see section 3.7.4.

Additionally, the height profile of the sample was examined in various directions and places within the scanned areas by an optical differential-interferometric measurement and a surface profiler. These measurements revealed that the flatness of the surface was below 20 nm and 10 nm, respectively.

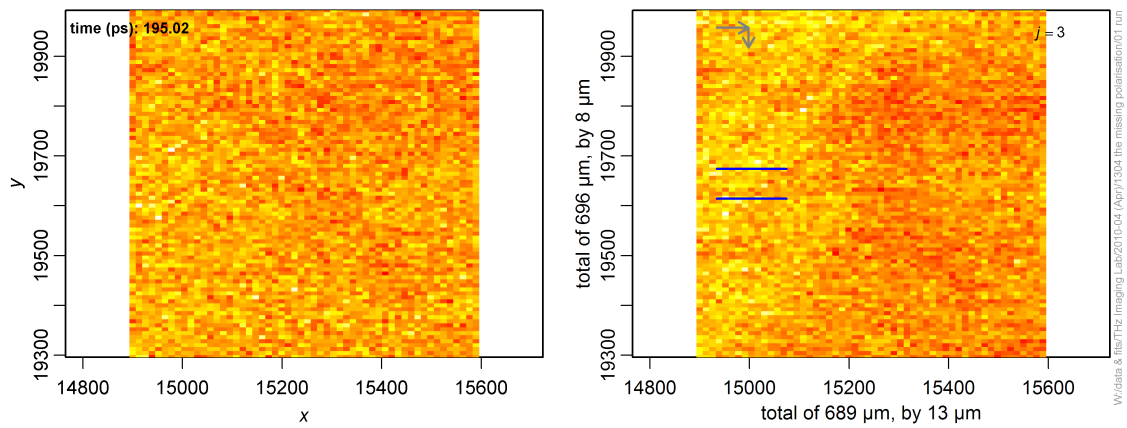
A projection similar to a *rSV* can be sometimes found in the time-cut of the set of the waveform. E. g. cf. figs. 3.28iii, 3.28iv, 3.30iii and 3.30iv. There we have to compare two pairs of 2D maps: one of the pair with the α -projection of a *rSV* with visible domains and one as a cut of the waveform in the *TD*. Additionally, the time profiles of the components displaying sensitivity to the local anisotropy does not correlate well (cf. fig. 3.28ii, $j = 3$, and fig. 3.30ii, $j = 2$). The *LSVs* (as well as the *rSVs* or the sensitive t -cuts) for a specific α response are not identical between measurements of the same sample area in different orientations. That may be a consequence of a fact that different components of the *E*-field (or lobes, fig. 3.14i) are employed at those scanings.

So, naked-eye observation of the raw dataset would predict the sample influence at different delay times: @ 190.97 ps for area D and @ 191.97 ps for area B, while there is a pale sign of a domain image for the close neighbourhood of 190.97 ps for area B and of 191.97 ps for area D. While, scanning with fixed time delay is possible (fig. 3.16ii) and good results can be expected for high contrast samples, e. g. made of metal and dielectric materials; scanning of a domain structure at fixed delay time show risky. Therefore, at least a narrow time delay of a couple of ps is needed to ensure resolution in results using some kind of data-separative method.



(i) A photograph of the scanned area.

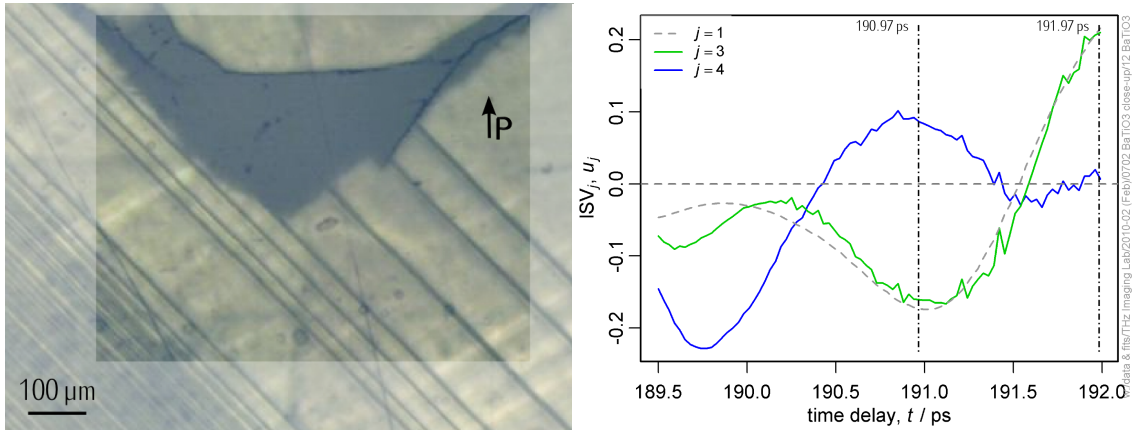
(ii) SV_1-SV_5 .



(iii) A time cut at 191.96 ps.

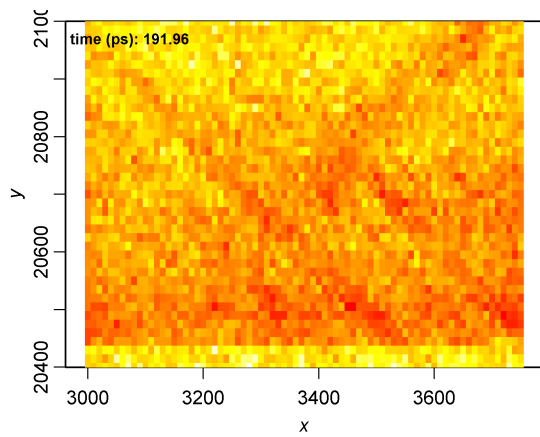
(iv) The rSV_3 .

Figure 3.27: Scanned area A (see fig. 3.24). Overview of main results.

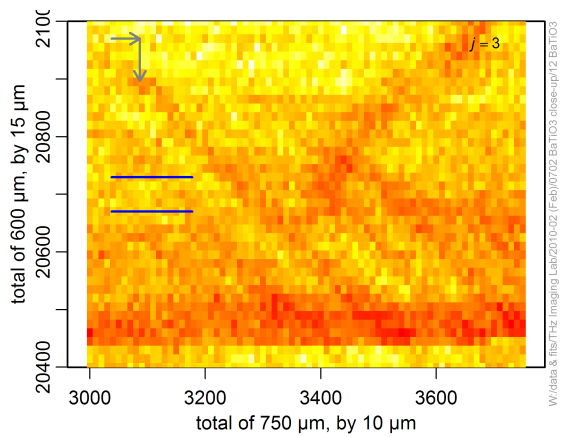


(i) A photograph of the scanned area.

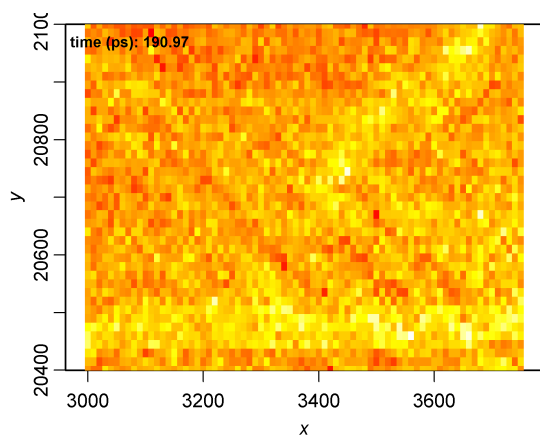
(ii) SV_1, SV_3 and SV_4 .



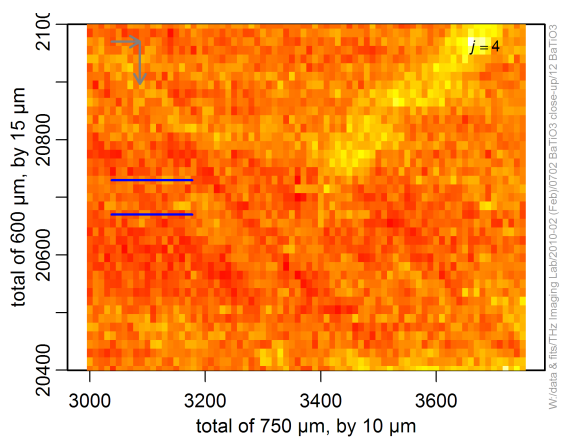
(iii) A time cut at 191.96 ps.



(iv) The rSV_3 .

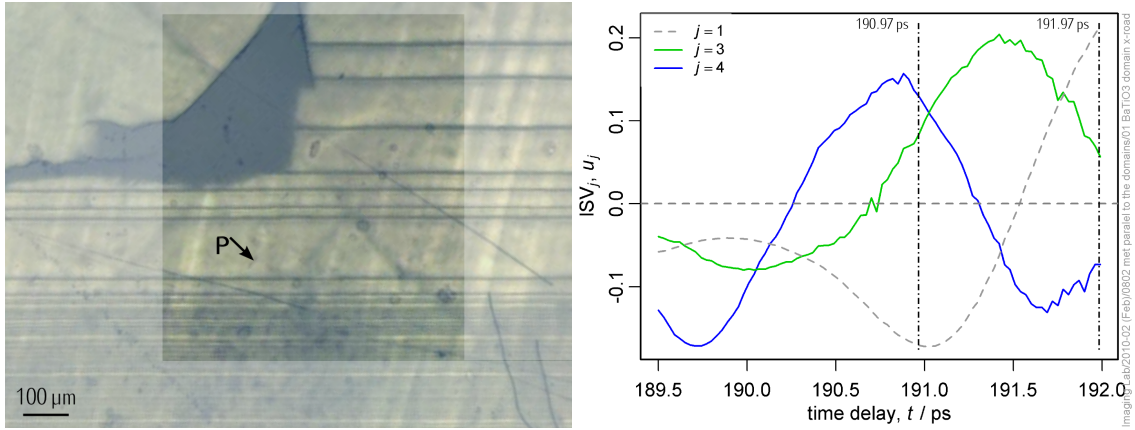


(v) A time cut at 190.97 ps.



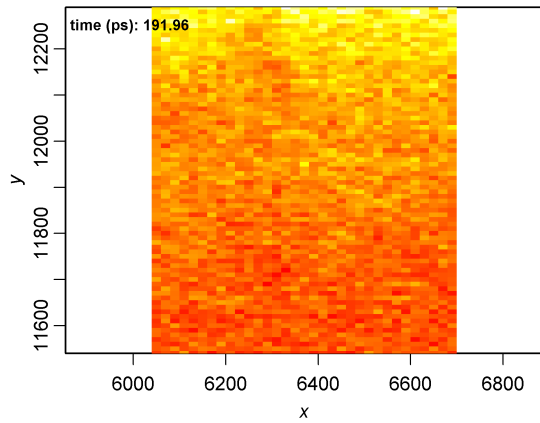
(vi) The rSV_4 .

Figure 3.28: Scanned area B (see fig. 3.24). Overview of main results.

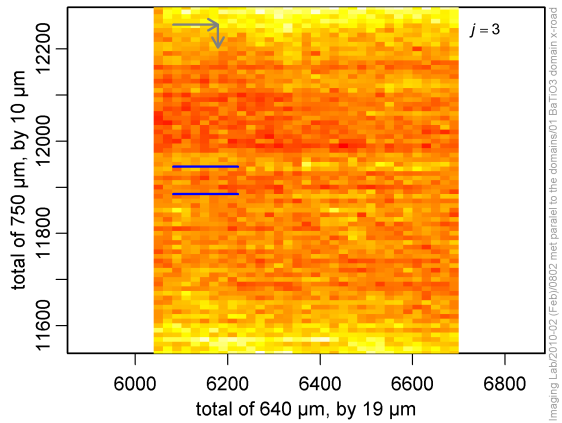


(i) A photograph of the scanned area.

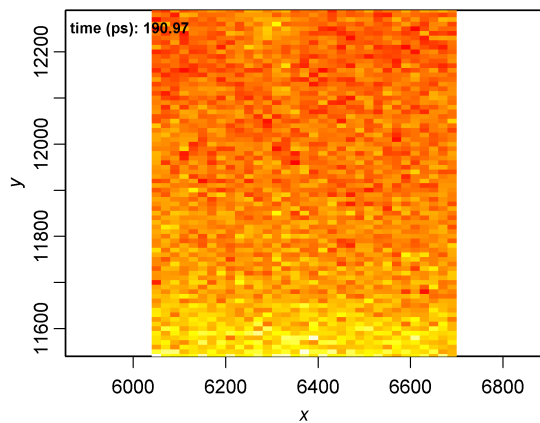
(ii) SV_1 , SV_3 and SV_4 .



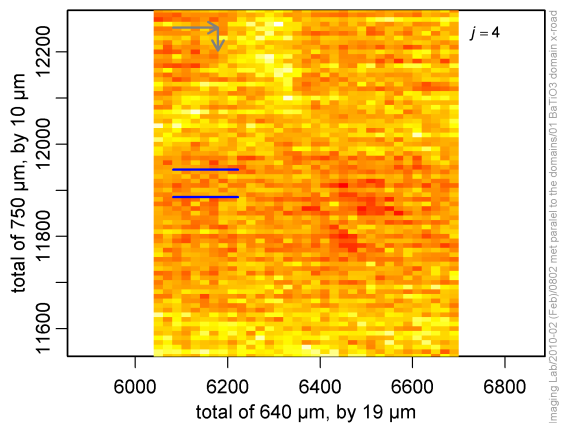
(iii) A time cut at 191.96 ps.



(iv) The rSV_3 .

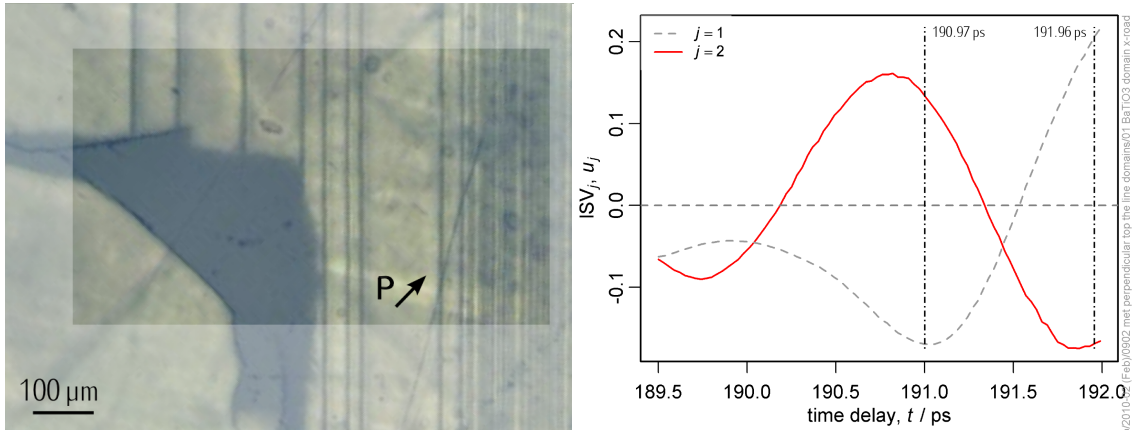


(v) A time cut at 190.97 ps.



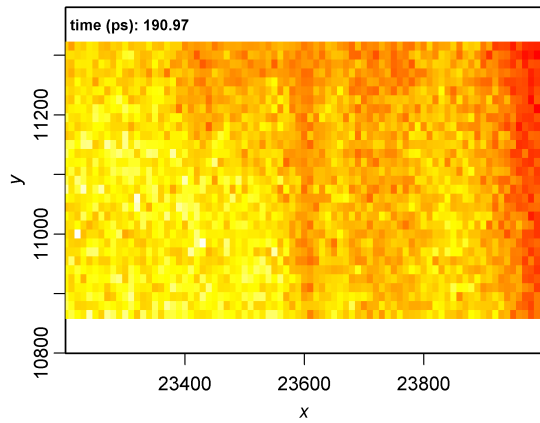
(vi) The rSV_4 .

Figure 3.29: Scanned area C (see fig. 3.24). Overview of main results.

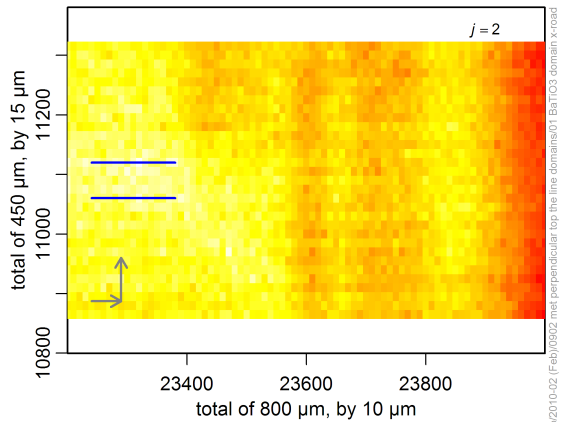


(i) A photograph of the scanned area.

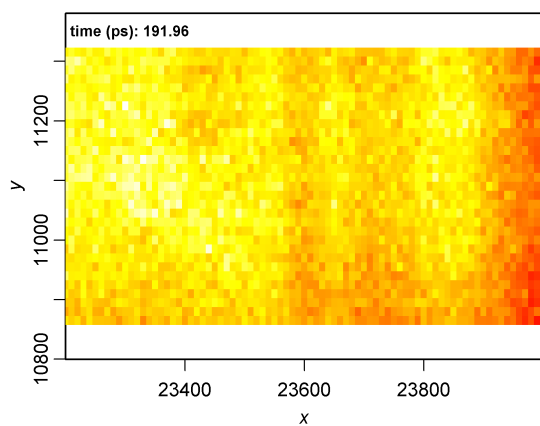
(ii) SV_1 and SV_2 .



(iii) A time cut at 190.97 ps.



(iv) The rSV_2 .



(v) A time cut at 191.96 ps.

Figure 3.30: Scanned area D (see fig. 3.24). Overview of main results.

3.7.4 Electromagnetic simulations of the domain-stripes

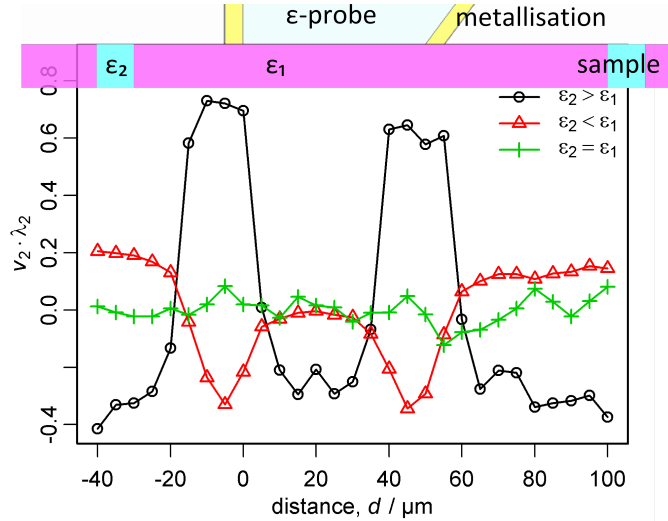


Figure 3.31: The response of a probe on a domain stripe was simulated and spatial resolution specified. The simulations were performed for different combinations of $(\epsilon_1, \epsilon_2) = \{60, 300\}$ of the domains to model various domain structures and the influence of the automeshing feature of the system. The response of the probe on a domain stripe at various positions was calculated. The functions represent one component of the pulse and the cross-correlation of these \mathbf{u}_2 components within the three sets of simulations is 0.71, 0.75 and 0.95—that counts for high cross-correlation; the cross-correlation with other components ($\mathbf{u}_3, \mathbf{u}_4$) belong to the set of $\{0.55, 0.45, \text{others} > 0.15\}$.

As in experiments presented above, the **CST MWS** simulation software environment was employed to get understanding of the underlying processes, including the fact that the spatial resolution was better than expected from the dimensions of the MDP. With respect to the computational time, a model of the MDP with the end-facet dimensions of $50 \mu\text{m} \times 100 \mu\text{m}$ and a sample in a total volume of $2 \text{mm} \times 2 \text{mm} \times 5 \text{mm}$ were simulated in the frequency range of 10 to 300 GHz using the automeshing features of the environment. The sample consisted of a large homogeneous block in which a thin stripe was placed, with permittivities ϵ_1 and ϵ_2 , respectively. The following parameters were common to three different runs: width of the end facet— $50 \mu\text{m}$, thickness of the metallisation— $5 \mu\text{m}$, thickness of the moving *domain* stripe— $10 \mu\text{m}$. The stripe was displaced across 29 equidistant positions in front of the probe. The permittivity of the probe was kept constant ($\epsilon_p = 11.4$), while those of the sample structure were altered to simulate various BaTiO_3 domain combinations and the influence of the automeshing:

$(\varepsilon_1, \varepsilon_2) = [(60, 300), (300, 60), (60, 60)]$. The changes in the waveforms analysed by SVD are shown in fig. 3.31 along with a cross-section of the MDP and the sample in the model.

A run with permittivities $\varepsilon_1 = \varepsilon_2 = 60$ was performed to estimate the error influence of the meshing system. This allowed us to estimate the error of the results obtained at other permittivity configurations to $\lesssim 10\%$.

In contradiction to expectations, the domain structure remained hidden for the MDP when optically thin stripes were embedded into the optically dense background (configuration A). That was explained by our electromagnetic transient simulations in which the permittivity of the slim and the wide stripe were altered. The A and B sample-probe configurations were simulated this way. The experimental configuration B corresponded to the permittivity combination $\varepsilon_2 > \varepsilon_1$, and the configuration A corresponded to $\varepsilon_2 < \varepsilon_1$. Analogously the simulations based on the permittivity combinations $(\varepsilon_2, \varepsilon_1) = (300, 60)$ and $(\varepsilon_2, \varepsilon_1) = (60, 300)$ did not yield the same magnitude of the contrast (fig. 3.31). In the case of an optically thin stripe surrounded by an optically dense *continuum*, the response of the near-field was weaker. We attribute our inability to resolve sample features in the configuration A to this result.

3.8 Resolution and sensitivity specification of the dual probes

The concept of the MDDP was described in section 2.1.3, where the time and space characteristics of the pulses' propagation were also elaborated in detail. In the following section, we describe the experiments and their results that characterised the resolution and sensitivity of a MDDP. Several MDDPs were created and tested for sensitivity, but only one MDDP was found displaying a cross-talk.

3.8.1 Preparing and positioning of the MDDP

The alignment of two MDPs constituting a single MDDP had to be accomplished first. A high-quality sapphire tip was chosen with the dimensions of the end facet $60\ \mu\text{m} \times 140\ \mu\text{m}$ (used at the measurements of BaTiO_3 domains, see section 3.7). A Teflon probe created by polishing (see section 2.1.2) with a sharpest possible ending (without an end facet) was selected. That Teflon probe was glued to the sapphire MDP using an alcohol-soluble polymerised BF-2 glue. It was necessary to find the optimal liquidity of the glue—a too thick solution did not

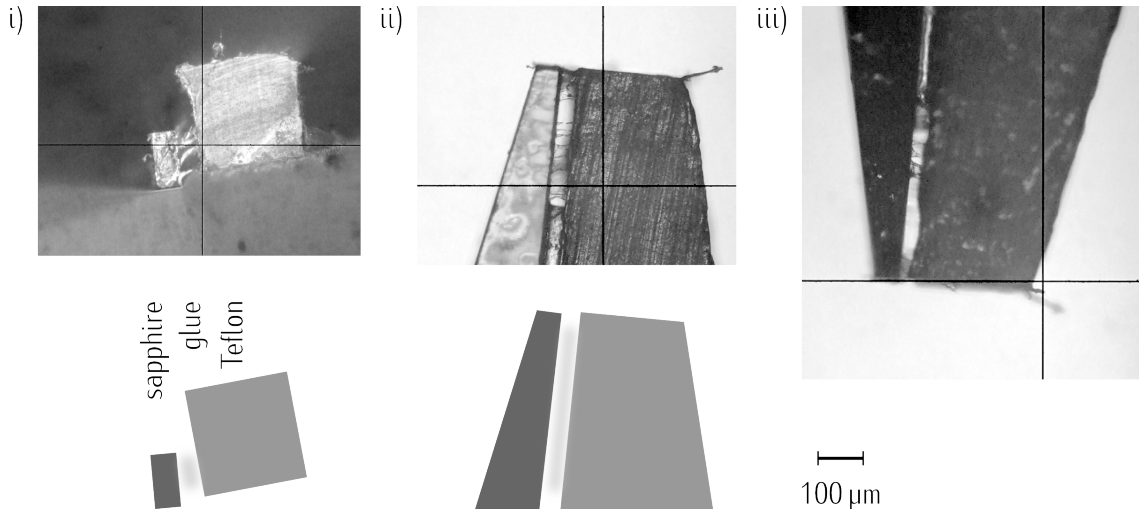


Figure 3.32: The **MDDP** consists of a **sapphire** and a **Teflon MDP** that are glued together (see also fig. 2.4). Here the structure of the **MDDP** is sketched for three views under a microscope (one top and two side views). The dimensions of the end facet of the **sapphire MDP** are $60\ \mu\text{m} \times 140\ \mu\text{m}$, those of the end facet of the **Teflon MDP** are ca. $250\ \mu\text{m} \times 250\ \mu\text{m}$ and the distance of the two **MDPs** at their very end spans from 40 to $50\ \mu\text{m}$.

allow for additional adjustment of the probes and a too liquid solution leaked out and covered the end and sides of the probes irregularly. After the glue dried completely, the sharp ending of the **Teflon** probe was cut by a razor blade to match that of the **sapphire** probe (fig. 3.32).

For an easier alignment of a **MDDP** in the **THz** beam, the length of the two **MDPs** differed by a small distance $l_{\Delta} \approx 0.5$ to $1.0\ \text{mm}$, as it was already discussed in section 2.1.3. If the length of the probes matched, the two input facets (that of **sapphire** and that of **Teflon MDP**) would create a single plane inhomogeneous mirror that would be difficult to centre in the **THz** beam. Therefore, this difference in lengths ensured a time delay of 3 to 6 ps in the input-facet reflections, and it made the positioning of the dual probe to its proper place convenient. A **THz** pulse is back-reflected to the detection system from the input facet by a coefficient R that is proportional to reflective area (while neglecting diffraction influences):

$$R = \left(\frac{n_p - n_1}{n_p + n_1} \right)^2 \propto \text{reflection area}, \quad (3.4)$$

in which n_p and n_1 are refractive indices of one of the probes and of the matter around from which the radiation is coming ($n_1 \approx 1$, for air). Reaching the optimal position of a **MDDP** in

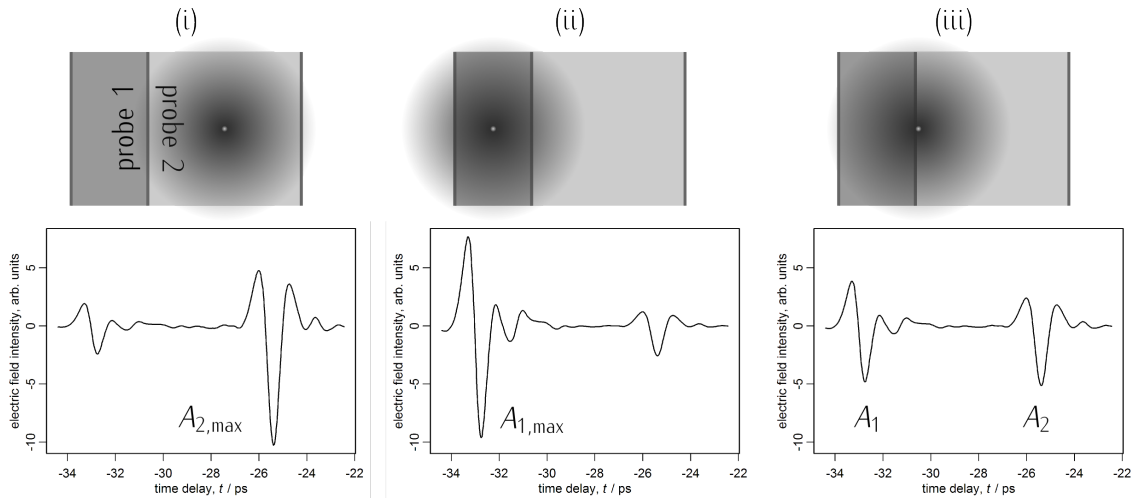


Figure 3.33: The dual probe had to be aligned in sequence of three steps. The two rectangles represent the end facets (not in plane) of a sapphire (1 mm × 2 mm) and a Teflon (2 mm × 2 mm) probe. The circle with a white dot at the centre represents the approximate area of the THz beam (FWHM ≈ 1.1 mm, see section 2.2.3 and fig. 2.11iii).

the THz beam requires two steps:

1. The MDDP has to be positioned so that the maxima for pulses reflected from the sapphire and from the Teflon input facet are reached. We denote the amplitudes for these maxima $A_{1,max}$ and $A_{2,max}$. The behaviour of the reflected THz pulses for these positions is schemed in fig. 3.33i and (ii).
2. Then the optimal position of the MDDP is for amplitudes (A_1 and A_2) of the two input-facet reflections following the relation

$$\frac{R_{MDDP1}}{R_{MDDP2}} = \frac{A_1}{A_2} \approx \frac{A_{1,max}}{A_{2,max}}. \quad (3.5)$$

In an ideal case when the input facets are much larger than the FWHM of the THz beam, the maxima would reduce to their halves in (fig. 3.33iii). This is not our case due to the limited area of the input facets. But due to the maximum energy of the THz beam concentrated within the perimeter 1.1 mm (section 2.2.3), the pulse energy is divided and reflected from the two input facets in a similar ratio.

For the locating of the cross-talking pulse one has to locate the maximum for reflection at time t_1 , the maximum for reflection at time t_2 , and that clearly defines the maximum of the position of the mid-pulse at time t_{12} (the cross-talk).

3.8.2 Scans by a dual probe with spatial resolution

Measurement on a sample with a metal–dielectric contrast (Au–LaAlO₃, see fig. 3.15) was accomplished with the above–described MDDP. From a total of ten lateral scans across the sample (fig. 3.34 on 116, top), two scans were performed to provide a calibration (data from the substrate alone were accumulated, scans *A* and *J*) and eight scans were lead through areas with metal–dielectric contrast (scans *B–I*). The measurements lasted 8 to 20 hours and were mainly scheduled overnight—it is important from the calibration point of view to have to same or at least a similar measurement conditions within the group of measurements. The lateral scans comprised 740 to 760 points in the spatial dimension (2220 to 2280 μm) times 201 to 401 points in the time–delay dimension (6 to 12 ps). The measurements datasets were then decomposed separately by the SVD process (table 2.1). Each of the decomposed scans contained 3 to 4 significant components belonging to an independent experimental feature. To pair and cluster the rSVs from different scans together, values of correlation r_p (eq. (2.18)) of all possible pairs among the first three significant components were calculated. These values were calculated at once as a correlation (similarity) matrix for all 30 rSVs (rSV₂–rSV₄). An example of the correlation matrix for the 10 rSV₂ vectors is shown in fig. 3.34. With the help of the correlation matrix of the 30 rSVs, four distinct clusters *a–d* could be defined. These four clusters represent four independent experimental features. Unfortunately, the analysis does not tell anything about the origin of these feature, this lays on the interpretation of the shapes of the rSVs. Because of its shape resembling the cross–sections of the sample, it is clear that the **cluster a** represents the components sensitive to the contrast in the sample. The calibration measurements were used to remove the background in the components of scans *E* and *F* displayed in fig. 3.35. There a photograph of the sample is placed in scale for convenient comparison. The other clusters identified in the measurements represents:

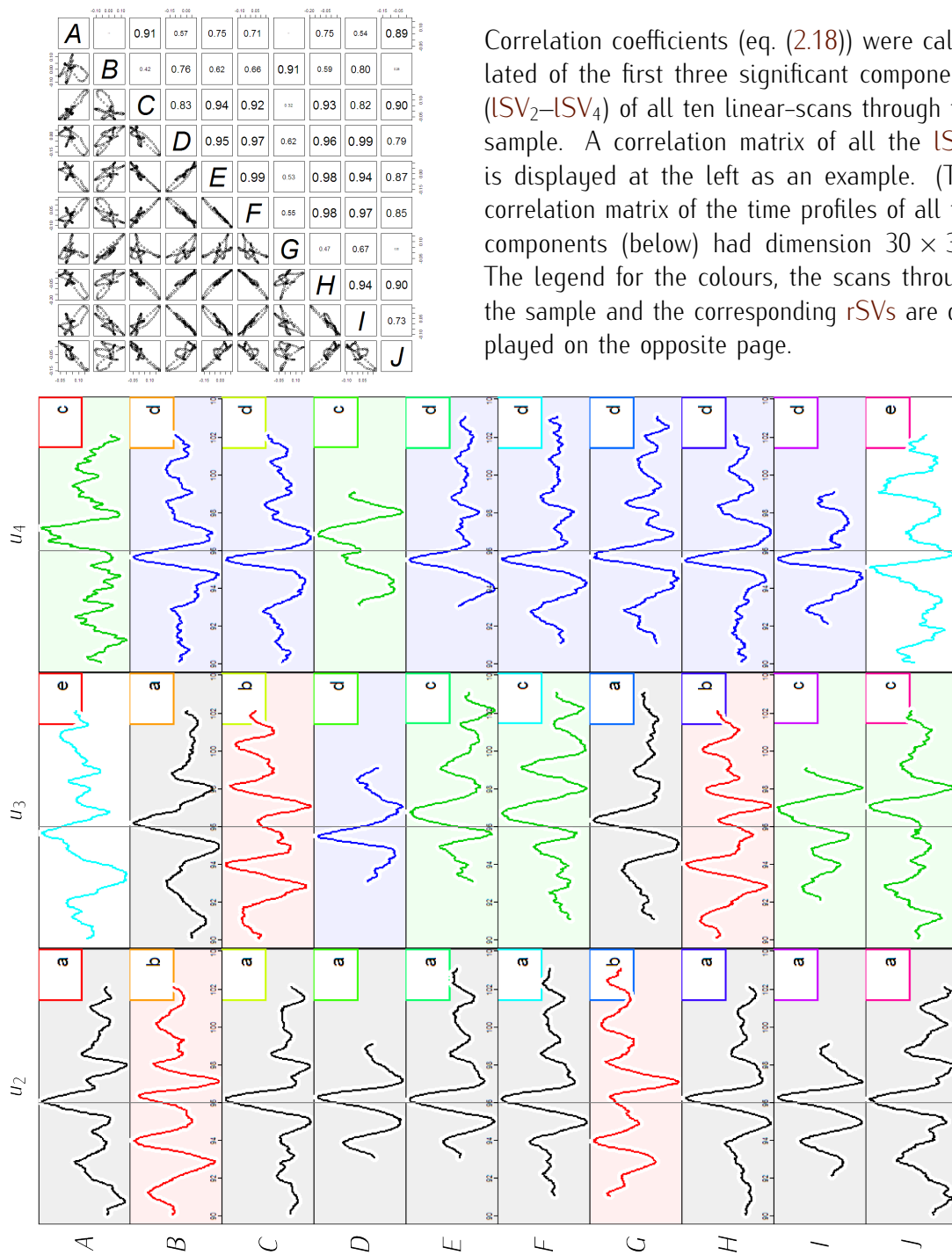
cluster b: unknown, but due to complementarity in appearance with the cluster *c*, this cluster may display the influence of the air–conditioning (too),

cluster c: the disturbance of the airflow and air–conditioning,

cluster d: the height profile of the sample or the contrast change, and

cluster e: unknown or without significant correlation.

The spacing between the end facet of the two MDPs glued together is 40 to 50 μm (fig. 3.32)—it may be introduced by the viscosity of the glue or by a tension in the Teflon probe. This distance is smaller than the dimensions of the resolved features (see v_2 and v_4 in



Correlation coefficients (eq. (2.18)) were calculated of the first three significant components (ISV_2 – ISV_4) of all ten linear-scans through the sample. A correlation matrix of all the ISV_2 is displayed at the left as an example. (The correlation matrix of the time profiles of all the components (below) had dimension 30×30 .) The legend for the colours, the scans through the sample and the corresponding $rSVs$ are displayed on the opposite page.

Figure 3.34: The time profiles (the $ISVs$, here with the x -axes in ps) of the SVD products of the linear scans over the metal–dielectric sample (fig. 3.15) were clustered using a correlation matrix (on top of the page; see the legend there, too).

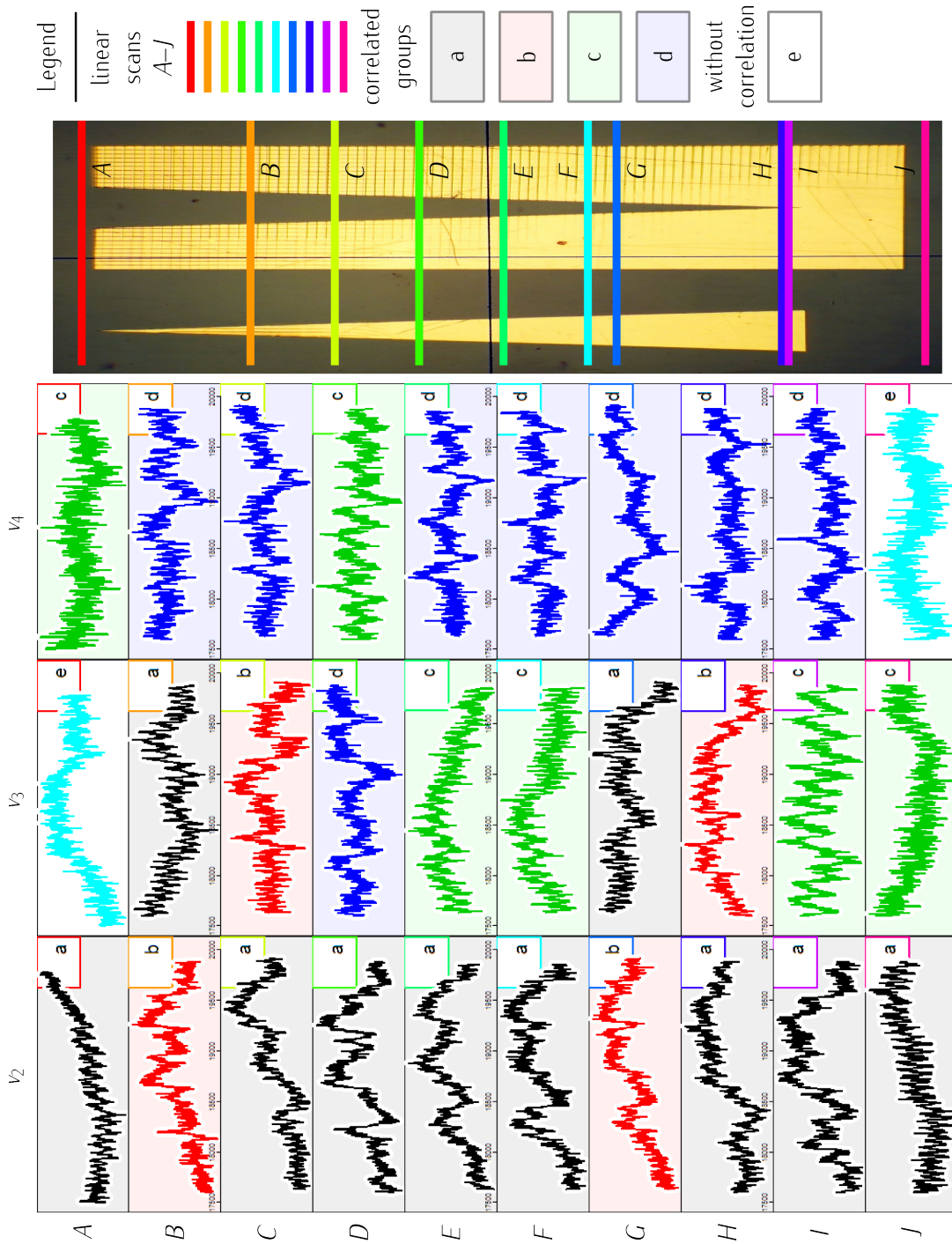


Figure 3.34: (cont.) The spatial profiles (the rSVs, here with the x-axes in μm) of the SVD products of the linear scans over the metal-dielectric sample (top) in clusters of their corresponding LSVs.

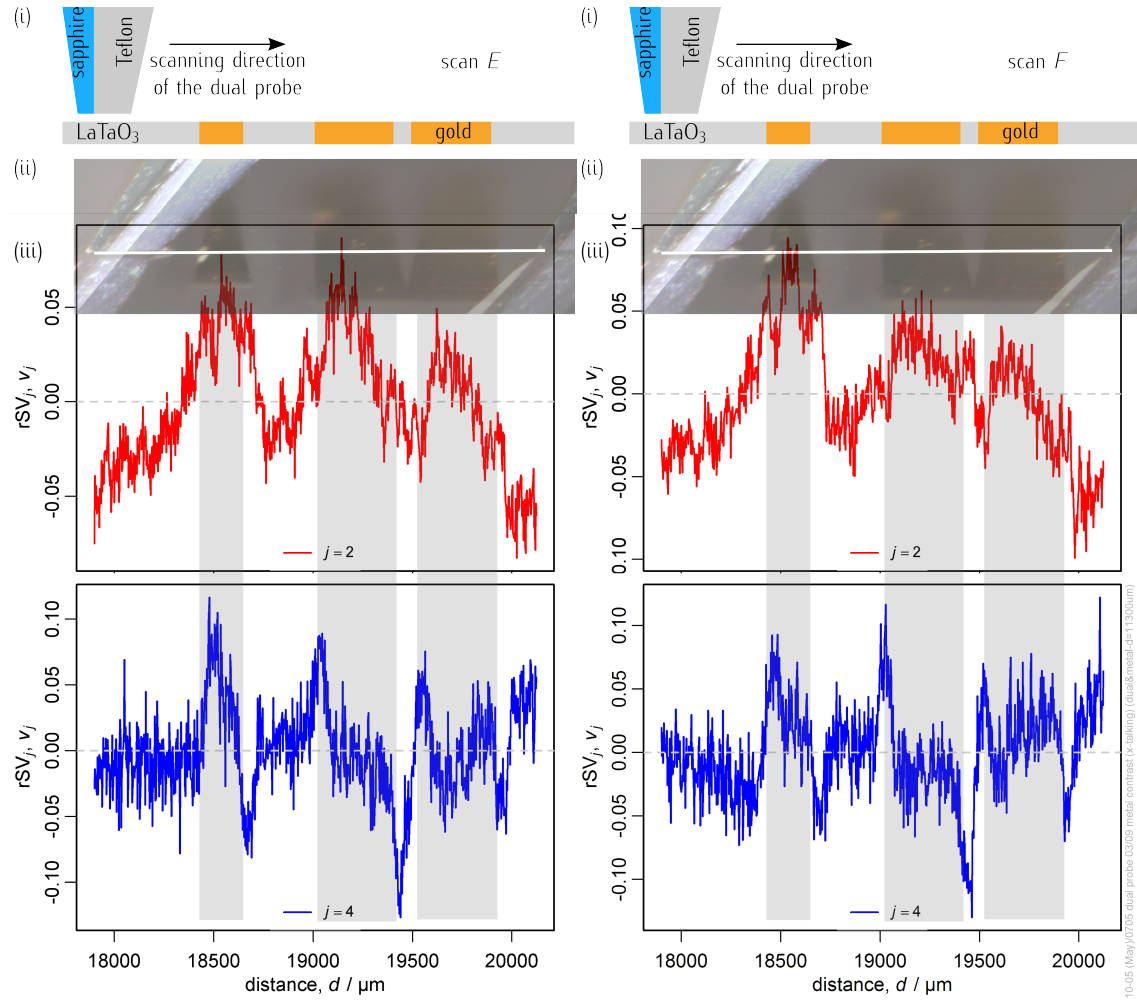
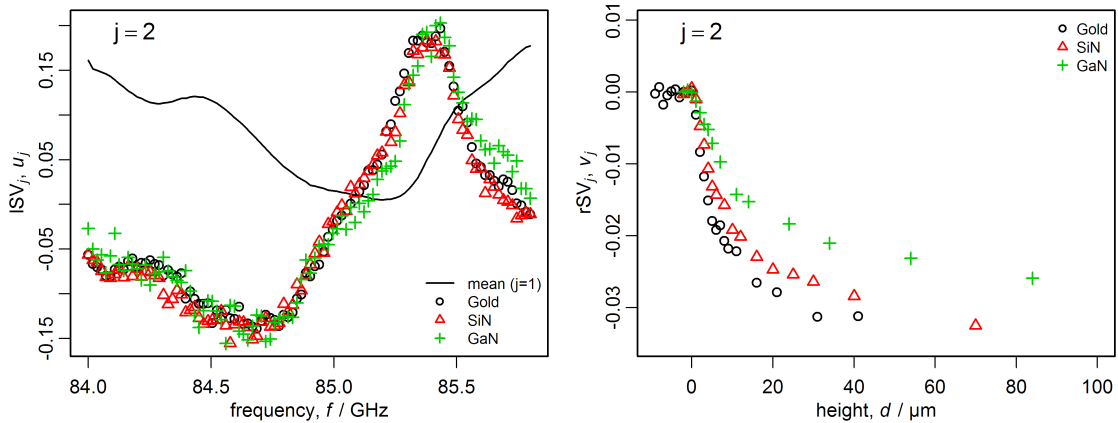


Figure 3.35: The spatial profiles of the scans E and F (iii) are superposed with the sample (ii) and its scheme (i). The widths of the metal coating at the place of the two linear scans were approximately (from left to right) $200 \mu\text{m}$, $400 \mu\text{m}$ and $400 \mu\text{m}$. The rSV_2 components were corrected by subtracting the normalised calibration scan J (e. g. $v_{2,E} \rightarrow v_{2,E} - v_{2,J} \frac{\lambda_{2,J}\lambda_{1,E}}{\lambda_{1,J}\lambda_{2,E}}$).

fig. 3.34). Thus, the unusual shape of v_4 , that resembling a derivative of a blurred step-like metal-dielectric profile in values of materials' refractive indices, is not a consequence of this gap. But such a gap is not desired in a MDDP and it might cause ghost (double) images or blurred image due to convolution of the broader sensing area and the sample features. Since the useful signal was weak, the metal-dielectric contrast low and the borders between metal and dielectric blurry, the method of the MDDP did not satisfy our expectations. But it showed its potential and with a more precise fabrication and glueing method, it might lead to better results.

3.9 Continuous-wave microwave measurements



(i) The frequency profiles of the rSV components $j = 2$ for all three samples are identical. That means they represent the same physical process.

(ii) The spatial profiles of the $j = 2$ components multiplied by the respective normalisation factor (λ_2/λ_1) were offset on the x and y -axis to share the $(x, y) = (0, 0)$ value for the position when the MDP touched the sample. The slope of the profiles differ due to different ϵ^* of the samples.

Figure 3.36: Results on height measurements in the CW-MW frequency range.

The concept of the CW-MW measurements and the setup in the frequency range 75 to 90 GHz was described in section 2.3. Here, we present only a part of the MW measurements related to our THz measurements. For this measurement we have prepared three samples: metal, undoped gallium nitride (Si_3N_4) and undoped gallium nitride (GaN) platelets (section 1.11).

The resonance frequency response was tested as a function of the sample-tip distance for these three samples. The 2nd rSV s (those displaying an exponential-like decay and thus,

belonging to the near-field) are drawn in fig. 3.36ii. The change of the resonance displays the same pattern for all three samples, see fig. 3.36i. A similar exponential-like behaviour of the near field shows up in these *CW-MW* measurements as it was in the *TD-THz* experiments section 3.6, i. e. the near field of the probe is sensitive to the presence of a sample in the similar way. Although the *CW-MW* technique does not supply information on the phase change in the measurement to clearly distinguish the complex permittivity of a sample ϵ^* , it possesses a high resolution in frequency and this way offers the ability to distinguish samples with various dielectric properties at the vicinity of the probe (as it was also demonstrated in [Berta et al., 2007; Danylyuk et al., 2007b]).

Chapter 4

Conclusions

In this work, we presented the results of our effort to exploit the possibilities offered by the near-field THz imaging technique based on a **metal-dielectric probe (MDP)**. After the initial stage when the experiment had to be set up, many improvements of the setup were made. Among these, namely we proceeded with stabilising the signal, increasing the **signal-to-noise ratio (SNR)** and implementing the method of **singular value decomposition (SVD)**. The latter enabled separating independent physical phenomena in the measured datasets and filtering external disturbances out of the signal. We have successfully employed the decomposition in various experimental configurations (fig. 3.6), which enabled us to determine the real capabilities of the technique. Our principal findings are summarised below.

Performance of probes

Although a substantial part of the generated **terahertz (THz)** radiation is propagating through the imaging probe near the location where a sample is placed (fig. 3.2i), only a small part of it adverts to the presence and properties of the sample. Therefore, the influence of the environment and that of the sample have to be separated from the acquired dataset at first. Employing a **multivariate analysis (MVA)** by using the method of **SVD** appears to be an efficient approach for identifying the small individual contributions to the experimentally obtained waveforms (section 3.4), namely the parts of the signal due to deliberately varied parameters, systematic and random errors (i. e. instability of experimental setup and noise). Distinguishing components

originating from systematic and random errors allowed us to reduce their influence and, thus, to improve the sensitivity of the experimental setup.

Structure of the EM field at the end facet of a MDP

The propagation of the **electromagnetic (EM)** field at the end of a MDP was simulated numerically by **CST MicroWave Studio® 2008 ver.06 (CST MWS)** and it was experimentally confirmed by measurements on a sample with a metal–dielectric contrast. Extremes of the E_z field-component (that along the probe axis) at the end of the probe are localised in the vicinity of the metallisation in two transversal lobes (fig. 3.14, see the 3rd column). These two localised lobes are sensitive to the change of the permittivity in the bulk of the sample as it was simulated (fig. 3.31). Other four extrema are located near the corners of the end facet, where the E_y field-component (that parallel with the metallisation on the sides) has its maxima (fig. 3.14, see the 2nd column). These extrema are sensitive to the local changes of permittivity in the plane of the sample. E. g. they are able to image areas of ferroelectric domains (see section 3.7.2, where the limit of the resolution was experimentally tested on an anisotropic sample of **barium titanate (BaTiO₃)**). The E_x field-component (that perpendicular to the metallisation on the sides) displays only one significant and broad zone close to the end facet (fig. 3.14, see the 1st column), therefore this component has no immediate effect on the measurement with high spatial resolution.

On-axis distribution of the EM field

The on-axis distribution of the field at the end of the probe was characterised by experiments with a varying sample distance from the tip, as well as by simulations (section 3.5.1). The dependence of the **right singular vectors (rSVs)** on the probe–sample distance h shows the expected behaviour. Within the probe–sample distance interval of 3000 μm studied in simulations and of ca. 200 μm examined in experiments, the amplitudes $v_j(h)$ consist of a mean, a near field and of a far field components. The exponential-like component (usually rSV_2) is the only component pertinent to the near field (fig. 3.9i) and those with oscillations belong to the far-field radiation (fig. 3.9ii). This result was not only obtained from our computer simulations but also observed in the experimental data. Due to the different frequency ranges in the simulations and

in the experiment a scaling invariant (probe distance times the mean frequency of the transient pulse) had to be employed. The good agreement between the shapes of the $v_j(h\nu_\mu)$ amplitudes obtained from experiments and simulations (fig. 3.12) shows clearly that this field distribution is a property of the near-field probe itself, and it is not significantly influenced by its deviations from ideal shape and EM characteristics.

Polarisation sensitivity of the probe

The electromagnetic field localised in the vicinity of the probe tip is well polarised (fig. 3.22), therefore characterisation of local sample anisotropy was also possible. Although the relevant amplitude $v_3(\varphi)$ is not much higher than the components corresponding to the noise floor in the experiment (by a factor of 5, see fig. 3.22i), we show that it is possible to determine the orientation of the highly anisotropic BaTiO₃ crystallographic axes from the output waveforms, i. e. the probe is sensitive to the orientation of the sample's domains. The results evidencing the sensitivity of the near-field probe with respect to local anisotropy are, to our knowledge, the first of this kind, except measurements of Gompf et al. in a continuous-wave (CW)-THz mode [Gompf et al., 2007].

This observation also brought the method a step closer to imaging applications with a high spatial resolution where the contrast among various parts of the samples is lower than that between a metal and a common dielectric. Indeed, we have shown that imaging of ferroelectric domains at the scale of tens of micrometers becomes feasible with convenient samples and probe tip dimensions (section 3.7).

Imaging of BaTiO₃ domains

We performed measurements of a domain structured BaTiO₃ sample under various angles of the polarisation of the probing field with respect to the direction of the domain walls (section 3.7). The aim was to measure the response of the metal-dielectric probe and to find the configuration with optimal sensitivity. The SVD data treatment allowed us to resolve more details and information than standalone time slices would allow (section 3.7.3). In some cases, the SVD can even allow one to define most sensitive time positions for sample scanning at a fixed time delay. Features on the sample surface with characteristic dimensions of 5 μm were resolved by a probe

with the end-facet dimensions of $60\ \mu\text{m} \times 140\ \mu\text{m}$ and employing wavelengths from 0.25 to 3 mm. We theoretically analysed the situation in all configurations and performed electromagnetic simulations to explain lower sensitivity in one of the configurations (fig. 3.31). The results of the simulations provided a qualitative agreement with our experimental observations in view of the achieved sensitivity.

Performance of the dual probe

We developed and implemented a method for fabricating MDPs from Teflon in view to construct a sapphire–Teflon metal–dielectric dual probe (MDDP) (section 2.1.3). The probe would allow us to achieve a better resolution determined by the size of the common interface of the two joined probes and to implicitly filter out the useful signal from the background (figs. 2.4 and 2.5). Although the usability of the dual probe was demonstrated on a sample with a metal–dielectric contrast (fig. 3.35), the useful signal and contrast was lower than that of the MDP.

Sensing of Mylar-covered samples

Several samples displaying distinct properties in the THz frequency range were examined by using the MDP in order to characterise the sensitivity of the probe with respect to refractive indices of the samples (section 3.6). As expected, the sensitivity to a variation in refractive index decreases with the growing refractive index (fig. 3.20, grey line, —).

Additionally, data were acquired from all the samples covered by a thin Mylar foil, and a similar tendency in contrast was observed (fig. 3.20, light-red line). That means that the samples may be distinguishable by the MDP, even if they are placed under a thin film of a transparent material. Covering by a plastic foil might be important for samples that are dangerous, unstable (e. g. chemicals or humid substances) or have a soft surface (e. g. biological samples).

Frequency resolution of the probes

We observe that it is difficult to find a correlation among amplitudes in frequency $u_j(\nu)$ in a given set of measurements, i. e. the frequency dependence of these components is yet unpredictable. In view of this observation, it appears that one can gain information about the complex space

and frequency distribution of the field at the end-facet of the probe, but imaging of a sample surface with a spectral resolution seems a hard task using this experimental technique. On the one hand, this is in contrary to expectations that a **time-domain (TD)** THz imaging employing a **MDP** could provide a full spectral and spatial characteristics of the sample. On the other hand, we have shown the power of the **SVD** in distinguishing the useful signal from the data. Therefore, one can expect that the technique would allow also imaging of samples where the contrast in complex permittivity ϵ^* is limited to a part of the spectral range employed.

Outlook

In our opinion, there are two main enhancements of the **MDP** method to achieve better performance characteristics in the light of our achievements and hurdles during the work. The one consists in reducing the end facet dimensions of the **MDP**. This project was started in **Forschungszentrum Jülich, Germany (FZJ)**, where some of the silicon probes were sharpened by using focused ion beam to achieve smaller dimensions of the end-facet width, namely lower than 100 nm [Danylyuk et al., 2007a,b]. Imaging and sensitivity experiments were conducted by Danylyuk et al. with yet unpublished results. Nevertheless, the strength of the useful signal will inevitably decrease with decreasing tip size.

The other possibility consists in reducing the dispersion of the pulses in the dielectric material of the probe. A confinement structure based on this idea was developed recently by Zhan et al., in which the radiation is confined in a construction resembling the negative of the **MDP**. In that method, two separate metal surfaces guide the THz pulses through air to a small volume in the vicinity of the sample [Zhan et al., 2010]. In contrast to our **MDP** approach, this method uses only air-guided THz pulses. This avoids both the impedance mismatch and the dispersion due to the dielectric material of the probe, and it leads to better performance characteristics.

Nomenclature

α	discrete parametre characterising a state of an experiment.
δ_{skin}	skin depth.
ε^*	complex permittivity, $\varepsilon^* = \varepsilon' + i\varepsilon''$.
ε_0	the permittivity of the vacuum, $\varepsilon_0 = 10^7 / (4\pi c_0^2)$ F m ⁻¹ = 8.854×10^{-12} F m ⁻¹ .
ε'	real part of complex permittivity, referred also as permittivity only.
ε''	imaginary part of complex permittivity, referred also as losses.
ε_{e0}	(ordinary) permittivity for polarization perpendicular to the axis of anisotropy, $\sqrt{\varepsilon_{e0}} = n_{e0}$.
ε_o	(extraordinary) permittivity for polarization parallel to the axis of anisotropy, $\sqrt{\varepsilon_o} = n_o$.
ε_r	relative permittivity.
κ	imaginary part of a complex refractive index, extinction coefficient, $\sqrt{\varepsilon''}$.
λ	wavelength, m.
λ_μ	mean (wavelength) of a frequency range, m.
μ	mean, a parameter of a distribution.
μ_0	the permeability of the vacuum, $\mu_0 = 4\pi \cdot 10^{-7}$ H m ⁻¹ $\approx 1.256\,637\,061\,4 \times 10^{-6}$ H m ⁻¹ .
μ_r	relative permeability.
ν	frequency, Hz.
ν_μ	mean (frequency) of a frequency range, Hz.
π	Ludolph's number, $\pi \approx 3.141593$.
ρ	bulk resistivity, Ω cm.
ρ_s	surface resistivity, Ω .
σ^2	variance, a parameter of a distribution.
ω	angular frequency, $\omega = 2\pi\nu$, Hz.
χ	dielectric susceptibility.

χ_{kl}	the k^{th} root of the l^{th} Bessel function $J_l(r)$.
χ_m	magnetic susceptibility.
c_0	the speed of light in the vacuum, $c_0 \approx 2.997 \times 10^8 \text{ m s}^{-1}$.
E	electric field, V m; or matrix displaying the values of the measured field.
e	Euler's number, $e \approx 2.718281828$.
e	the elementary charge, $e = 1.602\,176\,487(40) \times 10^{-19} \text{ C}$.
h	Planck constant, $h = 6.626\,068\,96(33) \times 10^{-34} \text{ J s}$.
k_B	Boltzmann constant, $k_B \approx 1.38 \times 10^{-23} \text{ J K}^{-1}$.
n	real part of a complex refractive index, referred also as refractive index only, $\sqrt{\epsilon'}$; or an integer.
\mathbb{R}	the set of all real numbers.
r_P	Pearson (product-moment) correlation coefficient, or Pearson's r .
T	temperature, K.

List of Acronyms

AFM	Atomic-Force Microscopy (or scanning force microscopy).
BaTiO ₃	Barium Titanate.
BWO	Backward-Wave Oscillator.
CAD	Computer-Aided Design.
CCD	Charge-Coupled Device.
CST MWS	CST MicroWave Studio® 2008.
CST SS	CST Studio Suite™.
CW	Continuous-Wave (radiation).
DAST	4- <i>N,N</i> -dimethylamino-4'- <i>N'</i> -methyl stilbazolium tosylate.
DNA	DeoxyriboNucleic Acid.
EM	ElectroMagnetic.
EOR	Electro-Optic Rectification.
FA	Factor Analysis.
FD	Frequency-Domain.
FEL	Free-Electron Laser.
FFT	Fast Fourier Transform.
FIR	Far-Infrared (radiation).
FIT	Finite Integration Technique.
FTIR	Fourier-Transform Infrared (spectroscopy).
FWHM	Full Width at Half Maximum.
FZJ	Forschungszentrum Jülich, Germany.
GaAs	Gallium Arsenid.
GaN	Gallium Nitride.

GHz	Gigahertz (radiation).
GUI	Graphical User Interface.
IoP	Institute of Physics of the AS CR, Prague.
IR	Infrared (radiation).
LiNbO ₃	Lithium Niobate.
LiTaO ₃	Lithium Tantalate.
ISV	left Singular Vector.
LTEM	Laser Terahertz-Emission Microscopy.
MDDP	Metal-Dielectric Dual Probe.
MDP	Metal-Dielectric Probe.
MIR	Mid-Infrared (radiation).
MVA	MultiVariate Analysis.
MW	Microwave (radiation).
Mylar	a tradename for poly(ethylene terephthalate) (PET) product.
NEP	Noise-Equivalent Power.
NIR	Near-Infrared (radiation).
PCA	Principal Components Analysis.
PEC	Perfect Electric Conductor.
Plexiglas	a trademark for poly(methyl methacrylate) (PMMA).
QCL	Quantum Cascade Laser.
rSV	right Singular Vector.
sapphire	α -Al ₂ O ₃ .
Si	Silicon.
Si ₃ N ₄	Silicon Nitride.
SiO ₂	Silicon Dioxide (silica, quartz).
SM	Singular Matrix.
SNOM	Scanning Near-field Optical Microscopy.
SNR	Signal-to-Noise Ratio.
SV	Singular Value.
SVD	Singular Value Decomposition.
TD	Time-Domain.

TDS	Time-Domain Spectroscopy.
TDTS	Time-Domain Terahertz Spectroscopy.
TE	Transverse Electric.
Teflon	a brand name for poly(tetrafluoroethylene) (PTFE).
TEM	Transverse ElectroMagnetic.
THz	Terahertz (radiation).
THz-ANSOM	(tip-enhanced) Terahertz Apertureless Near-field Optical Microscopy.
TM	Transverse Magnetic.
TPI	Terahertz-Pulse Imaging, also Terahertz Pulsed Imaging.
UV	Ultra-Violet (radiation).
WLOG	Without Loss Of Generality.
ZnTe	Zinc Telluride.

Bibliography

- D. Abbott and X. Zhang. Scanning the issue: T-ray imaging, sensing, and refection. *Proceedings of the IEEE*, 95(8):1509–1513, Aug. 2007. [10.1109/JPROC.2007.900894](https://doi.org/10.1109/JPROC.2007.900894). 2, 19
- M. Abo-Bakr, J. Feikes, K. Holldack, P. Kuske, W. B. Peatman, U. Schade, G. Wüstefeld, and H. Hübers. Brilliant, coherent Far-Infrared (THz) synchrotron radiation. *Physical Review Letters*, 90(9):094801(4pp), Mar. 2003. [10.1103/PhysRevLett.90.094801](https://doi.org/10.1103/PhysRevLett.90.094801). 6
- A. J. L. Adam, N. C. van der Valk, and P. C. Planken. Measurement and calculation of the near field of a terahertz apertureless scanning optical microscope. *Journal of the Optical Society of America B*, 24(5):1080–1090, May 2007. [10.1364/JOSAB.24.001080](https://doi.org/10.1364/JOSAB.24.001080). 31
- A. J. L. Adam, J. M. Brok, P. C. M. Planken, M. A. Seo, and D. S. Kim. THz near-field measurements of metal structures. *Comptes Rendus Physique*, 9(2):161–168, Mar. 2008a. [10.1016/j.crhy.2007.07.005](https://doi.org/10.1016/j.crhy.2007.07.005). 30, 31
- R. Adam, J. Guillet, L. Chusseau, A. Penarier, P. Nouvel, J. Torres, T. Grosjean, L. Billot, F. Baida, and D. Charrat. Near-field polarization-selective inspection of a bow-tie antenna and a passive radial polarizer at sub-THz frequencies. In *EOS Annual Meeting 2008*, 3, Paris, France, Oct. 2008b. ISBN 978-3-00-024188-8. 31, 32
- R. Adam, L. Chusseau, T. Grosjean, A. Penarier, J. Guillet, and D. Charrat. Near-field wire-based passive probe antenna for the selective detection of the longitudinal electric field at terahertz frequencies. *Journal of Applied Physics*, 106(7):073107(7pp), Oct. 2009. [10.1063/1.3236665](https://doi.org/10.1063/1.3236665). 28
- B. S. Alexandrov, V. Gelev, A. R. Bishop, A. Usheva, and K. . Rasmussen. DNA breathing dynamics in the presence of a terahertz field. *Physics Letters A*, 374(10):1214–1217, Feb. 2010. [10.1016/j.physleta.2009.12.077](https://doi.org/10.1016/j.physleta.2009.12.077). 4
- American National Standards Institute and Laser Institute of America. *ANSI Z136.1-2007 American National Standard for Safe Use of Lasers*. American National Standards Institute and Laser Institute of America, Orlando, FL, USA, revision of ANSI z136.1-1993. edition, 2007. ISBN 978-0-912035-65-9. DOI:[10.1109/IEEESTD.2006.99501](https://doi.org/10.1109/IEEESTD.2006.99501). 4
- C. D. Amico, A. Houard, S. Akturk, Y. Liu, J. L. Bloas, M. Franco, B. Prade, A. Couairon, V. T. Tikhonchuk, and A. Mysyrowicz. Forward THz radiation emission by femtosecond filamentation in gases: theory and experiment. *New Journal of Physics*, 10(1):013015(18pp), 2008. [10.1088/1367-2630/10/1/013015](https://doi.org/10.1088/1367-2630/10/1/013015). 8
- D. Andreuccetti. An internet resource for the calculation of the dielectric properties of body tissues in the frequency range 10Hz - 100 GHz, Aug. 2007. URL <http://niremf.ifac.cnr.it/tissprop/>. 4
- AS CAMO Software. Unscrambler®, 2008. URL <http://www.camo.com>. 73
- E. A. Ash and G. Nicholls. Super-resolution aperture scanning microscope. *Nature*, 237(5357):510–512, June 1972. [10.1038/237510a0](https://doi.org/10.1038/237510a0). 32
- G. A. Askar'yan. Cerenkov radiation and transition radiation from electromagnetic waves. *Soviet Physics Journal of Experimental and Theoretical Physics*, 15(5):943–946, 1962a. 8
- G. A. Askar'yan. Excess negative charge of an electron-photon shower and its coherent radio emission. *Soviet Physics Journal of Experimental and Theoretical Physics*, 14(2):441–443, 1962b. 8

- G. A. Askar'yan. Acceleration of charged particles by ultrashort light pulses which create a space-charge front at the axis of a channel in a medium. *Journal of Experimental and Theoretical Physics Letters*, 52(6):323–326, Sept. 1990. 8
- D. H. Auston. Subpicosecond electro-optic shock waves. *Applied Physics Letters*, 43(8):713–715, 1983. 10.1063/1.94486. 8
- D. H. Auston and M. C. Nuss. Electrooptical generation and detection of femtosecond electrical transients. *IEEE Journal of Quantum Electronics*, 24(2):184–197, 1988. 10.1109/3.114. 9, 14, 15
- D. H. Auston, K. P. Cheung, and P. R. Smith. Picosecond photoconducting hertzian dipoles. *Applied Physics Letters*, 45(3):284–286, 1984a. 10.1063/1.95174. 10, 11, 19
- D. H. Auston, K. P. Cheung, J. A. Valdmanis, and D. A. Kleinman. Cherenkov radiation from femtosecond optical pulses in electro-optic media. *Physical Review Letters*, 53(16):1555–1558, Oct. 1984b. 10.1103/PhysRevLett.53.1555. 8, 15
- M. Awad, M. Nagel, and H. Kurz. Terahertz near-field imaging with tapered sommerfeld-wire waveguides. In *IRMMW-THz 2009*, Busan, Korea, Sept. 2009. 28
- M. M. Awad and R. A. Chevillet. Transmission terahertz waveguide-based imaging below the diffraction limit. *Applied Physics Letters*, 86(22):221107(3pp), May 2005. 10.1063/1.1942637. 32, 33
- C. A. Balanis. *Antenna Theory: Analysis and Design, 2nd Edition*. Wiley, 2nd edition, May 1996. ISBN 0471592684. 31
- D. H. Barker, D. T. Hodges, and T. S. Hartwick. Far infrared imagery. *Proceedings of SPIE*, 67(44):27–34, 1975. 19
- E. A. Barry, V. N. Sokolov, K. W. Kim, and R. J. Trew. Large-signal analysis of terahertz generation in submicrometer GaN diodes. *IEEE Sensors Journal*, 10(3):765–771, Mar. 2010. 10.1109/JSEN.2009.2038132. 8
- J. Barta, M. Manela, and R. Fischer. Si₃N₄ and Si₂N₂O for high performance radomes. *Materials Science and Engineering*, 71:265–272, May 1985. 10.1016/0025-5416(85)90236-8. 38
- M. Bass, P. A. Franken, J. F. Ward, and G. Weinreich. Optical rectification. *Physical Review Letters*, 9(11):446–449, Dec. 1962. 10.1103/PhysRevLett.9.446. 9
- M. Bass, E. W. . V. Stryland, D. R. . Williams, and W. L. . Wolfe, editors. *Handbook of Optics vol1 : Fundamentals, Techniques, and Design*, volume 1. McGraw-Hill Professional, 2 edition, Sept. 1994. ISBN 0-07-047740-X. 22, 23, 36
- R. M. Bell, Y. Koren, and C. Volinsky. Chasing \$1,000,000: How we won the netflix progress prize. *Statistical Computing and Statistical Graphics Newsletter*, 18(2):4–12, Dec. 2007. 64
- R. M. Bell, J. Bennet, Y. Koren, and C. Volinsky. The million dollar programming prize, May 2009. URL <http://spectrum.ieee.org/computing/software/the-million-dollar-programming-prize>. 64
- D. P. Berrar, W. Dubitzky, and M. Granzow. *A Practical Approach to Microarray Data Analysis*. Springer, 1st edition, Dec. 2002. ISBN 1402072600. 62, 63
- E. Berry. Risk perception and safety issues. *Journal of Biological Physics*, 29(2):263–267, June 2003. 10.1023/A:1024461313486. 4
- E. Berry, G. C. Walker, A. J. Fitzgerald, N. N. Zinov'ev, M. Chamberlain, S. W. Smye, R. E. Miles, and M. A. Smith. Do in vivo terahertz imaging systems comply with safety guidelines? *Journal of Laser Applications*, 15(3):192–198, 2003. 10.2351/1.1585079. 4
- M. Berta and F. Kadlec. Near-field terahertz imaging of ferroelectric domains in barium titanate. *Phase Transitions*, in review:1–9, 2010. xv, 99
- M. Berta, F. Kadlec, S. Danylyuk, and N. Klein. Terahertz near-field spectroscopy and microscopy based on metal-dielectric antenna. In *2007 Joint 32nd International Conference on Infrared and Millimeter Waves and 15th International Conference on Terahertz Electronics*, volume 1–2, pages 487–488, Cardiff, UK, Sept. 2007.

- IEEE. ISBN 978-1-4244-1438-3. 119
- M. Berta, P. Kužel, and F. Kadlec. Study of responsiveness of near-field terahertz imaging probes. *Journal of Physics D: Applied Physics*, 42(15):155501(6pp), Aug. 2009. 10.1088/0022-3727/42/15/155501. xv, 99
- H. A. Bethe. Theory of diffraction by small holes. *Physical Review*, 66(7-8):163–182, Oct. 1944. 10.1103/PhysRev.66.163. 31
- E. Betzig and J. K. Trautman. Near-field optics: Microscopy, spectroscopy, and surface modification beyond the diffraction limit. *Science*, 257(5067):189–195, July 1992. 10.1126/science.257.5067.189. 28
- P. R. Bevington and D. K. Robinson. *Data Reduction and Error Analysis for the Physical Sciences*. McGraw-Hill, 3rd edition, Aug. 2003. ISBN 0-07-247227-8. 63
- L. J. Bignell and R. A. Lewis. Reflectance studies of candidate THz emitters. *Journal of Materials Science: Materials in Electronics*, 20(S1):326–331, Feb. 2008. 10.1007/s10854-008-9608-2. 9
- M. Bilodeau and D. Brenner. *Theory of Multivariate Statistics*. Springer Texts in Statistics. Springer, 1st edition, Aug. 1999. ISBN 0387987398. 63, 64
- J. R. Birch, J. D. Dromey, and J. Lesurf. The optical constants of some common low-loss polymers between 4 and 40 μ m. *Infrared Physics*, 21(4):225–228, July 1981. 0.1016/0020-0891(81)90053-1. 37, 38
- A. Bitzer and M. Walther. Terahertz near-field imaging of metallic subwavelength holes and hole arrays. *Applied Physics Letters*, 92(23):231101 (3pp), June 2008. 10.1063/1.2936303. 30
- A. Bitzer, H. Merbold, A. Thoman, T. Feurer, H. Helm, and M. Walther. Terahertz near-field imaging of electric and magnetic resonances of a planar metamaterial. *Optics Express*, 17(5):3826–3834, Mar. 2009. 10.1364/OE.17.003826. 30
- J. E. Bjarnason, T. L. J. Chan, A. W. M. Lee, M. A. Celis, and E. R. Brown. Millimeter-wave, terahertz, and mid-infrared transmission through common clothing. *Applied Physics Letters*, 85(4):519(3pp), 2004. 10.1063/1.1771814. 20
- R. Bogue. Terahertz imaging: a report on progress. *Sensor Review*, 29(1):6–12, 2009. 10.1108/02602280910926706. 5, 19
- A. Borak. Toward bridging the terahertz gap with silicon-based lasers. *Science*, 308(5722):638–639, Apr. 2005. 10.1126/science.1109831. 7
- M. Born and E. Wolf. *Principles of Optics: Electromagnetic Theory of Propagation, Interference and Diffraction of Light*. Cambridge University Press, 7th edition, Oct. 1999. ISBN 0521642221. 5, 22, 23
- T. W. D. Bosq, R. E. Peale, A. Weeks, P. Jardine, M. Stewart, J. Grantham, D. Dillery, D. Lee, D. Muh, and G. Boreman. Terahertz and millimeter wave transmission of soils. In R. J. Hwu and K. J. Linden, editors, *Terahertz and Gigahertz Electronics and Photonics IV*, volume 5727, pages 1–11, San Jose, CA, USA, Mar. 2005. SPIE. 10.1117/12.584925. 20
- T. W. D. Bosq, R. E. Peale, and G. D. Boreman. Terahertz/millimeter wave characterizations of soils for mine detection: Transmission and scattering. *International Journal of Infrared and Millimeter Waves*, 29(8):769–781, June 2008. 10.1007/s10762-008-9376-3. 20
- E. Budiarto, N. Pu, S. Jeong, and J. Bokor. Near-field propagation of terahertz pulses from a large-aperture antenna. *Optics Letters*, 23(3):213–215, Feb. 1998. 10.1364/OL.23.000213. 26
- F. Buergens, R. Kersting, and H. Chen. Terahertz microscopy of charge carriers in semiconductors. *Applied Physics Letters*, 88(11):112115(3pp), Mar. 2006. 10.1063/1.2186743. 28
- F. Buergens, G. Acuna, C. H. Lang, S. I. Potrebic, S. Manus, and R. Kersting. Shear force control for a terahertz near field microscope. *Review of Scientific Instruments*, 78(11):113701(6pp), Nov. 2007. 10.1063/1.2804077. 28
- T. Buma and T. B. Norris. Time reversal three-dimensional imaging using single-cycle terahertz pulses. *Applied Physics Letters*, 84(12):2196(3pp), 2004. 10.1063/1.1686896. 20
- M. B. Byrne, J. Cunningham, K. Tych, A. D. Burnett, M. R. Stringer, C. D. Wood, L. Dazhang, M. Lachab, E. H.

- Linfield, and A. G. Davies. Terahertz vibrational absorption spectroscopy using microstrip-line waveguides. *Applied Physics Letters*, 93(18):182904–3, Nov. 2008. 10.1063/1.3013349. 86
- J. E. Carlstrom and J. Zmuidzinas. Millimeter and submillimeter techniques. In W. R. Stone, editor, *Reviews of Radio Science 1993–1995*, pages 839–882. Oxford U. Press, Oxford, 1996. 5
- G. L. Carr, M. C. Martin, W. R. McKinney, K. Jordan, G. R. Neil, and G. P. Williams. High-power terahertz radiation from relativistic electrons. *Nature*, 420(6912):153–156, Nov. 2002. 10.1038/nature01175. 6
- G. L. Carr, M. C. Martin, W. R. McKinney, K. Jordan, G. R. Neil, and G. P. Williams. Very high power THz radiation sources. *Journal of Biological Physics*, 29(2):319–325, June 2003. 10.1023/A:1024481818029. 6
- L. W. Casperson. Gaussian beams in hollow metal waveguides. *Journal of the Optical Society of America A*, 17(6): 1115–1123, 2000. 10.1364/JOSAA.17.001115. 55
- R. B. Cattell. The scree test for the number of factors. *Multivariate Behavioral Research*, 1(2):245–276, Apr. 1966. 10.1207/s15327906mbr0102.10. 71
- P. A. Cerenkov. Visible emission of clean liquids by action of γ radiation. *Doklady Akademii Nauk SSSR*, 2: 451–454, 1934. 8
- J. M. Chamberlain, N. N. Zinovev, A. J. Fitzgerald, E. Berry, G. C. Walker, J. W. Handley, M. A. Smith, and R. E. Miles. What constitutes a useful and meaningful terahertz image? In J. M. Chamberlain, P. Harrison, R. E. Miles, A. G. Davies, E. H. Linfield, and S. Withington, editors, *THz 2002: IEEE Tenth International Conference on Terahertz Electronics Proceedings*, pages 81–84, Cambridge, England, Sept. 2002. IEEE. ISBN 0-7803-7630-7. 20
- W. L. Chan, J. Deibel, and D. M. Mittleman. Imaging with terahertz radiation. *Reports on Progress in Physics*, 70: 1325–1379, June 2007. 10.1088/0034-4885/70/8/R02. 19
- H. Chen, R. Kersting, and G. C. Cho. Terahertz imaging with nanometer resolution. *Applied Physics Letters*, 83 (15):3009–3011, Oct. 2003. 10.1063/1.1616668. 28
- Q. Chen, Z. Jiang, G. X. Xu, and X. Zhang. Near-field terahertz imaging with a dynamic aperture. *Optics Letters*, 25(15):1122–1124, Aug. 2000. 10.1364/OL.25.001122. 30
- G. C. Cho, H. Chen, S. Kraatz, N. Karpowicz, and R. Kersting. Apertureless terahertz near-field microscopy. *Semiconductor Science and Technology*, 20:S286–S292, June 2005. 10.1088/0268-1242/20/7/020. 28
- M. Cho. *Two-Dimensional Optical Spectroscopy*. CRC Press, 1st edition, June 2009. ISBN 1420084291. 46
- S. L. Chuang, S. Schmitt-Rink, B. I. Greene, P. N. Saeta, and A. F. J. Levi. Optical rectification at semiconductor surfaces. *Physical Review Letters*, 68(1):102–105, Jan. 1992. 10.1103/PhysRevLett.68.102. 9
- L. Chusseau. Photomixing and near field THz microscopy. In *4e Journées TéraHertz*, Bombannes, May 2007. 9, 32, 33
- Coherent Inc. Stabilized integrated FIR (THz) laser system, Mar. 2007. URL http://www.coherent.com/downloads/SIFIR50_DSrevB.pdf. 5
- D. J. Cook and R. M. Hochstrasser. Intense terahertz pulses by four-wave rectification in air. *Optics Letters*, 25(16): 1210–1212, 2000. 10.1364/OL.25.001210. 8
- G. Coombe. An introduction to principal component analysis and online singular value decomposition 1 abstract, 2006. URL <http://citeseerx.ist.psu.edu/viewdoc/summary?doi=10.1.1.101.4690>. 63
- D. Courjon. Near-Field imaging: Some attempts to define an apparatus function. *Journal of Microscopy*, 177(Part 2):180–185, Feb. 1995. 25
- D. Courjon. *Near-Field Microscopy and Near-Field Optics*. World Scientific Publishing Company, Mar. 2003. ISBN 186094258X. 5, 21, 22, 23, 26
- D. Courjon and C. Bainier. Near field microscopy and near field optics. *Reports on Progress in Physics*, 57(10): 989–1028, Oct. 1994. 10.1088/0034-4885/57/10/002. 26

- D. Crawley, C. Longbottom, V. P. Wallace, B. Cole, D. Arnone, and M. Pepper. Three-dimensional terahertz pulse imaging of dental tissue. *Journal of Biomedical Optics*, 8(2):303–307, Apr. 2003. 10.1117/1.1559059. 20
- CrysTec GmbH. Sapphire probe manufacturer, Mar. 2010. URL <http://www.crystec.de/contact-e.html>. Köpenicker Str. 325 D-12555 Berlin Germany. 42, 43
- CST. CST MicroWave studio®, 2008. URL <http://www.cst.com/>. 60
- G. L. Dakovski, B. Kubera, and J. Shan. Localized terahertz generation via optical rectification in ZnTe. *Journal of the Optical Society of America B*, 22(8):1667–1670, Aug. 2005. 10.1364/JOSAB.22.001667. 9, 30
- S. Danylyuk, U. Poppe, F. Kadlec, P. Kužel, M. Berta, N. Klein, R. C. Pullar, N. M. Alford, and H. Romanus. Broadband microwave-to-terahertz near-field imaging. Annual selected research reports 2006, Forschungszentrum Jülich, Germany, Jülich, Germany, June 2007a. 124
- S. Danylyuk, U. Poppe, F. Kadlec, P. Kužel, M. Berta, N. Klein, R. C. Pullar, N. M. Alford, and H. Romanus. Broadband microwave-to-terahertz near-field imaging. In *Microwave Symposium, 2007. IEEE/MTT-S International*, volume 1–6 of *IEEE/MTT-S International Microwave Symposium Digest*, pages 1383–1386, Honolulu, HI, June 2007b. IEEE. ISBN 1-4244-0688-9. 10.1109/MWSYM.2007.380471. 57, 75, 119, 124
- P. Dean, M. U. Shaikat, S. P. Khanna, S. Chakraborty, M. Lachab, A. Burnett, G. Davies, and E. H. Linfield. Absorption-sensitive diffuse reflection imaging of concealed powders using a terahertz quantum cascade laser. *Optics Express*, 16(9):5997–6007, Apr. 2008. 10.1364/OE.16.005997. 20
- M. C. Decretion and F. E. Gardiol. Simple nondestructive method for the measurement of complex permittivity. *Instrumentation and Measurement, IEEE Transactions on*, 23(4):434–438, 1974. 10.1109/TIM.1974.4314329. 26
- A. J. den Dekker and A. van den Bos. Resolution: a survey. *Journal of the Optical Society of America A*, 14(3): 547–557, Mar. 1997. 10.1364/JOSAA.14.000547. 23
- D. A. Depireux, J. Z. Simon, D. J. Klein, and S. A. Shamma. Spectro-Temporal response field characterization with dynamic ripples in ferret primary auditory cortex. *Journal of Neurophysiology*, 85(3):1220–1234, Mar. 2001. 64
- S. L. Dexheimer. *Terahertz Spectroscopy: Principles and Applications*. Optical Science and Engineering. CRC, 1st edition, Dec. 2007. ISBN 0849375258. 2, 16
- G. T. di Francia. Super-gain antennas and optical resolving power. *Il Nuovo Cimento (Suppl.)*, 9(3):426–438, Mar. 1952. 10.1007/BF02903413. 24
- C. Dodson, M. J. Fitch, R. Osiander, and J. B. Spicer. Terahertz imaging for anti-personnel mine detection. In R. J. Hwu, D. L. Woolard, and M. J. Rosker, editors, *Proceedings of SPIE*, pages 85–93, Orlando, FL, USA, June 2005. SPIE. 10.1117/12.604751. 20
- T. D. Dorney, D. M. Mittleman, and R. G. Baraniuk. Material parameter estimation with terahertz time-domain spectroscopy. *Journal of the Optical Society of America A*, 18(7):1562–1571, July 2001. 1364/JOSAA.18.001562. 19
- D. Dragoman and M. Dragoman. Time-frequency signal processing of terahertz pulses. *Applied Optics*, 43(19): 3848–3853, July 2004. 10.1364/AO.43.003848. 16
- A. Dreyhaupt, S. Winnerl, T. Dekorsy, and M. Helm. High-intensity terahertz radiation from a microstructured large-area photoconductor. *Applied Physics Letters*, 86(12):121114 (3pp), Mar. 2005. 10.1063/1.1891304. 11, 50
- A. Dreyhaupt, S. Winnerl, M. Helm, and T. Dekorsy. Optimum excitation conditions for the generation of high-electric-field terahertz radiation from an oscillator-driven photoconductive device. *Optics Letters*, 31(10): 1546–1548, May 2006. 10.1364/OL.31.001546. 11
- S. Dudorov. *Rectangular dielectric waveguide and its optimal transition to a metal waveguide*. PhD, Helsinki University of Technology Radio Laboratory, June 2002. 41, 42, 55
- I. Duling and D. Zimdars. Terahertz imaging: Revealing hidden defects. *Nature Photonics*, 3(11):630–632, Nov. 2009. 10.1038/nphoton.2009.206. 20

- U. Dürig, D. W. Pohl, and F. Rohner. Near-field optical-scanning microscopy. *Journal of Applied Physics*, 59(10): 3318–3327, May 1986. 10.1063/1.336848. 28
- A. Y. Elezzabi and M. R. Freeman. Ultrafast magneto-optic sampling of picosecond current pulses. *Applied Physics Letters*, 68(25):3546(3pp), 1996. 10.1063/1.116632. 15
- J. Faist, F. Capasso, D. L. Sivco, C. Sirtori, A. L. Hutchinson, and A. Y. Cho. Quantum cascade laser. *Science*, 264 (5158):553–556, Apr. 1994. 10.1126/science.264.5158.553. 7
- C. Fattinger and D. Grischkowsky. Point source terahertz optics. *Applied Physics Letters*, 53(16):1480–1482, Oct. 1988. 10.1063/1.99971. 15
- B. Ferguson, S. Wang, D. Gray, D. Abbot, and X. C. Zhang. T-ray computed tomography. *Optics Letters*, 27(15): 1312–1314, Aug. 2002. 10.1364/OL.27.001312. 20
- A. J. Fitzgerald, E. Berry, N. N. Zinovev, G. C. Walker, M. A. Smith, and J. M. Chamberlain. An introduction to medical imaging with coherent terahertz frequency radiation. *Phys. Med. Biol.*, 47(7):R67–R84, Mar. 2002. 10.1088/0031-9155/47/7/201. 19
- V. A. Flyagin, A. G. Luchinin, and G. S. Nusinovich. A submillimeter gyrotron with a pulsed magnetic field. *International Journal of Infrared and Millimeter Waves*, 3(6):765–769, Nov. 1982. 10.1007/BF01008642. 6
- V. A. Flyagin, A. G. Luchinin, and G. S. Nusinovich. Submillimeter-wave gyrotrons: Theory and experiment. *International Journal of Infrared and Millimeter Waves*, 4(4):629–637, July 1983. 10.1007/BF01009400. 6
- C. Gabriel, S. Gabriel, and E. Corthout. The dielectric properties of biological tissues: I. literature survey. *Physics in Medicine and Biology*, 41(11):2231–2249, 1996a. 10.1088/0031-9155/41/11/001. 4
- S. Gabriel, R. W. Lau, and C. Gabriel. The dielectric properties of biological tissues: II. measurements in the frequency range 10Hz to 20 GHz. *Physics in Medicine and Biology*, 41(11):2251–2269, 1996b. 10.1088/0031-9155/41/11/002. 4
- S. Gabriel, R. W. Lau, and C. Gabriel. The dielectric properties of biological tissues: III. parametric models for the dielectric spectrum of tissues. *Physics in Medicine and Biology*, 41(11):2271–2293, 1996c. 10.1088/0031-9155/41/11/003. 4
- G. Gallot, A. Podzorov, and A. Wojdyla. Beam waist measurement for terahertz time domain experiments. In *IRMMW-THz 2009*, Busan, Korea, Sept. 2009. 52
- A. Garcia-Etxarri, I. Romero, F. J. G. de Abajo, R. Hillenbrand, and J. Aizpurua. Influence of the tip in near-field imaging of nanoparticle plasmonic modes: Weak and strong coupling regimes. *Physical Review B: Condensed Matter and Materials Physics*, 79(12):125439–5, Mar. 2009. 10.1103/PhysRevB.79.125439. 28
- P. A. George, J. Strait, J. Dawlaty, S. Shivaraman, M. Chandrashekar, F. Rana, and M. G. Spencer. Ultrafast optical-pump terahertz-probe spectroscopy of the carrier relaxation and recombination dynamics in epitaxial graphene. *Nano Letters*, 8(12):4248–4251, Nov. 2008. 10.1021/nl8019399. 16
- Gigaoptics GmbH. Tera-SED: large-area terahertz emitter, Nov. 2009. URL http://www.gigaoptics.de/products_tera-sed.html. 12
- N. S. Ginzburg, N. I. Zaitsev, E. V. Ilyakov, I. S. Kulagin, Y. V. Novozhilova, R. M. Rozenhal, and A. S. Sergeev. Observation of chaotic dynamics in a powerful backward-wave oscillator. *Physical Review Letters*, 89(10): 108304(4pp), Sept. 2002. 10.1103/PhysRevLett.89.108304. 6
- G. Golub and C. Reinsch. Singular value decomposition and least squares solutions. *Numerische Mathematik*, 14 (5):403–420, Apr. 1970. 10.1007/BF02163027. 68
- G. H. Golub and C. F. van Loan. *Matrix Computations*. The Johns Hopkins University Press, third edition edition, Oct. 1996. ISBN 0801854148. 66, 67
- B. Gompf, M. Gerull, T. Müller, and M. Dressel. THz-micro-spectroscopy with backward-wave oscillators. *Infrared Physics & Technology*, 49(1–2):128–132, Sept. 2006. 10.1016/j.infrared.2006.01.021. 6, 20

- B. Gompf, N. Gebert, H. Heer, and M. Dressel. Polarization contrast terahertz-near-field imaging of anisotropic conductors. *Applied Physics Letters*, 90(8):082104(3pp), 2007. 10.1063/1.2680016. 122
- GovTrack.us and Civic Impulse, LLC. The political spectrum, June 2010. URL <http://www.govtrack.us/congress/spectrum.xpd>. 64
- J. P. Grant, R. N. Clarke, G. T. Symm, and N. M. Spyrou. A critical study of the open-ended coaxial line sensor technique for RF and microwave complex permittivity measurements. *Journal of Physics E: Scientific Instruments*, 22(9):757–770, 1989. 10.1088/0022-3735/22/9/015. 56
- J. Greffet and R. Carminati. Image formation in near-field optics. *Progress in Surface Science*, 56(3):133–237, Nov. 1997. 10.1016/S0079-6816(98)00004-5. 25
- Z. S. Gribnikov, R. R. Bashirov, and V. V. Mitin. Negative effective mass mechanism of negative differential drift velocity and terahertz generation. *IEEE Journal of Selected Topics in Quantum Electronics*, 7(4):630–640, Aug. 2001. 10.1109/2944.974235. 8
- D. J. Griffiths and R. College. *Introduction To Electrodynamics*. Prentice Hall, 1999. ISBN 0-13-805326-X. 42
- D. Grischkowsky, S. R. Keiding, M. van Exter, and C. Fattinger. Far-infrared time-domain spectroscopy with terahertz beams of dielectrics and semiconductors. *Journal of the Optical Society of America B*, 7(10):2006–2015, Oct. 1990. 10.1364/JOSAB.7.002006. 3, 37, 38, 40
- A. Gürtler, C. Winnewisser, H. Helm, and P. U. Jepsen. Terahertz pulse propagation in the near field and the far field. *Journal of the Optical Society of America A*, 17(1):74–83, Jan. 2000. 10.1364/JOSAA.17.000074. 11
- J. F. Hair, W. C. Black, B. J. Babin, and R. E. Anderson. *Multivariate Data Analysis*. Prentice Hall, 7 edition, Feb. 2009. ISBN 0138132631. 63, 65
- M. Halpern, H. P. Gush, E. Wishnow, and V. D. Cosmo. Far infrared transmission of dielectrics at cryogenic and room temperatures: Glass, fluorogold, eccosorb, stycast, and various plastics. *Applied Optics*, 25(4):565–570, Feb. 1986. 10.1364/AO.25.000565. 20, 37
- S. Hampshire. Silicon nitride ceramics – review of structure, processing and properties. *Journal of Achievements in Materials and Manufacturing Engineering*, 24(1):43–50, Sept. 2007. 38
- P. Y. Han and X. C. Zhang. Coherent, broadband midinfrared terahertz beam sensors. *Applied Physics Letters*, 73(21):3049–3051, Nov. 1998. 10.1063/1.122668. 10
- P. Y. Han, M. Tani, F. Pan, and X. Zhang. Use of the organic crystal DAST for terahertz beam applications. *Optics Letters*, 25(9):675–677, May 2000. 10.1364/OL.25.000675. 10
- P. Y. Han, M. Tani, M. Usami, S. Kono, R. Kersting, and X. Zhang. A direct comparison between terahertz time-domain spectroscopy and far-infrared fourier transform spectroscopy. *Journal of Applied Physics*, 89(4):2357–2359, Feb. 2001. 10.1063/1.1343522. 6
- W. Härdle and Z. Hlávka. *Multivariate Statistics : Exercises and Solutions*. Springer, 1st edition, July 2007. ISBN 0387707840. 64
- W. Härdle and L. Simar. *Applied multivariate statistical analysis*. Springer, 2nd edition, Sept. 2007. ISBN 3540722432. 64
- S. A. Harmon and R. A. Cheville. Part-per-million gas detection from long-baseline THz spectroscopy. *Applied Physics Letters*, 85(11):2128(3pp), 2004. 10.1063/1.1788896. 17
- T. S. Hartwick, D. T. Hodges, D. H. Barker, and F. B. Foote. Far infrared imagery. *Applied Optics*, 15(8):1919–1922, Aug. 1976. 10.1364/AO.15.001919. 19
- T. Hattori, K. Ohta, R. Rungsawang, and K. Tukamoto. Phase-sensitive high-speed THz imaging. *Journal of Physics D: Applied Physics*, 37(5):770–773, 2004. 10.1088/0022-3727/37/5/020. 33
- S. Haykin. *Adaptive Filter Theory*. Prentice Hall, 3rd edition, Sept. 2001. ISBN 0130901261. 62, 72

- Z. S. Hegedus and V. Sarafis. Superresolving filters in confocally scanned imaging systems. *Journal of the Optical Society of America A*, 3(11):1892–1896, Nov. 1986. 10.1364/JOSAA.3.001892. 24
- E. R. Henry, J. Hofrichter, L. Brand, and M. L. Johnson. Singular value decomposition: Application to analysis of experimental data. *Methods in Enzymology*, 210:129–192, 1992. 10.1016/0076-6879(92)10010-B. 64
- H. R. Hertz. *Electric waves: being researches on the propagation of electric action with finite velocity through space*. Cornell University Library, Jan. 1893. ISBN 1429740361. 10
- R. Hillenbrand. Near-field characterization of photonic nanostructures: From hot spot imaging to superlens studies. In *Photonic Metamaterials: From Random to Periodic*, page WB2. Optical Society of America, 2007a. 28
- R. Hillenbrand. Scattering-type near-field microscopy: From nanoscale infrared material recognition to superlens studies. In *Lasers and Electro-Optics/Pacific Rim 2007, CLEO/Pacific Rim 2007. Conference on*, pages 1–2, Seoul, Aug. 2007b. Optical Society of America. ISBN 978-1-4244-1173-3. 10.1109/CLEOPR.2007.4391104. 28
- F. Hindle, C. Yang, G. Mouret, A. Cuisset, R. Bocquet, J. Lampin, K. Blary, E. Peytavit, T. Akalin, and G. Ducournau. Recent developments of an opto-electronic THz spectrometer for high-resolution spectroscopy. *Sensors*, 9(11):9039–9057, Nov. 2009. 10.3390/s91109039. 5
- O. Hirsch, P. Alexander, and L. Gladden. Techniques for cancellation of interfering multiple reflections in terahertz time-domain measurements. *Microelectronics Journal*, 39(5):841–848, May 2008. 10.1016/j.mejo.2008.01.001. 19
- M. Hoffmann. *Novel techniques in THz-time-domain-spectroscopy: A comprehensive study of technical improvements to THz-TDS*. PhD, FakultÄat fÄur Mathematik und Physik der Albert-Ludwigs-UniversitÄat Freiburg im Breisgau, May 2006. 16
- M. C. Hoffmann, J. Hebling, H. Y. Hwang, K. Yeh, and K. A. Nelson. Impact ionization in InSb probed by terahertz pump—terahertz probe spectroscopy. *Physical Review B*, 79(16):161201(4pp), Apr. 2009a. 10.1103/PhysRevB.79.161201. 17
- M. C. Hoffmann, J. Hebling, H. Y. Hwang, K. Yeh, and K. A. Nelson. THz-pump/THz-probe spectroscopy of semiconductors at high field strengths. *Journal of the Optical Society of America B*, 26(9):A29–A34, 2009b. 10.1364/JOSAB.26.000A29. 17
- L. Hogben. *Handbook of Linear Algebra*. Chapman and Hall/CRC, 1 edition, Nov. 2006. ISBN 1584885106. 68
- B. B. Hu and M. C. Nuss. Imaging with terahertz waves. *Optics Letters*, 20(16):1716–1718, 1995. 10.1364/OL.20.001716. 19, 21
- A. J. Huber, F. Keilmann, J. Wittborn, J. Aizpurua, and R. Hillenbrand. Terahertz near-field nanoscopy of mobile carriers in single semiconductor nanodevices. *Nano Letters*, 8(11):3766–3770, Nov. 2008. 10.1021/nl802086x. 28
- S. Hunsche, M. Koch, I. Brener, and M. C. Nuss. Near-field THz optics. In *Lasers and Electro-Optics Society Annual Meeting, 1997. LEOS '97 10th Annual Meeting. Conference Proceedings., IEEE*, volume 2, pages 368–369, San Francisco, CA, USA, 1997. 10.1109/LEOS.1997.645471. 26
- S. Hunsche, M. Koch, I. Brener, and M. C. Nuss. THz near-field imaging. *Optics Communications*, 150(1–6):22–26, May 1998. 10.1016/S0030-4018(98)00044-3. 26, 28, 32
- J. S. Hwang and K. I. Lin. Characteristics of terahertz radiation and its applications in imaging and material science. *Research Express*, 1(7):9–13, Oct. 2007. 1
- IEEE International Committee on Electromagnetic Safety and Institute of Electrical and Electronics Engineers and IEEE-SA Standards Board and IEEE Xplore (Online service). *IEEE Standard for Safety Levels With Respect to Human Exposure to Radio Frequency Electromagnetic Fields, 3 kHz to 300 GHz (C95.1-2005)*. Institute of Electrical and Electronics Engineers, New York, N.Y., USA, 2006. ISBN 0-7381-4835-0. DOI:10.1109/IEEESTD.2006.99501. 4
- International Advisory Committee. Base annual report to international advisory committee. Technical report, Department of the Air Force – Air force Research Laboratory and World Health Organisation Collaborating Center on the Biological Effects of Electromagnetic Radiation, June 2006. 4

- International Commission on Non-Ionising Radiation Protection (ICNIRP). Guidelines on limiting exposure to time-varying electric, magnetic, and electromagnetic fields (up to 300 GHz). *Health Physics*, 74(4):494–522, Apr. 1998. 4
- International Commission on Non-Ionising Radiation Protection (ICNIRP). *Exposure to high frequency electromagnetic fields, biological effects and health consequences (100 kHz–300 GHz) – Review of the Scientific Evidence and Health Consequences*. International Commission on Non-Ionising Radiation Protection, Munich, 2009. ISBN 978–3–934994–10–2. 4
- J. R. Janesick and M. Blouke. Scientific charge-coupled devices: Past, present, & future. *Optics and Photonics News*, 6(4):16–20, Apr. 1995. 10.1364/OPN.6.4.000016. 61
- L. Jelínek and L. Pekárek. Informace NRL č. 16/2000 pro neionizující elektromagnetická pole a záření; elektromagnetické pole (0Hz – 300 GHz) – stav k 1. lednu 2009, 2009. URL http://www.szu.cz/uploads/documents/cpl/NRL_Eletromag/NRL_16.pdf. 4
- P. U. Jepsen, R. H. Jacobsen, and S. R. Keiding. Generation and detection of terahertz pulses from biased semiconductor antennas. *Journal of the Optical Society of America B*, 13(11):2424–2436, Nov. 1996a. 10.1364/JOSAB.13.002424. 15
- P. U. Jepsen, C. Winnewisser, M. Schall, V. Schyja, S. R. Keiding, and H. Helm. Detection of THz pulses by phase retardation in lithium tantalate. *Physical Review E*, 53(4):R3052–R3056, Apr. 1996b. 10.1103/PhysRevE.53.R3052. 14
- Z. Jiang, X. G. Xu, and X. Zhang. Improvement of terahertz imaging with a dynamic subtraction technique. *Applied Optics*, 39(17):2982–2987, June 2000. 10.1364/AO.39.002982. 30, 33
- Y. Jin, G. Kim, S. Jeon, and J. Kim. Rotary optical delay line for high speed scanning of terahertz pulse. In *2008 33rd International Conference on Infrared, Millimeter and Terahertz Waves*, pages 1–2, Pasadena, CA, Sept. 2008. ISBN 978–1–4244–2119–0. 10.1109/ICIMW.2008.4665666. 17
- G. K. Johnsen, O. G. Martinsen, and S. Grimnes. Estimation of in vivo water content of the stratum corneum from electrical measurements. *The Open Biomedical Engineering Journal*, 3(5):8–12, Apr. 2009. 10.2174/1874120700903010008. 4
- M. Johnston. Bridging the terahertz gap with novel sources and sensors. *SPIE Newsroom*, page (3pp), Apr. 2006. 10.1117/2.1200603.0108. 5
- M. Johnston, D. Whittaker, A. Corchia, A. Davies, and E. Linfield. Simulation of terahertz generation at semiconductor surfaces. *Physical Review B*, 65(16):165301(8pp), Mar. 2002. 10.1103/PhysRevB.65.165301. 10
- Y. M. Jung. Principal component analysis based two-dimensional correlation spectroscopy for noise filtering effect. *Vibrational Spectroscopy*, 36(2):267–270, Dec. 2004. 10.1016/j.vibspec.2003.11.019. 64
- U. Kaatze. The dielectric properties of water in its different states of interaction. *Journal of Solution Chemistry*, 26(11):1049–1112, Nov. 1997. 10.1007/BF02768829. 16
- F. Kadlec, P. Kužel, and J. L. Coutaz. Optical rectification at metal surfaces. *Optics Letters*, 29(22):2674–2676, Nov. 2004. 10.1364/OL.29.002674. 10
- F. Kadlec, P. Kuzel, and J. L. Coutaz. Study of terahertz radiation generated by optical rectification on thin gold films. *Optics Letters*, 30(11):1402–1404, June 2005. 10.1364/OL.30.001402. 10
- F. Kadlec, M. Berta, P. Kužel, F. Lopot, and V. Polakovič. Assessing skin hydration status in haemodialysis patients using terahertz spectroscopy: a pilot/feasibility study. *Phys. Med. Biol.*, 53(24):7063–7071, Dec. 2008. 10.1088/0031–9155/53/24/004. 17, 76
- D. W. Kammler. *A First Course in Fourier Analysis*. Cambridge University Press, 2007. ISBN 978–0–511–37689–4. 17
- G. Kantorowicz and P. Palluel. Backward wave oscillators (Chap. 4). In K. Button, editor, *Infrared and Millimeter Waves*, volume 1. Academic Press, 1979. 6

- J. Kauppinen and J. Partanen. *Fourier Transforms in Spectroscopy*. Wiley Publishing, Inc., 1 edition, 2001. ISBN 3-527-60029-9. 17
- A. Kaw and E. E. Kalu. *Numerical Methods with Applications: Abridged*. <http://www.autarkaw.com>, 2008. 66
- K. Kawase, J. ichi Shikata, and H. Ito. Terahertz wave parametric source. *Journal of Physics D: Applied Physics*, 34(3):R1–R14, Jan. 2002. 10.1088/0022-3727/35/3/201. 13
- K. Kawase, Y. Ogawa, H. Minamide, and H. Ito. Terahertz parametric sources and imaging applications. *Semiconductor Science and Technology*, 20:S258 – S265, June 2005. 10.1088/0268-1242/20/7/017. 20
- F. Keilmann. FIR microscopy. *Infrared Physics & Technology*, 36(1):217–224, Jan. 1995. 10.1016/1350-4495(94)00066-T. 32
- F. Keilmann and R. Hillenbrand. Near-field microscopy by elastic light scattering from a tip. *Philosophical Transactions of the Royal Society A: Physical, Mathematical and Engineering Sciences*, 362(1817):787–805, Feb. 2004. 10.1098/rsta.2003.1347. 28
- G. Kim, S. Jeon, J. Kim, and Y. Jin. Terahertz pulse detection using rotary optical delay line. *Japanese Journal of Applied Physics*, 46(11):7332–7335, Nov. 2007. 10.1143/JJAP.46.7332. 17
- M. F. Kimmitt. Reststrahlen to T-Rays—100 years of terahertz radiation. *Journal of Biological Physics*, 29(2):77–85, June 2003. 10.1023/A:1024498003492. 3
- P. Kinsler and W. T. Wenckebach. Hot-hole lasers in III–V semiconductors. *Journal of Applied Physics*, 90(4):1692–1697, 2001. 10.1063/1.1384492. 7
- T. Kiwa, M. Tonouchi, M. Yamashita, and K. Kawase. Laser terahertz-emission microscope for inspecting electrical faults in integrated circuits. *Optics Letters*, 28(21):2058–2060, Nov. 2003. 10.1364/OL.28.002058. 31
- G. Klatt, R. Gebis, C. Janke, T. Dekorsy, and A. Bartels. Rapid-scanning terahertz precision spectrometer with more than 6 THz spectral coverage. *Optics Express*, 17(25):22847–22854, Dec. 2009. 10.1364/OE.17.022847. 17
- N. Klein, P. Lahl, U. Poppe, F. Kadlec, and P. Kužel. A metal-dielectric antenna for terahertz near-field imaging. *Journal of Applied Physics*, 98(1):014910(5pp), July 2005. 10.1063/1.1978972. xv, 32, 39, 40, 74
- H. Kliem and S. Holten. Dielectric permittivity of Si₃N₄ and SiO₂ increased by electrode profile and material. In *1999 Annual Report Conference on Electrical Insulation and Dielectric Phenomena (Cat. No.99CH36319)*, volume 1, pages 70–73, Austin, TX, USA, Oct. 1999. ISBN 0-7803-5414-1. 10.1109/CEIDP.1999.804595. 38
- B. Knoll and F. Keilmann. Near-field probing of vibrational absorption for chemical microscopy. *Nature*, 399(6732):134–137, May 1999. 10.1038/20154. 28
- M. Koch, S. Hunsche, P. Schuacher, M. C. Nuss, J. Feldmann, and J. Fromm. THz-imaging: a new method for density mapping of wood. *Wood Science and Technology*, 32(6):421–427, Dec. 1998. 10.1007/BF00702799. 20
- S. Komiyama and S. Kuroda. Far-infrared laser oscillation in p-Ge. *Solid State Communications*, 59(3):167–172, July 1986. 10.1016/0038-1098(86)90202-4. 7
- S. Kono, M. Tani, and K. Sakai. Coherent detection of mid-infrared radiation up to 60 THz with an LT-GaAs photoconductive antenna. *IEE Proceedings - Optoelectronics*, 149(3):105–109, June 2002. 10.1049/ip-opt:20020262. 12
- A. Korenstein-Ilan, A. Barbul, P. Hasin, A. Eliran, A. Gover, and R. Korenstein. Terahertz radiation increases genomic instability in human lymphocytes. *Radiation Research*, 170(2):224–234, Aug. 2008. 10.1667/RR0944.1. 4
- G. Kozlov and A. Volkov. Coherent source submillimeter wave spectroscopy (Chapter 3). In G. Grüner, editor, *Millimeter and Submillimeter Wave Spectroscopy of Solids*, number 74 in Topics in Applied Physics, pages 51–109. Springer-Verlag Telos, 1 edition, Nov. 1998. ISBN 3540628606. 6
- S. Krishnamurthy, M. T. Reiten, S. A. Harmon, and R. A. Cheville. Characterization of thin polymer films using terahertz time-domain interferometry. *Applied Physics Letters*, 79(6):875(3pp), 2001. 10.1063/1.1389823. 37

- T. T. L. Kristensen, W. Withayachumnankul, P. U. Jepsen, and D. Abbott. Modeling terahertz heating effects on water. *Optics Express*, 18(5):4727–4739, Mar. 2010. 10.1364/OE.18.004727. 4
- J. Krupka. Frequency domain complex permittivity measurements at microwave frequencies. *Measurement Science and Technology*, 17(6):R55–R70, June 2006. 10.1088/0957-0233/17/6/R01. 56
- P. Kužel. PKGraph, 2010. URL kuzel@fzu.cz. 50
- P. Kužel and J. Petzelt. Time-resolved terahertz transmission spectroscopy of dielectrics. *Ferroelectrics*, 239(1):79–86, Feb. 2000. 10.1080/00150190008213308. 16
- Y. Kuznetsova, A. Neumann, and S. R. Brueck. Imaging interferometric microscopy—approaching the linear systems limits of optical resolution. *Optics Express*, 15(11):6651–6663, May 2007. 10.1364/OE.15.006651. 25
- L. N. Large and H. Hill. A compact pulsed gas laser for the far infrared. *Applied Optics*, 4(5):625–626, May 1965. 10.1364/AO.4.000625. 7
- M. R. Leahy-Hoppa, M. J. Fitch, X. Zheng, L. M. Hayden, and R. Oslander. Wideband terahertz spectroscopy of explosives. *Chemical Physics Letters*, 434:227 – 230, Jan. 2007. 10.1016/j.cplett.2006.12.015. 20
- R. Lecaque, S. Grésillon, N. Barbey, R. Peretti, J. Rivoal, and C. Boccara. THz near-field optical imaging by a local source. *Optics Communications*, 262(1):125–128, Jan. 2006. 10.1016/j.optcom.2005.12.054. 30
- R. Lecaque, S. Grésillon, and C. Boccara. THz emission microscopy with sub-wavelength broadband source. *Optics Express*, 16(7):4731–4738, Mar. 2008. 10.1364/OE.16.004731. 30
- S. W. Lee, J. W. Hong, M. Y. Wye, J. H. Kim, H. J. Kang, and Y. S. Lee. Surface modification and adhesion improvement of PTFE film by ion beam irradiation. *Nuclear Instruments and Methods in Physics Research Section B: Beam Interactions with Materials and Atoms*, 219–220:963–967, June 2004. 10.1016/j.nimb.2004.01.197. 44
- Y. Lee. *Principles of Terahertz Science and Technology*. Lecture Notes in Physics. Springer, 1st edition, Dec. 2008. ISBN 038709539X. 2, 5
- Y. Lee, N. Amer, and W. C. Hurlbut. Terahertz pulse shaping via optical rectification in poled lithium niobate. *Applied Physics Letters*, 82(2):170–172, Jan. 2003. 10.1063/1.1535268. 9
- I. Leiserson, S. G. Lipson, and V. Sarafis. Superresolution in far-field imaging. *Optics Letters*, 25(4):209–211, Feb. 2000. 10.1364/OL.25.000209. 24
- A. Leitenstorfer, S. Hunsche, J. Shah, M. C. Nuss, and W. H. Knox. Detectors and sources for ultrabroadband electro-optic sampling: Experiment and theory. *Applied Physics Letters*, 74(11):1516(3pp), 1999. 10.1063/1.123601. 15
- I. Leiserson, S. G. Lipson, and V. Sarafis. Superresolution in far-field imaging. *Journal of the Optical Society of America A*, 19(3):436–443, Mar. 2002. 10.1364/JOSAA.19.000436. 24, 25
- J. Leskovec. Dimensionality reduction PCA, SVD, MDS, ICA, and friends, Apr. 2006. URL http://www.cs.cmu.edu/~guestrin/Class/10701-S06/Handouts/recitations/recitation-pca_svd.ppt. 64
- D. E. Lewis, R. A. Stradling, and J. R. Birch. Fourier transform spectroscopic studies of a germanium hot hole laser. *Infrared Physics*, 33(4):293–299, 1992. 10.1016/0020-0891(92)90025-O. 7
- Y. Li, L. Li, A. Hellicar, and Y. J. Guo. Super-resolution reconstruction of terahertz images. In J. O. Jensen, H. Cui, D. L. Woolard, and R. J. Hwu, editors, *Terahertz for Military and Security Applications VI*, volume 6949, page 69490J(9pp), Orlando, FL, USA, Apr. 2008. SPIE. 10.1117/12.777814. 26
- Z. Li, M. Grimsditch, C. M. Foster, and S. Chan. Dielectric and elastic properties of ferroelectric materials at elevated temperature. *Journal of Physics and Chemistry of Solids*, 57(10):1433–1438, 1996. 10.1016/0022-3697(96)00009-1. 38, 99, 102
- D. R. Lide. *CRC Handbook of Chemistry and Physics, 82nd Edition*. Chapman & Hall/CRC, 82nd edition, June 2001. ISBN 0849304822. 42

- K. P. Liessmann. *Teorie nevzdělanosti*. Academia, Praha, 2008. ISBN 978-80-200-1677-5. EAN 9788020016775. 62
- K. Liu, J. Xu, and X. Zhang. GaSe crystals for broadband terahertz wave detection. *Applied Physics Letters*, 85(6): 863–865, Aug. 2004. 10.1063/1.1779959. 10
- E. V. Loewenstein and D. R. Smith. Optical constants of far infrared materials. i: Analysis of channeled spectra and application to mylar. *Applied Optics*, 10(3):577–583, Mar. 1971. 10.1364/AO.10.000577. 37
- T. Löffler, F. Jacob, and H. G. Roskos. Generation of terahertz pulses by photoionization of electrically biased air. *Applied Physics Letters*, 77(3):453(3pp), 2000. 10.1063/1.127007. 8
- T. Löffler, K. Siebert, S. Czasch, T. Bauer, and H. G. Roskos. Visualization and classification in biomedical terahertz pulsed imaging. *Physics in Medicine and Biology*, 47(21):3847–3852, Oct. 2002. 10.1088/0031-9155/47/21/324. 17, 20, 65
- T. Löffler, T. Hahn, M. Thomson, F. Jacob, and H. Roskos. Large-area electro-optic ZnTe terahertz emitters. *Optics Express*, 13(14):5353–5362, July 2005. 10.1364/OPEX.13.005353. 25
- L. Luo and M. Fan. High resolution imaging by random disturbing wave front phase. In *Proceedings of SPIE*, pages 662319–662319–9, Beijing, China, 2007. SPIE. 10.1117/12.791499. 26
- A. Maestrini, J. Ward, G. Chattopadhyay, E. Schlecht, and I. Mehdì. Terahertz sources based on frequency multiplication and their applications. *Frequenz, Journal of RF-Engineering and Telecommunications*, 62(5/6): 118–122, June 2008. 12
- S. Mair, B. Gompf, and M. Dressel. Spatial and spectral behavior of the optical near field studied by a terahertz near-field spectrometer. *Applied Physics Letters*, 84(7):1219–1221, Feb. 2004. 10.1063/1.1647707. 31
- H. Manohara. Field emission testing of carbon nanotubes for THz frequency vacuum microtube sources. In *Proceedings of SPIE*, volume 5343, pages 227–234, San Jose, CA, USA, Jan. 2004. SPIE. 10.1117/12.531403. 10
- H. M. Manohara, P. H. Siegel, C. Marrese, J. Xu, and B. Chang. Design and fabrication of a 1200 GHz nanoklystron. In *Proceedings of International Conference on Terahertz Electronics*, volume 818, pages 4–7, Charlottesville, VA, USA, Oct. 2001. 10
- H. Martens and T. Næs. *Multivariate Calibration*. John Wiley & Sons, Inc., Apr. 1991. ISBN 978-0-471-93047-1. 64, 68
- J. Masson, M. Sauviat, and G. Gallot. Ionic contrast terahertz time resolved imaging of frog auricular heart muscle electrical activity. *Applied Physics Letters*, 89(15):153904–3, Oct. 2006a. 10.1063/1.2360931. 31
- J. Masson, M. Sauviat, J. Martin, and G. Gallot. Ionic contrast terahertz near-field imaging of axonal water fluxes. *Proceedings of the National Academy of Sciences of the United States of America*, 103(13):4808–4812, Mar. 2006b. 10.1073/pnas.0510945103. 31
- L. M. Matarrese and K. M. Evenson. Improved coupling to infrared whisker diodes by use of antenna theory. *Applied Physics Letters*, 17(1):8–10, July 1970. 10.1063/1.1653250. 28
- K. A. McIntosh, E. R. Brown, K. B. Nichols, O. B. McMahon, W. F. DiNatale, and T. M. Lyszczarz. Terahertz photomixing with diode lasers in low-temperature-grown GaAs. *Applied Physics Letters*, 67(26):3844(3pp), 1995. 10.1063/1.115292. 9
- R. Mendis and D. Grischkowsky. Undistorted guided-wave propagation of subpicosecond terahertz pulses. *Optics Letters*, 26(11):846–848, June 2001. 10.1364/OL.26.000846. 32
- R. Mendis and D. M. Mittleman. An investigation of the lowest-order transverse-electric (TE₁) mode of the parallel-plate waveguide for THz pulse propagation. *Journal of the Optical Society of America B*, 26(9):A6–A13, 2009. 10.1364/JOSAB.26.0000A6. 55
- S. P. Micken, R. Shvartsman, J. Munch, X. C. Zhang, and D. Abbott. Low noise laser-based T-ray spectroscopy

- of liquids using double-modulated differential time-domain spectroscopy. *Journal of Optics B: Quantum and Semiclassical Optics*, 6(8):S786–S795, July 2004. 10.1088/1464-4266/6/8/025. 16
- Z. Mics, F. Kadlec, P. Kužel, P. Jungwirth, S. E. Bradforth, and V. A. Apkarian. Nonresonant ionization of oxygen molecules by femtosecond pulses: Plasma dynamics studied by time-resolved terahertz spectroscopy. *The Journal of Chemical Physics*, 123(10):104310–10, Sept. 2005. 10.1063/1.2032987. 16
- R. Miles, X. Zhang, H. Eisele, and A. Krotkus. *Terahertz Frequency Detection and Identification of Materials and Objects*. Number Physics and Biophysics in NATO Science for Peace and Security. Springer, 1st edition, Sept. 2007. ISBN 1402065019. 3
- O. Mitrofanov, I. Brener, R. Harel, J. D. Wynn, L. N. Pfeiffer, K. W. West, and J. Federici. Terahertz near-field microscopy based on a collection mode detector. *Applied Physics Letters*, 77(22):3496–3498, Nov. 2000. 10.1063/1.1328772. 31
- O. Mitrofanov, M. Lee, J. W. P. Hsu, I. Brener, R. Harel, J. F. Federici, J. D. Wynn, L. N. Pfeiffer, and K. W. West. Collection-Mode Near-Field imaging with 0.5-THz pulses. *IEEE Journal of Selected Topics in Quantum Electronics*, 7(4):600–607, Aug. 2001a. 10.1109/2944.974231. 31
- O. Mitrofanov, M. Lee, J. W. P. Hsu, L. N. Pfeiffer, K. W. West, J. D. Wynn, and J. F. Federici. Terahertz pulse propagation through small apertures. *Applied Physics Letters*, 79(7):907–909, 2001b. 10.1063/1.1392303. 31
- D. M. Mittleman, editor. *Sensing with Terahertz Radiation*. Springer, 1st edition, June 2004. ISBN 978-3-540-43110-7. 2, 19, 55
- D. M. Mittleman, S. Hunsche, L. Boivin, and M. C. Nuss. T-ray tomography. *Optics Letters*, 22(12):904–906, June 1997. 10.1364/OL.22.000904. 20
- P. Mukherjee and B. Gupta. Terahertz (THz) frequency sources and antennas – a brief review. *International Journal of Infrared and Millimeter Waves*, 29(12):1091–1102, Sept. 2008. 10.1007/s10762-008-9423-0. 5
- H. Murakami and M. Tonouchi. Laser terahertz emission microscopy. *Comptes Rendus Physique*, 9(2):169–183, Mar. 2008. 10.1016/j.crhy.2007.07.010. 31
- A. Nahata and T. F. Heinz. Detection of freely propagating terahertz radiation by use of optical second-harmonic generation. *Optics Letters*, 23(1):67–69, Jan. 1998. 10.1364/OL.23.000067. 15
- A. Nahata, D. H. Auston, C. Wu, and J. T. Yardley. Generation of terahertz radiation from a poled polymer. *Applied Physics Letters*, 67(10):1358–1360, 1995. 10.1063/1.115550. 10
- A. Nahata, D. H. Auston, T. F. Heinz, and C. Wu. Coherent detection of freely propagating terahertz radiation by Electro-Optic sampling. *Applied Physics Letters*, 68(2):150–152, Jan. 1996a. 10.1063/1.116130. 10, 14
- A. Nahata, A. S. Weling, and T. F. Heinz. A wideband coherent terahertz spectroscopy system using optical rectification and electro-optic sampling. *Applied Physics Letters*, 69(16):2321–2323, Oct. 1996b. 10.1063/1.117511. 15
- S. Nakajima, H. Hoshina, M. Yamashita, and C. Otani. Terahertz imaging diagnostics of cancer tissues with a chemometrics technique. *Applied Physics Letters*, 90(4):041102 (3pp), Jan. 2007. 10.1063/1.2433035. 20, 64
- S. I. Newton. *Opticks: or, a Treatise of the Reflections, Refractions, Inflections and Colours of Light. Also Two Treatises of the Species and Magnitude of Curvilinear Figures*. self-published, London, 4th edition, 1704. 23
- A. S. Nikoghosyan, E. M. Laziev, R. M. Martirosyan, A. A. Hakhoumian, J. M. Chamberlain, R. A. Dudley, and N. N. Zinov'ev. Generation of terahertz radiation in nonlinear waveguides. In *Infrared and Millimeter Waves, 2004 and 12th International Conference on Terahertz Electronics, 2004. Conference Digest of the 2004 Joint 29th International Conference on*, pages 313–314, Univ Karlsruhe, Karlsruhe, GERMANY, Sept. 2004. 10.1109/ICIMW.2004.1422082. 33
- L. Noakes and R. Kozera. The 2-D leap-frog: Integrability, noise, and digitization. In *Digital and Image Geometry*, volume 2243 of *Lecture Notes in Computer Science*, pages 101–112. Springer Berlin / Heidelberg, 2001. ISBN 978-3-540-43079-7. 60

- I. Noda and Y. Ozaki. *Two-Dimensional Correlation Spectroscopy: Applications in Vibrational and Optical Spectroscopy*. John Wiley & Sons, Ltd., July 2002. ISBN 0471623911. 64
- M. C. Nuss and J. Orenstein. Terahertz time-domain spectroscopy (chapter 2). In G. Grüner, editor, *Millimeter and Submillimeter Wave Spectroscopy of Solids*, number 74 in Topics in Applied Physics, pages 7–50. Springer-Verlag Telos, 1 edition, Nov. 1998. ISBN 3540628606. 16
- G. H. Nussbaum. *Physical Aspects of Hyperthermia*. Number 8 in Medical physics monograph. published for the American Association of Physicists in Medicine by the American Institute of Physics, New York, 1982. ISBN 0883184141. 4
- H. Němec. *Time-resolved terahertz spectroscopy applied to the investigation of magnetic materials and photonic structures*. Diploma thesis, Charles University, 2006. 16
- H. Němec, F. Kadlec, C. Kadlec, P. Kužel, and P. Jungwirth. Ultrafast far-infrared dynamics probed by terahertz pulses: A frequency domain approach. II. applications. *Journal of Chemical Physics*, 122(10):104504(8pp), Mar. 2005a. 10.1063/1.1857871. 17
- H. Němec, F. Kadlec, S. Surendran, P. Kužel, and P. Jungwirth. Ultrafast far-infrared dynamics probed by terahertz pulses: A frequency domain approach. i. model systems. *Journal of Chemical Physics*, 122(5):104503(12pp), Mar. 2005b. 10.1063/1.1857851. 17
- J. R. Oleson. Regional power deposition for hyperthermia: Theoretical approaches and considerations. *Cancer Research*, 44(10 Supplement):4761s–4764s, Oct. 1984. 4
- C. on Assessment of Security Technologies for Transportation and N. R. Council. *Assessment of Millimeter-Wave and Terahertz Technology for Detection and Identification of Concealed Explosives and Weapons*. National Academies Press, Mar. 2007. ISBN 0309104696. 20
- D. Palanker, G. Knippels, T. Smith, and H. Schwettman. Fast IR imaging with sub-wavelength resolution using a transient near-field probe. *Nuclear Instruments and Methods in Physics Research, Section B: Beam Interactions with Materials and Atoms*, 144(1–4):240–245, 1998a. 30
- D. V. Palanker, G. M. H. Knippels, T. I. Smith, and H. A. Schwettman. IR microscopy with a transient photo-induced near-field probe (tipless near-field microscopy). *Optics Communications*, 148(4):215–220, Mar. 1998b. 10.1016/S0030-4018(97)00702-5. 30
- V. V. Parshin. Dielectric materials for gyrotron output windows. *International Journal of Infrared and Millimeter Waves*, 15(2):339–348, Feb. 1994. 10.1007/BF02096245. 19
- A. Pashkin. *Terahertz spectroscopy of ferroelectrics and related materials*. Doctoral thesis, Charles University in Prague, Prague, 2004. 6
- J. Pei, Y. Hu, and W. Xie. PCA-based visualization of terahertz time-domain spectroscopy image. In H. Maître, H. Sun, J. Liu, and E. Song, editors, *Proceedings of SPIE*, volume 6787, pages 67871M–7, Wuhan Hubei, China, Nov. 2007. 10.1117/12.749995. 64
- J. B. Pendry. Negative refraction makes a perfect lens. *Physical Review Letters*, 85(18):3966–3969, Oct. 2000. 10.1103/PhysRevLett.85.3966. 25
- E. Pickwell and V. P. Wallace. Biomedical applications of terahertz technology. *Journal of Physics D: Applied Physics*, 39(17):R301–R310, Sept. 2006. 10.1088/0022-3727/39/17/R01. 20
- E. Pickwell, B. E. Cole, A. J. Fitzgerald, V. P. Wallace, and M. Pepper. Simulation of terahertz pulse propagation in biological systems. *Applied Physics Letters*, 84(12):2190(3pp), 2004. 10.1063/1.1688448. 20
- R. Piesiewicz, C. Jansen, S. Wietzke, D. Mittleman, M. Koch, and T. Kürner. Properties of building and plastic materials in the THz range. *International Journal of Infrared and Millimeter Waves*, 28(5):363–371, May 2007. 10.1007/s10762-007-9217-9. 20
- M. Planck. On the law of distribution of energy in the normal spectrum. *Annalen der Physik*, 4:553, 1901. 6

- P. C. Planken, H. K. Nienhuys, H. J. Bakker, and T. Wenckebach. Measurement and calculation of the orientation dependence of terahertz pulse detection in ZnTe. *Journal of the Optical Society of America B*, 18(3):313–317, Mar. 2001. 10.1364/JOSAB.18.000313. 14, 19
- P. C. M. Planken and N. C. J. van der Valk. Spot-size reduction in terahertz apertureless near-field imaging. *Optics Letters*, 29(19):2306–2308, Oct. 2004. 10.1364/OL.29.002306. 31
- P. C. M. Planken, C. E. W. M. van Rijmenam, and R. N. Schouten. Opto-electronic pulsed THz systems. *Semiconductor Science and Technology*, 20(7):S121–S127, July 2005. 10.1088/0268-1242/20/7/001. 31
- W. H. Press, S. A. Teukolsky, W. T. Vetterling, and B. P. Flannery. *Numerical Recipes : The Art of Scientific Computing*. Cambridge University Press, UK, 3rd edition, Sept. 2007. ISBN 0521880688. 63, 66, 67
- B. qing Wang and X. guo Li. Near range millimeter wave radiometer passive image high resolution restoration. In *2008 Global Symposium on Millimeter Waves*, pages 325–328, Nanjing, China, Apr. 2008. 10.1109/GSMM.2008.4534635. 26
- R Development Core Team. *R: A Language and Environment for Statistical Computing*. Vienna, Austria, 2010. ISBN 3-900051-07-0. URL <http://www.R-project.org>. 66, 73
- B. P. Ramsay, E. L. Cleveland, and O. T. Koppius. Criteria and the intensity-epoch slope. *Journal of the Optical Society of America*, 31(1):26–32, Jan. 1941. 10.1364/JOSA.31.000026. 23
- A. C. Rencher. *Methods of Multivariate Analysis*. Wiley-Interscience, 2nd edition, Mar. 2002. ISBN 0471418897. 63
- J. A. Riordan, F. G. Sun, Z. G. Lu, and X. Zhang. Free-space transient magneto-optic sampling. *Applied Physics Letters*, 71(11):1452(3pp), 1997. 10.1063/1.119934. 15
- B. Rosner, J. Peck, and D. van der Weide. Near-field antennas integrated with scanning probes for THz to visible microscopy: scale modeling and limitations on performance. *IEEE Transactions on Antennas and Propagation*, 50(5):670–675, May 2002a. 10.1109/TAP.2002.1011233. 32, 41
- B. T. Rosner, T. Bork, V. Agrawal, and D. W. van der Weide. Microfabricated silicon coaxial field sensors for near-field scanning optical and microwave microscopy. *Sensors and Actuators A: Physical*, 102(1-2):185–194, Dec. 2002b. 10.1016/S0924-4247(02)00341-2. 32
- R. Rozental, N. Ginzburg, M. Glyavin, and A. Sergeev. Novel source of the chaotic microwave radiation based on the gyrotron Backward-Wave oscillator. In *2005 European Microwave Conference*, volume 2, pages 1367–1370, CNIT la Defense, Paris, France, Oct. 2005. 10.1109/EUMC.2005.1610190. 7
- H. Rubens and B. W. Snow. On the refraction of rays of great wavelength in rock salt, sylvine, and fluorite. *Philosophical Magazine Series 5*, 35(212):35–45, Jan. 1893. 10.1080/14786449308620376. 3
- J. V. Rudd and D. M. Middleman. Influence of substrate-lens design in terahertz time-domain spectroscopy. *Journal of the Optical Society of America B*, 19(2):319–337, Feb. 2002. 10.1364/JOSAB.19.000319. 55
- C. Rullière, editor. *Femtosecond Laser Pulses: Principles and Experiments*. Springer, 2nd edition, 2003. ISBN 0-387-01769-0. 31
- K. Sakai. *Terahertz Optoelectronics*. Number 97 in Topics in Applied Physics. Springer, 1st edition, July 2005. ISBN 978-3-540-20013-0. 2, 9, 12, 16, 20
- B. E. A. Saleh and M. C. Teich. *Fundamentals of Photonics*. Wiley-Interscience, 2 edition, Mar. 2007. ISBN 0471358320. 22, 23, 36
- S. Sasic and Y. Ozaki. Statistical two-dimensional correlation spectroscopy: its theory and applications to sets of vibrational spectra. *Analytical Chemistry*, 73(10):2294–2301, May 2001. 10.1021/ac0014010. 64
- U. Schade, K. Holldack, P. Kuske, G. Wustefeld, and H. Hubers. THz near-field imaging employing synchrotron radiation. *Applied Physics Letters*, 84(8):1422–1424, Feb. 2004. 10.1063/1.1650034. 32
- U. Schade, K. Holldack, M. C. Martin, and D. Fried. THz near-field imaging of biological tissues employing

- synchrotron radiation. In *SPIE Proceedings, Photonics West*, volume 5725, pages 46–52, San Jose, CA, USA, Apr. 2005. SPIE. 10.1117/12.590731. Invited paper. 20, 32
- M. Schmidt, S. Rajagopal, Z. Ren, and K. Moffat. Application of singular value decomposition to the analysis of Time-Resolved macromolecular X-Ray data. *Biophysical Journal*, 84(3):2112–2129, Mar. 2002. 10.1016/S0006-3495(03)75018-8. 64
- C. A. Schmuttenmaer. Exploring dynamics in the far-infrared with terahertz spectroscopy. *Chemical Reviews*, 104(4):1759–1780, Apr. 2004. 10.1021/cr020685g. 16
- A. Schneider, I. Biaggio, and P. Günter. Optimized generation of THz pulses via optical rectification in the organic salt DAST. *Optics Communications*, 224(4–6):337–341, Sept. 2003. 10.1016/j.optcom.2003.07.013. 10
- A. Schneider, M. Neis, M. Stillhart, B. Ruiz, R. U. A. Khan, and P. Günter. Generation of terahertz pulses through optical rectification in organic DAST crystals: theory and experiment. *Journal of the Optical Society of America B*, 23(9):1822–1835, 2006. 10.1364/JOSAB.23.001822. 10
- M. Schnell, A. García-Etxarri, A. J. Huber, K. Crozier, J. Aizpurua, and R. Hillenbrand. Controlling the near-field oscillations of loaded plasmonic nanoantennas. *Nature Photonics*, 3(5):287–291, Apr. 2009. 10.1038/nphoton.2009.46. 28
- C. A. Schuttenmaer. A new method for measuring intramolecular charge transfer. *Science Progress*, 85(2):175–197, May 2002. 10.3184/003685002783238834. 3, 16
- C. J. Schwarz, Y. Kuznetsova, and S. R. J. Brueck. Imaging interferometric microscopy. *Optics Letters*, 28(16):1424–1426, Aug. 2003. 10.1364/OL.28.001424. 25
- K. Seeger. Microwave dielectric constants of silicon, gallium arsenide, and quartz. *Journal of Applied Physics*, 63(11):5439–5443, Feb. 1988. 10.1063/1.341153. 38, 40
- M. A. Seo, A. J. L. Adam, J. H. Kang, J. W. Lee, S. C. Jeoung, Q. H. Park, P. C. M. Planken, and D. S. Kim. Fourier-transform terahertz near-field imaging of one-dimensional slit arrays: mapping of electric-field-, magnetic-field-, and Poynting vectors. *Optics Express*, 15(19):11782–11790, Sept. 2007. 10.1364/OE.15.011781. 30, 31
- M. A. Seo, H. R. Park, S. M. Koo, D. J. Park, J. H. Kang, O. K. Suwal, S. S. Choi, P. C. M. Planken, G. S. Park, N. K. Park, Q. H. Park, and D. S. Kim. Terahertz field enhancement by a metallic nano slit operating beyond the skin-depth limit. *Nature Photonics*, 3(3):152–156, Mar. 2009. 10.1038/nphoton.2009.22. 31
- S. Sharma. *Applied multivariate techniques*. John Wiley & Sons, Inc., Oct. 1995. ISBN 978-0-471-31064-8. 68
- P. Siegel. Terahertz technology in biology and medicine. *IEEE Transactions on Microwave Theory and Techniques*, 52(10):2438–2447, Oct. 2004. 10.1109/TMTT.2004.835916. 17
- P. H. Siegel and V. Piov. THz in biology and medicine: toward quantifying and understanding the interaction of millimeter- and submillimeter-waves with cells and cell processes. In E. D. Jansen and R. J. Thomas, editors, *Optical Interactions with Tissues and Cells XXI*, volume 7562, page 75620H(13pp), San Francisco, California, USA, Feb. 2010. SPIE. 10.1117/12.845380. 4
- A. M. Sinyukov and L. M. Hayden. Generation and detection of terahertz radiation with multilayered electro-optic polymer films. *Optics Letters*, 27(1):55–57, Jan. 2002. 10.1364/OL.27.000055. 10
- F. Sizov. THz radiation sensors. *Opto-Electronics Review*, 18(1):10–36, Dec. 2009. 10.2478/s11772-009-0029-4. 5
- P. R. Smith, D. H. Auston, and M. C. Nuss. Subpicosecond photoconducting dipole antennas. *IEEE Journal of Quantum Electronics*, 24(2):255–260, Feb. 1988. 10.1109/3.121. 10
- A. Sommerfeld. Über die fortpflanzung elektrodynamischer wellen längs eines drahtes. *Annalen der Physik*, 303(2):233–290, 1899a. 10.1002/andp.18993030202. 28
- A. Sommerfeld. Über die fortpflanzung elektrodynamischer wellen längs eines drahtes. *Annalen der Physik und Chemie*, 67:233–290, 1899b. 28

- G. Staats, L. Fernandez, K. Holldack, U. Schade, and D. Schondelmaier. Coupling structures for terahertz near-field microspectroscopy. *Infrared Physics & Technology*, 49:122–127, Mar. 2006. 10.1016/j.infrared.2006.01.025. 32
- D. E. Steinhauer and S. M. Anlage. Microwave frequency ferroelectric domain imaging of deuterated triglycine sulfate crystals. *Journal of Applied Physics*, 89(4):2314–2321, 2001. 10.1063/1.1337600. 33
- T. Tamir. *Integrated Optics*. Springer-Verlag, 2 edition, Sept. 1979. ISBN 0387096736. 33
- M. Tani, Y. Hirota, C. Que, S. Tanaka, R. Hattori, M. Yamaguchi, S. Nishizawa, and M. Hangyo. Novel terahertz photoconductive antennas. *International Journal of Infrared and Millimeter Waves*, 27(4):531–546, Apr. 2006. 10.1007/s10762-006-9105-8. 12
- C. C. S. Technology. Design software tool with complete technology. *Microwave Journal*, 52(11):110–, Nov. 2009. 60
- TeraView Ltd. TPS spectra 3000, Jan. 2010. URL <http://www.teraview.com/files/uploaded/File/TPS3000access2.pdf>. 5
- L. Thiesan, D. W. Hannum, D. W. Murray, and J. E. Parmeter. Survey of commercially available explosives detection technologies and equipment 2004. Technical Report 208861, U. S. Department of Justice, United States of America, Nov. 2004. The National Law Enforcement and Correction Technology Center, a Program of the National Institute of Justice, U.S. Department of Justice. 20
- A. Thoma and T. Dekorsy. Influence of tip-sample interaction in a time-domain terahertz scattering near field scanning microscope. *Applied Physics Letters*, 95(25):251103 (3pp), June 2008. 10.1063/1.2949858. 28
- THz-BRIDGE and G. P. Gallerano. Tera-hertz radiation in biological research, investigations on diagnostics and study on potential genotoxic effects. Final report, THz bridge Consortium, Europe, May 2004. 4, 17
- N. H. Timm. *Applied multivariate analysis*. Springer, 1st edition, June 2002. ISBN 0387953477. 64
- M. Tonouchi. Cutting-edge terahertz technology. *Nature Photonics*, 1(2):97–105, Feb. 2007. 10.1038/nphoton.2007.3. 2
- L. N. Trefethen and D. I. Bau. *Numerical Linear Algebra*. SIAM: Society for Industrial and Applied Mathematics, June 1997. ISBN 0898713617. 66, 68
- A. Tselev, S. M. Anlage, H. M. Christen, R. L. Moreland, V. V. Talanov, and A. R. Schwartz. Near-field microwave microscope with improved sensitivity and spatial resolution. *Review of Scientific Instruments*, 74(6):3167–3170, June 2003. 10.1063/1.1571954. 33
- D. Turchinovich and J. I. Dijkhuis. Performance of combined $\langle 100 \rangle$ - $\langle 110 \rangle$ ZnTe crystals in an amplified THz time-domain spectrometer. *Optics Communications*, 270(1):96–99, Feb. 2007. 10.1016/j.optcom.2006.08.045. 19
- N. C. J. van der Valk and P. C. M. Planken. Electro-optic detection of subwavelength terahertz spot sizes in the near field of a metal tip. *Applied Physics Letters*, 81(9):1558–1561, Aug. 2002. 10.1063/1.1503404. 30, 31
- N. C. J. van der Valk, T. Wenckebach, and P. C. M. Planken. Full mathematical description of electro-optic detection in optically isotropic crystals. *Journal of the Optical Society of America B*, 21(3):622–631, Mar. 2004. 10.1364/JOSAB.21.000622. 14
- M. van Exter, C. Fattinger, and D. Grischkowsky. Terahertz time-domain spectroscopy of water vapor. *Optics Letters*, 14(20):1128–1130, Oct. 1989. 10.1364/OL.14.001128. 18
- D. S. Venables and C. A. Schmuttenmaer. Spectroscopy and dynamics of mixtures of water with acetone, acetonitrile, and methanol. *The Journal of Chemical Physics*, 113(24):11222(15pp), Dec. 2000. 10.1063/1.1328072. 20
- H. von Ribbeck, M. Brehm, D. W. van der Weide, S. Winnerl, O. Drachenko, M. Helm, and F. Keilmann. Spectroscopic THz near-field microscope. *Optics Express*, 16(5):3430–3438, Mar. 2008. 10.1364/OE.16.003430. 28
- M. Wächter, M. Nagel, and H. Kurz. Frequency-dependent characterization of THz sommerfeld wave propagation on single-wires. *Optics Express*, 13(26):10815–10822, 2005. 10.1364/OPEX.13.010815. 28

- M. Wächter, M. Nagel, and H. Kurz. Tapered photoconductive terahertz field probe tip with subwavelength spatial resolution. *Applied Physics Letters*, 95(4):041112(3pp), 2009. 10.1063/1.3189702. 33
- G. C. Walker, E. Berry, N. N. Zinov'ev, A. J. Fitzgerald, R. E. Miles, J. M. Chamberlain, and M. A. Smith. Terahertz imaging and international safety guidelines. In L. E. Antonuk and M. J. Yaffe, editors, *Medical Imaging 2002: Physics of Medical Imaging*, volume 4682, pages 683–690, San Diego, CA, USA, May 2002. SPIE. 10.1117/12.465614. 4
- M. E. Wall, A. Rechtsteiner, and L. M. Rocha. Singular value decomposition and principal component analysis. In D. P. Berrar, W. Dubitzky, and M. . Granzow, editors, *A Practical Approach to Microarray Data Analysis.*, pages 91–109. Norwell, M, Kluwer, 2003. 68, 70
- V. P. Wallace, A. J. Fitzgerald, S. Shankar, N. Flanagan, R. Pye, J. Cluff, and D. D. Arnone. Dermatological surgery and lasers: Terahertz pulsed imaging of basal cell carcinoma ex vivo and in vivo. *British Journal of Dermatology*, 151(2):424–432, 2004. 10.1111/j.1365-2133.2004.06129.x. 20
- M. Walther. *Modern spectroscopy on biological molecules: structure and bonding investigated by THz time-domain and transient phase-grating spectroscopy*. PhD, Fakultät für Mathematik und Physik der Albert-Ludwigs-Universität Freiburg im Breisgau, Breisgau, Nov. 2003. 16
- M. Walther, D. G. Cooke, C. Sherstan, M. Hajar, M. R. Freeman, and F. A. Hegmann. Terahertz conductivity of thin gold films at the metal-insulator percolation transition. *Physical Review B*, 76(12):125408(9pp), Sept. 2007. 10.1103/PhysRevB.76.125408. 20, 36
- K. Wang and D. Mittleman. Guided propagation of terahertz pulses on metal wires. In *Terahertz Frequency Detection and Identification of Materials and Objects*, volume 2007 of *NATO Security through Science Series*, pages 55–68. Springer Netherlands, 2007. ISBN 978-140206502-6. 10.1007/978-1-4020-6503-3_5. 28
- K. Wang, A. Barkan, and D. M. Mittleman. Propagation effects in apertureless near-field optical antennas. *Applied Physics Letters*, 84(2):305(3pp), 2004. 10.1063/1.1640473. 28
- R. Wang, W. Fang, P. Zhao, C. Zhang, L. Zhang, J. Ge, H. Zhang, J. Shao, S. Hu, X. Shen, and N. Dai. Growth and characterization of <110> oriented ZnTe single crystal. In Y. Cai, H. Gong, and J. Chatard, editors, *Infrared Materials, Devices, and Applications*, volume 6835, page 683519(8pp), Beijing, China, Nov. 2007. SPIE. 10.1117/12.754091. 19
- X. Wang, Y. Cui, D. Hu, W. Sun, J. Ye, and Y. Zhang. Terahertz quasi-near-field real-time imaging. *Optics Communications*, 282(24):4683–4687, Dec. 2009a. 10.1016/j.optcom.2009.09.004. 33
- Y. Wang, Z. Chen, Z. Zhao, L. Zhang, K. Kang, and Y. Zhang. Restoration of terahertz signals distorted by atmospheric water vapor absorption. *Journal of Applied Physics*, 105(10):103105(7pp), 2009b. 10.1063/1.3129308. 18
- Z. Wang. Generation of terahertz radiation via nonlinear optical methods. *IEEE Transactions on Geoscience and Remote Sensing*, 1(1):1–5, May 2005. 9
- J. S. Ward, G. Chattopadhyay, J. Gill, H. Javadi, C. Lee, R. Lin, A. Maestrinia, F. Maiwald, I. Mehdi, E. Schlecht, and P. Siegel. Tunable broadband frequency-multiplied terahertz sources. In *2008 33rd International Conference on Infrared, Millimeter and Terahertz Waves*, volume 1 & 2, pages 52–54, Pasadena, CA, USA, Sept. 2008. IEEE. ISBN 978-1-4244-2119-0. 5, 8
- R. R. Warner, M. C. Myers, and D. A. Taylor. Electron probe analysis of human skin: determination of the water concentration profile. *The Journal of Investigative Dermatology*, 90(2):218–224, Feb. 1988. 10.1111/1523-1747.ep12462252. 4
- T. Weiland. A discretization model for the solution of maxwell's equations for 6-component fields. *Archiv fuer Elektronik und Übertragungstechnik*, 31(3):116–120, Mar. 1977. 60
- T. Weiland. Time domain electromagnetic field computation with finite difference methods. *International Journal of Numerical Modelling: Electronic Networks, Devices and Fields*, 9(4):295–319, 1996. 10.1002/(SICI)1099-1204(199607)9:4<295::AID-JNM240>3.0.CO;2-8. 60

- G. P. Williams. High-power terahertz synchrotron sources. *Philosophical Transactions: Mathematical, Physical and Engineering Sciences*, 362(1815):403–414, Feb. 2004. 5, 6
- S. Winnerl, F. Peter, S. Nitsche, A. Dreyhaupt, B. Zimmermann, M. Wagner, H. Schneider, M. Helm, and K. Köhler. Generation and detection of THz radiation with scalable antennas based on GaAs substrates with different carrier lifetimes. *IEEE Journal of Selected Topics in Quantum Electronics*, 14(2):449–457, 2008. 10.1109/JSTQE.2007.910104. 14
- C. Winnewisser, P. U. Jepsen, M. Schall, V. Schuja, and H. Helm. Electro-optic detection of THz radiation in LiTaO₃, LiNbO₃ and ZnTe. *Applied Physics Letters*, 70(23):3069–3070, June 1997. 10.1063/1.119093. 9
- W. Withayachumnankul, G. M. Png, X. Yin, S. Atakaramians, I. Jones, H. Lin, B. S. Y. Ung, J. Balakrishnan, B. W. Ng, B. Ferguson, S. P. Mickan, B. M. Fischer, and D. Abbott. T-ray sensing and imaging. *Proceedings of the IEEE*, 95(8):1528–1558, Aug. 2007. 10.1109/JPROC.2007.900325. 20
- W. Withayachumnankul, B. M. Fischer, and D. Abbott. Numerical removal of water vapour effects from terahertz time-domain spectroscopy measurements. *Proceedings of the Royal Society A*, 464(2097):2435–2456, Sept. 2008. 10.1098/rspa.2007.0294. 18
- R. M. Woodward. Terahertz technology in the medical and pharmaceutical industry. *Preclinica Research Articles*, 2(5):328–335, Oct. 2004. 17
- R. M. Woodward, B. E. Cole, V. P. Wallace, R. J. Pye, D. D. Arnone, E. H. Linfield, and M. Pepper. Terahertz pulse imaging in reflection geometry of human skin cancer and skin tissue. *Physics in Medicine and Biology*, 47(21):3853–3863, Nov. 2002. 10.1088/0031-9155/47/21/325. 20
- D. Woolard, R. Brown, M. Pepper, and M. Kemp. Terahertz frequency sensing and imaging: A time of reckoning future applications? *Proceedings of the IEEE*, 93(10):1722–1743, 2005. 10.1109/JPROC.2005.853539. 20
- D. L. Woolard. *Terahertz Science And Technology For Military And Security Applications*. Selected Topics in Electronics and Systems. World Scientific Publishing Company, Sept. 2007. ISBN 9812771794. 20
- F. Wooten. *Optical Properties of Solids*. Academic Press, Inc., June 1972. ISBN 0127634509. no Abstract. 36
- Q. Wu and X. Zhang. Free-space electro-optic sampling of terahertz beams. *Applied Physics Letters*, 67(24):3523–3525, Dec. 1995. 10.1063/1.114909. 9, 14
- Q. Wu and X. Zhang. 7 terahertz broadband GaP electro-optic sensor. *Applied Physics Letters*, 70(14):1784(3pp), 1997a. 10.1063/1.118691. 9
- Q. Wu and X. Zhang. Free-space electro-optics sampling of mid-infrared pulses. *Applied Physics Letters*, 71(10):1285(2pp), 1997b. 10.1063/1.119873. 10
- Q. Wu, T. D. Hewitt, and X. C. Zhang. Two-dimensional electro-optic imaging of THz beams. *Applied Physics Letters*, 69(8):1026–1028, Aug. 1996. 10.1063/1.116920. 33
- T. Wu. Diamond schottky contact transit-time diode for terahertz power generation. *International Journal of Infrared and Millimeter Waves*, 29(7):634–640, Apr. 2008. 10.1007/s10762-008-9363-8. 8
- K. Wynne and D. A. Jaroszynski. Superluminal terahertz pulses. *Optics letters*, 24(1):25–27, Jan. 1999. 10.1364/OL.24.000025. 30
- Y. Yan, S. Liu, X. Li, W. Fu, and X. Yuan. Design and demonstration of a 0.22 THz gyrotron oscillator. *Chinese Science Bulletin*, 54(9):1495–1499, May 2009. 10.1007/s11434-009-0172-9. 6
- K. H. Yang, P. L. Richards, and Y. R. Shen. Generation of far-infrared radiation by picosecond light pulses in LiNbO₃. *Applied Physics Letters*, 19(9):320–323, Nov. 1971. 10.1063/1.1653935. 9
- J. Ye. Generalized low rank approximations of matrices. In *Proceedings of the twenty-first international conference on Machine learning*, volume 69, page 112(30pp), Banff, Alberta, Canada, 2004. ACM. ISBN 1-58113-828-5. 10.1145/1015330.1015347. 65
- X. X. Yin, K. M. Kong, J. W. Lim, B. W. H. Ng, B. Ferguson, S. P. Mickan, and D. Abbott. Enhanced T-ray signal

- classification using wavelet preprocessing. *Medical & Biological Engineering & Computing*, 45(6):611–616, June 2007. [10.1007/s11517-007-0185-y](https://doi.org/10.1007/s11517-007-0185-y). 65
- J. Yinon, editor. *Counterterrorist Detection Techniques of Explosives*. Elsevier Science, Aug. 2007. ISBN 0444522042. 20
- T. Yuan, H. Park, J. Xu, H. Han, and X. Zhang. THz wave near-field emission microscope. In *Ultrafast Phenomena XIV, Proceedings of the 14th International Conference*, volume 79, pages 759–761, Niigata, Japan, July 2004a. Springer Berlin Heidelberg. ISBN 978-3-540-27213-7. [10.1007/3-540-27213-5_232](https://doi.org/10.1007/3-540-27213-5_232). 30
- T. Yuan, J. Z. Xu, and X. C. Zhang. Development of terahertz wave microscopes. *Infrared Physics & Technology*, 45(5-6):417–425, Oct. 2004b. [10.1016/j.infrared.2004.01.016](https://doi.org/10.1016/j.infrared.2004.01.016). 30
- H. Zhan, R. Mendis, and D. M. Mittleman. Superfocusing terahertz waves below $\lambda/250$ using plasmonic parallel-plate waveguides. *Optics Express*, 18(9):9643–9650, Apr. 2010. [10.1364/OE.18.009643](https://doi.org/10.1364/OE.18.009643). 124
- X. Zhang. Terahertz wave imaging: Horizons and hurdles. *Physics in Medicine and Biology*, 47(21):3667–3677, Nov. 2002. [10.1088/0031-9155/47/21/301](https://doi.org/10.1088/0031-9155/47/21/301). 21
- X. Zhang. Three-Dimensional terahertz wave imaging. *Philosophical Transactions of the Royal Society A: Physical, Mathematical and Engineering Sciences*, 362:283–299, Feb. 2004. [10.1098/rsta.2003.1317](https://doi.org/10.1098/rsta.2003.1317). 20
- X. C. Zhang, X. F. Ma, Y. Jin, T. M. Lu, E. P. Boden, P. D. Phelps, K. R. Stewart, and C. P. Yakymyshyn. Terahertz optical rectification from a nonlinear organic crystal. *Applied Physics Letters*, 61(26):3080–3082, Dec. 1992. [10.1063/1.107968](https://doi.org/10.1063/1.107968). 10
- G. Zhao, R. N. Schouten, N. van der Valk, W. T. Wenckebach, and P. C. M. Planken. Design and performance of a THz emission and detection setup based on a semi-insulating GaAs emitter. *Review of Scientific Instruments*, 73(4):1715(5pp), 2002. [10.1063/1.1459095](https://doi.org/10.1063/1.1459095). 19
- V. S. Zuev and A. V. Frantnesson. Subwavelength electromagnetic-field narrowing. *Journal of Russian Laser Research*, 19(5):465–482, 1998. 28